

Modelling launch vehicle emissions in an evolving space sector



Robert J. Garner

Supervisor: **Dr Christie Maddock**

Department of Mechanical and Aerospace Engineering
University of Strathclyde

Submitted in partial fulfillment of the requirements for the degree of
Doctor of Philosophy

May 2022

I would like to dedicate this thesis to my loving grandparents, three of whom left us during the course of writing this thesis, and one who supports me to this day.

DECLARATION

This thesis is the result of the author's original research. It has been composed by the author and has not been previously submitted for examination which has led to the award of a degree.

The copyright of this thesis belongs to the author under the terms of the United Kingdom Copyright Acts as qualified by University of Strathclyde Regulation 3.50. Due acknowledgement must always be made of the use of any material contained in, or derived from, this thesis.

Robert J. Garner

May 2022

ABSTRACT

The space launch sector is currently undergoing intense change, where commercial competition increasingly dominates over traditional state-sponsored launch systems and the satellite market evolves with higher numbers of a small satellites requiring launch services. This has led to new types of vehicles, including reusable vertical launch, small rockets and winged vehicles and new propellants such as methane and propane being used. In parallel, concerns about anthropogenic climate change have led to further scrutiny and concern about the environmental impacts of all industries, and increasing application of tools such as environmental life cycle assessment to minimise emissions.

To be able to account for emissions of new or conceptual vehicles, an approach to estimate the emission profiles and environmental impacts is developed. This combines tools to model propulsion systems and optimise trajectories with various methods of quantifying environmental impact of emissions across the atmosphere. This approach has been applied to a set of different vehicles that represents the current state of the launch sector, as well as a number of future, conceptual vehicles (including air-launched winged vehicles, and a single-stage-to-orbit spaceplane). A new metric that combines the performance of a vehicle as well as its environmental impact is proposed, enabling the environmental impact of real and conceptual launch vehicles to be estimated and compared fairly.

The advantage of this modelling approach has also been investigated with two case studies to understand how environmental impact could be reduced during conceptual design, first through choice of rocket fuel, and the second by optimising the trajectory of a rocket to minimise radiative forcing instead of maximising useful payload.

ACKNOWLEDGEMENTS

This thesis is the culmination of a significant amount of time and effort. None of it would have been possible without those around me to support me. I would like to start by thanking the University of Strathclyde for funding this research and my supervisor Dr Christie Maddock for her support over the past years. I am also grateful to the Fulbright Commission for funding and Professor Steven Barrett for hosting me during my 6 months at MIT with his research group, a time that was fundamental to the work in this thesis. I'd also like to thank my colleagues at the UK Space Agency and CAA, who have given me their support to finish this thesis while working.

I'd like to recognise the friendship and support of my fellow PhD students at the university of Strathclyde: Ciara McGrath, for her endless support and friendship, Alessandro Mogavero, for his advice on modelling propulsion systems and Javier Herrera, for being a fantastic housemate and for being willing to help out. To Viola, who kept me fed and entertained, JJ for being at the heart of our Glaswegian family and to Federico for being my partner-in-crime - I will always miss having espressos four times a day, and the crazy conversations we used to have.

I owe a great debt to my family for supporting me in finishing this thesis. My Mum and Dad who are always there, always proud, and didn't mind too much when I moved half a world away. My brother who has graduated twice since I started this PhD. I have dedicated this thesis to my grandparents; WG, and Granny D and Gramps who are no longer with us (but look, it's almost finished!), and Granny who is always there in my support. Thanks as well to the endless list of friends who have been patient with me for many years, Joseph for his moral support and proofreading, Dan, Jeni and all those I've forgotten to mention here.

Finally, my love and endless gratitude to Áine, who has been enormously patient in her support of me finishing this thesis.

PUBLICATIONS

Conference proceedings and unpublished conference papers

Garner, Robert J.; Toso, Federico; Maddock, Christie Alisa. "Comparison of the emissions of current expendable launch vehicles and future spaceplanes." 67th International Astronautical Congress. 2016.

Garner, Robert J.; Maddock, Christie Alisa. "Emissions and environmental impact from the next generation of launch systems." 15th Reinventing Space Conference. 2017.

TABLE OF CONTENTS

Abstract	iv
Acknowledgements	v
List of figures	xii
List of tables	xix
Nomenclature	xxii
1 Introduction	1
1.1 Research questions	3
1.2 Approach and Methodology	3
1.3 Contributions to the field	4
1.4 Thesis organisation	4
2 Background	6
2.1 Aviation - environmental impact	6
2.1.1 Climate change	8
2.1.2 Air quality	13
2.1.3 Modelling approaches	14
2.1.4 Regulation & mitigation	16
2.2 Launch vehicles	18
2.2.1 State of the launch sector	22
2.2.2 Types of launch vehicles	25
2.2.3 Spaceplane concepts	26

2.3	Launch vehicles - environmental impact	28
2.3.1	Emissions	29
2.3.2	Plume effects	33
2.3.3	Modelling approaches and results	34
2.3.4	Measurements	41
2.3.5	Regulation	43
2.3.6	Life cycle assessment	45
2.4	Summary	46
3	Simulating and optimising trajectories	49
3.1	Simulating trajectories	49
3.1.1	Reference frames & coordinate systems	51
3.1.2	Equations of motion	53
3.1.3	Atmospheric model	56
3.1.4	Earth & gravitational model	56
3.2	Trajectory optimisation	58
3.2.1	Optimal control	59
3.2.2	Direct shooting and multiple shooting	62
3.2.3	First guess generation	65
3.2.4	Objective Functions	66
3.2.5	Existing software	67
3.3	Summary	68
4	Aerospace propulsion systems	69
4.1	Background	69
4.1.1	Rocket Engines	70
4.1.2	Airbreathing Engines	74
4.2	Modelling approaches	76
4.2.1	Chemistry	79
4.3	Modelling emissions	81
4.4	Summary	86

5	Modelling aerospace propulsion systems	87
5.1	Propulsion system modelling	87
5.1.1	Thermophysical properties	89
5.1.2	Gas dynamics	90
5.1.3	Intake	93
5.1.4	Injection	94
5.1.5	Mixer	95
5.1.6	Combustion	96
5.1.7	Solving the system	99
5.1.8	Propellants	100
5.1.9	Contributions to HyPro	105
5.2	Rocket engines	106
5.2.1	Modelling rockets with HyPro	107
5.2.2	Limitations	107
5.2.3	Comparison of HyPro with NASA CEA	109
5.2.4	RL10	111
5.2.5	Merlin	120
5.2.6	Raptor	132
5.3	Rocket based combined-cycle	141
5.4	Summary	148
6	Trajectory and emission determination	150
6.1	Medium lift rocket - kerosene	151
6.2	Medium lift rocket - hydrogen	164
6.3	Superheavy rocket - methane	171
6.4	Small launcher - kerosene	178
6.5	Air-launched spaceplane - kerosene	184
6.6	RBCC spaceplane - hydrogen	191
6.7	Summary	197
7	Quantification and evaluation of environmental impact	198
7.1	Quantifying environmental impact	198

7.1.1	Global warming potential (GWP)	199
7.1.2	Radiative Forcing Index	200
7.1.3	Estimating Radiative forcing	201
7.2	Comparison	206
7.2.1	Corrective factors	211
7.2.2	Sensitivity to black carbon	213
7.3	Influence of vehicle design	216
7.4	Reducing RF through vehicle and trajectory design	222
7.4.1	Design study: propellant choice in small launchers	222
7.4.2	Cost function: minimise RF	224
7.5	Summary	226
8	Conclusions and future work	228
8.1	Recommendations for future work	231
	References	233
	Appendix A Propulsion tables	248
A.1	Merlin1D Vacuum	248

LIST OF FIGURES

2.1	Increase in commercial air travel passengers 1970 - 2017 (International Civil Aviation Organisation, 2017)	7
2.2	Forecast for commercial air travel passengers 2016 - 2036 (IATA, 2017)	7
2.3	Historical and forecast revenue passenger kilometres (Airbus, 2018)	9
2.4	Radiative forcing components of global aviation from pre-industrial times until 2005 (Lee et al., 2009b)	11
2.5	Schematic representing emissions from aircraft and their potential impact on the environment and society. (Figure recreated from the updated figure adapted by Brasseur et al. (2016) from Wuebbles et al. (2007))	12
2.6	Historic growth of UK downstream and upstream sectors (London Economics, 2019)	19
2.7	Predicted number of (1 - 50kg) satellites launched (SpaceWorks, 2019)	22
2.8	A schematic of the plume interacting with the atmosphere (Sutton and Biblarz, 2010)	35
3.1	Planet-fixed reference frame, modified from Tewari (2007)	52
3.2	Direct shooting with discrete controls interpolated between points	63
3.3	Direct Multiple Shooting where continuity constraints have not been applied	63
3.4	Direct Multiple Shoot: Continuity Constraints are met	64
4.1	Schematic of a basic liquid rocket engine configuration	71
4.2	Rocket engine film cooling	72
4.3	Gas generator engine cycle	73

4.4	Specific Impulse of various aerospace propulsion systems as a function of operating Mach number (adapted from Fry (2004))	74
4.5	Black carbon mass fraction ratios from various modelling and measurement sources. Assumed mass fraction in lower stratosphere and upper stratosphere from DeSain and Brady (2014) . The blue shaded area contains the range of assumed mass fractions in Ross and Sheaffer (2014)	83
5.1	Block diagram showing set up of modules in HyPro	88
5.2	Block diagram of a ramjet/scramjet	89
5.3	Block diagram of a rocket modelled in HyPro	89
5.4	Diagram showing the converging-diverging inlet station names, adapted from Mogavero and Brown (2018)	94
5.5	Inlet pressure recovery MIL Spec E-5007D (Olds and Bradford, 2001)	94
5.6	Performance of a hydrogen fuel rocket engine based on the RL10 engine across a range of combustion pressures. Results shown frozen flow, partial equilibrium (freezing at the nozzle throat) and equilibrium flow to the nozzle exit are shown.	117
5.7	Performance of a hydrogen fuel rocket engine based on the RL10 engine across a range of O/F ratios. Results shown frozen flow, partial equilibrium (freezing at the nozzle throat) and equilibrium flow to the nozzle exit are shown.	118
5.8	Emissions mass fractions at nozzle exit of a hydrogen fuel rocket engine based on the RL10 engine across a range of combustion pressures ratios. Results shown frozen flow, partial equilibrium (freezing at the nozzle throat) and equilibrium flow to the nozzle exit are shown.	119
5.9	Emission mass fractions at nozzle exit of a hydrogen fuel rocket engine based on the RL10 engine across a range of O/F ratios. Results shown frozen flow, partial equilibrium (freezing at the nozzle throat) and equilibrium flow to the nozzle exit are shown.	119

5.10 Performance of a kerosene fuelled rocket engine based on the Merlin 1D engine across a range of combustion pressures. Results shown frozen flow, partial equilibrium (freezing at the nozzle throat) and equilibrium flow to the nozzle exit are shown.	126
5.11 Performance of a kerosene fuelled rocket engine based on the Merlin 1D engine across a range of mixture ratios. Results shown frozen flow, partial equilibrium (freezing at the nozzle throat) and equilibrium flow to the nozzle exit are shown.	127
5.12 Major species emissions of a kerosene fuelled rocket engine based on the Merlin 1D engine across a range of combustion pressures. Results shown frozen flow, partial equilibrium (freezing at the nozzle throat) and equilibrium flow to the nozzle exit are shown.	128
5.13 Minor species emissions of a kerosene fuelled rocket engine based on the Merlin 1D engine across a range of combustion pressures. Results shown frozen flow, partial equilibrium (freezing at the nozzle throat) and equilibrium flow to the nozzle exit are shown.	129
5.14 Major species emissions of a kerosene fuelled rocket engine based on the Merlin 1D engine across a range of mixture ratios. Results shown frozen flow, partial equilibrium (freezing at the nozzle throat) and equilibrium flow to the nozzle exit are shown.	130
5.15 Minor species emissions of a kerosene fuelled rocket engine based on the Merlin 1D engine across a range of mixture ratios. Results shown frozen flow, partial equilibrium (freezing at the nozzle throat) and equilibrium flow to the nozzle exit are shown.	131
5.16 Performance of a methane fuelled rocket engine based on the Raptor engine across a range of combustion pressures. Results shown frozen flow, partial equilibrium (freezing at the nozzle throat) and equilibrium flow to the nozzle exit are shown. Reported performance from NASA (2019)	135

5.17 Performance of a methane fuelled rocket engine based on the Raptor engine across a range of mixture ratios. Results shown frozen flow, partial equilibrium (freezing at the nozzle throat) and equilibrium flow to the nozzle exit are shown. Reported performance from NASA (2019)	136
5.18 Major species emissions of a methane fuelled rocket engine based on the Raptor engine across a range of combustion pressures. Results shown frozen flow, partial equilibrium (freezing at the nozzle throat) and equilibrium flow to the nozzle exit are shown.	137
5.19 Minor species emissions of a methane fuelled rocket engine based on the Raptor engine across a range of combustion pressures. Results shown frozen flow, partial equilibrium (freezing at the nozzle throat) and equilibrium flow to the nozzle exit are shown.	138
5.20 Major species emissions of a methane fuelled rocket engine based on the Raptor engine across a range of mixture ratios. Results shown frozen flow, partial equilibrium (freezing at the nozzle throat) and equilibrium flow to the nozzle exit are shown.	139
5.21 Minor species emissions of a methane fuelled rocket engine based on the Raptor engine across a range of mixture ratios. Results shown frozen flow, partial equilibrium (freezing at the nozzle throat) and equilibrium flow to the nozzle exit are shown.	140
5.22 Performance of the Hyperion ejector mode at a series of altitudes (indicated in the legend as altitude in m) modelled in HyPro and compared to Olds and Bradford (2001)	142
5.23 Performance of the Hyperion ramjet mode at a series of altitudes (indicated in the legend as altitude in m) modelled in HyPro and compared to Olds and Bradford (2001)	143
5.24 Performance of the Hyperion scramjet mode modelled in HyPro and compared to Olds and Bradford (2001)	143
5.25 Curve fit contour plots for the Hyperion ejector	145

5.26 Curve fit contour plots for the Hyperion ramjet mode. Point data are the points evaluated with HyPro. Red points indicate where dynamic pressure, $q > 120$ kPa.	146
5.27 Curve fit contour plots for the Hyperion scramjet mode. Point data are the points evaluated with HyPro. Red points indicate where dynamic pressure, $q > 120$ kPa.	147
6.1 Share of solid and liquid launch attempts 2003 - present. Launch vehicles are classed as ‘solid’ if any part of their first two-stages, including boosters, are solid rocket motors, but doesn’t include kick-stages or apogee motors. Launch history data from Kyle (2019)	151
6.2 C_D with M number for rockets (Ritter, 2012)	156
6.3 Position time history of the optimised solution for the medium-lift kerosene .	159
6.4 Control time history of the optimised solution for the medium-lift kerosene .	160
6.5 Additional state parameter time history of the optimised solution for the medium-lift kerosene rocket	161
6.6 Total mass of emissions by altitude bin for the medium kerosene test case . .	162
6.7 Major species emission by altitude bin for medium kerosene test case	163
6.8 Position time history of the optimised solution for the medium-lift hydrogen rocket	167
6.9 Control time history of the optimised solution for the medium-lift hydrogen rocket	168
6.10 Additional state parameter time history of the optimised solution for the medium-lift hydrogen rocket	169
6.11 Total mass of emissions by altitude bin for the medium hydrogen rocket test case	169
6.12 Major species emission by altitude bin for medium hydrogen rocket test case	170
6.13 Position time history of the optimised solution for the methane-fuelled super heavy rocket	173
6.14 Control time history of the optimised solution for the methane-fuelled super heavy rocket	174

6.15 Additional state parameter time history of the optimised solution for the methane-fuelled super heavy rocket	175
6.16 Total mass of emissions by altitude bin for the super heavy methane rocket .	176
6.17 Major species emission by altitude bin for the super heavy methane test case	177
6.18 Position time history of the optimised solution for the small kerosene-fuelled rocket	180
6.19 Control time history of the optimised solution for the small kerosene-fuelled rocket	181
6.20 Additional state parameter time history of the optimised solution for the small kerosene-fuelled rocket	181
6.21 Total mass of emissions by altitude bin for the small kerosene-fuelled rocket .	182
6.22 Major species emission by altitude bin for the small kerosene-fuelled rocket .	183
6.23 Position time history of the optimised solution for the air-launched spaceplane	187
6.24 Control time history of the optimised solution for the air-launched spaceplane	188
6.25 Additional state parameter time history of the optimised solution for the air-launched spaceplane	188
6.26 Total mass of emissions by altitude bin for the super heavy methane rocket .	189
6.27 Major species emission by altitude bin for the super heavy methane test case	190
6.28 Position time history of the optimised solution for the RBCC SSTO spaceplane	193
6.29 Control time history of the optimised solution for the RBCC SSTO spaceplane	195
6.30 Additional state parameter time history of the optimised solution for the RBCC SSTO spaceplane	196
6.31 Emissions profiles for the RBCC SSTO spaceplane	196
7.1 Schematic of Brewer-Dobson circulation (BDC) showing the circulation of Bönisch et al. (2011)	202
7.2 Radiative forcing for all launch vehicles by nozzle chemistry	208
7.3 Normalised radiative forcing for all launch vehicles by nozzle chemistry . . .	210
7.4 Radiative forcing from CO ₂ emissions with and without CO corrections for the medium kerosene rocket	212

7.5	Soot mass distribution profiles with altitude with various assumptions about soot production. Red line indicates the stratospheric boundary used to calculate radiative forcing.	215
A.1	Performance of a kerosene fuelled rocket engine based on the Merlin 1D Vacuum engine across a range of combustion pressures. Results shown frozen flow, partial equilibrium (freezing at the nozzle throat) and equilibrium flow to the nozzle exit are shown.	248
A.2	Performance of a kerosene fuelled rocket engine based on the Merlin 1D Vacuum engine across a range of mixture ratios. Results shown frozen flow, partial equilibrium (freezing at the nozzle throat) and equilibrium flow to the nozzle exit are shown.	249
A.3	Major species emissions of a kerosene fuelled rocket engine based on the Merlin 1D Vacuum engine across a range of combustion pressure. Results shown frozen flow, partial equilibrium (freezing at the nozzle throat) and equilibrium flow to the nozzle exit are shown.	250
A.4	Minor species emissions of a kerosene fuelled rocket engine based on the Merlin 1D Vacuum engine across a range of combustion pressure. Results shown frozen flow, partial equilibrium (freezing at the nozzle throat) and equilibrium flow to the nozzle exit are shown.	251
A.5	Major species emissions of a kerosene fuelled rocket engine based on the Merlin 1D Vacuum engine across a range of mixture ratios. Results shown frozen flow, partial equilibrium (freezing at the nozzle throat) and equilibrium flow to the nozzle exit are shown.	252
A.6	Minor species emissions of a kerosene fuelled rocket engine based on the Merlin 1D Vacuum engine across a range of mixture ratios. Results shown frozen flow, partial equilibrium (freezing at the nozzle throat) and equilibrium flow to the nozzle exit are shown.	253

LIST OF TABLES

2.1	Summary of key emissions indicators adapted from the European Aviation Environmental Report 2016 (European Aviation Safety Agency et al., 2016) .	13
2.2	Proposed constellations (Muelhaupt et al. (2019))	21
2.3	Small launch vehicles under development, adapted from Niederstrasser (2018, 2021)	24
2.4	Summary table of emitted chemicals and contribution to atmospheric impacts	30
2.5	Results from ozone loss models	38
2.6	In situ measurements of rocket plumes	42
2.7	Estimated SpaceX Starship and Super Heavy CO ₂ emissions per year (NASA, 2019)	44
5.1	Fuel Physical Properties (Sutton and Biblarz, 2010)	100
5.2	RP-1 Physical Properties (Edwards and Maurice, 2001)	102
5.3	RP-1 Surrogate Chemical Kinetics Scheme (Wang, 2001)	103
5.4	RP-1 Multi-Formula Surrogate Components (Farmer et al., 1997)	104
5.5	RP-1 Single-formula Surrogate Thermophysical Data (Wang, 2001)	104
5.6	Interaction of physical phenomena with performance loss calculations. Losses are on I_{sp} . <i>Not imp</i> are losses that are generally not important. Adapted from Dunn and Coats (1997)	108
5.7	RL10 Specifications	112
5.8	Equilibrium RL10-B2 Performance simulated with CEA and HyPro infinite-area combustion chambers.	113
5.9	RL10B-2 modelled by CEA and HyPro	115

5.10 RL10 Modified Specification Errors	116
5.11 Merlin Specifications	121
5.12 Merlin 1D modelled by CEA and HyPro	123
5.13 Merlin 1D Vacuum modelled by CEA and HyPro	124
5.14 Extracts of Merlin 1D mass fractions through the engine and plume from FAA (2020)	124
5.15 Raptor propulsion specification	132
5.16 Raptor modelled by CEA and HyPro	133
5.17 Raptor combustion chamber exit mass fractions from NASA (2019) compared to HyPro	134
6.1 The classes and propellants of vehicles	150
6.2 Kerosene fuelled vertical launch vehicles	152
6.3 Falcon 9 Versions - flight data as of end of 2021 (Space Launch Report, 2021)	153
6.4 Mass breakdown of the medium lift kerosene fuelled rocket (Blau, 2018b) . .	154
6.5 Falcon 9 Target Orbit	154
6.6 Initial conditions for medium lift kerosene, 28° 200 km orbit	154
6.7 Bounds for medium lift kerosene test case, 28° 200 km orbit	155
6.8 Variants of the Delta-IV Launch Vehicle (United Launch Alliance, 2013)	164
6.9 Mass breakdown of the Delta-IV M (4,0) vehicle (Blau, 2018c)	165
6.10 Mass breakdown of the super heavy lift methane fuelled rocket	172
6.11 Bounds for super heavy test case, 28° 200 km orbit	172
6.12 Assumed mass breakdown of the small kerosene-fuelled rocket	178
6.13 Rutherford Engine Specs	179
6.14 Assumed mass breakdown of the air-launched spaceplane	184
6.15 Initial conditions for the air-launched spaceplane	185
6.16 Bounds for air-launched spaceplane case, 28° 200 km orbit	185
6.17 Proposed Action GHG Emissions per Activity in Metric Tons (FAA, 2017) . . .	186
6.18 Initial conditions for RBCC SSTO spaceplane, 28° 200 km orbit	194
6.19 Bounds for the RBCC SSTO spaceplane test case, 28° 200 km orbit	194

7.1	Global warming potential (IPCC, 2013). Other substances are included in the IPCC GWP figures, but they are species not related to spaceflight.	199
7.2	Total emitted mass by species (where applicable, equilibrium rocket models are assumed and corrective factors are included)	207
7.3	Radiative forcing by species (where applicable, equilibrium rocket models are assumed and corrective factors are included)	208
7.4	Normalised radiative forcing by (where applicable, equilibrium rocket models are assumed and corrective factors are included)	211
7.5	Radiative forcing components for equilibrium nozzle for the medium kerosene launch vehicle	213
7.6	Results from black carbon sensitivity experiments	214
7.7	Total emitted mass by species split by mass emitted below the stratosphere (where applicable, equilibrium rocket models are assumed and corrective factors included)	221
7.8	Sea level engine comparison for kerosene, methane and propane	223
7.9	Vacuum engine comparison for kerosene, methane and propane	223
7.10	Comparison of the radiative forcing for kerosene, methane and propane small launcher variant	224
7.11	Results from using cost functions that minimise radiative forcing	225

NOMENCLATURE

C_p	Specific heat capacity, J kg K^{-1}
G	Gibbs free energy, J
H	Enthalpy, J
J	Scalar performance index
R	Gas constant, $\text{J K}^{-1} \text{mol}^{-1}$
RF	Radiative Forcing, W m^{-2}
S	Entropy, J K^{-1}
T	Temperature, K
T_a	Atmospheric Temperature, K
Ψ	Boundary constraints
\dot{m}	Mass flow rate (i.e. the rate of change of mass with time), kg s^{-1}
\dot{m}_p	Mass flow rate of expelled propellant, kg s^{-1}
F	Force, N
$F(t)$	Force as a function of time, N
M	Moment, N m
W	Weight, N
ρ_a	Atmospheric Density, kg m^{-3}

h	Altitude, m
m	mass, kg
p_a	Atmospheric Pressure, Pa
t	time, s

Roman Symbols

α	Angle of attack, rad
Δv	Change in velocity, m s^{-1}
μ	Bank angle, rad
Φ	Molar ratio between fuel and oxidant in stoichiometric conditions
Φ	Molar ratio between fuel and oxidant in stoichiometric conditions
σ_{CO_2}	Mass-specific absorption coefficient for CO_2 , $\text{m}^2 \text{kg}^{-1}$
RF_{CO_2}	Radiative forcing due to CO_2 , W m^{-2}
D	Drag, N
F_T	Vehicle thrust, N
g_0	Acceleration due to gravity, m s^{-2}
I_{LW}	Integrated long wave flux, W m^{-2}
I_{SW}	Integrated short wave flux, W m^{-2}
I_{SW}	Integrated short wave flux, W m^{-2}
I_{sp}	Specific impulse, s
L	Lift, N
m_0	Initial mass, kg
m_f	Final mass, kg

RF_{BC} Radiative forcing due to black carbon, $W m^{-2}$

W_1 Molecular weight at node 1

W_f Molecular weight of the fuel

X_{ox} Molar fraction of oxidiser

EI Emission Index, $g kg^{-1}$

Acronyms / Abbreviations

3DoF Three degrees of freedom

BC Black Carbon

CCM Chemical Climate Models

CCP Combined Cycle Propulsion

CPS Combination Propulsion System

CTM Chemical Transport Model

GCM Global Climate Model

GEO Geostationary Orbit

GHG Greenhouse gas

GWP Global warming potential

HTHL Horizontal Takeoff, Horizontal Landing

IPCC Intergovernmental Panel on Climate Change

LACE Liquid Air Cycle Engine

LCA Life Cycle Assessment

LEO Low Earth Orbit

LRE Liquid rocket engine

PFR Plug Flow Reactor

PSR Perfectly Stirred Reactor

RBCC Rocket-Based Combined Cycle

RFI Radiative Forcing Index

SSTO Single-stage-to-orbit

TBCC Turbine-Based Combined Cycle

TDK Two Dimensional Kinetic Model

TSTO Two-stage-to-orbit

VTHL Vertical Takeoff, Horizontal Landing

VTVL Vertical Takeoff, Vertical Landing

1 | INTRODUCTION

Space is more and more becoming part of our everyday lives. From satellite navigation and climate monitoring to communication services, it has huge benefits for our society, economy and environment. As with aviation and other industrial sectors, there is an environmental impact of space access. This needs to be understood and balanced against these social, economic and environmental benefits. This is especially true as the consequences of climate change have become clearer and people around the world work towards achieving net-zero carbon emissions.

Airbreathing aircraft use the atmosphere as a medium for lift as well as a working fluid and source of oxidiser for their propulsion systems. For rocket launchers, the most efficient route to orbit is to escape the atmosphere as fast possible to minimise losses due to atmospheric drag. Whether the flight is powered by jet or rocket engines, many of the aerospace vehicles today depend on combustion engines, which release combustion products into the atmosphere, altering the chemical balance of the atmosphere on a global scale (Lee et al., 2009b).

In the early days of aviation, when the number of flying aircraft was small, the impact of emitted pollutants on the environment was minimal. However, the rapid growth of aviation in the 20th century has changed this, with aircraft now having a major influence on the atmosphere and environment, around 3.5 % of human-caused contributions to changes in the energy balance (Lee et al., 2009a). The impacts are difficult to characterise, due to the complex relationship of the Earth - Atmosphere - Ocean system. However, strong evidence exists for aviation's impact on the climate, driven by long-term impacts from carbon dioxide (CO₂), and shorter-term impacts from other emitted species such as water vapour, particulates and nitrogen oxides (NO_x) (Lee et al., 2009b). These are all emitted from the

burning of fuel inside the engines of aircraft. Additionally, emissions around airports and at cruise altitudes have significant effects on surface air quality, with consequences for human health (Masiol and Harrison, 2014).

Similar change may be currently underway within the space sector which has grown by 176 % since 2005, even growing through the COVID-19 pandemic by 4.4 % to \$447bn during 2020 (Space Foundation, 2021). OneWeb and SpaceX have both made significant headway in the deployment of their internet constellation satellites, resulting in 1270 new payloads added to the space tracking catalogues between the 2020 and 2021, more than 1/6 of the 6257 payloads current in orbit. This represents a step change in the number satellites being launched, although this is only equivalent to 1/10 of the total mass (ESA, 2021).

This is reflected in the launch segment, which is no longer dominated by sovereign states, but is now seeing the growth of commercial operations, both large and small. SpaceX and Blue Origin are developing launchers powered by methane that can insert more than 70 tonnes of payload into orbit, and both have big ambitions to make use of them for mass expansion into space. Over 100 companies are developing small launchers that may extend space access to more than the handful of launching states that exists today (Niederstrasser, 2021).

Launch vehicles are unique in that their combustion products are emitted into each layer of the atmosphere. The overall environmental impact of launchers has largely been discounted in the past due to the low number of launches that occur each year. If the trends in growth continue, emissions produced by launchers could increase significantly and may be compounded by the range of different types of launch vehicles being developed. These changes, alongside the need for nations to reduce their environment impacts to meet climate change targets, may be the impetus to include considerations of emissions within vehicle design and also approaches to mitigate them. The impacts of this potential evolution in the space sector are already being considered in life cycle assessment (LCA) methodologies, for example in Wilson (2019) where LCA was applied to a current launch scenario as well as a future, higher launch rate scenario.

1.1 Research questions

The aim of this research is to explore how environmental impacts from launch vehicles can be considered during preliminary design. On this basis, the following three research questions are addressed by this work:

Question 1 *To what extent can low- to mid- fidelity methods of modelling propulsion systems be used in understanding their environmental impact?*

Question 2 *How do expected changes in vehicle designs and sustained operations alter the profile of emissions from transatmospheric vehicles into the atmosphere?*

Question 3 *Are there any strategies that may be used during the conceptual design phase to reduce the impact of emissions from novel launch vehicles?*

1.2 Approach and Methodology

These questions are addressed by developing models that can predict the emissions of varying types of propulsion systems used for launch vehicles, model optimal trajectories of existing and novel or conceptual vehicles, and combine these to produce emission profiles from which the environment impact can be evaluated:

Mid-fidelity propulsion model A software tool designed to optimise the configuration of propulsion systems has been extended to model specific engines such as rockets and combined-cycle engines and to predict their emissions.

Trajectory and emissions analysis For a range of existing and conceptual launch vehicles, the predicted propulsion system performance has been used within a trajectory optimisation framework to find optimal trajectories and the associated profile of chemical emissions into the atmosphere.

Evaluating emissions Various approaches for characterising the impact of chemical emissions have been evaluated for use in the space sector, including CO₂ equivalence, radiative forcing index and simple radiative forcing calculations ([Ross and Sheaffer](#),

2014). These have enabled a novel comparison of vehicle concepts and operations based on their potential environmental impact.

Strategies for mitigation of emissions Several strategies to reduce the emissions of launch vehicles are investigated, including optimising trajectories of an existing vehicle, and the use of the methodology developed here has been employed in several design examples.

1.3 Contributions to the field

The goal here is to establish how existing and future vehicles can affect the environment through the emissions they produce. Quantifying the impact of these changes, alongside the forecasts of the growth in the number of launches will mean that decisions can be made about how to address the environmental impact, if it needs to be addressed at all.

The approach described in this research does not require detailed information or analysis, such as CFD or vehicle data, to be in place before preliminary evaluations of a vehicle's environmental impact can be made. This enables vehicle designers to consider the emissions at an early stage where they have the most flexibility to address it, and also allows them to produce vehicle-specific emission figures for use in environmental life cycle assessment. It also enables researchers, policy makers and regulators to draw informed views on the effect of the sector without detailed information from operators or manufacturers.

1.4 Thesis organisation

This thesis is organised into the following chapters:

Chapter 2 - Background includes background information and a literature survey of three main areas. The first examines the emissions and environmental impacts of commercial aviation and how they are modelled. This is critical to understand the approaches that could be applied within the space sector, as the need to understand aviation's impact has been long prioritised with related and similar challenges. The second area introduces the space sector, changes taking place within the industry and the types of vehicles that launch

payloads. The third looks at prior research concerning the environmental impact of launch.

Chapter 3 - Modelling and optimising trajectories provides background on trajectory optimisation and its application to modelling transatmospheric vehicles. It describes the direct multiple shooting trajectory optimisation approach taken and justifies this choice of method.

Chapter 4 - Propulsion system introduces the range of propulsion systems that may be used for space access, reviews modelling approaches that could be used and discusses the influence of combustion on the emissions released.

Chapter 5 - Propulsion modelling describes the approach to modelling propulsion systems and estimating emissions from various propulsion systems. It also compares the results with other tools and discusses the limitations of methods available during early design stages.

Chapter 6 - Trajectory and emission determination presents the problem definition and trajectory and emission profile results for several test cases including current launchers and conceptual vehicles representing future classes of launch systems.

Chapter 7 - Quantification and evaluation of environmental impact presents an approach to understanding the climate change potential of the test cases in the previous chapter. It compares their environmental impact, and investigates what steps may be taken to reduce this at the design stage.

Chapter 8 - Conclusions and future work draws the thesis to a conclusion, discussing the major contributions of this work, and its key findings.

2 | BACKGROUND

The purpose of this chapter is to introduce the effects transatmospheric vehicles have on the environment and how these impacts can be characterised. It contains three strands of background research; the first in section 2.1 looks to commercial aviation and how this neighbouring and well established industry researches and addresses its environmental impact. This route of inquiry was used because there is only a relatively sparse set of research on the impact of launch vehicles and it made sense to expand the review to include aviation, which shares many characteristics with space, such as emissions across the atmosphere which have global impacts.

The second strand in section 2.2 introduces trends in space sector that are leading to changes in how payloads are launched to orbit, and also describes the types of launch vehicles in operation and conception. This is followed by a discussion of the reasons further research is needed, to understand how an evolving launch sector with increases in launch rates and changes in vehicles may effect the environment.

The final strand in section 2.3 summarises the state of existing research into the production of emissions and environmental impacts of launch vehicles, including measurement campaigns and prior research into the global impacts of launchers. Finally, section 2.4 summarises the topics in this chapter.

2.1 Aviation - environmental impact

This thesis focuses on the environmental impact of launch vehicles used for space access, but it is valuable to review approaches for assessing the environmental impact of commercial aviation, which is well established and faces many of the same challenges as the launch sector. Most aerospace vehicles in use today are piloted fixed wing or rotary-blade aircraft

for the transportation of people or cargo. The evolution of aviation industry also in many ways mirrors that of space access, first being driven by governments and the rich, and subsequently through commercialisation, and the ever increasing demand of passengers to travel by air. The growth rate in commercial air travel between 1970 and 2017 was more than eight-fold, as shown in fig. 2.1, and its expected that this rate of increase will continue over the next 20 years as shown in the passenger forecasts (fig. 2.2), largely driven by growth in developing economies in the Asia-Pacific region (IATA, 2017).

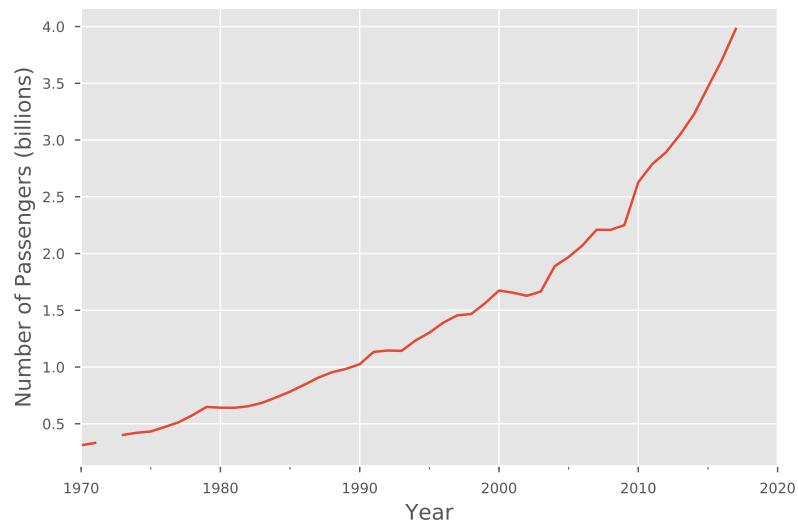


Fig. 2.1 Increase in commercial air travel passengers 1970 - 2017 (International Civil Aviation Organisation, 2017)

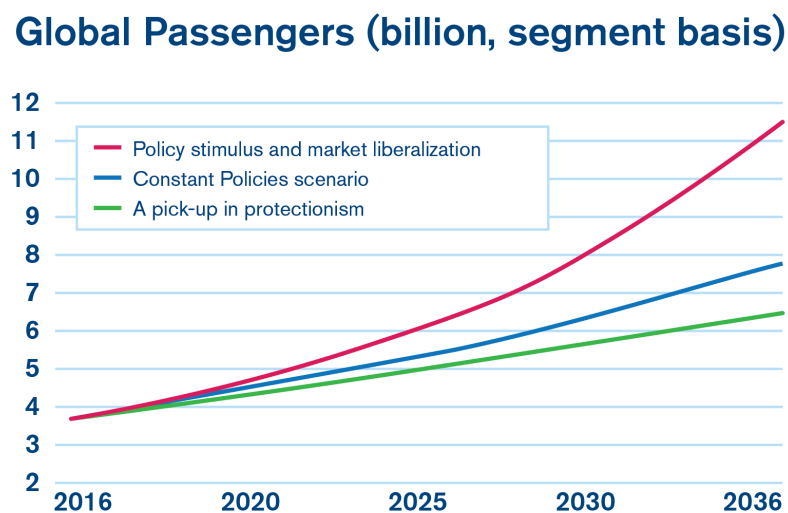


Fig. 2.2 Forecast for commercial air travel passengers 2016 - 2036 (IATA, 2017)

A more useful metric is the Revenue Passenger Kilometre (RPK), calculated by multiplying the number of revenue-paying passengers on board a vehicle by the distance travelled in their journey. This represents the basic unit of ‘production’ of the aviation sector, and is valuable for tracking the growth of aviation as it includes the number of passengers and the distances they travel. Historical trends in RPK and forecasts in the growth are shown in fig. 2.3.

Concerns about the impact of aviation on the environment were initially about the impact of supersonic aircraft on stratospheric ozone (Johnston, 1971). However, sustained use of commercial supersonic aircraft beyond the Concorde did not come to fruition due to their high operational costs and limitations on their flight paths due to sonic boom restrictions.

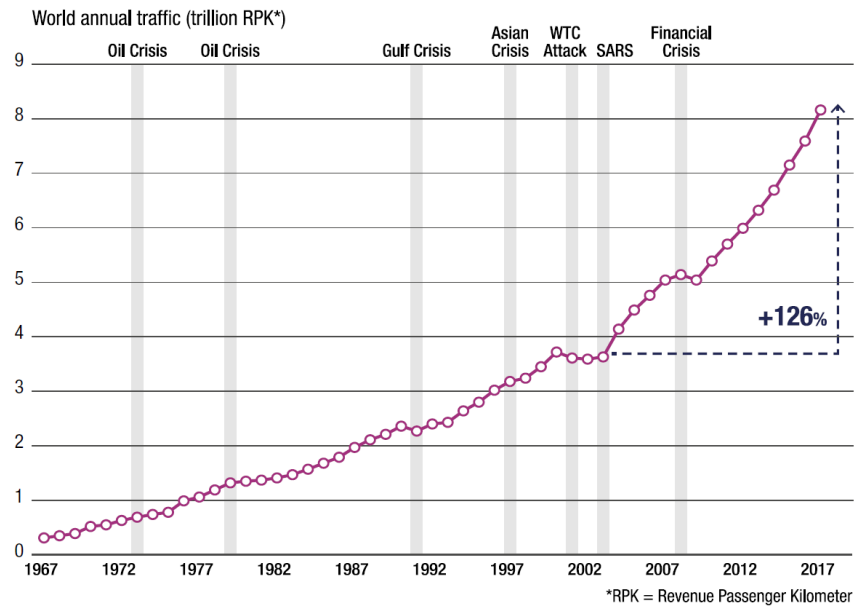
Beginning in the 1980s and 90s, concerns about the impact of aviation led it to become an increasingly priority area for research, driven by huge increases in air traffic and public concern about the effect of emissions on climate change and human health (Lee et al., 2009a).

Aviation’s impact on the climate and on air quality come primarily from chemical emissions from the combustion of aviation fuel, kerosene. Jet A-1 is the most common form of kerosene, with a mean carbon/hydrogen (C/H) ratio of $C_{12}H_{23}$, but is defined as a hydrocarbon mixture that matches a set of required physical properties, chemical composition and performance (Lee et al., 2009b). The combustion of kerosene mostly produces CO_2 and H_2O , but there are also traces of nitric oxide (NO), nitrogen dioxide (NO_2), sulfur dioxide (SO_2), carbon monoxide (CO), and particulates like soot.

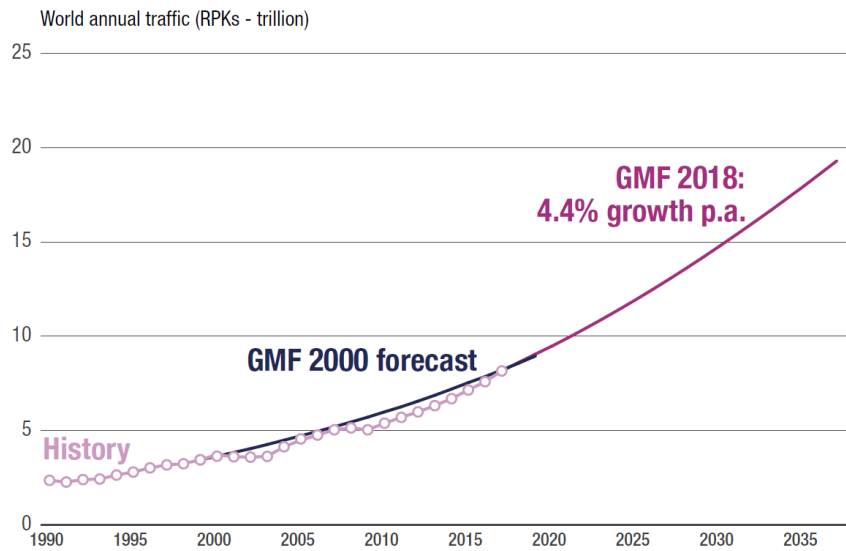
Aviation does not just affect the environment through climate change from chemical emissions, but also through local air-quality, noise, life cycle effects and end-of-life disposal of the aircraft. However, the impact of all industries on climate change is an increasingly visible issue, and is directly related to the number of passengers that fly each year and the efficiency of the aircraft they fly on.

2.1.1 Climate change

Aircraft distribute the products of the combustion of kerosene throughout the lower atmosphere. These emissions mix with the ambient air, and alter the energy balance of the atmosphere. The effect of aviation on the climate is generally characterised by the radiative



(a) Historical RPK



(b) RPK Forecast

Fig. 2.3 Historical and forecast revenue passenger kilometres (Airbus, 2018)

forcing (*RF*), which is defined by the intergovernmental Panel on Climate Change (IPCC) as ‘a measure of the influence a factor has in altering the balance of incoming and outgoing energy in the Earth-atmosphere system and is an index of the importance of the factor as a potential climate change mechanism.’ (IPCC, 2013).

Radiative forcing can be linked directly to the global mean surface temperature, ΔT_s by a sensitivity parameter λ ,

$$\Delta T_s \approx \lambda RF, \quad (2.1)$$

and so a positive RF contribution is warming, and a negative RF contribution cooling.

The IPCC estimated the overall contribution of aviation to anthropogenic radiative forcing in 2005 to be 3.5 %, or 55 mW m^{-2} , or, including cirrus cloud enhancement, 4.9 % (78 mW m^{-2}) (Lee et al., 2009b). This overall impact can be broken down into the following radiative forcing contributions:

- CO₂ emissions result (positive RF)
- NO_x: formation of tropospheric O₃ (positive RF), longer-term reduction in methane (negative RF), longer-term reduction in O₃ (negative RF)
- emissions of H₂O (positive RF)
- formation of contrails (overall positive RF)
- formation of clouds (overall positive RF)
- emissions of sulphate particles (negative RF)
- soot particles (positive RF)

NO_x gives a small picture of the complexity involved, in that there are multiple mechanisms through which it has an impact on RF, both positive and negative, and on different timescales. Figure 2.4 shows the relative contributions of these forcing components for different species. These are based on a series of calculations for the emissions produced by aviation traffic, and individual models for estimating the RF contributions. For example, a full time series of aviation fuel data was used to estimate CO₂ emissions, whilst other species were calculated using various fuel burn models accounting for developments in technology. Different

approaches to calculate radiative forcing are used depending on the emission, for example, the effect of CO₂ is relatively well known and can rely on a simpler approach without introducing uncertainties, whereas even with state-of-the-art chemical transport models and climate chemistry models, high uncertainty remains on effects of NO_x on ozone production (and the associated radiative forcing contribution). Simpler models are often calibrated against more in-depth assessments that use complex models, before being applied to examine future scenarios. In this case, Lee et al. (2009a) performed these calculations for the current scenario, as well as several other scenarios accounting for growth in aviation traffic and the inclusion of a fleet of supersonic airliners.

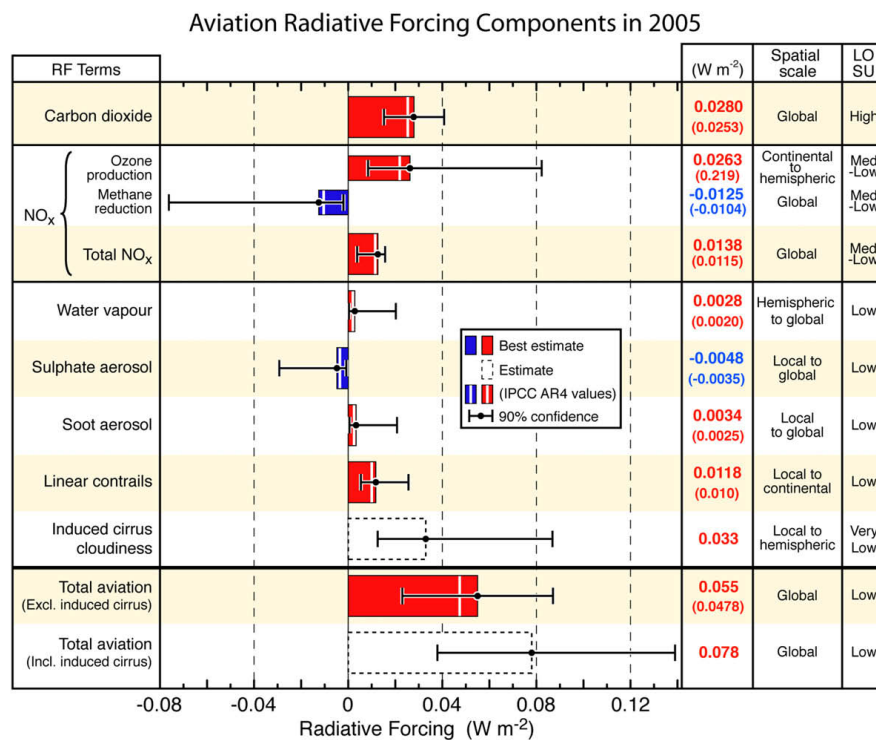


Fig. 2.4 Radiative forcing components of global aviation from pre-industrial times until 2005 (Lee et al., 2009b)

Figure 2.5 illustrates the main paths through which interactions of these emitted species can create changes in the RF balance of the Earth's climate. There are many different atmospheric processes that are involved, including chemical reactions (often as a function of radiation or light), microphysical processes (such as the contrails, clouds and aerosols) and also the ocean-atmosphere interface. It also shows how the emissions link to the impacts and damages of climate change. Many of these are applicable to launch vehicles, including the CO₂, NO_x, BC and H₂O pathways.

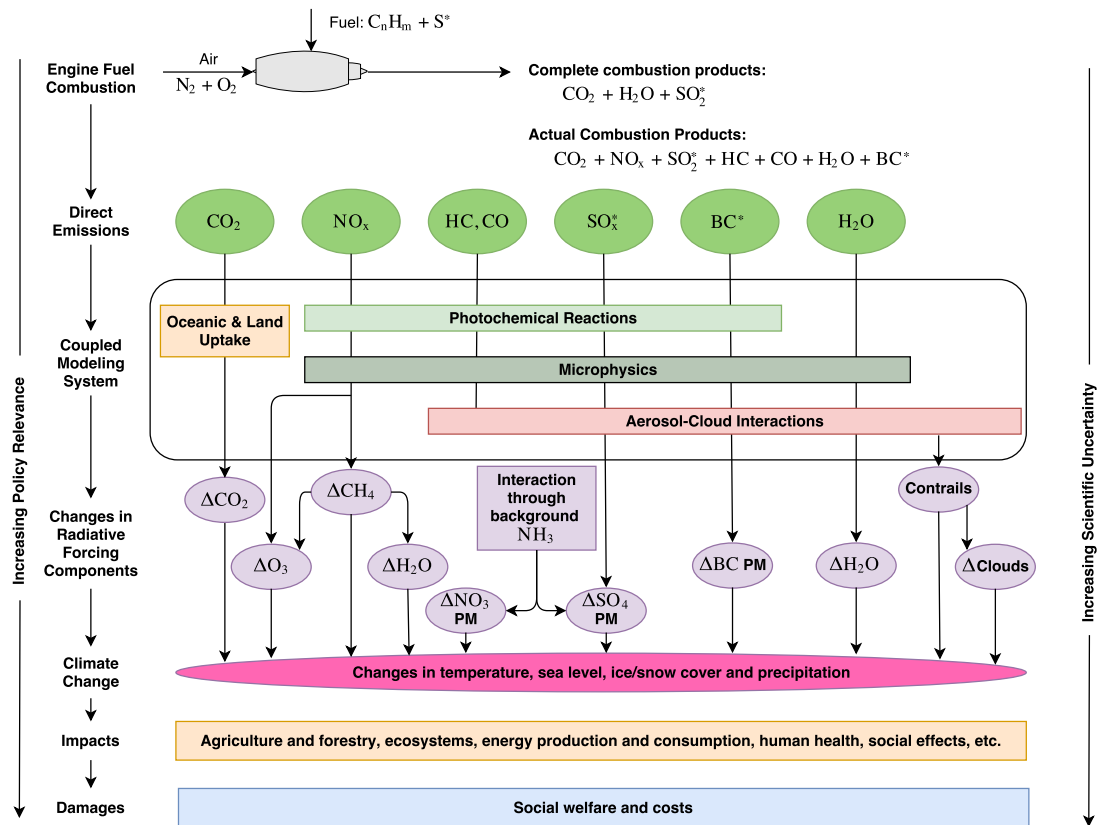


Fig. 2.5 Schematic representing emissions from aircraft and their potential impact on the environment and society. (Figure recreated from the updated figure adapted by [Brasseur et al. \(2016\)](#) from [Wuebbles et al. \(2007\)](#))

Table 2.1 contains a list of the major species emitted by aircraft that are of concern to the environment, and a forecast for 2035, based on current trends of decreasing average fuel burn and increasing passenger numbers in the European Union. Expected improvements in the efficiency of aircraft result in a decreased fuel burn per passenger per kilometer, shown in the top row, but considering the expected growth in aviation traffic (see fig. 2.3), this is outweighed by the higher total emissions caused by more journeys, shown in subsequent rows for CO₂, NO_x, CO and volatile and non-volatile particulate matter. As the growth of air travel in other parts of the world including the Asia-Pacific Region is even greater, the total increase in emissions is even more significant than shown here. Therefore, unless there is a disruption in aerospace technology, climate impacts of aviation are expected to increase during a period of higher scrutiny on anthropogenic contributions to climate change. This prediction is also based on the growth of conventional aviation (subsonic), and does not

include new classes of vehicle such as supersonic or hypersonic aircraft, or any space launch activity.

Table 2.1 Summary of key emissions indicators adapted from the European Aviation Environmental Report 2016 ([European Aviation Safety Agency et al., 2016](#))

	Units	2005	2014	Forecast 2035
Average fuel burn	kg km ⁻¹ per passenger	0.0388	0.0314	0.0209 - 0.0222
CO ₂	10 ⁶ t	144	151	207 - 219
NO _x	10 ³ t	650	732	920 - 1049
NO _x < 3000 ft	10 ³ t	53.3	58.8	73.3 - 83.1
HC	10 ³ t	20.8	17	22.9
HC < 3000 ft	10 ³ t	7.8	6.4	11.0
CO	10 ³ t	143	133	206
CO < 3000 ft	10 ³ t	52.4	48.2	85.5
Volatile PM	10 ³ t	4.18	4.47	6.93
Volatile PM < 3000 ft	10 ³ t	0.27	0.27	0.41
Non-volatile PM	10 ³ t	2.67	2.38	3.16
Non-volatile PM < 3000 ft	10 ³ t	0.15	0.13	0.17

The consequences of climate change are ever increasing impacts on the natural environment, including higher extreme temperatures, heavy precipitation, agricultural and ecological droughts and intense weather events, all of which impact the natural and human world ([IPCC, 2021](#)). Associated with these changes are huge implications for society and the economy. As an example, the [World Health Organisation \(2019\)](#) estimates that climate change could cause approximately 250,000 additional deaths per year from a variety of sources, with some vulnerable populations, such as developing nations, at greater risk than others.

2.1.2 Air quality

Aircraft emissions around airports have obvious and direct impacts on human health. However, the pollutants emitted at any altitude, including cruise conditions also have an impact on surface air quality ([Barrett et al., 2010](#)). Reduced air quality can have widespread impacts on human health ([Ostro et al., 2006](#); [Rückerl et al., 2011](#)), as well as causing damage to

visibility, crops and buildings. Of particular concern are ozone and particulate matter with a diameter less than 2.5 μm in diameter, called PM2.5 (Cameron et al., 2017).

Characterising the effect of aviation on local air quality around airports requires identifying which pollutants can contribute to a reduction in air quality, as well as isolating the sources of these emissions. The International Civil Aviation Organization (ICAO) identified carbon monoxide, nitrogen oxides, unburned hydrocarbons and smoke as key contributors that should be measured from engine emissions in the “Chicago Convention”, but there are other species that have been identified in exhaust product speciation studies (Anderson et al., 2006; Herndon et al., 2008). There are many more sources of species that can be considered polluting to local air quality beyond the emissions from aircraft engines (see Masiol and Harrison (2014) for a complete review of literature on local air quality).

The impacts of global emissions including cruise-level emissions cannot be directly measured because the contributions cannot be separated from other sources of emissions. This is because air quality measurements cannot be linked directly to an aircraft source because the emissions occur far away from the measurement location and the receptors (Cameron et al., 2017). Researchers must therefore rely on computational models to understand the mechanisms and consequences on surface air quality. Chemical-transport models (CTMs) and climate-response models (CRMs) are used to model the motion and chemistry of species emitted into the atmosphere, including meteorology. A key input into these models is the quantity and location of each emission, sometimes called the source term, of the emitted species across the atmosphere.

2.1.3 Modelling approaches

Modelling that characterises the impact of aviation emissions on the environment needs to answer two questions:

1. What is the quantity, the location and timing of each important chemical species emitted into the atmosphere?
2. What are the consequences of these emission on the atmosphere in terms of radiative forcing, air quality or other metrics?

The following description is one example of the general approach that has been used for global aviation, but the level of detail and precise number of steps depends on the objective of the model.

The first step is to produce a 3D gridded inventory of emissions for a particular scenario or forecast which describes the total emitted mass of a particular chemical species as a function of latitude, longitude and altitude. In some cases, it is important to maintain the temporal dimension as well (for example, stratospheric ozone loss is seasonal). This is generally done by analysing a historic set of flights and either extrapolating for a forecast or proposing a change (such as the growth of the number of flights or the introduction of more efficient aircraft) for a scenario. The next step calculates the emissions of a single flight for each airport pair and aircraft type, and integrates across the flight frequency and fleet mix for that route per year.

The gridded inventories are then used as inputs to chemical transport models (CTMs), or CTMs coupled with Global Climate Models - called Chemistry Climate Models (CCMs), which calculate the response of the atmosphere and the radiative forcing.

The calculation needed to establish the geographic distribution of the emissions from a flight needs two main inputs: the performance of a particular aircraft (i.e. a model of its motion and fuel consumption) and the emissions produced by aircraft. An emissions inventory that includes only the spatial distribution of emissions is a 3D emissions inventory (i.e. where), but this can be extended to create a 4D inventory by including the time-varying nature of emissions (when). [Wasiuk et al. \(2016\)](#) used the following process to establish their 4D emission inventory:

1. Process aircraft movement data from 2005 to 2011, containing city pairs, airlines, aircraft code and departure frequency.
2. Establish the performance characteristics of the aircraft included within the inventory. [Wasiuk et al. \(2016\)](#) used EUROCONTROL's Base of Aircraft Data (BADA) aircraft performance model, which includes the performance characteristics of 338 different aircraft. Other sources were used where aircraft weren't included within BADA. Each aircraft flight was split into six stages: taxi out, take-off, climb, cruise, descent and

taxi in. BADA was used to calculate the climb, cruise and descent fuel burn values. Taxi out, take-off and taxi in fuel burn values were taken from databases.

3. Emissions from aircraft were calculated using the Boeing Fuel Flow Method 2 (DuBois and Paynter, 2006). These are produced in the form of Emission Indices (EIs), which specify how many grams of the species are produced per kilogram of fuel burned.
4. A trajectory simulation is performed for each unique flight. This is combined with the information from previous steps to produce the 4D emission inventory.

The Boeing Fuel Flow Method 2 (BFFM2) uses empirical engine emissions data, but applies corrections for the Mach number and altitude of the vehicle (DuBois and Paynter, 2006; Wasiuk et al., 2015). Some emissions, such as CO₂, H₂O and SO_x are purely functions of the fuel flow (throttle) and the fuel used, and so these remain constant. However, NO_x, CO and HC depend also on the conditions within the engine, and are highly dependent on both the engine and the operating conditions. The origin of BFFM2 and similar empirical approaches are in establishing the emissions around airports, and so the EIs are calculated only at the several power settings (7 % (idle), 30 % (approach), 85 % (climb out) and 100 % (takeoff)) associated with the landing and take-off cycle (LTO). Linear approximations are made between these throttle values.

These approaches are similar to the same general method used in this research, described in section 1.3.

2.1.4 Regulation & mitigation

The environmental impact of aviation has been the subject of a huge amount of scrutiny from the international community. One of the ICAO's roles is to improve the environmental performance of aviation, which it does through a range of standards and policies (ICAO, 2016). This, together with regulation from national governments has forced aircraft manufacturers and operators to reduce the fuel burn by 49% and the fuel burn per seat by 82% since the first civil airliner, the De Havilland Comet in 1952 (Blakey et al., 2011). Although regulation has a large part to play in this, reducing operating (fuel) costs is also an economic driver to reduce fuel burn. Vast increases in passengers have counteracted the effects of these improvements in efficiency, and so aviation's contribution to global emissions is growing.

The reduction in emissions produced by aviation has been driven primarily by improvements in technology. In the face of ambitious targets for reductions in both fuel burn and emissions set by governments and international bodies, it is likely this will hold true in the future ([Lee et al., 2009b](#)). The reliance of airlines on old aircraft fleets (with many airlines operating aircraft more than 20 years old) means there is a significant lag between technology innovation and the benefit.

At some point, developments in technology that improve efficiency and reduce emissions will become prohibitively expensive or physically impossible. One way to address this is to subscribe to or create emissions trading schemes. For example, the European Commission included aviation within the European Union Emissions Trading Scheme (ETS), a carbon market, which enables companies or countries to trade carbon emissions allowances with the goal of reducing overall emissions. The ETS operates using a two part system, which includes "caps" and "trades" in the following manner:

- The overall amount of greenhouse gases that can be emitted for each power plant, factory, company etc. in the scheme is capped for each ETS phase.
- This cap is reduced each year for most industries (for 2013 - 2020 the cap is reduced by 1.74% each year). For aviation this is 5% below the emissions for 2004 - 2006 period.
- Emission allowances give the holder the right to emit 1t of CO₂ or an equivalent amount of other greenhouse gases (GHGs).
- Allowances can be acquired free from governments, by purchasing additional allowances, or carried over from previous years.
- Heavy fines are given to companies who do not have allowances for their emissions.

This system creates an incentive for companies to reduce their emissions, by investing in the development of technology or alternative sources of energy ([European Commission, 2021](#)). The ETS is not just for aviation, but also applies to other industries.

In 2016, ICAO members agreed to address the greenhouse gas emissions produced by international aviation, by implementing the Carbon Offsetting and Reduction Scheme (CORSIA) ([ICAO, 2018](#)). This is an international carbon offsetting scheme, where companies

pay for emissions units. The proceeds go directly to forestry projects, resulting in real offsetting of the GHGs produced by aviation. CORSIA also only applies to international flights, not domestic. In Europe, the ETS will cover domestic European flights ([European Commission, 2021](#)).

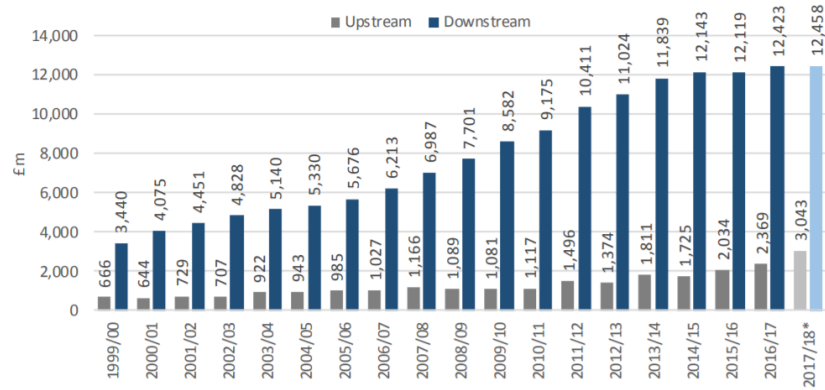
Another way of reducing the overall impact of aviation is to improve the sustainability of the propellant. Traditionally, aircraft have used kerosene derived from fossil fuels. An alternative is to use biofuels, which are manufactured from biomass rather than fossil fuel reserves. This has the benefit of not releasing carbon stored for millions of years, however growing and processing biomass into fuel is not without its negatives, including economic and environment costs. Additionally, the environmental impact of kerosene combustion is not just the emission of CO₂, but also the effect of other pollutants on climate change and human health. A key challenge of developing biofuels is achieving a balance of all these trade-offs ([Blakey et al., 2011](#)). Several launch companies including Orbex and Skyrora have chosen to use sustainable propellants, biofuel (bio-propane) and waste plastic-derived artificial kerosene, 'Ecosene', respectively ([Orbex, 2019](#); [Skyrora, 2021](#)).

Future developments of aircraft, including super- and hypersonic aircraft will have to fit within the existing regulatory regime. International bodies, regulators and governments will set aggressive targets to minimise emissions. Regardless of the potential economic benefits of high speed transport, if these targets cannot be met through technology or operations, regulations are likely to be created that could have significant consequences for the business case of these new transportation systems.

2.2 Launch vehicles

The landscape of the space sector is undergoing a period of growth and change, mostly due to increasing commercial activity. Space has evolved from being largely used for exploration, science and defence purposes to being used for commercial activities, such as telecommunications and the downstream applications of space data. This has driven steady growth in the space sector over the past few decades, as shown in [fig. 2.6](#). This is despite relatively flat levels of institutional or government investment.

UK space industry income (upstream and downstream), 1999/00 – 2017/18*



Note: 2017/18 forecasted based on survey respondents' forecasts and analysis of available annual reports
 Source: London Economics analysis

Fig. 2.6 Historic growth of UK downstream and upstream sectors (London Economics, 2019)

One factor in this growth is that the miniaturisation of technology has enabled a shift towards the use of smaller satellites. These require shorter development times, can use commercial off the shelf components (COTS) and, coupled with the creation of satellite platform standards such as the cubesat specification, have driven down the cost and barrier to entry of space access and use. These smaller satellites are becoming more capable for their cost, which whilst not a new concept (SSTL, 2019), is enabling new business cases to become feasible.

Small satellites enable a similar concept to be used for a number of different missions, and for a lower capital expenditure. Planet (formerly PlanetLabs) have developed a constellation of cubesats that are capable of providing high-resolution, high-revisit time satellite imagery to users. Their current fleet consists of about 140 satellites in three constellations (Dove, SkySat and RapidEye) (Planet, 2019a). Dove is made up of cubesats developed in-house by Planet and mass-manufactured. RapidEye and SkySat are both made of small satellites in the 100 - 150kg range, and were bought from BlackBridge and Terra Bella respectively (Planet, 2019b). Other constellations of cubesats are in development and operation, including Spire, who have around 60 satellites in orbit (Spire, 2019) and provide location services called Automatic Identification System (AIS) to shipping.

Schools, universities and startups are able to design, build and launch a satellite for less than a million dollars, and have taken advantage of the opportunities this presents. For startups and established businesses, cubesats provide an affordable path to demonstrate

new technology, sensors or business concepts in orbit. Universities can leverage them for education or research purposes, and have done so - thirty percent of the first thousand cubesats were used for this purpose (Villela et al., 2019). Companies like OpenCosmos are starting to leverage the concept of space as a service, providing the opportunity for researchers and businesses to fly their payloads without needing to develop capacity in engineering, regulation and operations. SpaceWorks (2019) expects the number of 1 - 50kg satellites launched per year to continue growing. For some customers, the cost is going to be the overriding parameter when considering their launch path. For others, it is going to be time to orbit or the orbit the satellite is placed in.

One particularly interesting use of space is for constellations of small satellites in Low Earth Orbit (LEO) for communications. In the 1990s, several large, commercial telecommunications constellations were developed and launched; Iridium (95 satellites), Orbcomm (35 satellites) and Globalstar (40 satellites). Other, larger constellations were also proposed including Teledesic, which would have been made up of over 840 satellites had it been successful. These were designed to use smaller satellite buses in LEO instead of the monolithic spacecraft used in Geostationary Orbit (GEO) by traditional satellite telecommunications companies, like Inmarsat and Intelsat.

In recent years, several new constellations providing global internet or communications services consisting of 250kg - 500kg small satellites have been proposed with the goal of providing ubiquitous internet access across the globe. If all of these constellations (table 2.2) are successful, over 20 000 new space objects will be launched, significantly more than the 8100 that have been launched to date (Muelhaupt et al., 2019).

SpaceX are the clear leader for global internet services with Starlink, intending on launch more than 1500 satellites in phase 1 to 550km orbits, with plans for significantly more. Similarly, OneWeb intends to launch 650 satellites with a mass of 150kg in batches of 34 - 36 (Foust, 2019a) using the Russian Soyuz rocket provided commercially by Arianespace. OneWeb initially intended for constellation replenishment to be provided by Virgin Orbit's LauncherOne rocket, although at the time of writing this thesis the status of this contract is unclear (Foust, 2019b). Other companies such as Amazon and Boeing have also expressed interest in developing their own internet constellations. The number of operational satellites is certain to be different from table 2.2 as concepts evolve and companies commit to develop

their constellations or withdraw. It is unclear if any of these concepts are viable, and if they are how many operators the market will sustain.

Table 2.2 Proposed constellations (Muelhaupt et al. (2019))

Constellation	Number of satellites	Altitude (km)
SpaceX V-band	7518	335-345
Capella	48	350-650
Planet Swift	6	350-650
Black Sky	300	500
Satellologic NuSat	300	500
Kepler	140	550
Skybox	30	576
Fleet	100	580
Amazon Kuiper	3236	590-630
Commsat	800	600
Kineis	20	600
Yalini	135	600
Spire	100	651
Planet Doves	150	675
Orbcomm	31	750
Iridium	72	780
Theia	112	800
Lucky Star	156	1000
Telesat LEO	72	1000
Hongyan	300	1100
Xinwei	32	1100
SpaceX Starlink	2825	1110 - 1325
OneWeb	720	1200
Telesat LEO	45	1248
Astrome Tech	600	1400
LeoSat	108	1400
Globalstar	40	1412

These changes in the satellite industry, resulting from miniaturisation of satellite technology are having a profound effect on the launch market. More organisations need launch services than ever before, including universities, governments of developing nations and companies with business plans taking advantage of the lower cost of small satellites and the reduced risk of testing new ideas. Forecasts indicate the launch rate of nano/microsatellites will increase year-upon-year, as shown in fig. 2.7, with SpaceWorks (2019) predicting 1370 nano/microsatellites to be launched from 2020 to 2023.

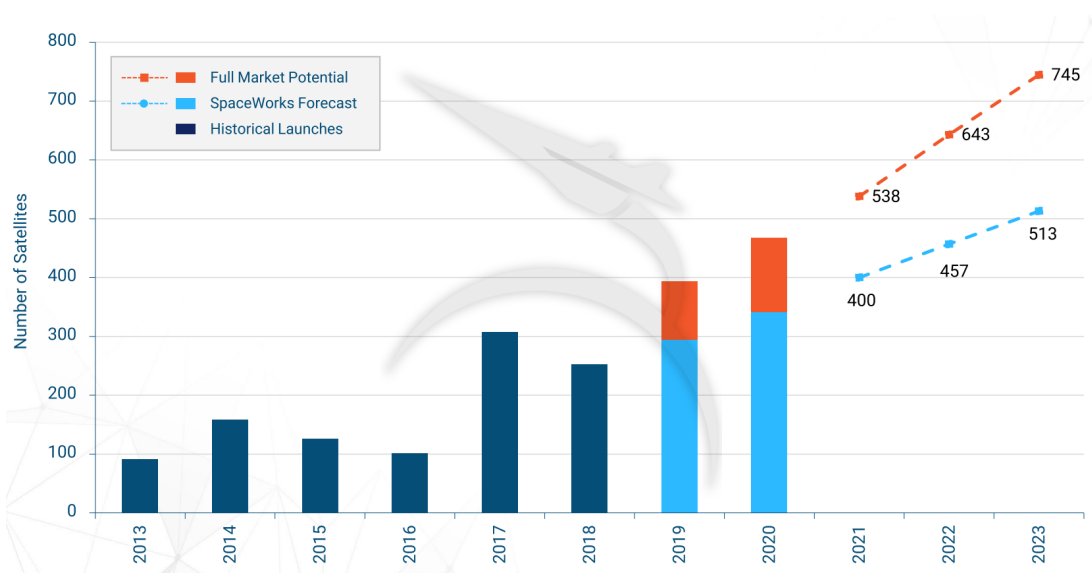


Fig. 2.7 Predicted number of (1 - 50kg) satellites launched (SpaceWorks, 2019)

2.2.1 State of the launch sector

Accompanying developments in satellite technology and the use of space data is the evolution of the way payloads are launched to orbit. In the early period of humanity's use of space, launch was the realm of governments. As the business of space has developed, so has the commercial nature of launch. Europe's Ariane rocket family, and the US's Delta and Atlas families were developed with government or institutions acting as anchor customers. These vehicles are expendable launch vehicles (ELV) and are composed of several rocket stages (typically liquid-fuelled) with optional solid rocket boosters to provide a range of tailored payload masses.

Since 2000, some companies in the US have been developing commercial launch vehicles using capital investment, rather than funding from governments. SpaceX developed their Falcon 1, and subsequently Falcon 9 independently, although they received support through commercial contracts to resupply the ISS with NASA. One potentially revolutionary development by SpaceX has been the capability to land and reuse Falcon 9 boosters, with landing tests beginning in 2013, and the first re-used first stage in 2017. In December 2018, SpaceX re-used a first stage for its third flight. This partially reusable launch vehicle (RLV) has the potential to drive down the costs of spaceflight, although it is unclear what this impact might be as there has not yet been a noticeable decrease in launch costs for customers. This could be due to the expense of refurbishment and maintenance of the first stage booster,

or a lack of incentive to reduce the price as they effectively have a captive market at their current pricing. In 2019 they successfully beat the Northrop Grumman Pegasus XL in cost terms for the launch of a small NASA payload, a vehicle which has a much smaller payload capacity of 400kg ([Space Launch Report, 2016](#)).

SpaceX's impact in the launch market has led to many major launch providers having to rethink their offering to the market to become more competitive. In Europe, ESA and its commercial partners embarked on developing the Ariane 6 launch vehicle to replace the Ariane 5, with the aim of being cheaper, more flexible and using common components with other European vehicles. Incidentally, ESA requirements for Ariane 6 include a mandatory life cycle assessment of the production, launch campaign and launch event of the vehicle to be performed ([Gallice et al., 2018](#)). ULA are developing the Vulcan rocket, and have openly discussed a potential upgrade path to partial reusability.

The development of the commercial small satellite market, along with the potential for a constellation resupply market opportunity has led to a new set of small satellite or "micro" launch vehicles being developed. To understand why small satellite launchers might be attractive in an age of reusable rockets, it is useful to talk about the different ways in which a launch slot can be acquired. The first is by purchasing a dedicated launch slot on a launcher as the primary payload. This enables the customer to dictate the launch schedule (within the launch manifest) and target orbital parameters. This has been out of reach of nanosatellites such as cubesats until recently, as the smallest orbital vehicle prior to the Rocket Lab Electron was the Pegasus XL. Thus, only clusters of smaller satellites like Iridium-NEXT or SpaceX's Starlink, where the customer is able to fill the entire payload capacity are able to take advantage of the schedule security that a dedicated launch can offer.

Instead, most small satellites are launched as piggyback payloads, where they are a secondary payload to a primary customer. However, the primary payload will dictate the target orbital parameters, which means the piggyback satellites must be flexible in terms of their operational orbit or wait for the right primary payload to secure a launch opportunity.

The final approach is to purchase a rideshare slot, where the customer purchases a slot in a multi-manifested launch. Launch providers often offer these opportunities to fill excess

payload margin on their launches, and specialist "launch as a service" providers are now operating (Spaceflight Industries, 2020).

One of the bottlenecks that new space companies have identified in getting their products to market is the launch segment. Satellite operators who purchase piggyback or rideshare services must wait until the primary payload is ready to fly, often resulting in major delays to their operations. Operators care about availability as well costs and are willing to pay higher costs-to-orbit to in order to dictate the launch schedules themselves (Frost and Sullivan, 2018). Over 100 small launchers are in active development with the goal of addressing this need at the time of writing this thesis (Niederstrasser, 2021). A subset of these are shown in table 2.3. Within the UK, several spaceports and small launch developers are competing for government funding and a share of the global small launch market. Several nations, including the UK, Portugal and Australia are developing regulatory frameworks to allow launches to occur from their shores for the first time.

Table 2.3 Small launch vehicles under development, adapted from Niederstrasser (2018, 2021)

Organisation	Vehicle name	Country	Status
ABL Space Systems	RS1	USA	
Firefly Aerospace	Alpha	USA	In development
Orbex	Prime	UK	In development
PLD Space	Arion 2	Spain	In development
Skyrora	Skyrora XL	UK/Ukraine	In development
Rocket lab	Electron	New Zealand/USA	Operational

In parallel to this trend of developing reusable and small satellite launchers, is the development of several heavy lift rocket systems. In addition to the government-funded and NASA-led Space Launch System (SLS), two commercial rocket builders are developing very large vehicles; SpaceX with a two-stage system using Super Heavy booster and Starship reusable upper stage, and Blue Origin with the New Glenn. In terms of payload capacity, both of these are larger than NASA's Saturn V rocket, and similar in size to the Space Launch System (SLS) system in development by NASA. Both companies expect to be launching in the early 2020s. Interestingly, SpaceX and Blue Origin have selected new propellants for their propulsion systems, methane and liquified natural gas respectively. For SpaceX, this choice was justified partly because methane can be manufactured on the surface of Mars using the Sabatier process, but it also provides a balance in the trade-off in terms of

efficiency and storability (compared to cryogenic fuels). SpaceX have also proposed using Starship for the point-to-point suborbital transport across the Earth.

2.2.2 Types of launch vehicles

This section describes the main launch vehicle configurations, and the key concepts that can be used to describe them; payload mass capability, propulsion systems, reusability configurations and launch assist.

In section 2.2.1 two classes of vehicle, expendable and reusable launchers were introduced, which reflects whether the system is discarded each launch or if it is partially or fully reused. The classic launch vehicle is the expendable rocket, with two or more stages and sometimes, external boosters, both of which are intended to improve mass fractions by removing dead mass during the flight. Launch vehicles can also be classified by propulsion system type (e.g. rocket, airbreathing or state of the propellant such as solid, liquid or hybrid). The type of propulsion system and relative staging sizes has a strong influence on the shape of the trajectory. For example, airbreathing engines require the atmosphere to operate and will be installed on lifting body or winged vehicles that are designed to produce lift.

Launch vehicles can also be categorised by payload mass capability by using terms such as "small launch vehicle" or "medium payload launch vehicle". NASA's payload classification system considers small payloads to be <2 t, medium to be 2 – 20t, large to be 20 – 50t and super heavy to be >50 t. This is useful to understand the overall size and capability of a launcher, which is important to the customer, although care should be taken with the injection orbits.

Finally, the term launch assist refers to various approaches to assist launch vehicles with the early stages of launch, which includes the use of carrier aircraft in launch systems such as Pegasus and Virgin Orbit's LauncherOne, but also more exotic systems such as electromagnetic catapults.

2.2.3 Spaceplane concepts

The drive to reduce the costs of space access has led to some searching for potential solutions. Two of these are to drastically increase launch rates, or to reuse the vehicle and the expensive systems and components it formed from.

The Space Shuttle was the first serious attempt to develop a system that could vastly reduce the cost of launch by being reusable. In its original guise, it was also intended as a step towards the idea of aeroplane-like operations. Whilst the Space Shuttle did enable reusability of some parts of the launch system, in operation it was an extremely expensive system, and did not achieve the launch rates or aeroplane-like operations necessary to reduce costs significantly.

Studies from NASA identified that expendable launch vehicles are not capable of reducing the cost of launch enough, and that airbreathing engines might enable reusable launchers (Goldstein, 1988). Airbreathing propulsion systems reduce the amount of propellant carried onboard by using the air as a working fluid, and therefore increase the mass fraction available for systems to enable re-use.

A review by Mankins (2002) called Highly Reusable Space Transportation (HRST) identified a strategy for reducing the cost of launches by a factor of 10. They also described how in the 80s and 90s, there were many similar exercises by NASA and DoD, where the question posed was "what is next, after the space shuttle?". HRST considered a broad range of reusable concepts. These included a number of types of propulsion; combination propulsion systems (CPS), combined-cycle propulsion (CCP), all rocket systems and other "launch assist" approaches (catapults, air launch, staging). It also considered different operations, including Vertical Takeoff, Horizontal Landing (VTHL), Vertical Takeoff, Vertical Landing (VTVL) and Horizontal Takeoff, Horizontal Landing (HTHL).

However, neither NASA or the DoD have been able to develop a system that lives up to this vision of capability. Since the Space Shuttle ceased operations in 2011, all new entrants into the US launch sector have been from commercial entities. In Europe, the only new entry over this period was an institutional launcher, the Avio Vega rocket. Additionally, the only operating reusable launcher is the Falcon 9. Interestingly, given SpaceX's success with reuse of the Falcon 9, HRST only considered a CCP VTVL system, and not rocket-powered VTVL

variant. The conclusion of the study selected CCP as the long-term cost effective solution, but it is worth noting that a system using CCP is still not in operation, and so the debate over which of the approaches is cost effective in the long term is still open.

A relatively light-touch alternative would be to simply replace one stage of a traditional rocket system with an airbreathing-powered stage. The challenge of scramjet systems is that they only have a narrow operating window, beginning at Mach 6 and ending at Mach 12 (although faster operations have been proposed). Some method of accelerating the vehicle to Mach 6 is always required. [Smart and Tetlow \(2009\)](#) proposed a 3-stage vehicle with a second-stage scramjet, a CPS, with a mass payload fraction of 1.47% to 200km low Earth orbit (typical expendable launch vehicle mass fractions are about 2.5%). The advantage of this approach is that only one of the stages is completely unproven as a concept, especially if the first and third stage are based on existing expendable launch systems.

Others considered an all-rocket reusable launch vehicle to be a more feasible next step. HRST rejected this type of system because they did not believe it capable of achieving their cost objectives, but also noted that it had the "highest degree of technical maturity". For some, the higher maturity is an advantage. The SpaceLiner concept from the German Aerospace Centre (DLR) is a proposal for a point-to-point liquid-hydrogen and liquid-oxygen powered vehicle ([Sippel et al., 2016](#)). It has also been proposed as a reusable Two-Stage-To-Orbit (TSTO) fully reusable system. NASA themselves had an all rocket Single-Stage-To-Orbit (SSTO) concept called Venturestar and had a development programme called X-33, which was aimed at developing the maturity of a number of key technologies, including thermal protection systems, composite cryogenic tanks and aerospike rocket engines (nozzles that adapt to the ambient atmospheric pressure).

The alternative is to take a more aggressive approach, and develop a system that combines multiple cycles into a single engine (i.e. a CCP). The advantage here is that less mass is required for the integrated propulsion system, at the expense of increased development costs. There are three forms of combined-cycle engines. The first, Rocket-Based Combined Cycle (RBCC) uses a rocket engine as the core of the system. The primary flow from the rocket exhaust is augmented by the secondary atmospheric flow. In a gas turbine with bypass, momentum is transferred from the core to the bypass flow through the fan. In the case of a ducted rocket, the momentum is transferred purely through the friction between the rocket

exhaust and the air. Several RBCC engines have been proposed. Marquardt proposed the Supercharged Ejector RamJet (SERJ) (Escher and Roddy, 2000), which was intended to be operable at a number of increasing Mach conditions in different modes: supercharged ejector, ramjet, scramjet and rocket.

The second type of CCP is the Turbine-Based Combined Cycle (TBCC) engine, where the rotational core of an engine like a turbojet is integrated within other technologies like a ramjet or scramjet. One approach is to have a turbojet and a ramjet/scramjet on a single flowpath and to switch between modes via flow diversion. However, TBCC's have largely been the realm of engine concepts, with the exception of the J-58 engine on the SR-71 Blackbird, which demonstrated much of the functionality that defines a TBCC.

The final type are Liquid-Air Cycle (LACE) or pre-cooled engines. The distinguishing feature here is that the incoming air is cooled, in the case of LACE until it changes state into a liquid, and in some cases separated from the airflow (Hirakoso et al., 1990). At high velocities, the incoming air is at a very high temperature, making it a significant engineering challenge to design and build a system that is capable of operating in these conditions. More recently, the Reaction Engines SABRE and SCIMITAR engine concepts use a pre-cooler to reduce the temperature of the incoming air, but it does not reach a liquid state. The cooled air is then compressed and combusted in a rocket engine (Varvill and Bond, 2003). These are in a different category to RBCC and TBCC engines because they contains components from both (a compressor and turbine, as well as a rocket combustion chamber and nozzle).

Advances in materials science, simulation and other engineering fields have brought spaceplane concepts closer to reality, especially SSTO spaceplanes - a goal of aerospace engineering for many decades. A potential hypersonic arms race may accelerate the development of the propulsion system needed for space access. Both the UK government and the US's DARPA have invested in the development of Reaction Engine's pre-cooler technology, given its potential application to weapons as well as launch and point-to-point aircraft.

2.3 Launch vehicles - environmental impact

Launch vehicles impact the environment in similar ways to aviation, but as the size of the space sector is significantly smaller than aviation, the impact is proportionally lower.

However, launch vehicles are the only source of anthropogenic emissions injected directly into the upper atmosphere, primarily from the deposition of combustion products. These affect the radiative balance of the Earth system and can also cause the destruction of ozone. Indeed, the earliest work considering rocket emissions focused on the effects of hydrochloric acid (HCl) and particulates produced by solid rockets on stratospheric ozone as part of the Climate Impact Assessment Program (CIAP) (Hoshizaki et al., 1975; Potter, 1978).

Understanding the precise effect on the atmosphere requires consideration of the propellant and propulsion system, the interaction of the combustion products with the atmosphere in the plume, and the long-term interaction of the deposited species with the atmosphere. Each of these is a complex domain with a separate physical and chemical phenomena at a range of temporal and spatial scales.

2.3.1 Emissions

The emissions produced by rocket engines can be categorised based on the propellant combinations and type of rocket engines: solid rocket motors (SRM), hydrocarbon liquid rocket engines (LRE), hypergolic rocket engines, cryogenic liquid rocket engines. Table 2.4 shows the major species that are emitted by various types of rocket engines, and whether they contribute to ozone depletion, radiative forcing, or both. These have been selected based on a literature review (including DeSain and Brady (2014); Murray et al. (2013); Ross and Sheaffer (2014)) as the major species that can contribute to either radiative forcing or ozone depletion. However, there are other species that are important to consider, including N_2 which when entrained in a hot plume can result in NO_x formation, and CO which eventually oxidises in the atmosphere to form CO_2 .

Once the propellant has been combusted in the combustion chamber, it passes through the nozzle and enters the plume, where it continues to react quickly. Eventually the plume mixes with the atmosphere and cools, after which slower reactions dominate. The next few sections describe each key emission product, the types of propulsion systems in which they form, and the pathways through which they can damage the atmosphere.

Table 2.4 Summary table of emitted chemicals and contribution to atmospheric impacts

Name	Species	Source	Impact
Inorganic Chlorine	Cl _x	SRM	Ozone Depletion
Alumina	Al ₂ O ₃	SRM	Ozone Depletion
Carbon Dioxide	CO ₂	Hydrocarbon LRE, Hydropergolic LRE, SRM	Radiative Forcing,
Black Carbon (soot)		Hydrocarbon LRE, SRM	Radiative Forcing
Water vapour	H ₂ O	LRE, SRM	Ozone depletion, Radiative Forcing
Sulfates		Hydrocarbon LRE	Radiative Forcing
Nitrogen Oxides	NO _x	All (plume after-burner)	Ozone depletion, Radiative Forcing

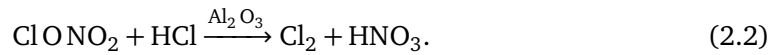
Inorganic Chlorine

Solid rocket motors typically use ammonium perchlorate as an oxidiser and aluminium as a fuel. The combustion of these two reactants produces hydrogen chloride (HCl). Afterburning in the plume converts some HCl into Cl and Cl₂ (Brady et al. (1997) claims 21 - 65% of the HCl by mass, depending on the altitude). In the troposphere, these products react rapidly with the air and have little effect on the ozone. However, in the stratosphere, these species react with O₃ in a catalytic destruction cycle, resulting in ozone loss. Cl or Cl₂ will continue to react with ozone until they are converted back into HCl through reactions with molecules of methane or hydrogen.

Alumina particles

Solid rocket motors also generate particulates of Al₂O₃, called alumina. These particles form in a range of sizes, from a few nanometers to 10 μm in diameter, but only those between 0.01 μm and 1 μm are small enough to remain suspended in the stratosphere for more than a year (Danilin et al., 2001). Particles smaller or larger than this are removed relatively quickly from the stratosphere through coagulation or gravitational settling (Schmid, 2003).

Alumina can participate in heterogeneous reactions within the plume resulting in local ozone loss and as well as longer term ozone loss at a larger scale (Danilin, 2003). An example of a reaction that influences the global scale is:



The overall impact of alumina is highly dependent on the properties of the particulates, specifically the size distribution, which governs timescales in the atmosphere, and the reactivity in these type of reactions, which has not yet been well understood ([Murray et al., 2013](#)).

Alumina may be able to affect the atmosphere's radiative balance through two routes; through stratospheric ozone destruction which has a net cooling impact, and also directly by either scattering solar short wave radiation into space or absorbing long wave radiation from the lower atmosphere and Earth's surface. These last two are competing effects, and as discussed in [Ross and Sheaffer \(2014\)](#), it is unclear what the overall effect may be.

Carbon Dioxide

Carbon dioxide is formed in the rocket engines of launch vehicles operating with several different liquid fuel types, including liquid kerosene, methane, propane as well hydrazine-based fuels like Aerozone 50, UDMH and MMH. Additionally, although the primary constituents of solid rocket motors do not contain carbon, the binder material often does, which also combusts and forms CO₂. Another source of CO₂ from rocket emissions is carbon monoxide, which may be under-oxidised during combustion and reactions in the plume, but has a lifetime of several months in the atmosphere and is generally removed by being oxidised to carbon dioxide.

Relatively slow rates of removal of carbon dioxide from the atmosphere means carbon dioxide has an extremely long lifetime in the atmosphere, on the order of several hundred years, although it is important to note that this is calculated by estimating the rate at which various carbon sinks, such as the ocean and the biosphere are able to remove CO₂ from the atmosphere ([Archer and Brovkin, 2008](#)). Some will remain in the atmosphere for thousands of years, including carbon dioxide emitted during early days of spaceflight. This lifetime may be extended due to the human-driven destruction of natural carbon sinks such as rainforests. The long timescales of CO₂ in the atmosphere also mean that carbon dioxide released at any altitude contributes to the radiative balance.

Black Carbon (soot)

Soot or carbon particulates are formed during combustion when carbon is not fully oxidised to CO₂. The rate of soot production is a function of the mixture ratio. Fuel-rich combustion produce significantly more than lean combustion ([Nickerson and Johnson, 1992](#)). All types of hydrocarbon fuelled rocket engines can produce soot, but RP-1 produces more than fuels like methane and propane. Hydrazine rockets also generate soot given their high fuel-oxidiser ratios, but the amount of carbon in the propellant by mass is lower ([DeSain and Brady, 2014](#)). The binding material in solid fuel rockets also contains carbon that can form soot during combustion.

Soot has a lifetime ~ 4 years in the atmosphere ([DeSain and Brady, 2014](#)) and absorbs solar short wave radiation. Over time increasing the amount of heat added to the upper atmosphere (net warming radiative forcing). Black carbon emissions from a fleet of hybrid space tourism vehicle has been proposed as one of the more damaging scenarios due to the lifetime in the atmosphere and its relatively significant effect on radiative forcing ([Ross and Sheaffer, 2014](#)).

Water Vapour

Water vapour is emitted by all major propellants, but the amount depends on the individual propellants and ratios. It is the primary product of oxygen/hydrogen combustion, but is also formed when the long carbons chains in hydrocarbon fuels (such as kerosene) are oxidised. The location of deposited water vapour is important, tropospheric water vapour becomes part of the hydrological cycle, but stratospheric water has a much longer lifetime and can accumulate over many launches. As discussed in [Ross and Sheaffer \(2014\)](#), there are significant differences in the impact on radiative forcing between different altitudes. In the lower stratosphere, water vapour absorbs long wave radiation from the troposphere and then re-emits it, which does not occur in the rest of the stratosphere. Additionally, stratospheric water vapour may have an uncertain and potentially significant role in the formation of mesospheric clouds ([Murray et al., 2013](#); [Ross and Sheaffer, 2014](#)).

Sulfates

Sulfur is found in hydrocarbons as impurities, although the forms of kerosene used for launch vehicles are usually highly refined variants, such as RP-1, and are likely to have very small amounts of sulfur. During combustion, sulfur oxidises to create aerosols, which scatter solar radiation and therefore have a net cooling impact on radiative forcing. [DeSain and Brady \(2014\)](#) concluded that any radiative forcing impacts from sulfur oxides would be negligible (about $-0.03 \mu\text{W m}^{-2}$ for the period 2000 to 2009).

Nitrogen oxides

Nitrogen oxides can affect the Earth's radiative balance directly within the troposphere, increasing forcing by forming tropospheric ozone, and decreasing forcing through methane destruction. NO_x released in the stratosphere contributes to radiative forcing through the destruction of ozone.

There are two potential sources of nitrogen oxides from rocket-powered launch vehicles. The first requires the presence of nitrogen in the fuel or oxidiser, such as nitrogen tetroxide (NTO), commonly used with hydrazines in some Russian launchers. Additionally, all rocket-powered launch vehicles produce NO_x through afterburning, where the hot exhaust reacts with atmospheric air that mixes in the plume. This occurs throughout the troposphere, but the effect gradually reduces with altitude. As few modern launch vehicles use nitrogen-based propellants, and the production of NO_x through afterburning is relatively small, the overall production is relatively minor.

2.3.2 Plume effects

There are complex interactions between the rocket plume, the surrounding atmosphere and the vehicle that introduces a range of phenomena that detailed studies need to account for. The plume begins at the nozzle exit, expands as the gas moves away from the vehicle, and ends when its velocity relative to the ambient air tends to zero.

One distinctive feature of plumes is the formation of a series of oblique and normal shocks called Mach diamonds. These occur as the inviscid core flow expands until reaching the external flow, where the dynamic pressure causes the expansion to form an oblique

shock. In fig. 2.8 the oblique shock is labelled a barrel shock. The oblique shock tends towards the centre of the flow, where a normal shock forms. The regions behind the normal shocks have significantly higher pressures and temperatures. A reflected shock is formed as the inner flow reflects off its boundary. The repeating pattern of this series of shocks forms the Mach diamond.

A mixing layer forms on the outside of the plume, where the atmosphere and hot gases mix. Remaining fuel in the nozzle flow and species that have not completely reacted in combustion chamber and nozzle, such as CO, are further oxidised by atmospheric oxygen in the mixing layer. This increases the temperature, and the plume becomes a strong emitter of radiation. As the launch vehicle increases in altitude, the atmospheric pressure drops and the length and width of the plume expands. Early research into plume phenomenology was motivated by the need for global missile detection, which is usually based on observation systems that detect electromagnetic radiation (Elliott and Stringfield, 2003; Simmons, 2000).

The configuration of the launcher, specifically the presence of multiple engines close to each other, changes the properties of the afterburning process in the plume. Modelling by Lohn et al. (1999) has shown that multiple engine interactions could increase HCl dissociation (conversion of HCl to Cl) by 10 %, and increase NO_x production in the plume by 1 %, which together results in less than 10 % increase in local stratospheric ozone destruction in the plume.

2.3.3 Modelling approaches and results

The general approach to estimate the environmental impact of launchers is similar to that previously discussed in section 2.1.3: estimate the emissions from the launcher, model the response of the atmosphere, integrate across the expected launch activities. An extra step is often inserted to model the evolution of the plume, and the interaction of the nozzle emissions with the atmosphere in its earliest stages.

Estimating emissions

The fidelity and complexity of approaches to estimating the emissions for a particular scenario can vary significantly. The simplest approach is to rely on estimations of the emissions based on simple approximations about the propellant combustion, for example,

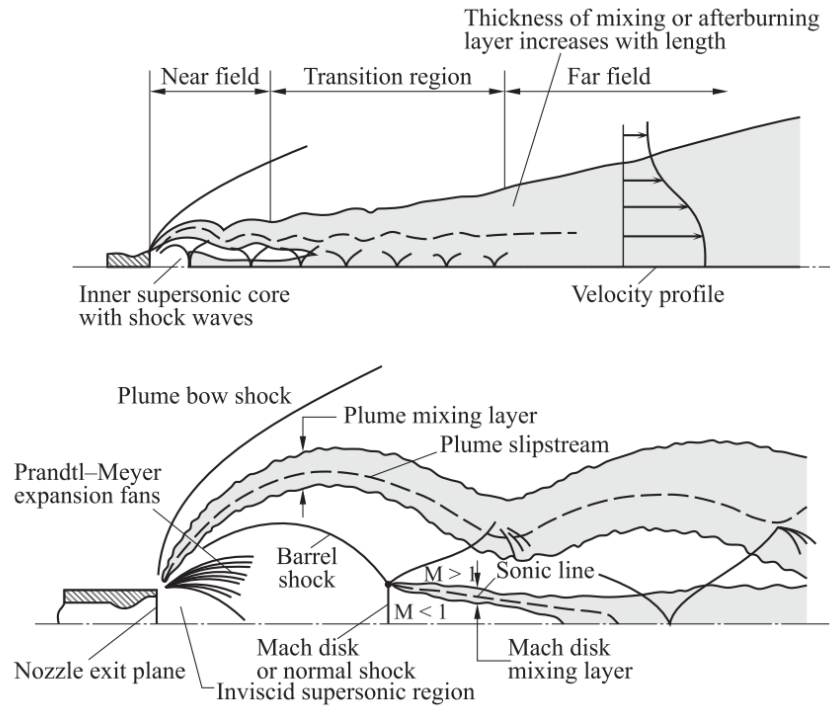


Fig. 2.8 A schematic of the plume interacting with the atmosphere (Sutton and Biblarz, 2010)

the mass of CO₂ produced from the combustion of kerosene is assumed to be:

$$m_{\text{CO}_2} = m_{\text{kerosene}} \frac{12.01 \text{ g} + 16.00 \text{ g} * 2}{12.01 \text{ g} + 1.008 \text{ g} * 2}, \quad (2.3)$$

where 12.01, 16.00 and 1.008 are the molar masses of carbon, oxygen and hydrogen respectively, and the formula therefore represents the overall ratio by mass of the reaction. Similar formulae can be produced for a range of other emission products, and have been used where errors associated with these emission estimates may be small compared to other contributions like the atmospheric response, as in the global inventory of DeSain and Brady (2014).

The propulsion system can also be modelled in further levels of detail, the choice of which depends on the purpose of the model. Murray et al. (2013) explored the important properties of modelling rocket exhausts by using a simple model where rocket exhaust products are mixed with air and reactions are modelled including their finite-rate kinetics. A common approach is to assume equilibrium is reached in a rocket combustion chamber, and the evolution of the gas through nozzle is then modelled separately.

The assumption that the gas is in a shifting chemical equilibrium throughout the nozzle can be used (McBride and Gordon, 1996), although many instead consider finite-rate chemistry. The Method of Characteristics (Anderson, 2001) coupled with a kinetic scheme is often used in "engineering models" that are able to predict the evolution of the chemical makeup through the nozzle and early plume, whilst achieving faster computational performance (Bauer et al., 2013; Denison et al., 1994; Karol et al., 1992; Lohn and Wong, 1996). These approaches split the plume into two parts, a hot plume where afterburning reactions occur, which is modelled using the same method as the nozzle, and the cold plume where the temperature reaches that of the ambient atmosphere.

Significant uncertainties are introduced with current modelling of the emissions produced in a propulsion system and their interactions with the atmosphere in the plume. Murray et al. (2013) identified three priority areas of research to address this:

- Laboratory experiments to understand the production of alumina in SRMs,
- Ground rocket testing to characterise the conditions at the exit plane,
- Flight tests to understand the full dynamics of a real plume at a range of altitudes.

The second part of characterising the emissions is profiling where they are emitted. Previous studies assume that a certain proportion of the propellant is burnt in particular altitude bands. For example, Ross et al. (2004) assumes "33% of first stage fuel load and 50% of second stage fuel load is burned between 10 and 60 km altitude" and states that detailed simulations show this error is no more than 20%. This may hold true for all vertical launch vehicles, but it is unclear if this is valid for novel launch systems such as air-dropped horizontal rockets and winged spaceplanes. Modelling the trajectories of these vehicles would be necessary to understand the emissions profile of novel vehicles, reduce the error of traditional vehicles.

Atmospheric response

The two atmospheric responses that are of greatest concern are the loss of stratospheric ozone, which can impact the health of people on Earth's surface, and changes to the radiative balance of the atmosphere. Reduction in stratospheric ozone also has a net cooling effect on radiative forcing, which can balance out the warming effects of other pollutants.

As the plume cools, it disperses into and reacts with the wider atmosphere, driven by diffusion caused by atmospheric turbulence. Modelling this process indicates that lower diffusion rates result in more time for chemical reactions in the dispersing plume, which can lead to more ozone loss if the pollutants are inorganic chlorine or alumina particles (Denison et al., 1994). This is a local atmospheric response rather than the global response, but it can provide valuable information about the effect of launchers on the atmosphere because, unlike the global response, they can be measured directly (discussed in section 2.3.4).

At the global scale, two forms of high fidelity models are used; Chemical Transport Models (CTM), and Global Climate Models (GCM). The first models only the atmosphere, and focuses on the chemistry occurring within it, whereas GCMs consider the entire Earth-Atmosphere-Ocean system and the interfaces between them. A common feature of both models is the division of the atmosphere into a grid, with typical cells being significantly larger than even widely dispersed plumes. Murray et al. (2013) identifies this as a particularly difficult problem to resolve when integrating local plume models with global climate models, but also recommends that the development of accurate climate and atmospheric models to be a priority for future research in this area.

Results from high fidelity models can also be generalised and used in simpler approaches with appropriate identification of the limits and assumptions that are made. This is the approach taken by Ross and Sheaffer (2014) and DeSain and Brady (2014), where results from other studies are used to estimate the overall impact of different propellant types and the historic launch record respectively.

Key results

The majority of the most detailed models have examined the affect that launchers have on stratospheric ozone (as shown in table 2.5). In most of these cases, it is local ozone destruction from chlorine species and in some cases, aluminium oxide particles that are modelled. Ross et al. (2004) instead examined ozone destruction from NO and H₂O produced by 10 annual launches of the hydrazine-fuelled Proton launch vehicle. The last two examine different high cadence launch scenarios.

Larson et al. (2017) examined the atmospheric response to emissions from large-scale space utilisation (10⁵ launches per year) using a reusable space launch system, based on

Table 2.5 Results from ozone loss models

Type	Model	Scenario	Results	Ref
2D CTM	AER	9 Space shuttle, 3 Titan launches	0.12 % northern mid-latitude upper stratosphere ozone loss. Total column loss <0.1 %	Prather et al. (1990)
2D CTM	GSFC			
3D CTM (chemistry tracers)	GISS			
2D	GSFC	9 Space Shuttle, 3 Titan launches	Gas phase only, average ozone loss 0.006 % Gas phase and heterogeneous reactions on sulphate aerosols, 0.015 %	Jackman et al. (1996)
		Historic launch rates of Space Shuttle, Titan III, Titan IV	0.025 % average ozone for 1997	Jackman et al. (1998)
2D CTM	Cambridge 2D	10 Ariane V launches per year (20 model years)	0.1 % locally and globally. Increase in stratospheric aerosols of 1 %. Recovery time of 5 years.	Jones et al. (1995)
2D CTM	-	10 Proton launches (hydrazine fuel)	0.012 % global average ozone loss	Ross et al. (2004)
3D GCM	WACCM	1000 hybrid fuelled suborbital vehicles per year		Ross et al. (2010)
3D GCM	WACCM	10 ⁴ - 10 ⁵ Skylon launches per year	0.5 global ozone loss. Exceeds 2 % at the poles.	Larson et al. (2017)

the Reaction Engines Skylon vehicle. The ozone depletion was predicted to be a 0.5 % loss of the global average ozone column, about 10 % of peak depletion in the 1990s. The global effective radiative forcing was estimated to be 0.03 W m^{-2} , similar to the current contribution of aviation. Generally, the atmospheric impact of water vapour from launchers has been ignored because of the presence of much more damaging species, such as Cl from SRMs and NO_x from air-breathing engines, but it is clear that even water vapour could have significant consequences on radiative forcing of the atmosphere.

Ross et al. (2010) investigated the effect of a successful space tourism industry, assuming 1000 annual launches of hybrid-rocket suborbital vehicles. Each flight distributed black carbon (BC) across the altitude column equally with an $EI(\text{BC})$ of 60 g kg^{-1} . This comes from an assumption that hybrid rockets produce more BC than traditional hydrocarbon propellant rockets (kerosene), which Byun and Baek (2007) estimate to be 20 - 40 g kg^{-1} . The response of the Earth system was then modelled using a global climate model, and estimated the radiative forcing to be 43 mW m^{-2} , well matched by a simplified radiative forcing calculation. This approach made assumptions about the distribution of emissions throughout the atmosphere, and did not account for any reduction in BC from afterburning in the plume, which is reported throughout the literature (Alexeenko et al., 2002; Plastinin et al., 2002, 2004, 2005).

These models and results have focused primarily on either verifying understanding of the impact of launch vehicles on a small scale (e.g. a single vehicle or propellant type) or future extreme scenarios. Another approach is to quantify the overall impact of launches across the world. The Aerospace Corporation performed a series of emissions estimates for global space launches for the US Air Force (DeSain and Brady, 2014), the last of which covered the period of 1985 - 2013. Emission estimates were based on simple assumptions and values estimated from other authors, and so their dataset of emissions sources is formed of data with varying levels of fidelity. This is not a major issue because simplified approaches to calculate both radiative forcing and stratospheric ozone loss are also used.

They consider the emissions of CO_2 and NO_x at all altitudes, stratospheric soot, H_2O and sulfates. They categorise emissions into regions of the atmosphere (troposphere and stratosphere), and estimate the ozone loss and radiative forcing components for each emission type, making several assumptions. For example, the radiative forcing from carbon

dioxide is estimated based on calculations for long term CO₂ growth and radiative impacts from all sources:

$$RF = \frac{m_{\text{CO}_2}}{M_{\text{CO}_2}} \frac{12.01 \text{ g}}{44.01 \text{ g}} RE k_{\text{CO}_2} \quad (2.4)$$

where m_{CO_2} is the mass of CO₂ released between 1985 and 2013, M_{CO_2} is the total annual mass increase of atmospheric CO₂, RE is the radiative efficiency for atmospheric CO₂, 0.015 48 Wm⁻² per ppmv, and k_{CO_2} is the underlying long-term atmospheric CO₂ growth rate, 1.9 ppm yr⁻¹. 12.01 and 44.01 are the molecular mass of carbon and carbon dioxide respectively.

Similar calculations are used for other radiative forcing contributions, as well as the radiative forcing associated with stratospheric ozone loss. The worldwide radiative forcing from all launch activity in the 1985 - 2013 period is estimated to be 0.0021 W m⁻², although there is a great deal of uncertainty in some of the radiative forcing contributions. This study puts the overall impact of launch into context and is similar to the global inventories that are used to quantify aviation's emissions. However, it does not attempt to forecast future impacts, and the launch sector has evolved significantly since the study was last performed.

They also were able to look at the evolution of this radiative forcing due to a reduction in US launch rates (15.6 launchers per year in the 1990s, compared to 11.7 launchers per year in 2000s). On a global scale, emissions of CO₂ reached a minimum in 2003, and increased until the end of the study in 2013. They also identified that changes in the launch sector may lead to increases in the numbers of solid-fuelled launches and kerosene-fuelled launches (due to the SpaceX Falcon rocket and new Chinese launch vehicles). [Wilson \(2019\)](#) quantifies the effect of two launch scenarios (one based on current rates, and one a future scenario considering 750 launches per year) in a life cycle assessment context. The impact on climate change for these scenarios is characterised using a global warming potential metric measured as mass of CO₂ equivalent. Approaches like this are reliant on data about the radiative forcing for different emissions enabling characterisation factors for different propellants to be defined.

[Ross and Sheaffer \(2014\)](#) used a novel approach to estimate the instantaneous radiative forcing from four propellant combinations: hydrogen/LOX, solid rocket motors,

kerosene/LOX and hypergolic fuels. This was judged to be appropriate for comparing the orders of magnitude of propellant combinations, but makes simple assumptions on the distribution of the emissions in the atmosphere, as well as the emission indices (particularly for soot). It also includes direct forcing from alumina (net warming) instead of only the net cooling effect from alumina-caused ozone destruction. The radiative forcing was calculated by assuming that the pollutants would accumulate in a specific region of the stratosphere, and then using the mass specific absorption or scattering factor, σ_j to estimate the radiative forcing,

$$RF = I \left[\frac{2M}{3} NEI_j \tau \right] \sigma_j A_{NH}^{-1} \quad (2.5)$$

where M is the mean mass of propellant burned per launch, N is the annual launch rate, EI_j is the emission index of species j , I is the mean solar shortwave or terrestrial longwave radiation, τ is the e-folding time for the species to be removed from the accumulation region of the atmosphere, the area of which is A_{NH} . σ_j is the mass-specific scattering or absorption factor for species j and the $2/3$ represents the proportion of propellant burn that occurs above the troposphere.. The key conclusion is that the radiative forcing contributions of H_2O and CO_2 are minor compared to particulate matter; soot for hydrocarbon propellants and alumina for solids, but the scale of the warming is sensitive to precise particulate source terms, which are not well understood due to a lack of measurements. The overall radiative forcing of solid rockets is difficult to quantify, because of the combination of warming (radiative forcing from alumina) and cooling (stratospheric ozone destruction).

2.3.4 Measurements

Measuring the rocket emissions from launch vehicles in flight is extremely difficult, due to their high speed, and vast distances travelled in short periods of time. Despite this a number of in-situ measurements have been carried out, focusing particularly on characterising the particle size distribution of alumina from solid rockets, a key factor in determining their effect on the atmosphere. All known in-flight measurements are shown in table 2.6, and all were taken by flying an aircraft with a measurement package through the plume several minutes after launch.

Table 2.6 In situ measurements of rocket plumes

Rocket type	Motor	Site ^a	Altitude	Plume age (min)	Published results on species	Dates	Ref
Space Shuttle	SRM	CC	4.6 - 7.6		Al ₂ O ₃ PSD	30/10/1985	Cofer et al. (1987)
Space Shuttle	SRM	CC	2.4, 3.0, 3.2, 7.4		Al ₂ O ₃ PSD	18/10/1989	Cofer et al. (1991)
Titan IV	SRM	CC	19.8	29	O ₃ , Cl ₂ , PSD (0.01 - 4 μm), cn	24/4/1996, 20/12/1996	Ross et al. (1997a), Ross et al. (1997b), Ross et al. (1999)
Space Shuttle	SRM	CC	17-19.5	5-125	PSD (0.01 - 4 μm), cn	04/04/1997, 08/08/1997	Ross et al. (1999)
Delta II	SRM LOX/kerosene	VA	18-19.4 11-12	12, 39	O ₃ , ClO, CO ₂ , CH ₄ , cn, PSD, cn	7/11/1996, 17/05/1998, 15/04/1999	Ross et al. (2000), Gates (2002)
Athena II	SRM	VA	16-19	4-26	ClO, CO ₂ , H ₂ O, NO _y , HNO ₃ , part. comp., PSD, cn	9/24/1999	Schmid (2003), Popp et al. (2002), Gates (2002), Cziczo (2002)
Atlas IIAS	SRM, LOX/kerosene	CC	19	-	CO ₂ , PSD, cn	12/04/1999	Gates (2002)
Space Shuttle	SRM, LOX/hydrogen	CC	-	5-90	part. comp.	09/09/2000	Gates (2002)

^aCC - Cape Canaveral, VA - Vandenberg

Plumes are often highly radiative, and therefore remote measurements of the radiative flux can be made. Efforts to do so at first were focused on missile tracking and to understand how plumes could be made less radiative for stealthier weapon systems. However, the composition of the plume is highly influential on the radiation emitted by the plume, particularly particulate matter, and so it has also been used to understand the process of afterburning in the plume of rocket engines ([Simmons, 2000](#)).

Measurements are able to provide valuable information on the local effects of launches on the atmosphere. One of the key results of these measurement campaigns is that in some cases 100 % of the ozone in the plume was depleted by launch, but that ozone levels in these regions recovered in a period of hours as the atmosphere mixes. However, they are unable to provide information on the global effects, as it is difficult to distinguish their effect from the contributions of other anthropogenic sources - this is the same limitation that aviation has. Therefore experiments and measurements should be used to validate models, and it is modelling capability that is used to understand the overall consequences.

2.3.5 Regulation

The space sector is significantly smaller than aviation, and each nation has its own regulatory environment that enables it to fulfil its obligations as a signatory of international treaties such as the Outer Space Act, which largely involve safety and liabilities for launchers. Some launching states have additional environment requirements.

In the US, the National Environmental Policy Act requires federal agencies such as NASA or the FAA Office of Commercial Space to include environmental concerns with their decisions. They do this assessment themselves for launch site and launch operator licenses that they issue. The assessments characterise and address the effect of the activity on a number of environmental concerns: land use/visual resources, noise, biological resource, cultural resources, air quality, climate, hazardous materials, water resources, geology and soils, transportation, utilities, health and safety and socioeconomics ([FAA, 2013](#); [NASA, 2019](#)) . They also consider the cumulative impacts of the activity on each of these areas.

For climate impacts, an estimate of the emissions produced by the activity is used. For example, table [2.7](#) shows the estimated CO₂ emissions in NASA's draft environmental assessment for the SpaceX Starship and Super Heavy launch vehicle.

Table 2.7 Estimated SpaceX Starship and Super Heavy CO₂ emissions per year (NASA, 2019)

Annual emission sources (24 launches)	Metric tons CO ₂ per year
Global 2018 total CO ₂ emissions	3710 × 10 ¹¹
US 2018 total GHG emissions	5140 × 10 ⁶
2017 KSC GHG emissions	96 645
24 Starship/Super Heavy launches	83 794
24 Starship landings	1369
24 Super Heavy booster landings	5544
24 Starship static fire tests	4294
24 Super Heavy static fire tests	16 526

Greenhouse gas (GHG) emissions from the proposed activities are more than the normal emissions from the Kennedy Space Centre (KSC), so if this launch rate was achieved the emissions from KSC would more than double, excluding other launch operations. There is no attempt to quantify the influence of the released CO₂, or indeed any other species, and conclude that:

‘The estimated CO₂ emissions from annual operations of Starship/Super Heavy are significantly less than the total GHG emissions generated by the United States in 2018 and the total CO₂ emissions generated worldwide.’

For species that affect air quality, there are federal limits on chemicals (CO, lead, NO_x, O₃, PM10, P2.5, SO₂) in ambient air. Launch sites such as the Kennedy Space Centre monitor the actual levels of these species. The FAA include the effect of launch activities and failures, especially when toxic propellants are involved. They quantify the amount of emitted chemicals, and confirm that they are within these limits. In the case of the Starship/Super Heavy, they estimate the amounts of NO_x and CO released below the mixing altitude to be 0.29 tons per year for NO_x and CO and compare these to the overall amounts released by the county, concluding that they are negligible.

The environmental assessments the FAA produces ignore the effects of emissions above the mixing height (3000 feet above ground level) on air quality. For aircraft, this has been demonstrated not to be a good assumption, although it depends on whether the purpose of the assessment is to check if local populations are affected, or wider non-attributable global air quality effects.

Within the UK, launch operators must perform an *Assessment of Environmental Effects* that the Civil Aviation Authority (CAA) must take account of when issuing a launch operator licence (UK Parliament, 2018). In 2021, the UK Department for Transport Secretary of State set out the environmental objectives for the CAA to take account of when make their licensing decisions, which included the objective for the regulator to ‘*minimise emissions contributing to climate change resulting from spaceflight activities*’ (Department for Transport, 2021).

For other nations, it is not clear how the environmental impact of space access will be regulated, beyond other environmental legislation such as the EU REACH regulations. ESA’s approach is to understand the environmental impact of their launchers, and to require life cycle assessment during their development in order to better address their environmental impacts (Gallice et al., 2018). It isn’t yet clear how other jurisdictions will respond to the increasing commercialisation of space and potential need for environmental regulation.

2.3.6 Life cycle assessment

A common approach to quantifying the overall environmental impact of an activity is through life cycle assessment (LCA). This is an approach which assess the environmental impacts of a product or service over their entire life cycle from the extraction and processing of raw materials, through to the manufacture of components, assembly, transportation, use and their end of life. This takes a step beyond simply assessing adverse environmental impacts of only the activity itself (in this case, the launch event).

LCA is used internationally and in many industries, and so has been standardised to provide a common framework for all LCAs in several ISO standards (ISO 14040:2006 and 14044:2006 (International Organization for Standardization, 2006a,b)). Sustainability has been a focus of the space community for many years. The "Guidelines for the long-term sustainability of outer space activities" are a set of non-binding guidelines agreed by the UN Committee on the Peaceful Use of Outer Space (COPUOS), and contains guideline 27.3, which states that space actors ‘should promote the development of technologies that minimise the impact of manufacturing and launching space assets’. LCA will continue to play a major role in future for companies and other organisations to ensure their environmental impact is minimised.

A key requirement of LCA is for an inventory of emissions or other types of environment impacts that can be coupled with the life cycle being studied to estimate the impacts. The inventory database is then associated with environment impact categories, which have a standard comparison that allows the environment impacts of the entire life cycle to be applied in a consistent way. For example, climate change is measured with the unit kgCO₂ eq, which allows the effects of other pollutants to be converted into the equivalent amount of carbon dioxide in terms of their global-warming potential (GWP). Other examples of impact categories are ozone depletion, toxicity for freshwater aquatic, human and marine life. ESA has a recommended set of environmental impact categories and units, which introduce three specific space impact categories for Al₂O₃ emissions, and mass disposed in the ocean and space (Wilson, 2019).

Inventory databases require estimations of the environmental impact of emissions for the flights of launch vehicles. For some emissions, this is not a significant challenge as there are standard characterisation factors that enable the specific impacts to be incorporated in the assessment (Department for Business Energy & Industrial Strategy, 2020). However, for some launch vehicle emissions which are unique either in their production or in the location of their emission, further efforts are needed to model these effects specifically (for example, soot deposited in the stratosphere). Indeed, some early calculations produced in this work have been used within the Strathclyde Space Systems Database, a new framework that attempts to extend the existing space environmental LCA methodology to a wider view of sustainability (Wilson, 2019).

2.4 Summary

There are three important trends that have been described in the previous sections. The first, is that the long term sustainability of transportation is an ever higher priority in the political and public consciousness, driven by climate change and awareness of the human health impacts of air quality. In aviation, this has resulted in regulator and international body driven reductions in per air mile emissions, and carbon trading schemes where the limits of innovation are reached. In space, emphasis has been placed on sustainable use of space, increasingly by accounting for the social and environmental life cycle impacts of

manufacturing and launch. Although worse case scenarios, such as a peak of 10 % ozone depletion are unlikely to occur in the near term, it would likely lead to significant public concern if it did. [Ross et al. \(2009\)](#) explored this idea, discussing how the reduction of other ozone-depletion substances controlled by regulation (for example, Chlorofluorocarbons), would increase the importance of considering the impact of launches on stratospheric ozone, especially as technology and the market evolves. They predicted the ozone depletion for a number of future large-scale utilisation scenarios by parameterising the global total ozone loss per mass launched to LEO. Their conclusion was that revolutionary changes in the access and utilisation of space could have significant impacts on stratospheric ozone - even in the case of using propellants traditionally associated as "clean", i.e. $1\text{-H}_2/1\text{-O}_2$. There is already evidence that the expectations of the public on environmental damage is shifting. In recent years, significant public opposition to even small-scale new launch activity in the UK has arisen for the Newquay and Sutherland spaceports ([McKenzie, 2018](#); [Whitehouse and Reines, 2019](#)). Similarly, the space tourism projects by Virgin Galactic and Blue Origin received significant amounts of negative attention during 2021 when they flew their first commercial flights, largely due to the perception that they had environmental impacts without any larger benefits to society ([Mondale, 2021](#)). Further to this, the COVID-19 pandemic has drastically reduced the amount of international air travel, but the impacts to the launch sector have been more limited. If this or similar reductions in air travel persist, launch will remain as a higher proportion of the overall emissions into the stratosphere than they currently are, becoming an even further target for opposition.

The second trend is the evolution of vehicle design, operations and global growth in the launch sector. The last decade has seen a major change in the companies and vehicles performing launches, and a similarly large increase in the number of objects launched to space. Together, these make it likely that the space sector will grow over the coming decades. A limitation of prior research is that it has been focused on understanding the effects of current vehicle, or extreme scenarios. Few studies have looked at future vehicle concepts, and none have attempted to include emissions within the preliminary design phase, where less is known about a vehicle, but where key decisions that have environmental consequences, such as propellant choices, are made.

The third trend is that many sectors now embrace life cycle assessment, which enables engineers to quantify the emissions, resources depleted and pressures on human health and the environment throughout the design, build, operation and demise of an activity or product (Neumann, 2018; Wilson, 2019). Traditional launch systems may have well established emissions profiles that can be directly included in LCA, but well characterised emissions profiles of novel concepts and new vehicles are needed to consider the impacts of their flights.

3 | SIMULATING AND OPTIMISING TRAJECTORIES

Producing a profile of the emissions released into the atmosphere by a vehicle during flight requires two things, knowledge of the chemical species produced by the vehicle's propulsion system and the trajectory of the flight. Trajectory optimisation is used to find optimal and feasible trajectories for conceptual and real vehicles, based on mathematical models representing the vehicle, environment and operations.

Section 3.1 introduces the general approach used to numerically determine the trajectories including the system dynamics, required reference frames and the specific form of the equations of motion used throughout. It is followed by an overview of trajectory optimisation techniques in section 3.2, and formulation of the multi-shooting optimisation solver used to find optimal control laws of the launchers in chapter 6.

3.1 Simulating trajectories

General equations of motion can be derived by applying Newton's second law to a rigid body with constant mass:

$$\begin{aligned}\sum \mathbf{F} &= m\mathbf{a}_I && \text{Force} \\ \sum \mathbf{M} &= [I]\dot{\boldsymbol{\omega}}_I && \text{Moment}\end{aligned}\tag{3.1}$$

where the force equation provides the evolution of the translation position and velocity of the body and the moment equation provides the angular orientation and the rate of change of this orientation. This is a six degree of freedom set of 2nd order differential equations for the acceleration.

The rotational dynamics may be decoupled and neglected by assuming the vehicle is a point mass. Under this assumption, only the translational dynamics are included, where the force, \mathbf{F} is the sum of the vector forces on the vehicle, including thrust, \mathbf{T} , aerodynamics forces \mathbf{A} and the weight of the vehicle, \mathbf{W} as function of time, t . This results in a three degrees of freedom (3DoF) set of equations of motion:

$$\begin{aligned}\dot{\mathbf{r}}(t) &= \mathbf{v}(t) \\ \mathbf{F}(t) &= m\dot{\mathbf{v}}(t) = \mathbf{T}(t) + \mathbf{A}(t) + \mathbf{W}(t),\end{aligned}\tag{3.2}$$

with the position of the vehicle represented by \mathbf{r} and the velocity vector by \mathbf{v} . The attitude of the vehicle is represented by aerodynamic angle of attack and the bank angle (between the velocity of the vehicle and the body axes of the vehicle). The vector of the thrust angle is either assumed to be fixed in the body frame or can be controlled by setting the relative angle of the engines.

For the use case presented in this thesis, where only the motion of the centre of mass of the vehicle is needed to characterise the emissions profile, a three degree of freedom approach is well suited. The purpose of the trajectory model is to determine a feasible trajectory for the vehicle concept in order to extract its position in space and the associated emissions. Therefore, only a preliminary or representative control law is needed. As the objective is not to produce a control law for use in a vehicle's guidance system, detailed design of the control law of the vehicle is not necessary (and typically not available for conceptual vehicles).

The system may be extended to a variable-mass point by introducing another equation,

$$\dot{m} = -\dot{m}_p\tag{3.3}$$

where \dot{m} is rate of change of mass with time and \dot{m}_p is the mass flow rate of expelled propellant.

These equations need to be applied considering the reference frame, coordinate system and vehicle models that best represent the flight of the vehicle. There is no closed form analytical solution for this equation set, so they must be integrated numerically.

3.1.1 Reference frames & coordinate systems

A short discussion of reference frames and coordinate systems is necessary to understand and derive the specific equations of motion used within this thesis. The reference frame is a rigid grid attached to an observer, from which the motion of an object can be measured. The coordinate system is the construct that enables the measurement of the object relative to the frame's observer, i.e. a cartesian or polar coordinate system (Koks, 2017).

Earth-centered inertial (ECI)

The Earth-centered inertial (ECI), or \mathcal{F}^I , reference frame is a non-accelerating (inertial) frame of reference, with its origin at the Earth's centre of mass, and is sometimes denoted as $OX_iY_iZ_i$. It is defined by:

- The origin is located at the centre of mass of the Earth.
- The Z_i -axis is along the axis of the Earth's rotation through the north pole.
- The X_i -axis is in the equatorial plane pointing towards the vernal equinox.
- The Y_i -axis completes the right-handed set (90 degrees to the east of the x axis).

In a Cartesian coordinate system, sometimes known as the Earth-centered Inertial Cartesian (ECIC) frame, the position and velocity of a vehicle are defined by two rectangular vectors, $\mathbf{r} = [r_x, r_y, r_z]$ and $\mathbf{v} = [v_x, v_y, v_z]$. However, it may also be convenient to use a spherical coordinate system, using latitude, longitude and altitude (or radius).

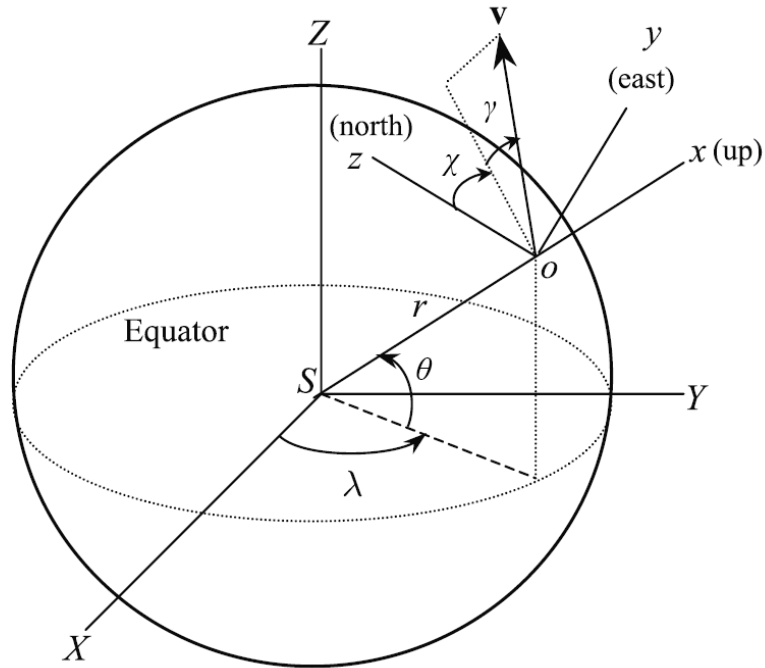
Earth-centered, Earth-Fixed (ECEF)

The Earth-centered, Earth-fixed (ECEF), or \mathcal{F}^E system is similar to the ECI frame but is noninertial and rotates with the Earth (shown in fig. 3.1). It is defined by:

- The origin is located at the centre of mass of the Earth.
- The z axis is along the axis of the Earth's rotation through the north pole.
- The x axis passes through the equatorial plane and a reference meridian (usually the Greenwich meridian).

- The y axis completes the right-handed set (90 degrees to the east of the x axis).

Fig. 3.1 Planet-fixed reference frame, modified from [Tewari \(2007\)](#)



It is sometimes referred to more generally as the Planet-Centered, Planet-Fixed (PCPF) frame, and can also be represented with polar coordinates instead of cartesian coordinates. To develop equations of motion in the ECEF frame, the effect of the rotation of the Earth needs to be included in the formulation - the so-called fictitious forces.

Vehicle Velocity Frame

The velocity frame \mathcal{F}^v tracks the velocity vector of the vehicle, with no knowledge of its attitude. It is a rotation from a local Earth reference frame through the vertical flight path angle γ and the heading angle χ :

$$\mathbf{R}^{vi} = \mathbf{R}_2(\gamma)\mathbf{R}_3(\chi). \quad (3.4)$$

Wind Frame

It is convenient to express the aerodynamic forces of the vehicle using the wind frame \mathcal{F}^w , since these are relative to the velocity direction of the incoming air and the plane of

symmetry of the vehicle. This is a rotation from \mathcal{F}^v through the bank angle μ :

$$\mathbf{R}^{vw} = \mathbf{R}_1(\mu) \quad (3.5)$$

Body Frame

The body frame, \mathcal{F}^b , is fixed to the vehicle in question, for a winged vehicle this is usually with one axis through the length of the aircraft, one through the tips of the wing, and the final axis through the centre of mass.

It can be defined as either a rotation from \mathcal{F}^w through the angle of attack α and sideslip β :

$$\mathbf{R}^{bw} = \mathbf{R}_2(\alpha)\mathbf{R}_3(-\beta) \quad (3.6)$$

or from the local earth frame, \mathcal{F}^l with a rotation through roll, ϕ , pitch, θ , and yaw ψ :

$$\mathbf{R}^{bl} = \mathbf{R}_1(\phi)\mathbf{R}_2(\theta)\mathbf{R}_3(\psi) \quad (3.7)$$

Since the body frame is fixed to the vehicle, the direction of the thrust from a fixed engine is usually defined in this reference frame.

3.1.2 Equations of motion

The equations of motion are formulated to represent the translational flight dynamics of a vehicle in flight in the Earth-centred, Earth-fixed (rotating) reference frame, shown in fig. 3.1. The atmosphere is assumed to move with the Earth's rotation. A spherical coordinate system is used because it holds more meaning in terms of a vehicle's geographic position. The position is represented as $\mathbf{r} = [r, \theta, \lambda]$, where r is the magnitude of the radial distance, θ is the geodetic latitude and λ is the geodetic longitude. The velocity is $\mathbf{v} = [v, \gamma, \chi]$, where v is the magnitude of the velocity, γ is the flight path angle and χ is the heading angle.

The equations of motion are:

$$\dot{r} = v \sin \gamma \quad (3.8a)$$

$$\dot{\lambda} = \frac{v \cos \gamma \cos \chi}{r} \quad (3.8b)$$

$$\dot{\theta} = \frac{v \cos \gamma \sin \chi}{r \cos \lambda} \quad (3.8c)$$

$$\dot{v} = \frac{(F_T(\tau) \cos \alpha - D)}{m} - g_r \sin \gamma + g_\phi \cos \gamma \cos \chi \quad (3.8d)$$

$$+ \omega_E^2 r \cos \lambda (\sin \gamma \cos \lambda - \cos \gamma \cos \chi \sin \lambda) \quad (3.8e)$$

$$\gamma = \frac{1}{v} \left(\frac{(F_T(\tau) \sin \alpha + L) \cos \mu}{m} - g_r \cos \gamma - g_\phi \sin \gamma \cos \chi \right) + \frac{v}{r} \cos \gamma + \frac{\omega_E^2 r}{v} \cos \lambda (\sin \gamma \cos \chi \sin \lambda + \cos \gamma \cos \lambda) + 2\omega_E \sin \chi \cos \lambda \quad (3.8f)$$

$$\dot{\chi} = \frac{1}{v \cos \gamma} \left(\frac{(F_T(\tau) \sin \alpha + L) \sin \mu}{m} - g_\phi \sin \chi \right) + \frac{v}{r} \cos \gamma \sin \chi \tan \lambda + \omega_E^2 r \frac{\sin \chi \sin \lambda \cos \lambda}{v \cos \gamma} + 2\omega_E (\sin \lambda - \tan \gamma \cos \chi \cos \lambda) \quad (3.8g)$$

where:

m is the mass of the vehicle

F_T is the magnitude of the engine thrust

L is the lift force

D is the drag force

α is the angle of attack

μ is the bank angle

$r = R_e + h$ is the radius from the centre of the Earth

ω_E is the rotational velocity of the Earth

g_r is the radial component of the gravitational acceleration vector

g_ϕ is the tangential component of the gravitational acceleration vector

The flight path angle γ is defined as being the angle between the local horizon and the velocity vector, and the flight heading angle χ is defined as the angle between north and

the horizontal component of the velocity vector. The control law governs the angle of attack α , bank angle μ and the propulsion throttle of the vehicle.

The final equation governing the motion of a variable point mass under 3 degrees of freedom is the mass change equation,

$$\dot{m} = -m_p, \quad (3.9)$$

where m_p is the mass of the propellant expelled from the vehicle during flight.

To simulate the flight of a particular vehicle, the initial-value problem for this set of differential equations is solved. There are many algorithms that may be employed solve these equations computationally, with the classic example being the Runge-Kutta family (Griffiths and Higham, 2010). There are implementations of powerful integration methods in many programming languages, including Julia (Rackauckas and Nie, 2017), MATLAB, C++/FORTRAN (Hindmarsh et al., 2005) and Python (Jones et al.). In this case, a non-adaptive (fixed step) explicit numerical integrator is used, which utilises the Dormand-Prince method. Control of the order of solver, between 1 and 5 is given to the user, which enables the trade-off between the errors and solution speed.

Aerodynamics

The drag, D and lift, L produced by the vehicle during flight are calculated using the standard equations,

$$D = \frac{1}{2} \rho C_D v^2 A \quad (3.10)$$

and

$$L = \frac{1}{2} \rho C_L v^2 A \quad (3.11)$$

where:

ρ is the atmospheric density

C_D is the coefficient of drag of the vehicle

C_L is the coefficient of lift of the vehicle

v is the vehicle's velocity

A is the reference area of the vehicle

The parameter C_L is usually a function of the Mach number, M , and the angle of attack, α , and is vehicle dependent. The Mach number is:

$$M = \frac{V}{a} \quad (3.12)$$

where a is the speed of sound, an output of the atmospheric model.

3.1.3 Atmospheric model

A model of the atmosphere is required to estimate the drag and lift of a vehicle during flight. The atmosphere is dynamic and complex system, which makes it difficult to create a definitive and accurate model. The aerospace community has developed a number of atmospheric models that are representative of the atmosphere in varying levels of fidelity that can be used for modelling flight vehicles.

One common model is the International Standard Atmosphere ([NOAA and US Air Force, 1976](#)). This provides the atmospheric pressure p_a and temperature T_a as a function of altitude, h , from which the air density, ρ_a and local speed of sound a , can be calculated. This model divides the atmosphere into 11 layers, each with a linear temperature distribution with altitude. The pressure and the density are found by solving the vertical pressure variation and the ideal gas law.

Other, more advanced models that represent the atmosphere in more detail could be used. For example, the NRLMISISE-00 ([Picone et al., 2002](#)) model includes time and latitudinal/longitude variance as well as altitude and accounts for the influence of solar flux in the upper atmosphere. However, given the level of fidelity of the other models used in this thesis such as the aerodynamics and propulsion system models, the ISA was judged to be an appropriate balance between accuracy and performance. Wind was not considered in any of the trajectory simulations.

3.1.4 Earth & gravitational model

The Earth is modelled as a spherical, rotating planet with radius $R_E = 6375253$ m and an angular velocity of $\omega_E = 7.292115 \times 10^{-5} \text{ rad s}^{-1}$.

A gravitational model is used to approximate the gravitational field around the Earth. The simplest approach is to assume a single value based on the acceleration due to gravity at the Earth's surface, $g = 9.81 \text{ m s}^{-1}$. An improvement in accuracy can be gained by including its variation with altitude using Newton's law of gravitation,

$$g = \frac{\mu_E}{r^2} = \frac{\mu_E}{(h + R_E)^2} \quad (3.13)$$

where the standard gravitational parameter, $\mu_E = 398\,600.4418 \text{ km}^3 \text{ s}^{-2}$.

However, the Earth is not a perfect sphere, and so its gravitational field is variable with position. One such model is used within the trajectory optimisation tool in this thesis, where the gravity field is represented by a series of spherical harmonics, with the accuracy tailored to the application by adding terms to the expansion. Here, a fourth order expansion of the radial (g_r) and tangential (g_ϕ) acceleration due to gravity was used:

$$g_r = -\frac{GM_E}{r^2} \left\{ 1 - \frac{3}{2}J_2 \left(\frac{R_e}{r}\right)^2 [3\cos^2\phi - 1] - 2J_3 \left(\frac{R_e}{r}\right)^3 \cos\phi [5\cos^2\phi - 3] - \frac{5}{8}J_4 \left(\frac{R_e}{r}\right)^4 [35\cos^4\phi - 30\cos^2\phi + 3] \right\} \quad (3.14a)$$

$$g_\phi = \frac{3GM_E}{r^2} \left(\frac{R_e}{r}\right)^2 \sin\phi \cos\phi \left\{ J_2 + \frac{1}{2}J_3 \left(\frac{R_e}{r}\right) \sec\phi [5\cos^2\phi - 1] + \frac{5}{6}J_4 \left(\frac{R_e}{r}\right)^2 [7\cos^2\phi - 1] \right\} \quad (3.14b)$$

where:

$$J_2 \text{ is } 1.082\,635\,9 \times 10^{-3}$$

$$J_3 \text{ is } 2.532\,153 \times 10^{-7}$$

$$J_4 \text{ is } 1.610\,987\,6 \times 10^{-7}$$

ϕ is the latitude

r is the radius of the vehicle

M_E is the mass of the Earth

R_E is the radius of the Earth

3.2 Trajectory optimisation

During the design process of a new vehicle, the open loop control law that produces an optimal trajectory of the concept vehicle will not be known. This is especially true of new classes of vehicles, such as spaceplanes or hypersonic aircraft. The combined effect of the environment, the vehicle and the dynamics may be highly non-linear, thus making it difficult to define intuitively what the optimal trajectory will be. Additionally, optimal trajectories of current and commercially available launchers are not published, so to ensure a level playing field when comparing emissions, it is useful to produce these trajectories using the same approach, so any systemic errors are replicated in all the data sets.

In launch vehicle conceptual design, the incentive to find optimal trajectories is to maximise performance and reduce costs. The solution is to apply mathematical optimisation to the problem, which has been used in aerospace engineering for decades. Increasing computational capability has enabled the use of its application on larger, more complicated problems, and several specific frameworks for optimising flight trajectories have been developed.

A general continuous optimisation problem can be framed as:

$$\text{Minimise } f(x) \quad (3.15a)$$

$$\text{Subject to } g_i(x) \leq 0, \quad i = 1, \dots, m \quad (3.15b)$$

$$h_j(x) = 0, \quad j = 1, \dots, p \quad (3.15c)$$

where:

f is the objective function to be minimised for the n -dimensional vector x

$g_i(x) \leq 0$ are inequality constraints

$h_j(x) = 0$ are equality constraints

For trajectory optimisation, the parameter space is the open loop control law, and the objective function is something of interest to the designer, such as to:

- Minimise take-off weight;

- Minimise or maximise flight time;
- Maximise mass-to-orbit;
- Minimise fuel consumption.

The problem needs to be set up to reflect how a launch is constrained by various limitations on the vehicle (such as aerodynamic forces), hence the problem is a constrained optimisation problem.

3.2.1 Optimal control

Finding the optimised trajectory of a vehicle in flight is an optimal control problem (OCP). The problem to be solved is to find the control law that optimises some measure of optimality given the dynamics of the system (i.e. the equations of motion). Simple optimal control problems can be solved analytically through the calculus of variations, like John Bernouilli's famous Brachistocrone problem. However, this is not feasible for the optimal control of a launch vehicle, due to the complexity of the problem, so numerical solutions are required.

The optimal control problem can be formulated in general as follows. The objective is to determine what control law, $\mathbf{u}(t)$, can minimise the cost function:

$$\text{Minimise} \quad J = \Phi(x_f, t_f) + \int_{t_0}^{t_f} \mathcal{L}(\mathbf{x}, \mathbf{u}, t) dt \quad (3.16a)$$

$$\text{Subject to} \quad \dot{\mathbf{x}} = f(\mathbf{x}, \mathbf{u}, t), \quad (3.16b)$$

$$\mathbf{g}(\mathbf{x}, \mathbf{u}, t) \geq 0 \quad \text{for} \quad t_0 \leq t \leq t_f, \quad (3.16c)$$

$$\Psi_0(\mathbf{x}_0, t_0) \geq 0, \quad (3.16d)$$

$$\Psi_f(\mathbf{x}_f, t_f) \geq 0. \quad (3.16e)$$

where:

J is a scalar performance index

\mathbf{g} are path constraints (equality or inequality)

Ψ are boundary constraints (equality or inequality)

In the optimal control problem shown in eq. (3.16), the control law, $\mathbf{u}(t)$ is actually a continuous control function, rather than a set of control parameters. Ideally, the solution to an OCP would be an analytic function, but this is very difficult in practice.

Flights of launch vehicles have inherent discontinuities within their trajectories, due to physical models or the mission profile. This can include features like multi-staging in rockets, propulsion system mode switches in combined-cycle engines, and the transition from subsonic to supersonic flight speeds (where the aerodynamic model changes). To address this, the optimal control problem is often formulated as a collection of n_p phases. An additional set of constraints, called linkage constraints are added to ensure different phases are linked together. Different models, dynamic equations, constraints and objective functions can be used in each phase.

There are several approaches to solving optimal control problems. In general, they contain two features; the problem formulation, and the method of solving the differential equations (Betts, 1998, 2010; Conway, 2012; Rao, 2010). There are two classes of problem formulation:

Indirect numerical approaches where optimality conditions are found from *calculus of variations*, and the resulting two point boundary value problem is solved numerically (i.e. by introducing some sort of discretisation).

Direct numerical approaches whereby the continuous time problem is discretised in time and transcribed into a nonlinear programming (NLP) problem, which is solved using optimisation techniques.

Indirect methods use the calculus of variations to solve the optimal control problem. Betts (2010) refers to this as *optimize then discretize* - where the optimality conditions are derived first, and the resultant boundary value problem is then numerically solved. The main advantage of an indirect approach is the accuracy of the resultant guidance law, but this is at the expense of the detailed mathematical analysis required to formulate each problem (Betts, 2010).

Direct methods discretise the problem's continuous control function into a set of parameters (and sometimes state parameters) in time - a process called transcription. The resultant

non linear programming problem is then solved to find an optimal trajectory. [Betts \(2010\)](#) calls this approach *discretize then optimize* to differentiate it from the indirect methods.

The solution from a direct approach is approximate, and therefore some features of the real solution may be lost. The main advantage is the mathematical simplicity, the only equations that are required are those that represent that dynamics of the problem (e.g. a vehicle in flight). Conveniently, the initial conditions of the problem are also physical parameters (initial velocity, position etc).

In the scope of this work, the trajectory optimisation software is applied to a series of vehicle concepts which may have very different concepts of operations, dynamics and guidance laws (e.g. vertical launchers vs. airbreathing spaceplanes). For these reasons, indirect methods are unsuitable for the purposes of this work, as for each of these problems to be solved, a new set of optimality conditions will need to be derived. Additionally, the purpose of the study is to generate an optimal trajectory that enable emissions profiles to be found for a range of different (even arbitrary) vehicles, rather than control laws to be used on real vehicles. Therefore accuracy is not as important as flexibility, and for this reason a direct approach is selected.

Regardless of whether an indirect or direct approach to solving the optimal control problem is used, the dynamic equations must be solved, which may be done with either:

Shooting methods where the future state is calculated based on information about the current state, using time-marching integration. This is the mechanics as has previously been used to describe the process of simulating a trajectory, the dynamic equations are integrated using numerical integration such as the Runge-Kutta method.

Collocation methods use a polynomial (or more generally, an interpolating function) to represent the state of the system. A series of polynomials will be linked by collocation nodes, where a constraint is applied on the derivative of the polynomial, called a defect constraint.

A direct approach was adopted as the problem is too complex to formulate, and different problems may need to be solved depending on the vehicle's concept of operations. Either direct multiple shooting or collocation methods could be used for this problem, but multiple shooting was chosen as the focus is on numerical accuracy rather than computational speed.

3.2.2 Direct shooting and multiple shooting

In a direct shooting method the controls are parameterised as a finite set of parameters:

$$\mathbf{u}(t) \approx \sum_{i=1}^m \mathbf{a}_i \psi_i(t) \quad (3.17)$$

where ψ are the known functions and \mathbf{a} are the parameters to be determined by the optimisation. The dynamics are evaluated based on a control law formed by the interpolated control parameters (see fig. 3.2) by integrating the differential equation set using a time-marching technique, such as a Runge-Kutta or similar. The objective function is determined from the solution of this integration problem, and an optimisation algorithm will then modify the control parameters until the constraints are met, and an optimal solution is found. This process is described in algorithm 1.

Algorithm 1: Direct Single Shooting

Result: Parameterised control law for an optimal trajectory
Input : Initial guess of control parameters
Output : Optimal value of control parameters and optimal state
while *Cost is not optimal and constraints not satisfied* **do**
 foreach *phase* **do**
 | Integrate trajectory from t_0 to t_f ;
 end
 Compute error in constraints;
 Compute objective function;
 Optimisation algorithm modifies the control parameters;
end

Shooting approaches have the advantage of being conceptually simple, and the problem has a small number of variables. Their biggest flaw is that small errors can propagate to large errors at the end of the trajectory. This can be addressed by modifying the direct shooting approach into a multiple shooting approach. The time interval $[t_0, t_f]$ is partitioned into a major grid of $M + 1$ segments, and the direct shooting approach is then applied to each of these segments over the time period $[t_i, t_{i+1}]$. Figure 3.3 shows a series of multiple shooting segments. At this point in the process, there are major discontinuities in the states of the solution, however the state must be continuous. Continuity conditions, in the form of,

$$\mathbf{x}(t_i^-) = \mathbf{x}(t_i^+), \quad (3.18)$$

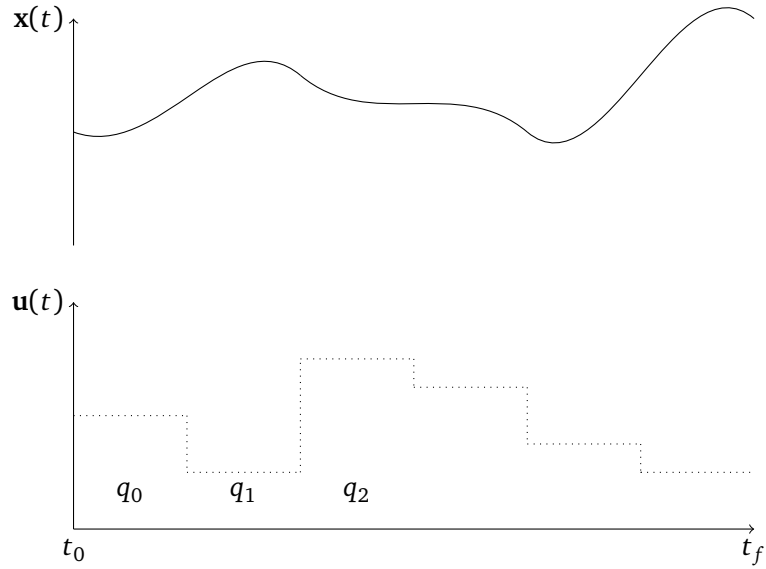


Fig. 3.2 Direct shooting with discrete controls interpolated between points

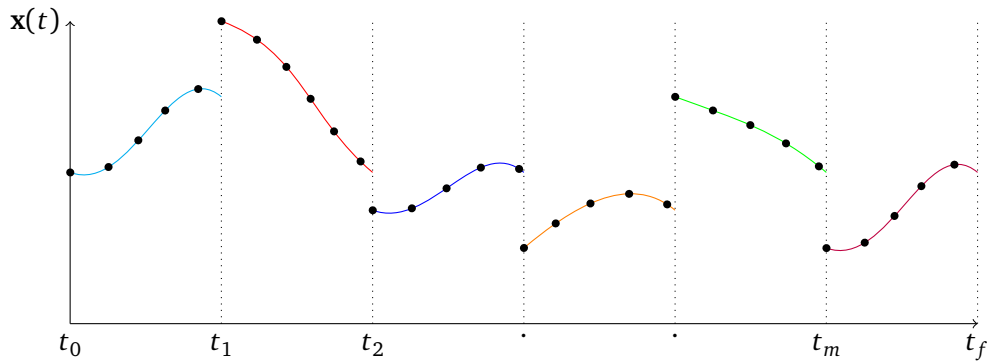


Fig. 3.3 Direct Multiple Shooting where continuity constraints have not been applied

are applied at each segment interface. The resultant state is shown in fig. 3.4, where the optimisation solver has also fulfilled these continuity constraints. This increases the number of variables that have to be optimised, but reduces the numerical errors that can occur when integrating over long time periods.

This is the approach used within this research. The optimal control problem is transcribed into an nonlinear programming (NLP) problem using a multi-phase, multiple-shooting approach. The mission is initially divided into n_p user-defined phases. Within each phase, the time interval is further divided into n multiple shooting segments.

$$\bigcup_{k=1}^{n_p} \bigcup_{i=0}^{n-1} [t_{i,k}, t_{i+1,k}] \quad (3.19)$$

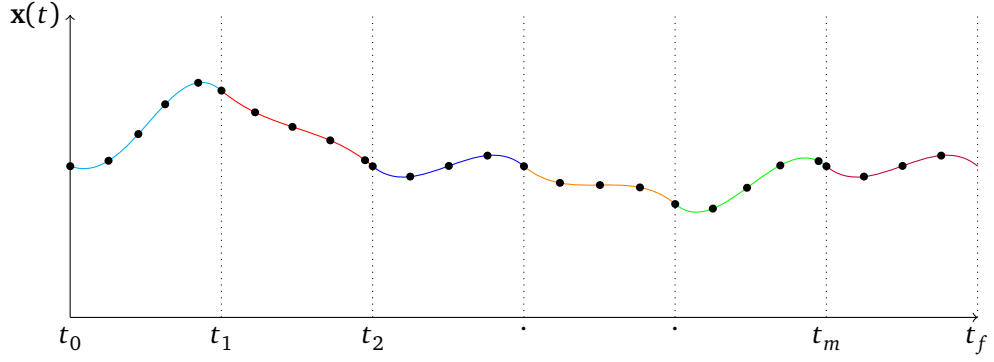


Fig. 3.4 Direct Multiple Shoot: Continuity Constraints are met

Within each interval $[t_{i,k}, t_{i+1,k}]$, the control is further discretised into n_c control nodes $\{u_0^{i,k}, \dots, u_{n_c}^{i,k}\}$ and collocated either linearly or on Tchebycheff points in time.

Continuity constraints on the control and states are imposed:

$$\left. \begin{aligned} \mathbf{x}_{i,k} &= F([t_{i-1,k}, t_{i,k}], \mathbf{x}_{i-1,k}) \\ \mathbf{u}_{n_c}^{i-1,k} &= \mathbf{u}_0^{i,k} \end{aligned} \right\} \text{ for } k = 1, \dots, n_p \quad (3.20)$$

$$\left. \begin{aligned} \mathbf{x}_{1,k} &= \mathbf{x}(t_{n+1,k-1}) \\ \mathbf{u}_0^{1,k} &= \mathbf{u}_{n_c}^{n+1,k-1} \end{aligned} \right\} \text{ for } k = 2, \dots, n_p \quad (3.21)$$

where $F([t_{i-1,k}, t_{i,k}], \mathbf{x}_{i-1,k})$ is the final state of the numerical integration on the interval $[t_{i-1,k}, t_{i,k}]$ with initial conditions $\mathbf{x}_{i-1,k}$. This approach increases the degree of freedom of the optimisation process reducing the sensitivity of the overall problem to its variables although at a cost of a steep increase in the number of optimisation variables.

The optimisation variables are therefore:

- The initial state vector of each shooting segment within every phase (excluding the first segment of the first phase) $\mathbf{x}_{i,k}$
- The control nodes of each shooting segment $\{\mathbf{u}_0^{i,k}, \dots, \mathbf{u}_{n_c}^{i,k}\}$
- The time of flight for each shooting segment $\Delta t_{i,k}$

The discretised optimisation problem is defined as

$$\min_{\{\mathbf{u}_j^{i,k}\}, \{\mathbf{x}_{i,k}\}, \{\Delta t_{i,k}\}} \phi(\mathbf{x}_{n,n_p}) + \sum_{k=1}^{n_p} \sum_{i=0}^{n-1} \Delta t_{i,k} f_0(\mathbf{x}_{i,k}, \mathbf{u}_j^{i,k}) \quad (3.22)$$

subject to

$$\begin{aligned}
\mathbf{x}_{i,k} &= F([t_{i-1,k}, t_{i,k}], \mathbf{x}_{i-1,k}), \\
\mathbf{u}_{n_c}^{i-1,k} &= \mathbf{u}_0^{i,k}, \\
\mathbf{x}_{1,k} &= \mathbf{x}(t_{n+1,k-1}), \\
\mathbf{u}_0^{1,k} &= \mathbf{u}_{n_c}^{n+1,k-1}, \\
c(x(t), u(t)) &\leq 0, \quad t \in [t_0, t_f] \\
g(\mathbf{x}_{n,k}, \mathbf{u}_{n_c}^{n,k}) &\leq 0, \\
\omega(\mathbf{x}_{0,1}, \mathbf{x}_{n,n_p}) &= 0
\end{aligned}$$

for $i = 1, \dots, n-1$, $k = 1, \dots, n_p$ and $\Delta t_{i,k} = t_{i+1,k} - t_{i,k}$. Path constraints are evaluated at a discrete set of points based in time, and $g(\mathbf{x}_{n,k}, \mathbf{u}_{n_c}^{n,k})$ are the inequality constraints for phase switching.

This nonlinear programming problem is then solved using the sequential quadratic programming and interior point methods included within MATLAB's `fmincon` optimisation function. This approach forms the backbone of a software package called TROPICO, which provides the tools to solve the nonlinear programming problem, coupled with models described in section 3.1.

3.2.3 First guess generation

One challenge with using direct shooting methods is the need for a good initial guess of the solution, with success more likely if the first guess satisfies the dynamics and parameter bounds (Conway, 2012). A common approach is "homotopy", through which a first guess can be constructed by optimising a series of problems where each subsequent attempt further resembles the problem that is to be solved. This can be done by making assumptions or simplifications to both the physics or models included, as well as the difficulty of the optimisation problem.

In TROPICO, there are a number of ways to generate a first guess to maximise the convergence. The first generates a series of random optimisation parameters, attempts to optimise each using a local optimiser, ranks the solutions and then performs a more detailed

optimisation of the best performing solution. This random search approach to finding a good first guess is limited to relatively simple optimisation problems because it essentially surveys the optimisation space randomly. For the launch vehicles investigated here, which contain only a few hundred optimisation parameters this works well, and coupled with homotopy, has been used for most of the trajectories in this thesis. However, if the optimisation problem is more complex, it becomes computationally inefficient to use this approach, and other methods such as the global optimisation algorithms can be more effective.

A second method is to use an existing solution for the trajectory as the initial guess even if some parameters have changed, such as the target orbit parameters, or some performance aspects of the vehicle. This can also work across different launch vehicles. This works because the control law solution space for a vertical rocket is limited, especially if two vehicles have similar properties, such as stage mass fractions and thrust to weight ratios. However, there is a risk that a previous solution is a global minimum for the initial vehicle, but is not a global minimum for the second vehicle. This method has no mechanism to search the optimisation space further, and so has only seen limited application within this work.

The third method is to use a global optimisation algorithm for the first guess. This is possible in TROPICO, but hasn't been used for any of the trajectories in this research as approximate solutions are already known and a larger, smarter, exploration of the search space is unnecessary.

3.2.4 Objective Functions

Several objective functions are used throughout this work. When initially searching for an optimal control law for a launch vehicle, maximising the payload to a particular orbit is generally used:

$$\min(-m_f). \tag{3.23}$$

If a payload mass is known, either from a previous optimisation or from the expected capability of the vehicle, other objective functions can be used, such as minimising the peak stresses on the body, maximising feasibility, or maximising the total energy (C_3) of the

launcher. In section 7.4.2 of this thesis, an attempt to find optimal low environmental impact trajectories is made using a new objective function, which is to minimise the estimated radiative forcing:

$$\min(\text{RF}). \quad (3.24)$$

3.2.5 Existing software

Significant effort has been invested in the development of software to perform optimisation of trajectories. The problems that can be solved are broad, and include launch vehicles, aircraft, orbital transfers of spacecraft (particularly important for complex missions, or those with high ΔV requirements) and the efficient motion (minimise energy) of robotic systems. One of the oldest software tools used for launch vehicle trajectory optimisation, is the *Program to Simulate and Optimize Trajectories (POST)* (Brauer et al., 1975, 1977), originating in the mid-1970's. This package makes use of multiple-shooting, and includes a number of planet, gravitation, atmospheric and vehicle models. POST has been continually upgraded, and POST2 (NASA), is freely available to US citizens. It has been used for over 40 years by NASA and others for trajectory optimisation problems, including launch vehicles (Lugo et al., 2017), planetary re-entry scenarios (Davis et al., 2008, 2013; Fisher et al., 2006) and aero-braking (Prince and Striepe, 2007).

As previously discussed, OTIS was the first direct-collocation approach used for trajectory optimisation of launch vehicles, similarly to POST, it is available to US citizens. In Europe, the commercial package ASTOS was first developed by the University of Stuttgart, and later spun-out on a commercial basis. It is also capable of multidisciplinary design optimisation for the conceptual design of vehicles, as well as the design of orbital missions. Recent developments of the ASTOS have been to include flexible dynamics and hardware-in-the-loop (HIL) testing of guidance systems. The solver used within ASTOS for optimisation is called CAMTOS, which contains direct collocation and multiple shooting approaches and also a novel indirect approach for fuel-optimal rocket arcs in a vacuum (Gath, 2003).

Additionally, in literature there a large number of research-specific optimisation packages used by academics to develop optimisation algorithms, or used to investigate the behaviour of launchers and aircraft. The software used in this thesis, TROPICO, has been developed at

the University of Strathclyde for use in trajectory and multidisciplinary design optimisation for spaceplanes and other launch vehicles. It has been applied to various problems, including the MDO of a novel air-dropped two-stage-to-orbit spaceplane design (Maddock et al., 2018) and analysis of payload capability of SSTO spaceplanes (Toso and Maddock, 2016).

3.3 Summary

This chapter has set out how trajectories can be modelled through the application of Newton's laws of motion using appropriate models for aerodynamics, gravity and the atmosphere. The formulation of the 3DoF equations of motion is discussed, which assumes the launch vehicle is a variable point mass and that control of the vehicle can be described as a thrust angle and magnitude.

Section 3.2 sets out the approach to solving the optimal control problem, which finds open-loop control laws that produce optimal trajectories for any type of launch vehicle. The problem is transcribed as a direct multiple-shooting problem solved using local optimisers with random multi-start to generate first guesses.

This is a key component of the approach used throughout this research, enabling realistic trajectories to be produced with low-fidelity models of novel vehicles or concepts. Coupled with the propulsion models discussed in chapter 5, emissions profiles can be produced, with the trajectory dictating where emissions are emitted and the propulsion model predicting the amount of each emission.

4 | AEROSPACE

PROPULSION SYSTEMS

This chapter introduces propulsion systems that can be used as part of launch systems in section 4.1, including rocket engines, ramjets, scramjets and combined-cycle engines that can be used across the operational regimes required for space access. Section 4.2 describes various approaches that can be used to model propulsion systems including considerations for modelling chemical reactions, and in section 4.3, a discussion about predicting emissions with an additional focus on black carbon produced in rocket engines. The approach used during this research and associated results are described in chapter 5.

4.1 Background

The past century has seen great advancements in propulsion systems that can be used for aerospace vehicles. With the exception of the internal combustion engine used for propeller systems, all aerospace propulsion systems are forms of *Jet Propulsion* - where force is applied to the vehicle due to the momentum of expelled matter. The application of jet propulsive devices to launch vehicle's can be investigated using the classic rocket equation,

$$\Delta v = I_{sp} g_0 \ln \left(\frac{m_0}{m_f} \right), \quad (4.1)$$

which relates the efficiency of the engine, the specific impulse, I_{sp} , with the mass fraction of the launch vehicle. A more efficient engine will enable a higher mass fraction to be launched to orbit, but there are limitations dictated by this law. Assuming a single staged rocket with a specific impulse of 452s (space shuttle main engine (SSME)), and a

Δv to LEO of 9700 m s^{-1} , the resultant mass fraction is 0.884. In other words, 88.4% of the initial mass must be propellant, and only 11.6% is available for engines, structure and the payload.

There are two strategies to address this fundamental limitation of the rocket equation; vastly improving the efficiency of the propulsion system (e.g. using an airbreathing engine), or by adding additional stages to the rocket. The designers of most launch vehicles have chosen to add stages or boosters, and the only vehicles to use airbreathing engines until today are air-carried rockets, such as Pegasus or LauncherOne.

4.1.1 Rocket Engines

Rocket engines are the traditional propulsion system used for launch vehicles as they are capable of generating large amounts of thrust and are able to operate within and outside the atmosphere. For a rocket-equipped vehicle to deliver useful mass to orbit, they are used in conjunction with staging. Liquid rocket engines inject and burn fuel and oxidiser in a combustion chamber, and accelerate the hot gas through a nozzle which converts the thermal energy into kinetic energy (see fig. 4.1). Solid rockets work with the same principle, except the solid propellant is pre-mixed and cast into a form with a central void where the combustion takes place. A third type of rocket engine, hybrids, combines a gas or liquid with a solid propellant, again a central void is where combustion occurs.

Rocket technology has been fundamentally the same since the 1960's, but some recent advances in rocket propulsion are noteworthy. RocketLab have developed the Rutherford engine, which uses an electric pump instead of a turbopump. This possibly improves the performance of small rocket engines, which have previously relied upon pressure-fed feed systems. Secondly, several companies including SpaceX and Blue Origin are now developing rocket engines using methane or liquid natural gas as a fuel. Although there has been extensive ground testing of methane fuelled rocket engines, there is limited flight heritage, at the time of writing this is only with SpaceX's suborbital tests of the Starship reusable vehicle (Burkhardt et al., 2004; Sutton and Biblarz, 2010). Finally, SpaceX are reusing engines on a large scale for the first time, with less maintenance than the Space Shuttle Main Engines. It is now possible to examine rocket engines after flight to better understand

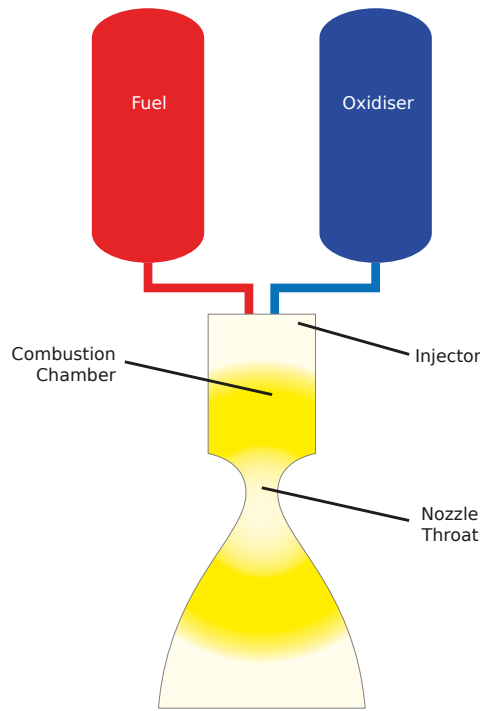


Fig. 4.1 Schematic of a basic liquid rocket engine configuration

how to design and maintain them, possibly introducing long term benefits to reliability and performance.

The general physics and chemistry of rocket propulsion operation are well understood. In a LRE, the oxidiser and fuel generally enters the combustion chamber in a liquid state at low temperatures and a very high pressure. The injector is responsible for mixing the high-pressure flow of fuel and oxidiser, often as droplets, which enables them to ignite. The propellant also vaporises during this process. These phenomena require very detailed approaches to modelling, but a good approximation for performance calculations can be reached by assuming the flow of both propellants is well mixed by the injector. Additionally, the speed of the flow is very low in the combustion chamber, and the combustion can therefore be assumed to reach chemical equilibrium. However, this is a simplification of a number of complicated processes that may be important in the production of pollutants, so care should be taken with the conclusions drawn from modelling at this level of detail.

One example is the application of film-cooling in rocket combustion chambers and nozzles. The combustion gases can reach temperatures in excess of the melting temperature of the metals used and whilst the mixture ratio in the engine can be altered to lower the temperature, this results in reduced performance. As such, engines are usually cooled either

by pumping cool propellant through tubes embedded in the combustion chamber and nozzle walls (regenerative cooling), or by injecting a film of propellant on the inside of the walls (film-cooling, see fig. 4.2). This film-cooling approach can result in high fuel-oxidiser ratios near the wall which in the case of hydrocarbon propellants may result in soot production.

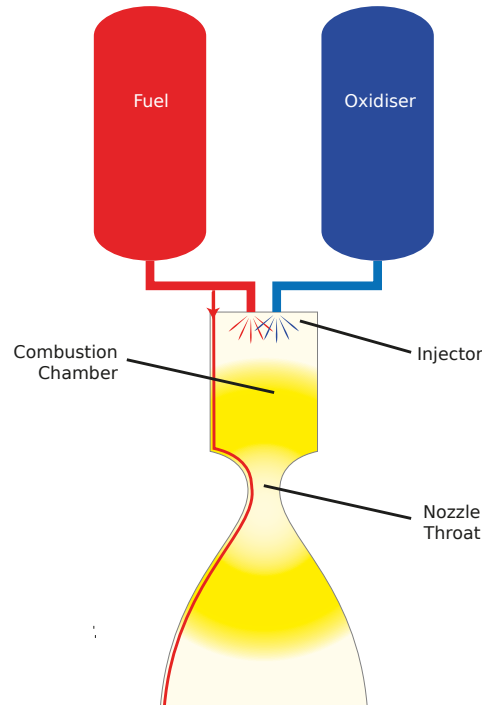


Fig. 4.2 Rocket engine film cooling

Similarly, the approach to pressurising and injecting propellant into the combustion chamber can influence emissions produced. The simplest method is where the propellant is pressurised in the tanks and injection into the engine only requires the opening of a valve. This is a pressure-fed engine cycle. A pump can be used to take advantage of the performance increases of higher injection pressures without building heavy tanks capable of withstanding high propellant storage loads (this is a mass trade-off). Although recently electric pumps have been used for the first time in launch vehicle stage rocket engines, pumps are typically turbopumps utilising some propellant flow. The exact configuration of how this is powered is the engine cycle.

The gas generator engine cycle is commonly used and illustrates how the cycle can have an influence on emissions. The fuel and oxidiser lines (red and blue lines respectively in fig. 4.3) are split, with some entering a gas generator, where they are combusted together to make high-pressure hot gas that then drives a turbo-pump to pressurise the inlet flow

to the engine . The gas is then exhausted out of a separate nozzle to the main engine (shown in fig. 4.3 as the yellow line exiting the gas generator, through the turbine and then exhausted from the engine). In a regeneratively cooled rocket engine, the other part of the fuel flow is pumped through cooling channels in the combustion chamber and nozzle, enabling the engine to operate at hotter temperatures. The warmed flow is then injected into the combustion chamber. In fig. 4.3 this is indicated by the set of horizontal lines that move left to right across the engine. The gas generator does not necessarily operate at the same mixture ratio as the main combustion generator, and may operate fuel-rich or oxidiser-rich, although it is difficult to make turbines that can survive hot-oxidiser flows.

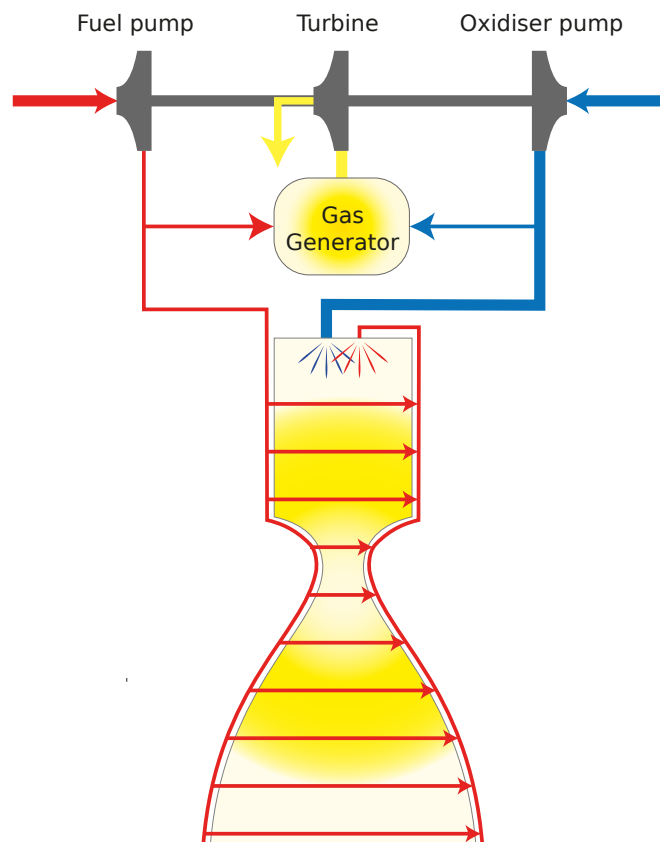


Fig. 4.3 Gas generator engine cycle

After combustion the gas enters the nozzle of the rocket engine in a well mixed state and close to chemical equilibrium. As it moves through the nozzle, the flow velocity increases and temperature decreases. This shifts the equilibrium, which recombines previously dissociated products and adds thermal energy into the system. Eventually, the rate at which the flow moves and the rate at which the equilibrium state shifts are comparable, and the rate of the

chemical reactions becomes important. Additionally, there is a point further downstream where the flow speed is much faster than the reaction rate, and the flow can be considered frozen. In some rocket engines with short nozzles (e.g. H₂/O₂ with nozzle ratios up to 50), these points may never be reached and a shifting equilibrium can be modelled throughout the nozzle (Zhukov, 2019). The chemistry of the propellants and the engine design both have an influence on the emission indices of the rocket engines, even at a simple "whole-engine" level. In all of these conditions, the influence of the geometry must also be accounted for, in preliminary design often by assuming quasi-one-dimension isentropic flow, or by using the method of characteristics in 2-dimensions.

4.1.2 Airbreathing Engines

The alternative strategy to staging and higher efficiency rocket engines is to use the oxygen in the atmosphere as an oxidiser, instead of carrying it on board. This results in a much higher specific impulse than rocket engines. Figure 4.4 shows a comparison of the performance in terms of specific impulse of rocket engines and several forms of airbreathing propulsion systems.

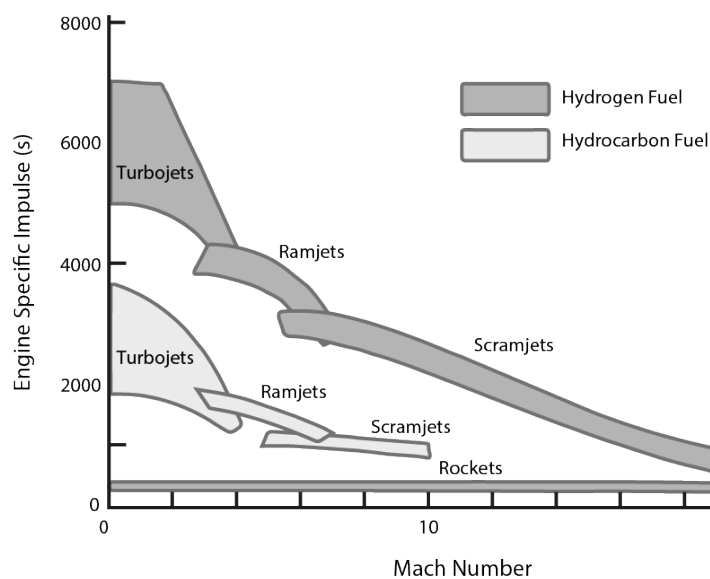


Fig. 4.4 Specific Impulse of various aerospace propulsion systems as a function of operating Mach number (adapted from Fry (2004))

Turbofans are the most efficient of all jet propulsion systems, hence their use in commercial airliners. However, their efficiency drops quickly with increases in Mach number. Faster

aircraft are less efficient, but this may be justified by the economic benefits of reduced flight times that increases in speed may bring. The Aérospatiale/BAC Concorde was designed to take advantage of this, using an afterburning turbojet engine to push its cruise speed to Mach 2.04. The flight speed limitation of turbofans is due to the thermal loading on the rotating components within the engine. Turbofans can also be used as part of a launch system, in the form of air-dropped launch systems where a turbine-powered carrier aircraft carries a rocket such as the Northrop Grumman Pegasus and Virgin Orbit LauncherOne.

Between Mach 3–4, ramjets are an attractive proposition. Instead of using rotating-machinery to compress incoming air, as in a turbofan or turbojet engine, they use ram compression, where a change of area is used to compress the air, reducing the flow to subsonic speeds. Removing the rotating components increases the maximum temperature that can be reached within the engine. Fuel is injected into the compressed flowstream, which is then combusted and accelerated through a nozzle. Ramjets are generally operable between $3 < M < 6$. The efficiency of a ramjet drops throughout this range, as the temperature of the compressed air approaches exhaust temperature, and the amount of energy that can be extracted reduces. Additionally there are greater pressure losses due to the terminal shock of the inlet, caused by reducing the flow speed to subsonic velocities.

At this point, it becomes more efficient to keep the flow at supersonic velocities throughout the engine. This is the scramjet, or supersonic-combustion ramjet engine. The advantages over a ramjet from Mach 6 onwards are the reduction of the maximum operating temperature within the engine, and the improved pressure recovery of the inlet and diffuser (Segal, 2009).

Operational use of ramjets and scramjets is limited by the need for some other propulsion system to accelerate the vehicle to the minimum operating conditions of the engine. There are two approaches to this, the first of which combines multiple separate propulsion systems onto the same vehicle, called a *Combination Propulsion System*. For example, a rocket is used to accelerate the vehicle to Mach 3 and the ramjet is used for subsequent supersonic flight. This enables a propulsion system to be used that is optimised for each regime of the flight, at the cost of additional mass needed for each propulsion system.

The second, the *Combined Cycle Propulsion System*, integrates different operating regimes into a single engine flow path (i.e. the engine can operate as a ramjet and then a scramjet,

sometimes called a dual-mode scramjet). The disadvantage is the increased complexity and difficulty to design and operate the engine.

An alternative to both of these is to have different stages with different propulsion systems of a launch vehicle, combining the two strategies discussed previously to addressing the limitations of the rocket equations. An example of this is the proposed rocket-scramjet-rocket small launcher of [Smart and Tetlow \(2009\)](#), or an air-launched rocket from a subsonic aircraft.

4.2 Modelling approaches

Designing, building and performing experimental tests for components or full systems of rockets, ramjets or scramjets is very expensive and time-consuming. Computers have enabled scientists and engineers to investigate propulsion systems and the phenomena that impact their design at a reduced cost. The objective of computer simulation is to create a model of the system that can produce results as quick as possible whilst being as accurate as necessary, by making assumptions and neglecting unnecessary physics. The results of mathematical models should never be seen as the truth, whilst well-designed experiments can be, and therefore must be validated against experimental results where possible. They also cannot necessarily be trusted outside of the areas of validation because complicated phenomena aren't modelled, and instead the performance is tuned to the few data points available from validation data sets. The limited amount of accessible data on rocket engines, ramjets and scramjets across their entire operating regime from either CFD or experimentation limits the usefulness of low-fidelity models. Although CFD attempts to model phenomena in more detail, it is itself a model and cannot be treated as truth without validation.

Mathematical models of propulsion systems can be broadly split into higher-fidelity methods that solve in the Navier-Stokes equations for flows in 2D or 3D, Computational Fluid Dynamics (CFD), and lower-fidelity methods that make assumptions to reduce the problem complexity. Low-fidelity models are commonly used for system design studies, as well as Multi-disciplinary Design Optimisation (MDO). One traditional low-fidelity approach is to describe the flow of gas through a propulsion system in a one-dimensional or quasi-

one-dimensional formulation, which includes area change. Similar equations can be applied to both rocket and airbreathing engines.

For rockets, simpler approaches for estimating the performance of rocket engines can be done by hand. Numerous textbooks, such as [Sutton and Biblarz \(2010\)](#) develop equations that represent an expanding hot gas, often using the following simplifying assumptions:

- One-dimensional, adiabatic, steady-state and frictionless flow
- The fluid is a perfect gas (constant c_p)
- The fluid is homogeneous
- Single equation combustion reaction
- There are no discontinuities in the geometry

Moving the calculations from paper to the computer provides the option for equilibrium or finite-rate chemistry to be considered in both the combustion chamber and throughout the nozzle. There are essentially three ways to model the flow through the nozzle:

- **Frozen flow** - If the composition calculated in the combustion chamber is assumed to be constant throughout the nozzle.
- **Instantaneous or shifting equilibrium** - Where the composition of the flow is assumed to be in equilibrium at every point through the nozzle. A combination of this and the frozen flow assumption can be used in a single nozzle model (i.e. shifting equilibrium to the nozzle throat, followed by the frozen flow assumption to the exit), which is called partial equilibrium in this thesis.
- **Nonequilibrium chemistry or chemical kinetics** - Where the rate of the chemical reactions is included in the modelling.

The classic software package for preliminary performance calculations is NASA's Chemical Equilibrium with Application (CEA) ([Gordon and McBride, 1994](#)), which models the combustion in the chamber as reaching equilibrium, and either frozen flow or shifting equilibrium through the nozzle. This could be described as a jump solver, as it solves the states at the end of the nozzle, rather than along the flowpath.

The commercially available (in the US) Two Dimensional Kinetic code includes a one-dimensional equilibrium nozzle analysis tool, but also includes a one-dimensional kinetic nozzle tool that includes finite-rate chemistry (Nickerson et al., 1985). It also introduces a 2D approach, based on the Method of Characteristics that is capable of predicting the shocks in the nozzle and early plume, as well as the finite-rate chemistry. TDK is part of a set of tools developed and sold by Sierra Engineering & Software[id=RG], Inc, which includes more detailed models for combustors, plumes and injectors.

Computational Fluid Dynamics is often applied to understanding the design of a rocket engine, or the phenomena associated with its operation (e.g. optimization of the nozzle design (Cai et al., 2007), investigating the effect of kinetic schemes in models (Zhukov, 2019)). However, CFD is rarely used during early stage design studies, where a large range of propulsion systems must be considered, because of its computational cost.

For airbreathing engines, one-dimensional or quasi-one-dimensional approaches can also be applied, which results in a set of ordinary differential equations that can be numerically integrated. Phenomena including wall friction, heat exchange, chemical reaction and phase changes can be included (Shapiro, 1953).

Solving these equations results in a system-level analysis tool that can be used to understand the performance of hypersonic engines include ramjets and scramjets. O'Brien et al. (2001) built upon the general equations to include a mixing model based on experiments, and finite-rate chemistry using the CHEMKIN II package. Birzer and Doolan (2009) used a very similar model, assuming that the scramjet was mixing limited rather than kinetically limited (i.e. the timescale on which the fuel and airflow mixed together is much greater than the reaction time), which enabled them to use equilibrium chemistry instead of finite-rate chemistry. Modelling dual-mode scramjets during the transition phase is more complicated, because there is a singularity in the basic equations when $M = 1$. Torrez et al. (2013a) extended the earlier approach by O'Brien to model the transition between ram and scram modes of a dual-mode scramjet, without solving the time-dependent problem, which is the traditional approach to the Mach singularity issue and is often used for modelling rocket nozzles where $M = 1$ at the nozzle throat (Griffin and John D., 1977).

4.2.1 Chemistry

Common to modelling all types of propulsion systems is the need to account for chemical reactions, both in areas of combustion and other areas through the engine. These are broadly divided into two categories, *fast chemistry* and *finite-rate chemistry* (Kee et al., 2003).

Fast chemistry assumes that chemical reactions are instantaneous. This is valid in situations where the rate of reactions is limited by the rate of the mixing. There are two ways of including this, by assuming that reactions are infinitely fast or by assuming the mixture is in chemical equilibrium. These approaches are often used when the residence time (or timescales of the flow) are longer, and therefore it can be assumed that reactions will have time to occur.

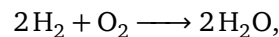
In real flows, chemical reactions are not infinitely fast, and this may need to be modelled, particular when the timescales of chemistry and the flow properties are comparable. Finite-rate chemistry is useful when the flow is not mixing limited, and the rate of the chemical reactions needs to be included. Rate equations are used to describe the rate at which chemical species are formed or destroyed:

$$-\frac{d[A]}{dt} = k[A]^\alpha[B]^\beta, \quad (4.2)$$

where k , α and β are experimentally determined constants, and $[A]$ is the concentration of a particular species.

Infinitely Fast Reactions

A single global equation or set of global equations are assumed to be infinitely fast, and governed by a single reaction, such as:



for the combustion of hydrogen and oxygen. The heat release is calculated based on the heat of formation. When using this to model combustion, it is necessary to ensure the mole fraction balance between reactants and products.

Chemical Equilibrium

Chemical equilibrium is the state where all chemical species in a mixture are in equilibrium (i.e. forward reaction rates = backward reaction rates) at a particular thermodynamic state. The composition where a mixture is in chemical equilibrium can be identified by finding the minimum of the Gibbs Free Energy (Kee et al., 2003),

$$G = \sum_{k=1}^N n_k \left(G_{f,k}^{\circ} + RT \ln \frac{p_k}{p^{\circ}} \right) = \sum_{k=1}^N n_k \left(G_{f,k}^{\circ} + RT \ln X_k \right) \quad (4.3)$$

Chemical equilibrium can be stated with a number of thermodynamic parameters, including temperature and volume (minimising of Helmholtz), temperature and pressure (minimising Gibbs free energy), or maximising entropy. Two other methods of solving the chemical equilibrium problem are using equilibrium constants, or the "atomic potential" method. HyPro uses Cantera (Goodwin et al., 2017) for base thermodynamic calculations it performs, including the chemical equilibrium solver. Two solvers are available for use in Cantera based on algorithms described by Smith and Missen (1982).

Global Reactions

Global reactions can be used to introduce a single rate equation of the form in eq. (4.2) to model an entire combustion process. Typically, experimental data or a detailed reaction mechanism is used to tune the rate parameters such that the single equations represents the overall behaviour. Global rate equations are usually only valid within a narrow range of conditions, with errors resulting when used outside (Kee et al., 2003). Even if a detailed model is used to tune the global reaction, not all properties of the reaction system may be included. For example, Varma et al. (1986) compared a one-step global model with two more detailed mechanisms. Physical properties of the flame, such as burning velocity and flame thickness, were similar between reaction schemes, but there were significant differences in even the major chemical species.

Detailed Reaction Mechanisms

Detailed reaction mechanisms or elementary reactions are a comprehensive set of rate equations that more completely model the reactions of chemicals, and can include many species and hundreds or thousands of reversible reactions. An example is the GRI-Mech 3.0 optimised mechanism for natural gas combustion, which has 325 reactions and 53 species (Smith et al.). Kee et al. (2003) contains an in-depth discussion of how detailed reaction mechanism are created, and the types of equations that they are made up of.

4.3 Modelling emissions

Low fidelity approaches to modelling propulsion systems are able to predict the major chemical products formed during combustion. For example, in rocket engines the major products are highly dependent on the mixture ratio of the engine, and for airbreathing engines, the equivalence ratio at each performance condition. It is more difficult to estimate minor species that are dependent on finite-rate chemistry such as NO_x, or other, complex phenomena such as non-uniform mixing or vaporisation. These are elements that are difficult to address with the early stage design tools, and other approaches are needed to address.

The formation of some species of emissions such as NO_x, is governed by the finite-rate kinetics and the residence time in the combustor. A common approach used to model the production of NO_x emissions in gas turbines is through the use of networks of chemical reactors - mathematical approximations of physical chemical reactors. Two common types are perfectly stirred reactors (PSR) and plug flow reactors (PFR). The PSR is a zero-dimensional reactor that assumes the fluid is well mixed, and is therefore suited to modelling areas of high turbulence, such as close to a burner. Plug flow reactors model a "plug" of fluid down a one-dimensional reactor, and are well suited to areas with high cross-stream mixing but with insignificant flow direction mixing (Kee et al., 2003).

The basic usage in gas turbine emission modelling is to use a PSR for the burner, other PSRs with different air-fuel ratios to represent recirculation regions, and a PFR to represent

the downstream flow, but there are variations on this approach (Lebedev et al., 2009; Osgerby, 1974).

Reactors can be useful in understanding potential emission formation even without modelling the entire propulsion system. For example, Ingenito (2016) used a single perfectly stirred reactor to understand the design parameter trade-offs for NO_x production in scramjet engines. Specifically, shorter combustors lead to lower residence time and less NO_x production, and similar reductions can be achieved with leaner mixtures of fuel.

Tanbay et al. (2019) developed a model of non-linear equation representing the thermodynamic cycle of the SCIMITAR engine, a combined cycle engine proposed as part of the European Commission LAPCAT project utilising the technology of the SABRE engine.

Black Carbon

Black carbon or soot is produced by incomplete combustion of carbon in hydrocarbon fuels, and can be formed at various stages of the rocket cycle in hydrocarbon rocket engines, and is particularly difficult to understand without highly detailed models. Generally, the lower the mixture ratio (fuel rich), the more soot is formed through this incomplete combustion. This relationship can be seen by the model motor results in fig. 4.5 from Simmons (2000), where the soot mass fraction is logarithmically related to the mixture ratio.

These results are from model motors, where it may be possible to reach a high level of mixing in the combustion chamber. The production of black carbon is also related to the heating and vaporisation process of fuel droplets (Simmons, 2000) or formed in film cooling fuel streams or in fuel-rich gas generators where lower O/F ratios exist. Predicting the black carbon produced by a real engine is significantly more complicated than the overall mixture ratio.

Experimental data of soot production in rocket engines is fairly limited. One of the only examples apart from the model motor data is from the experiments of Hernandez and Mercer (1987), who attempted to determine the sooting conditions of methane, kerosene and propane gas generators. They indirectly measured the sooting, by measuring the pressure drop across the turbine. The results show that the soot production is mostly a function of the mixture ratio, rather than combustion pressure. They observed that the

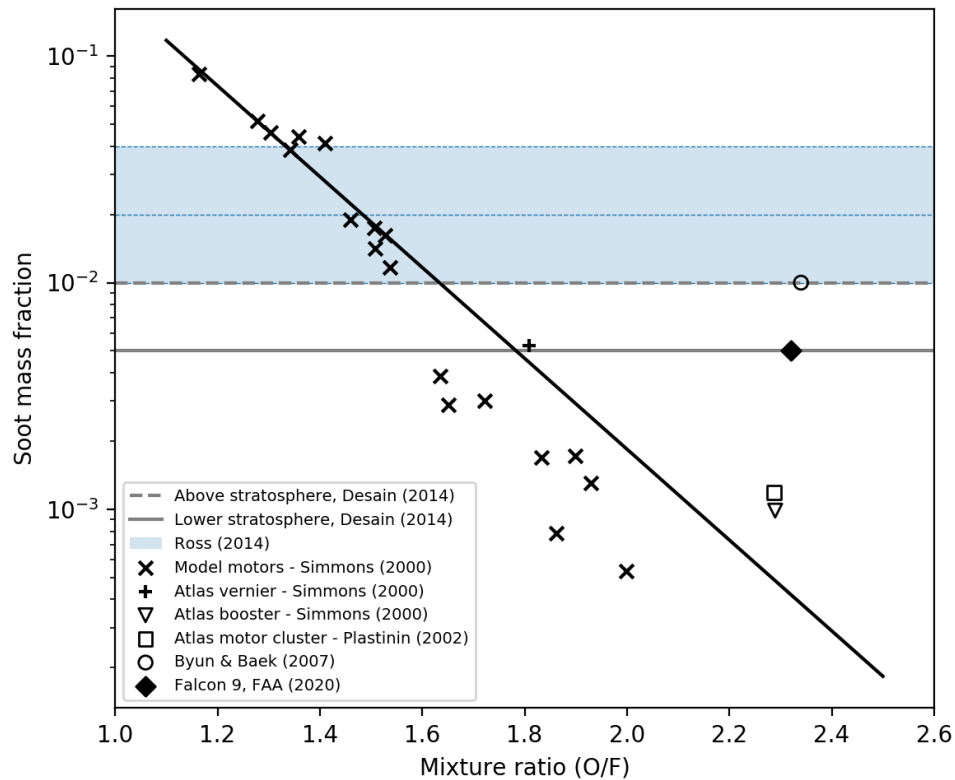


Fig. 4.5 Black carbon mass fraction ratios from various modelling and measurement sources. Assumed mass fraction in lower stratosphere and upper stratosphere from DeSain and Brady (2014). The blue shaded area contains the range of assumed mass fractions in Ross and Sheaffer (2014).

formation threshold for LOX/propane and LOX/RP-1 was a MR 0.4, whilst no significant soot production was observed for methane.

Computer simulations are more common. Nickerson and Johnson (1992) included a soot combustion model within the TDK software package, which considered various phenomena included vaporization, and compared the results to Hernandez’s experiments. Modelling has also been used to quantify the potential contributions of gas generators, such Foelsche et al. (1994); Song and Song (2017); Yu and Lee (2007) who used vaporization models coupled with perfectly stirred reactors and the soot deposition (coking) from film cooling such as Kulakhmetov and Pourpoint (2019).

Overall, there is a significant gap in knowledge on the production of BC in hydrocarbon rocket engines, but some trends that can be used in launcher design can be identified. Firstly, the combustion of methane is unlikely to produce significant quantities of soot whilst kerosene and propane will. The amount produced is governed by the mixture ratio within gas generators, combustion chambers and through the effects of film cooling.

It is also useful to discuss the approaches taken by the authors of other work attempting to understand the environment impact of launch vehicles. In fig. 4.5, the assumptions take by [Ross and Sheaffer \(2014\)](#) are shown as the blue shaded area, and corresponds to an estimated range of EI_{BC} of 10–20–40 g kg^{-1} for any mixture ratio of rocket engine considered, which relate to the blue dotted line: low, central and high assumptions. This is notable because the low assumption is significantly greater than any other data for MR greater than 1.6. This was extracted from a CFD study of the formation of soot and its effect on the thermal properties of the design of a kerosene rocket engine ([Byun and Baek, 2007](#)), but were discarded by [DeSain and Brady \(2014\)](#) in their assessment of global launch emissions as likely an order of magnitude too high. Their estimates were also assumed to not be subject to any afterburning. The assumptions made by [DeSain and Brady \(2014\)](#) are also shown in fig. 4.5, as the solid and dash grey lines, which distinguish between values in the lower stratosphere and above the stratosphere.

At preliminary stages of vehicle design, the key parameters are the engine size, performance and the art-of-the-possible with regards to engine technology. Detailed knowledge is not known about the design and configuration. For this reason, detailed analyses are not appropriate at this stage, and so many approaches that may be able to predict black carbon produced are inappropriate. An ideal solution might be software such as PERCORP or TDK, which are tightly export controlled. Indeed, SpaceX used PERCORP as part of the FAA's environmental assessment to predict the emissions, including black carbon, of the Falcon 9 launch vehicle for their environmental assessment ([FAA, 2020](#)). The full table (table 5.14) is included in section 5.2.5, but it predicts a mass fraction of 0.005 at the engine exit. Performance Correlation Program (PERCORP) uses known engine performance to estimate mixing and vaporization efficiencies in liquid rocket engines, but it is unclear how reliable the results are.

One potential approach is to use the limited data available to derive a relationship that related to designed mixture ratio of a kerosene-fuelled rocket engine. To test this idea, a least-squares regression is performed considered the data taken from [Plastinin et al. \(2002, 2004, 2005\)](#); [Simmons \(2000\)](#) for the mass fraction of black carbon vs. mixture ratio, shown as the line of best fit in fig. 4.5. It can be seen that compared to the limited alternative data from [Byun and Baek \(2007\)](#); [FAA \(2020\)](#) and even the Atlas booster ([Simmons, 2000](#)) and

motor cluster (Plastinin et al., 2002) data that this will underpredict the amount of black carbon produced, probably because it does not consider the additional complexities of a real engine. This is the best case for kerosene fuelled engines, and perhaps can be used alongside an extremely conservative assumption such as that of Ross and Sheaffer (2014) to bound the potential black carbon emissions and their impacts.

Second to the production of black carbon in the engine is the effect of afterburning in the plume, especially in the lower stratosphere and troposphere. This greatly reduces the concentrations that are deposited in the atmosphere after the plume is considered. Alexeenko et al. (2002) simulated plumes with mass fractions of 0.001 at 15km and 0.02 at 40km that matched observations at these altitudes. Viswanath et al. (2005) used an overlay approach to demonstrate very similar results. To account for this, DeSain and Brady (2014) used a conservative estimate of 0.5 % mass fraction in the lower stratosphere, and 1 % percent above the stratosphere. Here, a simple linear approximation based on Alexeenko’s observations and models is used to scale the amount of soot that survives the plume-afterburning process, where:

$$\epsilon_{soot} = \begin{cases} 0.05 & \text{if } h < 15 \text{ km} \\ 0.038h - 0.52 & \text{if } 15 \text{ km} \leq h \leq 40 \text{ km} \\ 1 & \text{if } h > 40 \text{ km.} \end{cases} \quad (4.4)$$

This will most likely overpredict the amount of black carbon in the lower atmosphere, as afterburning in rocket plumes almost completely removes black carbon (FAA, 2020). However, this is unlikely to have a significant effect on the conclusions made on the environmental impact as black carbon in the troposphere is recycled out of the atmosphere very quickly.

There is no generally accepted approach to predicting the production of black carbon in rocket engines, especially considering the various sources within real engine cycles. The approach proposed here is to attempt to bound the production rate, but include the better understood effect of afterburning as a hydrocarbon fuelled rocket travels through the atmosphere. Further understanding of hydrocarbon combustion and formation of BC within engines, as well as a more detailed understanding of the afterburning process in

hydrocarbon fuelled rockets is critical to enable a more accurate emission index to be used within preliminary design like this.

4.4 Summary

This chapter presents background on aerospace propulsion systems that are used as part of launch vehicle systems, first discussing rocket engines in section 4.1.1, and then various airbreathing propulsion systems that could be used to power launch systems in section 4.1.2.

The second part of this chapter (section 4.2) describes the application of simulation and modelling to predict the performance of propulsion systems, which are similar for both rocket and airbreathing engines. A range of approaches are discussed, including low to mid-fidelity methods and potential applications of each are introduced. This is supplemented by a deeper discussion of how chemistry is included in these modelling approaches, specifically around the assumptions made about the speed of reactions.

Finally, section 4.3 introduces approaches to modelling emissions produced by propulsion systems, with a particular focus on soot in section 4.3.

5 | MODELLING AEROSPACE

PROPULSION SYSTEMS

This chapter contains in section 5.1 a description of the modification and extension of a propulsion systems model originally designed for optimising propulsion systems, HyPro. This software is extended to provide two new capabilities: predicting the performance of specific rocket engines, and a set of additional models that can be used in modelling combustion. Together, these improve the ability of HyPro to model specific engines, extending its use from optimising configurations of airbreathing engines to the modelling of all types of launch vehicle engines and further applications in conceptual design.

In section 5.2, several rocket engine models are constructed using the modified version of HyPro representing real rocket engines. These are compared against an external industry-standard software package, CEA (Gordon and McBride, 1994), and against other models where published data exists. The comparison parameters include both performance, considering the level of information usually available in early stage design and emissions. Subsequently, in section 5.3, an existing model from open-literature of a rocket based combined-cycle engine that has been previously modelled in HyPro is extended to include the scramjet mode.

5.1 Propulsion system modelling

The HYbrid PPropulsion Optimiser (HyPro) is a code developed by Mogavero (2016); Mogavero and Brown (2018) with the goal of modelling and optimising general propulsion systems. The original implementation focused on using simple low-fidelity models with

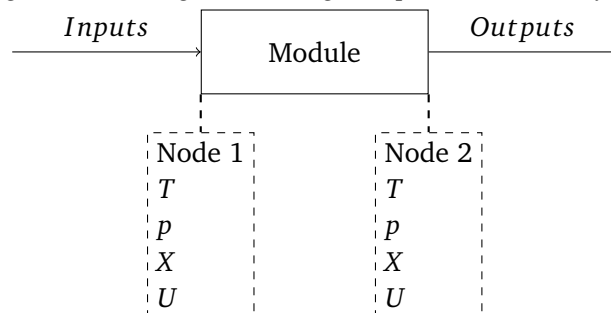
experimental- or CFD- derived efficiency factors to match real performance. This was to ensure its computational performance was sufficient to be used in an engine configuration optimisation context, particularly for hybrid hypersonic engines, although it lends itself to use within an MDO context as well.

It uses a jump-solver approach, where each component of an engine can be broken down into a number of modules and solved sequentially. Similar approaches have been used before, such as Georgia Tech’s SCCREAM software (Olds et al., 1999). However, this had a very specific focus of modelling rocket-based combined cycle engines, whereas HyPro is capable of modelling a broader range of propulsion systems, including rockets, ramjets, scramjets and combined cycle engines.

In order to be able to simulate the emissions produced by general propulsion systems, additional capabilities better representing combustion were added. The following section summarises the models originally implemented as described in Mogavero (2016); Mogavero and Brown (2018), as well as the additions made to produce estimates for the emissions.

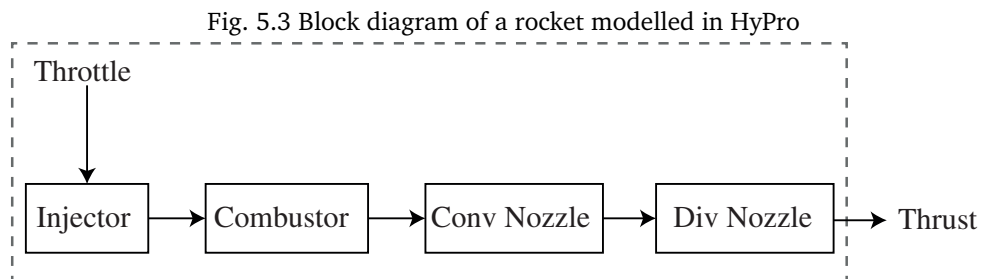
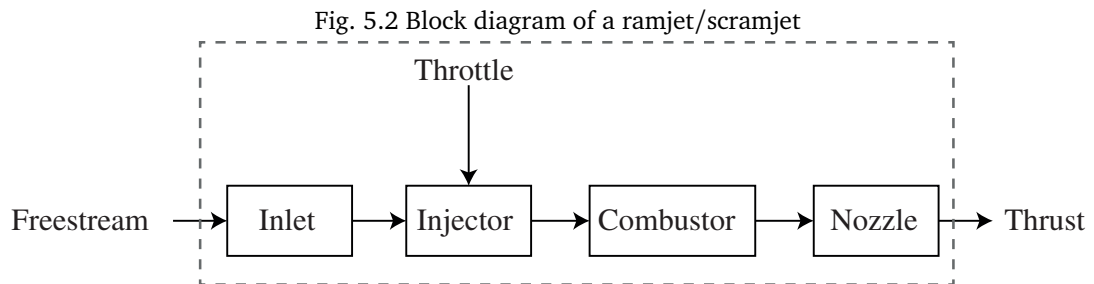
One of the key features of HyPro is its inherent flexibility, which is needed to deliver its configurational optimisation capability. In order to be this flexible, it relies heavily on the object-oriented paradigm of C++. Every component in an engine can be defined as a module, a C++ class that is set up as in fig. 5.1, with an input node and output node. Some modules have more than two nodes - these will be described later (e.g. in section 5.1.5). Each node contains the complete thermodynamic and kinetic state of either the beginning or the end of the module.

Fig. 5.1 Block diagram showing set up of modules in HyPro



Each module also implements the methods that are required to model the physics of its type. For example, an injector module will alter the gas composition and thermokinetic

state according to the injection module used. A series of modules are combined to create the configuration of an engine. Figure 5.2 and fig. 5.3 show the makeup of modules that are used to build a ramjet/scramjet engine and a rocket engine respectively in HyPro. These configurations can be much more complicated, especially when modelling hybrid (or combined-cycle) propulsion systems.



5.1.1 Thermophysical properties

To be able to characterise and calculate the behaviour of a fluid or any thermodynamic process, data about the thermodynamic state of each species involved is required. The standard approach is to use a library of least-squares coefficients that can be used to calculate the thermodynamic and/or transport properties of any particular species (Mcbride et al., 1993). The heat capacity $C_p(T)$, enthalpy $H(T)$, entropy $S(T)$ as a function of temperature are the three thermodynamic parameters that are parameterised, and can be calculated

from:

$$\frac{C_p^0(T)}{R} = a_0 + a_1 T + a_2 T^2 + a_3 T^3 + a_4 T^4 \quad (5.1a)$$

$$\frac{H^0(T)}{RT} = a_0 + \frac{a_1}{2} T + \frac{a_2}{3} T^2 + \frac{a_3}{4} T^3 + \frac{a_4}{5} T^4 + \frac{a_5}{T} \quad (5.1b)$$

$$\frac{S^0(T)}{R} = a_0 \ln T + a_1 T + \frac{a_2}{2} T^2 + \frac{a_3}{3} T^3 + \frac{a_4}{4} T^4 + a_6, \quad (5.1c)$$

where $a_0 \dots a_6$ are seven coefficients calculated from experimental results. This is known as the NASA 7-Coefficient Polynomial Parameterization. In this system, it is possible to have two temperature ranges (e.g. one set of coefficients $200 < T < 1000$ and another set for $1000 < T < 6000$). HyPro uses the Cantera library to import thermodynamic data and calculate the thermodynamic states of gases (Goodwin et al., 2017).

5.1.2 Gas dynamics

Two main gas dynamic models are used. The first is isentropic one-dimensional expansion or compression, and the second is a general one-dimensional balance equation solver.

Isentropic Expansion or Compression

The first general gas dynamic solver implemented is the isentropic expansion or compression solver. Generally this is the solver used when a change of area is needed in an propulsion system model. The analytical solution found in many textbooks (e.g. Sutton and Biblarz (2010)) is not used since it is valid only for constant ratio of specific heats, γ , an assumption of a calorically perfect gas. An iteration loop where a trial Mach number, M_2 is chosen and the temperature at node 2 is calculated from the energy equation:

$$h_2 + \frac{M_2^2 a_2^2}{2} = h_1 + \frac{M_1^2 a_1^2}{2} \quad (5.2)$$

The temperature, T_2 is calculated in an inner iteration loop, which is required for the h_2 . The pressure at node 2, p_2 is then calculated from the entropy equation:

$$S^0(T_2) - R \ln \frac{p_2}{p^0} = S^0(T_1) - R \ln \frac{p_1}{p^0}, \quad (5.3)$$

which is only valid for constant entropy. In most cases this means gas composition must be constant, but the shifting equilibrium assumption can be made under the assumption of constant entropy, as in [McBride and Gordon \(1996\)](#). Once the thermokinetic state at N_2 is calculated, the mass flow rate is compared against that of the inlet node, N_1 . If there is a difference, the iteration loop (starting with the choosing of a new M_2) is repeated, until a tolerance is met.

Correction factors can be applied to the *IsentropicDuct* module to tailor the modelled performance; for a total pressure drop:

$$\frac{P_{02}}{P_{01}} \quad (5.4)$$

and a total temperature drop,

$$\frac{T_{02}}{T_{01}}. \quad (5.5)$$

These are applied to a virtual node, which triggers a new instance of the above iterative procedure to find the mass flow rate matching node 1.

Balance Equation Solver

The general one-dimensional balance equation assumes that the module has a constant cross-sectional area. The mass, momentum and energy conservation equations can therefore be written:

$$\rho_1 U_1 - \Delta G = \rho_2 U_2 \quad (5.6a)$$

$$p_1 + \rho_1 U_1^2 - \Delta I = p_2 + \rho_2 U_2^2 \quad (5.6b)$$

$$\frac{G_1}{G_2} \left(h_1 + \frac{U_1^2}{2} - \Delta H \right) = h_2 + \frac{U_2^2}{2}, \quad (5.6c)$$

where subscript $_1$ is at the inlet of the module and subscript $_2$ is at the exit. ΔG , ΔI and ΔH represent the mass, momentum and energy fluxes across the duct.

These equations are solved with a set of nested root-searching algorithms. The outer loop assumes a tentative value for M_2 , and then solves the mass balance equation. Within

this loop, a static temperature T_2 is found with a second root-search algorithm using the energy equation. Initial versions of the balance solver implementation assumed that the gas was weakly a function of pressure, and therefore p_2 could be calculated directly from the momentum equation. Given the composition of the gas can now change during the solving process (being set to equilibrium for every state change), this is no longer true. Therefore once a tentative temperature is found, a second loop attempts to find an associated pressure which allows the energy equation to be balanced. This whole process attempts to find a solution for M_2 , p_2 and T_2 which balances the previous equations.

Losses

Two additional models allow the user to include friction and heat flux losses to the balance equation solver. At supersonic speeds, friction is an important loss than cannot be ignored. It would contribute a major source of error for some of the propulsion systems investigated here (ramjets and scramjets). Friction is modelled as a momentum flux added to flow:

$$\Delta I = \bar{\tau} \frac{A_w}{A_1} \quad (5.7)$$

$$\text{where } \bar{\tau} = \frac{\rho_1 U_1^2}{2} C_f,$$

which assumes that the friction coefficient, C_f is constant along the module duct. Whilst this is not true, it is a useful simplification that results in reasonable accuracy given input from higher-fidelity models, see [Mogavero \(2016\)](#) for more details. The reason for using this simple model is to keep the cost of including this loss within the balance solver low. It does not negatively affect performance when the solver is used for modules with a larger computational cost (e.g. the combustor or injector).

The second loss model that has been included takes into account heat flux through the walls of an engine duct. This is created in much the same way as the friction model, with the Stanton number, St instead of the friction coefficient coming from experiments or other

models:

$$\Delta H = \frac{\dot{q}}{\dot{m}_1} \frac{A_w}{A_1} \quad (5.8)$$

where $\dot{q} = \rho_1 U_1 \left(h_1 + \frac{U_1^2}{2} - h_w \right)$.

This equation normalises the heat flux with a reference heat flux (at the inlet). Again, the main limitation here is that the heat flux is calculated based on the conditions at node 1, and so it ignores any changes to the heat flux across the duct.

5.1.3 Intake

Several different intake models are available; an adaptive convergent-divergent inlet, fixed inlets with a fixed pressure drop and a central body intake. The first two are described below as they are used later in the test cases (see [Mogavero \(2016\)](#); [Mogavero and Brown \(2018\)](#) for further detail on the central body intake).

The first is a convergent-divergent intake, which is modelled after a type of intake with variable geometry, which is able to vary the intake throat section in order to start the inlet. To model this, HyPro used a collection of sub-modules and nodes, as shown in [fig. 5.4](#), which are able to model their areas within the maximum area set by the user.

For a non-adapted nozzle, the conditions at N_{in} can be assumed to be different to those of N_1 . If the external flow is subsonic, the external flowpath is assumed to be isentropic. If the external flow is supersonic, then a normal shock is assumed to be sufficiently strong enough to fully adapt the intake. If the flow is not adapted, an intake drag is calculated and applied to the overall engine thrust:

$$D = \dot{m}_{in} (U_{in} - U_1) + A_{in} (p_{in} - p_1). \quad (5.9)$$

The flow from N_{in} to N_t is then modelled assuming an isentropic compression with a total pressure drop consistent with the semi-empirical relationship in [fig. 5.5](#), and from N_t to N_2 as an isentropic expansion.

Fig. 5.4 Diagram showing the converging-diverging inlet station names, adapted from [Mogavero and Brown \(2018\)](#)

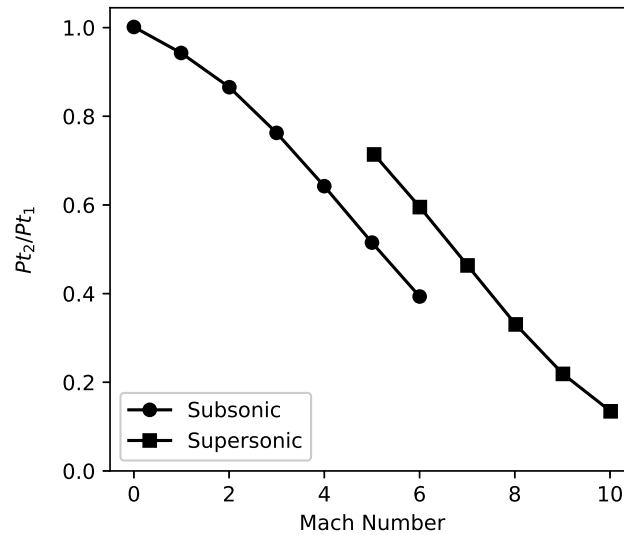
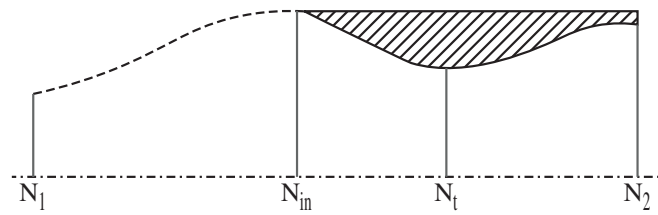


Fig. 5.5 Inlet pressure recovery MIL Spec E-5007D ([Olds and Bradford, 2001](#))

The second model is used for scramjet inlets, and is assumed to be an isentropic duct with a pressure drop modelled using the relationship in [fig. 5.5](#). The intake drag is also calculated using [eq. \(5.9\)](#).

5.1.4 Injection

The injection of fuel is considered separately to other modules, such as combustion chambers, in order to support any kind of flowpath. There are several different injection scenarios that must be accounted for. The first scenario is where fuel is injected into an existing flowstream, such as in a scramjet. The approach to this is unchanged from the original implementation of [Mogavero \(2016\)](#), but is included here for completeness. There are two models that can be used for this. The simplest assumes that the pressure is increased at node 2 of the model by:

$$p_2 = \frac{p_1}{1 - X_{\text{fuel}}} \quad (5.10)$$

where X_{fuel} is the molar fraction of the fuel. The second model is more complex, and assumes that the momentum of the injected fuel is negligible compared to the main flow. It makes use of the balance solver previously discussed in section 5.1.2. The user sets an equivalence ratio, ϕ , as well as the fuel temperature T_{inj} and fuel composition, and the fluxes for eq. (5.6) are calculated according to:

$$\Delta G = -(\phi\Phi) \frac{W_f}{W_1} (X_{\text{ox}})_1 \rho_1 U_1 \quad (5.11a)$$

$$\Delta I = 0 \quad (5.11b)$$

$$\Delta H = \Delta G h_f. \quad (5.11c)$$

The second type of injection scenario is when both the oxidiser and the fuel are injected into a combustion chamber, as in a rocket engine. There are two such models in HyPro, the *InjectionPlate* module and the *InjectionPlatePressure*. The first uses the composition of the injected fluid (the combination of both the fuel and the oxidiser), the mass flow rate, \dot{m} , the Mach number, M_2 and the static temperature, T_2 at N_2 . The pressure at node 2 is then calculated:

$$p_2 = \rho_2 R T_2 \quad (5.12)$$

$$\text{where } \rho_2 = \frac{\dot{m}}{M_2 a_2 A_2} \quad (5.13)$$

The *InjectionPlatePressure* module is a new addition to HyPro, and is essentially the reverse of the previous calculation. The composition, mass flow rate and injection pressure, p_2 are defined, and the Mach number at node 2 is calculated. For both of these models, if a module downstream chokes, the mass flow rate is reduced.

5.1.5 Mixer

The mixer model enables two flows to be combined. It was originally designed for use in combined cycle engines where there is a primary and secondary flow which need to be merged. There are two modules that enable this to be performed, both use the balance equation solver described in section 5.1.2. The first assumes that the pressure around the

injected flow is equal to the pressure at node 1 (i.e. if the injection points is close to node 1), but injected at an angle. The flux equations are then:

$$\Delta G = -\frac{A_3}{A_1} \rho_3 U_3 \quad (5.14a)$$

$$\Delta I = \eta \left(\Delta G U_3 - \frac{A_3}{A_1} (p_3 - p_1) \right) \cos \theta \quad (5.14b)$$

$$\Delta H = \Delta G \left(\frac{U_3^2}{2} + h_3 \right) \quad (5.14c)$$

where η is the mixer efficiency and θ is the angle of the injected flow to lateral walls. This assumes that the area of node 3 (A_3) is small compared to the overall area of the duct. If this is not true, the second module can be used.

The second formulation is only valid for a parallel flow, and assumes that $A_2 = A_1 + A_3$, in which case the flux equations can be written as:

$$\Delta G = -\frac{A_3}{A_2} \rho_3 U_3 \quad (5.15a)$$

$$\Delta I = \eta \left(\Delta G U_3 - \frac{A_3}{A_2} p_3 \right) \quad (5.15b)$$

$$\Delta H = \Delta G \left(\frac{U_3^2}{2} + h_3 \right). \quad (5.15c)$$

5.1.6 Combustion

The combustion chamber of propulsion systems is difficult to model due to the complexity of the phenomena that occur within them. Real gas effects cannot be ignored because of the high temperatures that are reached, and the effect of both mixing and finite-rate chemical reactions should be accounted for. HyPro is intended to model a number of propulsion systems with different combustion conditions, from the subsonic combustion in rockets or ramjets to supersonic combustions in scramjets. In an effort to find a way of modelling combustion effectively, a number of different approaches have been implemented, and will be described here. All of these approaches make significant assumptions, as the tool is intended to be used for configurational optimisation or multidisciplinary design optimisation.

The original method used in HyPro assumed complete combustion of a global reaction mechanism. The composition at node 2 of the combustor was found using this assumption, and the other thermophysical properties were found with the general one-dimensional balance equation solver in eq. (5.6). For a hydrogen-oxygen combustor, the single forward chemical reaction of the combustion of molecular hydrogen with molecular oxygen, $2\text{H}_2 + \text{O}_2 \longrightarrow 2\text{H}_2\text{O}$ is assumed, and the associated heat released is calculated. This reaction continues until either all of the oxidiser or all of the fuel is used up, whichever is sooner. An overall efficiency factor, η , can be applied to represent inefficiencies the combustion process, which reduces the downstream enthalpy:

$$\Delta H = (1 - \eta) [h(T_{ref}, X_1) - h(T_{ref}, X_2)] G_1. \quad (5.16)$$

An error is introduced here, as although the enthalpy is reduced to simulate combustion inefficiencies, no changes to the combustion products are made. Contributions to combustion inefficiency could be incomplete combustion (i.e. formation of intermediate species such as CO for hydrocarbon fuels) or unreacted fuel. With this approach, the causes of the inefficiency have been accounted for in energy, but the fluid does not have the corresponding composition. An overall efficiency factor could be found using experimental data, or from higher-fidelity simulations, often by matching the pressure and temperature at the end of the module.

One of the limitations of this approach is that it is difficult to include multiple species, a new global reaction needs to be introduced for each propellant combination. It also relies upon the balance solver (eq. (5.6)), and therefore comes with the same limitations such as that a duct of constant area can be modelled.

The following approaches to modelling combustion have been added as extension to HyPro to enable better modelling of emissions as part of this project. The next approach is to assume that the gas mixture within the combustor reaches chemical equilibrium. That is, the reactions are infinitely quick and are in equilibrium at the end of the combustor. The balance solver is used to calculate the balance of mass, momentum and energy, but the mixture is assumed to reach equilibrium at the end of the module. This is added as another module built upon the balance solver, but as Cantera library has been implemented to replaced OpenFoam

for thermodynamic calculations, its equilibrium solvers can be used to find the chemical equilibrium point. The equations are fundamentally identical to section 5.1.2, but for each iteration the equilibrium condition at node 2 is calculated as well. Cantera has two chemical equilibrium solvers, *ChemEquil* and *MultiPhaseEquil* (Goodwin et al., 2017). The *ChemEquil* is a non-stoichiometric chemical equilibrium solver using the Element Potential Method (Smith and Missen, 1982), and is applied first. If it does not converge, the *MultiPhaseEquil* method is used automatically.

Using this approach assumes that the reactions are infinitely fast, or that the residence times in the combustor are relatively high. Rocket combustors are often modelled as in chemical equilibrium at the exit with residence times close to one second (Sutton and Biblarz, 2010). In conditions where this assumption applies, the production of major species such as CO₂ and H₂O is driven by the mixture ratio and chamber pressure. However, the limited fidelity of the simulation, including lack of consideration for chemical reactions rates, non-homogeneous variation in mixture ratio in the chamber, and droplet vaporisation prevents it from being able to model emissions of minor species that are only formed by these phenomena, such as soot production.

Models for scramjets (Birzer and Doolan, 2009; Doolan and Boyce, 2008) have also assumed chemical equilibrium chemistry in their quasi-one-dimensional models for mixing-limited scramjet combustors, which requires an appropriate mixing model. Since HyPro currently uses a jump solver approach, where the state is only calculated at the end of the module, rather than integrating along the length of module with a classic quasi-one-dimensional model, a mixing model based on length is not possible to implement. However, an approach which instead only allows part of the overall flow to react could be used. This emulates the total mixing that is allowed to occur. In HyPro this is modelled using the mixer (section 5.1.5) to combine flows, and the splitter module, which separates flows:

$$sr = \frac{\dot{m}_{reacting}}{\dot{m}_{tot}} \quad (5.17)$$

where $\dot{m}_{reacting}$ is the mass flow rate of the flow that is allowed to react, and the \dot{m}_{tot} is the total mass flow through the combustor.

If the mixing that can occur over the combustor is known or can be correlated from data or higher fidelity models, then this approach can be used. The modules use to model complete combustion can also be used with the splitter modules. A key limitation of this model is that as currently implemented, it does not enable finite-rate chemistry to be modelled, which limits its applicability to predicting the emissions produced by engines such as scramjets, where the reaction speed limits the production of NO_x , which requires considering the residence time in the combustion. This has been excluded from consideration here, because it would require a completely different modelling approach.

5.1.7 Solving the system

The propulsion system in HyPro is built up of a series of modules, each with its own physical model and connections to its neighbours. Each module has a consistent interface with others in the system, and the interaction between modules is managed by the system module. The system module solves each module sequentially, and if a module chokes, a feedback loop which reduces the mass flow rate at a previous module (usually an inlet or an injector) is started. Eventually, the system converges on a solution whereby no module is choked. Once a valid solution for the flowpath has been calculated, the thrust produced by the engine can be calculated:

$$F = \dot{m}_2 U_2 - \dot{m}_1 U_1 + (p_2 - p_1) A_2 - D \quad (5.18)$$

which includes the drag of any modules in the system, currently only from inlet models.

Several other performance parameters are automatically calculated, including the specific impulse:

$$I_{sp} = \frac{F}{\dot{m} g_0} \quad (5.19)$$

where \dot{m} is the total mass flow rate of propellant injected into the system. The thrust coefficient is useful for comparing different airbreathing propulsion systems as it is nondimensionalised:

$$c_t = \frac{F}{q A_1} \quad (5.20)$$

where the q is the dynamic pressure and A_1 is the maximum area of the inlet.

5.1.8 Propellants

This section describes the propellants that are likely to be used in future launch vehicles and hypersonic systems. The selection of propellants is a complicated trade off between physical properties of the propellant (density, boiling point), performance, engine design and other parameters (toxicity, storage, cost). Finally, the environmental cost of propellants should also be considered. In the past, this has been a feature of fuels for other industries (e.g. removing lead from petrol, sulfur from kerosene).

The general physical properties of three common fuels (hydrogen, methane and kerosene) are displayed in table 5.1.

Table 5.1 Fuel Physical Properties (Sutton and Biblarz, 2010)

Property	Hydrogen	Methane	RP-1
Approximate Formula	H ₂	CH ₄	C _{H1.98}
Molecular Mass	2.016	16.03	~175
Freezing Point [K]	14.0	90.5	225
Boiling Point [K]	20.4	111.6	460 - 540
Heat of vaporization [kJ kg ⁻¹]	446	510	246
Specific heat [kJ kg ⁻¹ K ⁻¹]	7.32 (20.4K)	3.49 (111.6K)	1.88 (298K)
Specific gravity	0.071	0.424	0.58

Hydrogen

Hydrogen is the highest performing fuel used in rocket engines today, reaching an I_{sp} of 465.5 s for the RL10B-2 (Aerojet Rocketdyne, 2018). This performance is offset by several downsides, primarily its low density and low boiling point. This has a significant influence on the design of a vehicle using hydrogen, particularly the size of the propellant tanks that tend to make a large vehicle. It is also one of two fuels that have been used in scramjet propulsion systems.

Methane

Methane offers several significant advantages over both of the main liquid alternatives: hydrogen, and hydrocarbon-based fuels. Some properties of physical properties of methane as a propellant are shown in table 5.1. Whilst methane is cryogenic, it has a higher boiling

point than Hydrogen, so can be stored at a closer temperature to that of the liquid oxygen [Neill et al. \(2009\)](#). It's higher density than hydrogen results in smaller tank sizes. Methane consists of a single chemical species, which means its properties are highly reproducible ([Sutton and Biblarz \(2010\)](#)). The achievable rocket performance lies in between that of Hydrogen and RP-1 engines.

Methane or liquefied natural gas (LNG) (which is a mixture of methane and propane) being used as a propellant in operational launch vehicles is a relatively new development. Companies like Aerojet have developed O₂/CH₄ rocket engines in the past ([Neill et al., 2009](#)), however the advent of the SpaceX Raptor engine and the Blue Origin BE-3/BE-4 LNG engines indicates that engines using methane fuels are more likely in the future, probably for the combination of reasons above. Generally speaking, combustion of methane or liquefied natural gas has an environmental advantage over kerosene, producing reduced emissions indices for NO_x, CO, C_nH_m. This is largely because of the greater C/H ratio of kerosene compared to methane, as discussed by [Lebedev et al. \(2009\)](#). Methane fuelled rocket engines produce significantly less soot than other hydrocarbon fuels. This reduces the maintenance needed for reusable rocket engines [Burkhardt et al. \(2004\)](#), as well as having an obvious environmental advantage.

Due to interest in methane and LNG as fuels for industrial purposes, significant effort has been made to create an optimised thermodynamic and kinetic mechanism for modelling its combustion. GRI-Mech 3.0 ([Smith et al.](#)) uses thermodynamic data provided by the standard NASA database ([Burcat and McBride, 1997](#); [McBride et al., 1993](#)). The GRI-Mech 3.0 thermodynamic data and equation mechanisms have been created from a large number of reactor, shock tube and ignition delay experiments, and have been used for all methane combustion problems in this work.

Kerosene

A significant challenge of modelling hydrocarbon combustion is the selection of suitable physical and chemical models. Kerosene fuel mixtures for aviation and rocket propulsion are defined by a set of general physical properties, rather than a specific chemical formulae. Different batches of a particular fuel can vary in properties and chemical makeup. [Table 5.2](#) shows the physical properties of RP-1, although these parameters vary slightly between

different publications, even from the same authors (Edwards, 2003; Sutton and Biblarz, 2010; Wang, 2001).

Table 5.2 RP-1 Physical Properties (Edwards and Maurice, 2001)

Property	RP-1
Approximate Formula	C ₁₂ H ₂₄
H/C ratio	1.98
Boiling Range [K]	449.817 - 546.039
Freeze point [K]	224.817
Flash point [K]	329.817
Net Heating Value [kJ kg ⁻¹]	43379.9
Specific Gravity	0.81
Critical Temperature [K]	683.15
Critical Pressure [Pa]	2.172e+6
Average Composition	
Aromatics [vol %]	3
Naphthenes [vol %]	58
Paraffins [vol %]	39
Sulphur [ppm]	20

Surrogate models are used to standardise the fuels used in modelling and experiments. Broadly speaking, there are two types of surrogates: *Physical Surrogates* are designed to have the same physical properties as the fuel, and *Chemical Surrogates* are mixtures designed to contain the same chemical properties, i.e. proportion of aromatic, naphthene or paraffin components. Chemical surrogates should have similar combustion properties to the real fuel, but may not produce the same trace combustion products. Selecting the appropriate surrogate model for the phenomenon being investigated is important for detailed studies. Edwards and Maurice (2001) has assembled a summary of surrogates used to represent aviation and rocket fuels, and suggests using a ‘surrogate that matches the major important chemical classes’ to understand combustion of NO_x emissions.

Wang (2001) proposed single formula RP-1 surrogate with an accompanying quasi-global kinetics formulation. This model uses a single chemical formula, C₁₂H₂₄ to represent the averaged properties of the range of components. The quasi-global kinetic (shown in table 5.3) includes two reactants with the formula, C₁₂H₂₄, 41.7% paraffin and 58.7% naphthene, which matches the approximate split of paraffin and naphthene measured in RP-1. This split is important for modelling the production of soot with finite rate chemistry.

Table 5.3 RP-1 Surrogate Chemical Kinetics Scheme (Wang, 2001)

Reaction ^a	A	B	E/R	Form
Paraffin global step				
$C_{12}H_{24} + 6 O_2 \longrightarrow 12 CO + 12 H_2$	3.888×10^4	1	1.220×10^4	$p^{0.3}[C_{12}H_{24}]^{0.5}[O_2]$
Naphthene global step				
$C_{12}H_{24} + 6 O_2 \longrightarrow 12 CO + 12 H_2$	2.132×10^7	1	1.965×10^4	$p^{0.3}[C_{12}H_{24}]^{0.5}[O_2]$
Wet CO mechanism				
$H_2 + O_2 = OH + OH$	1.700×10^3	0	2.407×10^4	
$OH + H_2 = H_2O + H$	2.190×10^{13}	0	2.590×10^3	
$OH + OH = O + H_2O$	6.023×10^{12}	0	5.500×10^2	
$O + H_2 = H + OH$	1.8×10^{10}	1	4.48×10^3	
$H + O_2 = O + OH$	1.22×10^{17}	-0.91	8.369×10^3	
$M + O + H = OH + M$	1×10^{16}	0	0	
$M + O + O = O_2 + M$	2.55×10^{18}	-1	5.939×10^4	
$M + H + H = H_2 + M$	5×10^{15}	0	0	
$M + H + OH = H_2O + M$	8.4×10^{21}	-2	0	
$CO + OH = H + CO_2$	4×10^{12}	0	4.03×10^3	
$CO + O_2 = CO_2 + O$	3×10^{12}	0	2.5×10^4	
$CO + O + M = CO_2 + M$	6×10^{13}	0	0	
Soot formation global step				
$C_{12}H_{24} \longrightarrow 12 C_s + 12 H_2$	4.4947×10^{15}	-1.94	1.61×10^4	$[C_{12}H_{24}]^{1.81}[O_2]^{-0.5}$
Heterogeneous soot oxidation				
$C_s + 0.5 O_2 \longrightarrow CO$	1.0	0	0	$72 R_{OX}[C_s]/(\rho_s D_s)^b$
K_A	2×10^1	0	1.5098×10^4	
K_B	4.45×10^{-3}	0	7.6497×10^3	
K_T	1.51×10^5	0	4.8817×10^4	
K_Z	2.13×10^1	0	-2.063×10^3	
Homogeneous soot oxidation				
$C_s + OH = CO + H$	1.22×10^9	0.5	0	

^aM is a third-body collision partner and $K = AT^B \exp(-E/RT)$

^bwhere $R_{OX} = K_A p_{O_2} \chi / (1 + K_Z p_{O_2}) + K_B p_{O_2} (1 - \chi)$ and $\chi = 1 / [1 + (K_T/K_B) p_{O_2}]$

Another approach is the multi-formula model. According to Wang (2001), Farmer and Anderson (1995) developed a three-formula surrogate, consisting of 17.4% C₁₃H₁₂ (methylbiphenyl), 45.4% C₁₂H₂₄ (n-heptylcyclopentane) and 37.2% C₁₂H₂₈ (n-tridecane). The same authors later developed a new surrogate containing more components, reproduced in table 5.4 (Farmer et al., 1997). Huber et al. (2009) developed 5-component surrogates for RP-1 and RP-2, focusing specifically on reproducing the thermodynamic and transport properties.

Table 5.4 RP-1 Multi-Formula Surrogate Components (Farmer et al., 1997)

Component	% Volume
<i>n</i> -undecane	4.7
<i>n</i> -dodecane	6.0
<i>n</i> -tridecane	18.8
<i>n</i> -tetradecane	12.5
<i>n</i> -hexylcyclopentane	2.7
<i>n</i> -heptylcyclopentane	3.6
<i>n</i> -octylcyclopentane	11.2
<i>n</i> -nonylcyclopentane	7.5
Bicycloparaffin 1 C ₁₁ H ₂₀	11.3
Bicycloparaffin 2 C ₁₂ H ₂₂	14.7
Pentamethylbenzene	1.3
Hexamethylbenzene	1.7
Dimethylnaphthalene	4.0

As this thesis does not model the formation of soot using chemical kinetics, it is not necessary to consider which of these surrogates is the most appropriate for modelling the engine performance and emission production. However, it is important to use appropriate thermophysical data for RP-1. The single-formula RP-1 surrogate C₁₂H₂₄ by Wang (2001) has been chosen, the properties of which are shown in Table 5.5.

Table 5.5 RP-1 Single-formula Surrogate Thermophysical Data (Wang, 2001)

Coefficient	300 - 1000K	1000 - 5000K
a_0	$0.395\ 086\ 91 \times 10^1$	$0.364\ 402\ 06 \times 10^2$
a_1	0.102 079 87	$0.546\ 148\ 01 \times 10^{-1}$
a_2	$0.131\ 244\ 66 \times 10^{-4}$	$-0.160\ 911\ 51 \times 10^{-4}$
a_3	$-0.766\ 492\ 84 \times 10^{-7}$	$0.214\ 784\ 97 \times 10^{-8}$
a_4	$0.345\ 037\ 63 \times 10^{-10}$	$-0.101\ 311\ 80 \times 10^{-12}$
a_5	$-0.520\ 935\ 74 \times 10^5$	$-0.638\ 901\ 09 \times 10^5$
a_6	$0.219\ 809\ 51 \times 10^2$	$-0.157\ 989\ 73 \times 10^3$

5.1.9 Contributions to HyPro

Although HyPro is an existing software package and was stable platform to build on, it required further development to be capable of modelling rocket engines. The following modifications have been made to extend its capability:

Chemical Engine HyPro originally used the thermophysical model from OpenFOAM (v2.2.x).

This was completely replaced by the Author in favour of Cantera, an open-source set of tools used to solve chemical kinetic, thermodynamic and transport problems. There were a number of reasons to do this

- Access to robust, validated chemical equilibrium solvers.
- Ease of access to thermophysical and kinetic data - Cantera is able to import .cti/.xml files defining the NASA polynomials and kinetic equations. This is particularly useful when looking at combustion of hydrocarbons, since the data can consist of hundreds of species and thousands of equations.
- Cantera has additional capabilities which may be useful for future modelling of combustion and emissions (zero-dimensional reactors, one-dimensional flames)

This required an almost complete rewrite of the fundamental core of HyPro, which tracks and calculates the thermodynamic and kinetic state of the gas flow. Whilst doing so, the root-solving algorithms used within many of the gas dynamics modules were exchanged from custom implementations to robust, well-validated algorithms.

Combustion Modelling The ability to model combustors has been improved with the addition of an equilibrium chemistry module. Previous versions of HyPro could only assume complete combustion of a single global reaction, with efficiencies to tailor the performance. Furthermore, splitter and mixer modules have been added. These enable a user to use HyPro to model certain phenomena, such as mixing, in more detail. For example, using mixing parameters calculated from CFD to split the flow into two parts, taking into account areas where combustion does not occur in a combustor. The rationale behind these developments was explained in section 5.1.6, and their effectiveness for modelling rocket engines is evaluated in section 5.2.

Nozzle flow The isentropic flow solver previously implemented assumed a constant composition throughout the duct. This module was reconstructed to enable the ability to assume shifting equilibrium through any isentropic duct. This is a critical development that enables nozzle chemistry and rocket engines to be modelled, and for the requirements of engine models during conceptual design for understanding their environment to be evaluated.

Addition of the injection model The second of the two injector models introduced in section 5.1.4 has been added to HyPro to model rocket engines. This enables the injection pressure to be defined, and for the Mach number to be calculated - the opposite of the previous module.

Once these changes were implemented, they were used to model a series of rocket engines including the RL10, RS-68, Merlin 1D, Merlin 1D Vac, Raptor engines. HyPro was previously incapable of modelling these systems, and additionally required significant work to introduce new propellants, as a single reaction equation must be added by hand. This is important during conceptual design where a propellant has not been selected, and a wide variety of propellant combinations, and engine design conditions need to be evaluated.

The rockets modelled are compared against an industry standard tool to understand the capability of HyPro to model these systems, as well as other sources of data where available in section 5.2.

5.2 Rocket engines

The approach taken in this thesis to estimate the emissions from rockets engines is to bound the major species emissions by examining the two scenarios; that of the shifting equilibrium through the nozzle and the frozen flow assumption. A third simulation where the flow is in shifting equilibrium until the throat and then is frozen for the remainder of the nozzle is run to establish a third data point, which in some cases may provide a better estimate. This does not provide detailed knowledge on the production of some emissions that are produced by more complex phenomena, such as soot in regions of low O/F ratios in kerosene engines, but may be able to provide enough information to include emissions within the design process.

5.2.1 Modelling rockets with HyPro

Modelling rockets within HyPro is conceptually similar to the approach of CEA, however the rocket engine is constructed by combining general modules from the HyPro toolkit. Any rocket can be modelled with the following building blocks:

1. Injector (InjectionPlatePressure)
2. Combustion Chamber (EquilCombustor or EffComb)
3. Convergent Section (EffIsentropicDuct)
4. Divergent Section (EffIsentropicDuct).

The inputs provided by the user are the injection pressure, P_{inj} , the O/F ratio, and T_{inj} for fuel and oxidisers, the area profile of the rocket engine, only required at each node between modules and an estimated mass flow rate.

5.2.2 Limitations

There are a number of phenomena that occur in real nozzles which are not simulated using this approach:

- **Flow Divergence** - Caused by the separation of the flow from the walls of the nozzle. This is reduced for bell-shaped nozzles compared to simpler shapes, such as cones. [Sutton and Biblarz \(2010\)](#) provide a correction factor as a function of divergence angle for conical nozzles.
- **Friction** - Friction with the walls of the nozzle due to a slow boundary layer can result in a reduction in the exit velocity (estimated to be between 0.5 % and 1.5 %).
- **Multiphase Phenomena** - The presence of additional states of matter in the flow, such as a solid particles or liquid droplets reduces performance. In some situations, these could be included in lower-fidelity models, such as vaporisation of fuel/oxidiser droplets in the combustion chamber.

- **Ablative Cooling** - Rockets that utilise ablative cooling in the nozzle, will see a gradual alteration of the nozzle geometry during use, as the ablative material is eroded by the flow.
- **Unsteady Combustion** - Unsteady combustion, which results in oscillations within the combustion chamber can provide major issues for the engine's designers, but also a loss of performance.
- **Finite Rate Chemistry** - The assumption made by assuming shifting equilibrium is that all chemical reactions are infinitely fast, when in fact they have a limited-rate. In some circumstances this changes the flow significantly (if the reaction times are on the same order as the flow residence time).

Table 5.6 shows the relationship between phenomena and performance losses in rocket engines (Dunn and Coats, 1997). Many of these can only be improved by increasing the detail of the modelling.

Table 5.6 Interaction of physical phenomena with performance loss calculations. Losses are on I_{sp} . *Not imp* are losses that are generally not important. Adapted from Dunn and Coats (1997).

Phenomena	Performance Losses				
	Divergence Loss	Boundary Layer Loss	Finite Rate Kinetics Loss	O/F Maldistribution Loss	Energy Release Loss
Non- 1-D Flow	-	1st Order (>0.2%)	2nd Order (<0.2%)	Not imp	Not imp
Viscous and heat transfer	Not imp	-	Not imp	Not imp	Not imp
Finite rate chemistry	Not imp	2nd Order (<0.2%)	-	Not imp	Not imp
Non-Uniform Mixture Ratio	Not imp	1st Order (>0.2%)	1st Order (>0.2%)	-	Not imp
Incomplete Energy Release	Not imp	2nd Order (<0.2%)	1st Order (>0.2%)	Not imp	-

In general, the use of the equilibrium chemistry assumption results in an over-prediction of performance in rocket nozzles, whilst the frozen-flow assumption results in an under-prediction (without correction factors) (Humble et al., 1995; Sutton and Biblarz, 2010).

This difference is because these two cases are extremes of what actually occurs in a nozzle, where chemistry does occur but at a finite-rate, and does not result in the performance gains of the additional heat release from reaching equilibrium.

5.2.3 Comparison of HyPro with NASA CEA

For initial design, sizing and performance characteristics, a common approach is to assume the propellant is at a low velocity ($u = 0$) in the combustion chamber, where it is allowed to reach chemical equilibrium at the rated combustion pressure. This approach is used by NASA's Chemical Equilibrium with Applications (CEA) tool ([Gordon and McBride, 1994](#); [McBride and Gordon, 1996](#)), which enables users to solve generic thermodynamic, chemical equilibrium and rocket combustion problems. This tool is used to benchmark the performance of HyPro in this thesis. CEA is capable of modelling:

- Infinite-area Combustion (IAC) Chambers:
 - With frozen flow after the throat
 - With frozen flow after the combustion chamber
 - With shifting equilibrium through the nozzle
- Finite-area Combustion (FAC) Chambers:
 - With shifting-equilibrium through the nozzle

Both types of combustors are based on one-dimensional continuity, energy and momentum equations, and assume adiabatic combustion (no heat transfer from the fluid) as well as isentropic expansion through the nozzle (constant entropy). The gas is assumed to be a homogeneous ideal gas, and although condensed species can be included, there are no temperature or velocity lags between the species. Finally, the velocity at the combustion chamber inlet is assumed to be zero, $u = 0$ ([Gordon and McBride, 1994](#)). For the finite-area combustor, the area of the combustion chamber area is assumed to be constant and the combustion assumed to be a non-isentropic, irreversible process.

The one-dimensional conservation equations are:

$$\rho_2 A_2 u_2 = \rho_1 A_1 u_1 \quad (5.21a)$$

$$P_2 + \rho_2 u_2^2 = P_1 + \rho_1 u_1^2 \quad (5.21b)$$

$$h_2 + \frac{u_2^2}{2} = h_1 + \frac{u_1^2}{2}. \quad (5.21c)$$

These equations are similar to those solved by HyPro and described in section 5.1, so the results should be similar accounting for implementation details. The advantage of HyPro is that as the rocket engines are constructed out of general modules that be integrated tightly with design or trajectory optimisation, and any future developments can be rolled into modelling rocket engines easily. The flexibility of modular approach is highlighted by the ability to consider equilibrium flow to the nozzle throat and frozen through the expansion section, which is not implemented within CEA.

Performance figures

The characteristic velocity, c^* is calculated from the pressure of the infinite chamber, rather than the p_c produced in the FAC case:

$$c^* = \frac{P_{inf} A^*}{\dot{m}}. \quad (5.22)$$

This means it is the same for both infinite and finite combustor modelling instances. The mass flow rate is calculated with the standard equation:

$$\dot{m} = \rho A u, \quad (5.23)$$

and the coefficient of thrust, is defined as:

$$C_f = \frac{u}{c^*}, \quad (5.24)$$

where u can be calculated from the Mach number M and speed of sound a , both of which are outputs from CEA. The thrust can be calculated from the results CEA outputs using the primary rocket engine sizing parameter, the throat area, A^* . The performance of the new

capability in HyPro is compared against other models and the real performance of three specific cases with different propellant combinations (l-H₂/LOX, RP-1/LOX and CH₄/LOX). These tests are based on real engines for which some level of performance data is available. Each engine is modelled in both CEA and HyPro, and the results are compared to each other and the reported performance of that engine. The parameters used in this comparison are the key performance figures, specific impulse and thrust, as well as the calculated mass flow rate and combustion temperature of the rocket engine. Additionally, the mass fractions of the flow at the nozzle exit are compared, which provide the basis for the emissions produced from the engines.

5.2.4 RL10

The Aerojet RL10 family of liquid-fuel cryogenic rocket engines are designed to be used for the upper stages of launch vehicles. The first versions of the RL10 were tested by Pratt & Whitney in the 1950's, and evolved versions are used in both the United Launch Alliance Atlas V (RL10A-4-2) and Delta IV (RL10B-2) launch vehicles today. The manufacturers rarely release comprehensive specifications to the public, but a variety of sources have been used to create a complete engine specification, displayed in table 5.7 (Aerojet Rocketdyne, 2018; Blau, 2018a). The exit area is calculated from the diameter of the engine under the assumption that the widest part of the engine is the exit of the nozzle, and ignoring the thickness of the nozzle walls. The throat area is calculated using the exit area and the expansion ratio. The chamber area is assumed to be at least four times the area of the throat, as this is where contraction losses become negligible (Sutton and Biblarz, 2010). The reference mass flow rates are calculated from the definition of the specific impulse:

$$I_{sp} = \frac{F}{\dot{m}g_0}. \quad (5.25)$$

Note that for the RL10A-4-2 and RL10B-2 the throat areas do not match. This is unusual given that the engines have a common heritage, and will be discussed further later on in the discussion about the finite area combustion chamber results on page 114.

Table 5.7 RL10 Specifications

	RL10A-4-2	RL10B-2
Thrust, kN	99.2	110.1
Weight kg	167.8	301.2
Mixture Ratio	5.5:1	5.88:1
Specific Impulse, s	451	465.5
Expansion Ratio	84:1	285:1
Diameter, m	1.17	2.21
Length, m	2.29	4.14
Chamber Pressure, Pa	4.206e+6	4.413e+6
Calculated Values		
Flow Rate, kg s ⁻¹	22.42	24.11
Exit Area, m ²	1.075	3.836
Throat Area, m ²	0.0128	0.0135
Chamber Area (est), m ²	0.0512	0.0538

Infinite Area Combustion Chamber

The RL10B-2 was modelled in both CEA and HyPro in order to validate HyPro's rocket simulation capabilities against an industry standard code. First, a comparison between CEA and HyPro in modelling rocket engines using the infinite combustion chamber assumption is made. In this case, the area of the combustion chamber is assumed to be infinite, and the velocity within the chamber approaches 0. Additionally the entropy, s_c is assumed to be constant and the combustion chamber pressure is equal to the combustion chamber total pressure, $p_c = p_{c0}$. To model an infinite combustion chamber in HyPro, the area of node 1 of the combustion chamber is set to a very large number compared to the nozzle throat. Two nozzle modes are evaluated, consistent with CEA; the first where the combustion chamber products are held frozen throughout the nozzle, and the second where the gas is allowed to reach equilibrium at the nozzle exit, the shifting equilibrium assumption.

The HyPro results for the modelling of the RL10 engine compared with CEA with infinite area combustor are shown in table 5.8. HyPro overpredicts the mass flow rate, which is likely due to the difference in the overall modelling approach, or the numerical methods used. The exit pressure and temperature have errors of 1.49 % and 3.18 % respectively, and the errors in the mass fraction of the major components, H₂ and H₂O, are < 1 %.

Table 5.8 Equilibrium RL10-B2 Performance simulated with CEA and HyPro infinite-area combustion chambers.

	Frozen		Equilibrium	
	HyPro	CEA2	HyPro	CEA2
Performance				
Chamber Temperature T_c (K)	3449	3417	3449	3417
Chamber Pressure p_c (MPa)	4.413	4.413	4.413	4.413
Exit Temperature T_e (K)	556	552	839	813
Exit Pressure p_e (Pa)	545	546	720	709
Characteristic Velocity c^* (m s^{-1})	2275	2262	2322	2305
Specific Impulse (vac) $I_{sp,v}$ (s)	455	452	486	481
Thrust Coefficient C_F	1.96	1.93	2.05	2.00
Thrust F (kN)	116.5	114.4	121.9	118.9
Mass Flow \dot{m} (kg s^{-1})	26.1	25.8	25.6	25.2
Exit Mass Fractions Y_i				
H	0.003 11	0.002 86	0.0	0.0
H ₂	0.0399	0.0397	0.0377	0.0377
H ₂ O	0.884	0.888	0.962	0.962
H ₂ O ₂	2.21×10^{-5}	1.96×10^{-5}	0.0	0.0
HO ₂	7.19×10^{-5}	6.22×10^{-5}	0.0	0.0
O	0.005 00	0.004 20	0.0	0.0
O ₂	0.009 60	0.008 11	0.0	0.0
OH	0.0580	0.0569	0.0	0.0

In both the results using the infinite area combustor and the finite area combustor, the exit pressures are significantly lower (e.g. for the infinite area combustor ~ 550 Pa from ~ 720 Pa) for the frozen nozzle flow assumption. However, the performance is still consistent. Looking first at the thrust equation (Sutton and Biblarz, 2010):

$$F = \dot{m}v_e + (p_e - p_0)A_e, \quad (5.26)$$

where \dot{m} is the mass flow rate, v_e is the exit velocity, p_e is the exit pressure, p_0 is the ambient pressure, in this case 0 Pa and A_e is the exit area. As these simulations are performed in a vacuum, the second term is $p_e A_e$, which is where this pressure difference has an impact. However, the first term is much larger, so small changes in the exit pressure do not dominate the calculated thrust. The reason for this is the additional chemical reactions occurring with the shifting equilibrium assumption release additional energy into the flow - for a constant pressure ratio this would result in a larger area ratio, but in this case the area ratio is fixed, and so the pressure is higher (Sutton and Biblarz, 2010). Similarly, the temperature of the gas is also higher in the shifting equilibrium assumption.

Finite Area Combustion Chamber

The next step is to model the finite area rocket combustor, whereby combustion is non-isentropic. It cannot be assumed that the entropy of the combustor is the same as the entropy of the injected propellant, $s_c \neq s_{\text{injection}}$. The results are shown in table 5.9, where 'Equil', 'Partial' and 'Frozen' indicate the nozzle chemistry mode (shifting equilibrium assumption to the end of the nozzle, partial equilibrium to the throat and frozen flow respectively).

It is expected that the real performance of a rocket nozzle lies between the frozen and equilibrium case, and that the results from the frozen and equilibrium cases can be used as "extreme" cases to bound the emissions released in the atmosphere. However, as shown in table 5.9, this is not the case with these engine parameters, which are derived from publicly available information. A brief computational experiment was performed to see if this error could be explained by an error in these assumed parameters.

In table 5.7, the throat areas are not the same for the two different engines. However, it is a reasonable assumption that engines from the same family might have identical combustion

Table 5.9 RL10B-2 modelled by CEA and HyPro

	CEA	HyPro		
	Equil	Equil	Partial	Frozen
Chamber Conditions				
Temperature [K]	3411	3462	3462	3462
Chamber Pressure [MPa]	4.302	4.409	4.409	4.406
Exit Conditions				
Exit Temperature [K]	813.2	853.3	598.0	556.7
Exit Pressure [Pa]	701	731.2	561.7	543.6
Performance				
Specific Impulse (vac) [s]	481.2	488.2	463.5	456.8
Thrust [kN]	120.2	122.9	114.5	116.7
Mass Flow [kg s^{-1}]	25.5	25.7	25.7	26.0
Relative Error compared to reported performance				
Specific Impulse (vac) [%]	3.38	4.88	-0.420	-1.87
Thrust [%]	9.15	11.6	4.03	6.02
Exit Mass Fractions				
H ₂	0.0377	0.0377	0.0392	0.0400
H ₂ O	0.962	0.962	0.898	0.881
HO ₂	0.0	0.0	0.000 044	0.000 076
H ₂ O ₂	0.0	0.0	0.000 013	0.000 023
H	0.0	0.0	0.002 74	0.003 21
O	0.0	0.0	0.003 80	0.005 32
OH	0.0	0.0	0.0488	0.0602
O ₂	0.0	0.0	0.007 57	0.0101

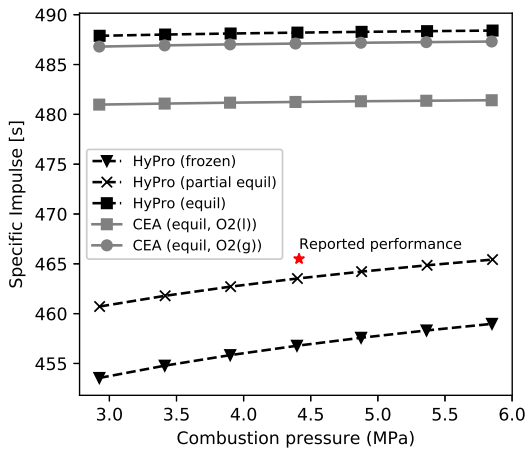
chamber designs. Therefore, a modified RL10B-2 specification was derived, using the A^* (0.012799 m^2) from the RL10A-4-2, and the area ratio of the RL10B-2, resulting in an exit area $A_e = 3.648 \text{ m}^2$, just 4.91 % less.

Table 5.10 RL10 Modified Specification Errors

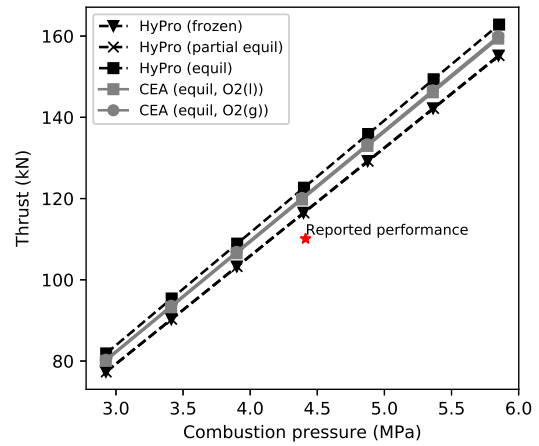
	RL10B-2	RL10B-2 Mod
Thrust		
CEA	9.15 %	3.79 %
HyPro w/ Frozen	3.51 %	-1.57 %
HyPro w/ Equil	8.81 %	3.47 %
Specific Impulse		
CEA	3.38 %	3.38 %
HyPro w/ Frozen	-2.21 %	-2.21 %
HyPro w/ Equil	4.33 %	4.33 %

The errors displayed in table 5.10 are much more in line with the expected behaviour. The modified engine specification has no effect on either the I_{sp} or the mass fractions at the exit, as A^* is purely a sizing factor for the engine. This indicates how the engine specification impacts the ability of software like HyPro or CEA to predict the performance of an existing engine.

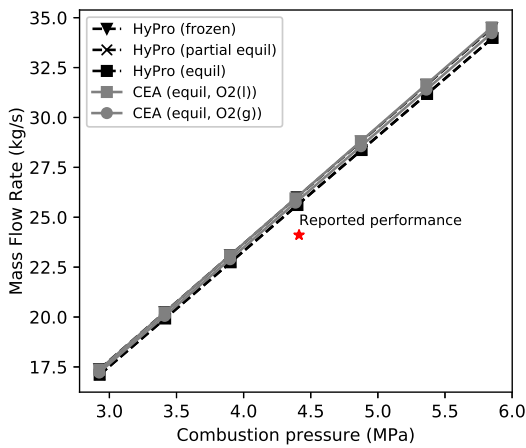
To further test how HyPro and CEA compare to each other, a series of simulations varying the combustion pressure and then the mixture ratio were performed (using the nominal RL10B-2 engine parameters). Figure 5.6 show the specific impulse, thrust, mass flow rate and combustion temperature for the range combustion pressures between 3 MPa to 6 MPa. Similarly, fig. 5.7 shows same parameters at a range of mixture ratios between 5 and 6.5. The performance is bound neatly between the HyPro equilibrium and frozen models. CEA predicts about a 10 s reduction in specific impulse compared to HyPro with the default setup. This is because CEA includes the latent heat of vaporisation within its calculation. To test this, CEA was run again with the gaseous oxygen at the same inlet temperature and pressure, this time matching much more closely. This is an assumption that HyPro makes which could be corrected, but as seen in fig. 5.8 and fig. 5.9, it makes very little difference to the predicted emissions of the vehicle.



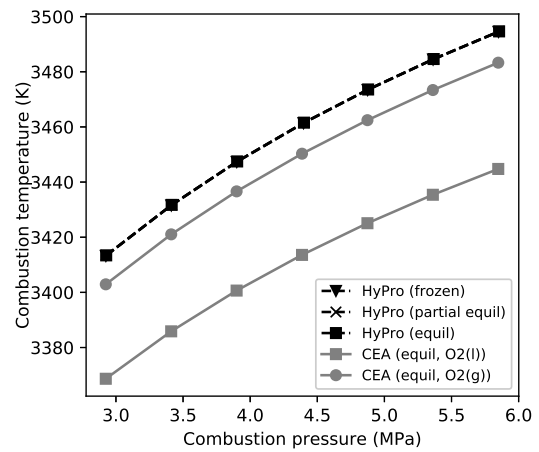
(a) Specific impulse vs combustion pressure



(b) Thrust vs combustion pressure

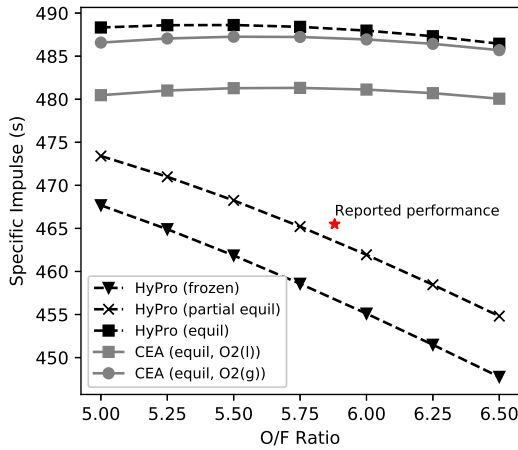


(c) Mass flow rate vs combustion pressure

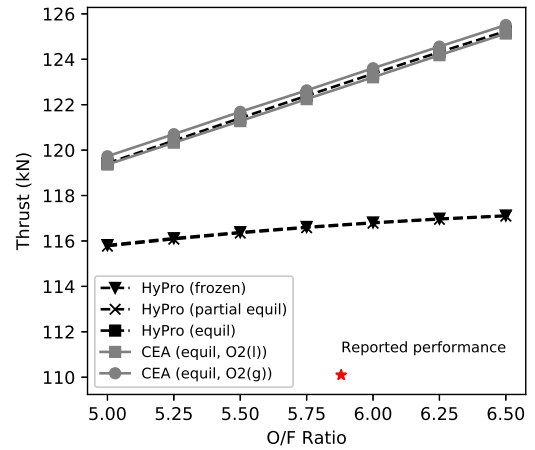


(d) Combustion temperature vs pressure

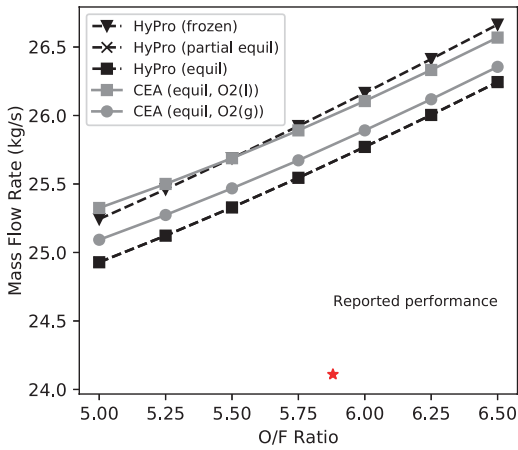
Fig. 5.6 Performance of a hydrogen fuel rocket engine based on the RL10 engine across a range of combustion pressures. Results shown frozen flow, partial equilibrium (freezing at the nozzle throat) and equilibrium flow to the nozzle exit are shown.



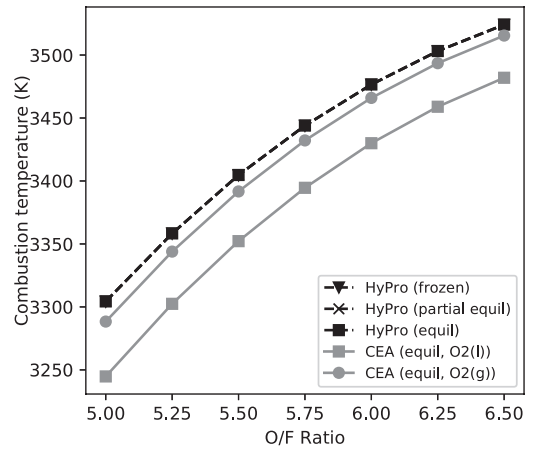
(a) Specific impulse vs O/F ratio



(b) Thrust vs O/F ratio

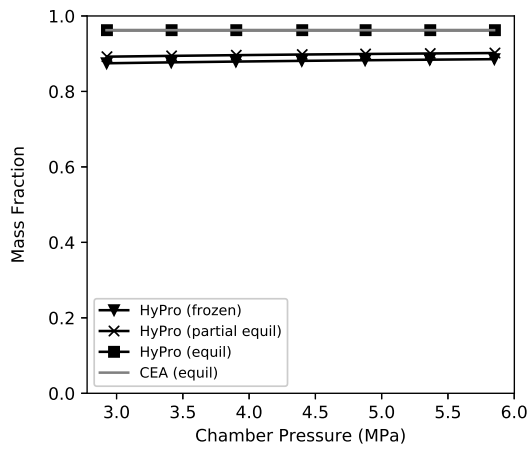


(c) Mass flow rate vs O/F ratio

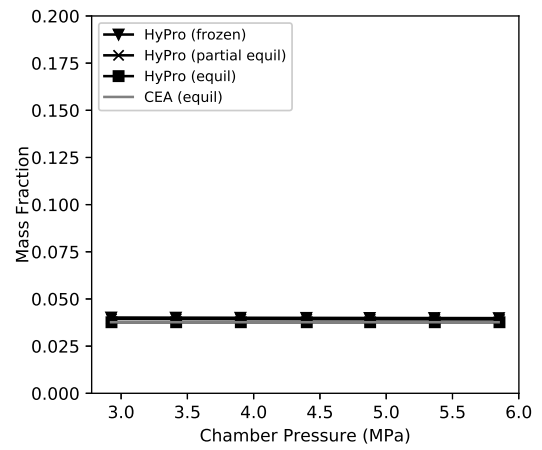


(d) Combustion temperature vs O/F ratio

Fig. 5.7 Performance of a hydrogen fuel rocket engine based on the RL10 engine across a range of O/F ratios. Results shown frozen flow, partial equilibrium (freezing at the nozzle throat) and equilibrium flow to the nozzle exit are shown.

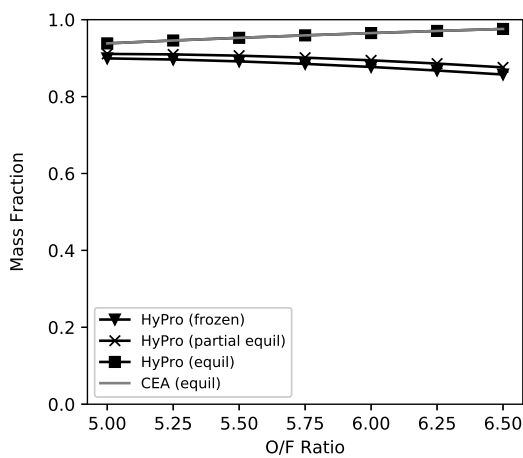


(a) H₂O mass fraction vs combustion pressure

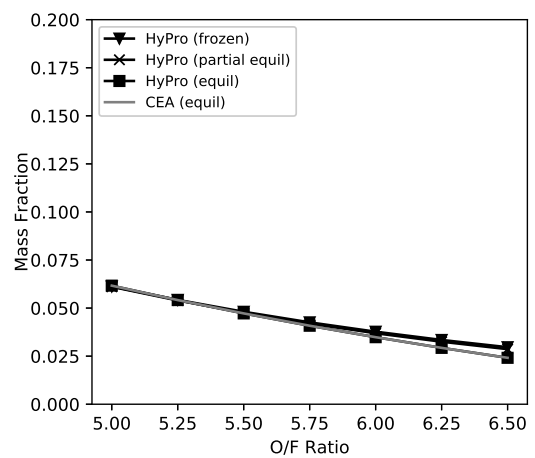


(b) H₂ mass fraction vs combustion pressure

Fig. 5.8 Emissions mass fractions at nozzle exit of a hydrogen fuel rocket engine based on the RL10 engine across a range of combustion pressures ratios. Results shown frozen flow, partial equilibrium (freezing at the nozzle throat) and equilibrium flow to the nozzle exit are shown.



(a) H₂O mass fraction vs O/F ratio



(b) H₂ mass fraction vs O/F ratio

Fig. 5.9 Emission mass fractions at nozzle exit of a hydrogen fuel rocket engine based on the RL10 engine across a range of O/F ratios. Results shown frozen flow, partial equilibrium (freezing at the nozzle throat) and equilibrium flow to the nozzle exit are shown.

5.2.5 Merlin

The Merlin rocket engines are designed and manufactured by SpaceX for their Falcon family of launch vehicles. Each Falcon 9 uses 10 Merlin-derived engines, 9 optimised for ascent in the atmosphere for the first stage, and 1 vacuum-optimised (dubbed Merlin Vac) for the second stage. There have been several generations of Merlin engines, but they have all used RP-1 and liquid oxygen for propellant, and make use of a gas-generator power cycle.

Like many rocket engines, detailed specifications for SpaceX's Merlin engines are not in the public domain. Additionally, the design of the Merlin engine has evolved rapidly, so there are conflicting reports on the engine parameters. The assumed engine parameters are shown in table 5.11. The sources of this information are based on [Blau \(2018b\)](#) and [SpaceX \(2019\)](#).

The mixture ratio can be estimated based on the amount of LOX and RP-1 carried in the first stage of the vehicle (assuming the ratio of the flow rates for the fuel and oxidiser is constant during the flight):

$$MR = \frac{M_{\text{ox}}}{M_{\text{f}}} = \frac{287430}{123570} = 2.32, \quad (5.27)$$

which is a reasonable value as the optimal mixture ratio for LOX/RP-1 is between 2.24 and 2.56 ([Sutton and Biblarz, 2010](#)).

Table 5.12 shows the performance characteristics and exit mass fractions for the Merlin 1D calculated by CEA2, and by HyPro in both frozen and equilibrium mode. Table 5.13 shows the same for the Merlin 1D Vac engine. CEA and HyPro both overpredict the thrust and the specific impulse for each test case. CEA and HyPro with equilibrium have very similar errors in thrust and specific impulse, as well as in terms of the exit mass fractions. This indicates the errors are potentially due to the same source. Further, the HyPro w/ frozen chemistry also has superior performance to the rated performance of the engine. It is expected that the frozen performance should be less than that of the real engine performance. As with the RL10, this is most likely due to either, a) an error in the engine specifications due to the unreliability of data sources, or b) some limitation in the modelling approach of both CEA2 and HyPro as discussed in section 5.2.2. It is also possible that the assumption that

Table 5.11 Merlin Specifications

	Merlin 1D+	Merlin 1DVac
Thrust (SL) [kN]	845	-
Thrust (Vac) [kN]	914	934
Weight [kg]	470	> 470
Specific Impulse (SL) [s]	282	-
Specific Impulse (Vac) [s]	311	348
Expansion Ratio	16:1	165:1
Diameter [m]	1	3.21
Chamber Pressure [MPa]	11	11
Calculated Values		
Mixture Ratio	2.32:1	2.32:1
Calculated Flow Rate [kg s ⁻¹]	300	274
Calculated Exit Area [m ²]	0.785	8.10
Calculated Throat Area [m ²]	0.0491	0.0491
Chamber Area (est) [m ²]	0.196	0.196

the Merlin 1D and Merlin 1D Vacuum are fundamentally the same (with an extended nozzle skirt) is incorrect. Without exact specifications of the Merlin engine family, it is difficult to investigate this error further.

It is interesting to note that the reported $I_{sp,v} = 311$ of the Merlin 1D is significantly below the predicted performance of HyPro and CEA in all cases. The closest is the frozen nozzle flow case, which has a 4.18% error compared to the reported performance. Both HyPro and CEA simulate ideal rocket performance, so the most likely reasons for this discrepancy are related to the limitations of the modelling approach as discussed in section 5.2.2. In particular, the vaporization of the liquid droplets of liquid oxygen and RP-1, as well as the more complex chemical reactions needed to break complex hydrocarbons within kerosene could be causing this issue.

This does mean that it could be difficult to use HyPro (or CEA) for the design of rocket engines that use RP-1 propellant without considering the errors in more detail. However figs. 5.12 to 5.15 show that O/F is the main driver in the production of emission species. The proposed solution for the use of HyPro or CEA is therefore to model the rocket engine using the correct O/F ratio, and then to match the mass flow rate produced by HyPro to

that of the reported performance. The mass flow appears to be well matched by HyPro and CEA in these test cases. Performance corrections could then be used to tune the predicted performance based on a larger set of simulation cases.

As with the RL10 test case, the performance of an engine based on the Merlin 1D at a range of combustion pressure and O/F ratios is established. This is to investigate the key parameters which can effect the emissions produced, and to benchmark HyPro against CEA for a range of engine conditions. Figure 5.10 shows the performance at a range of combustion pressures between 9 MPa and 13 MPa, whilst fig. 5.11 shows the variation with O/F ratio. This largely mirrors the results of the RL10 engine, although the difference between the two equilibrium models is closer. As with the RL10, combustion pressure does not have a great influence on the mass fractions of species (figs. 5.12 and 5.13), whilst O/F ratio (figs. 5.14 and 5.15) mostly has an effect on the ratio of CO to CO₂. Section A.1 contains a set of extra graphs showing the performance and emissions of the Merlin 1D Vacuum engine, which is fundamentally the same engine but with a longer nozzle skirt. This affects the shifting equilibrium nozzle, where the pressure at the end of the longer nozzle is lower.

Unlike the RL10, there is some information on the mass fractions produced by the Merlin1D engine. The results of a simulation modelling the Merlin 1D using the PERCOP engine model as well as the reactions of the emissions in the plume were published in the draft environmental report (FAA, 2020). This report does not contain the detailed engine specification to reconstruct the engine exactly, so it difficult to directly compare with confidence. Some key results from this analysis have been shown in table 5.14.

The estimated mass fraction of CO is much greater than that in the more detailed model. This may indicate that the assumed O/F ratio is different to that of the actual engine. This is supported by slightly different ratios of CO, CO₂ and H₂O in the mixed chamber, which are quite similar to the frozen case in table 5.12 - no reactions occur after the combustion chamber in this mode. The "mixed" chamber is probably the mass fraction in the combustion chamber, whilst the chamber exit is at the nozzle throat (rocket engine combustion chambers are usually considered integral with the convergent part of the nozzle), but this is an assumption. There are also a number of inconsistencies in the table in FAA (2020) such as the amount of O₂ in the entrained air, which is 100 % but should be 20.95 %.

Table 5.12 Merlin 1D modelled by CEA and HyPro

	CEA	HyPro		
	Equil	Equil	Partial	Frozen
Chamber Conditions				
Temperature [K]	3631	3646	3646	3646
Chamber Pressure [MPa]	10.72	11.01	11.01	11.00
Exit Conditions				
Exit Temperature [K]	1773	1774	1455	1389
Exit Pressure [Pa]	75 950	77 280	66 980	66 280
Performance				
Specific Impulse (vac) [s]	335.8	338.1	328.2	324.2
Thrust [kN]	968.4	988.8	960.0	962.7
Mass Flow [kg s^{-1}]	294	298	298	303
Relative Error compared to reported performance				
Specific Impulse (vac) [%]	7.99	8.70	5.54	4.24
Thrust [%]	5.95	8.18	5.04	5.33
Exit Mass Fractions				
CO	0.384	0.386	0.448	0.455
CO ₂	0.345	0.339	0.241	0.230
H	0.000 01	0.000 006	0.001 02	0.001 22
H ₂	0.0136	0.0141	0.0107	0.0108
H ₂ O	0.257	0.261	0.270	0.264
O	0.0	0.0	0.002 27	0.003 40
OH	0.000 01	0.000 01	0.0218	0.0279
O ₂	0.0	0.0	0.004 93	0.007 10

Table 5.13 Merlin 1D Vacuum modelled by CEA and HyPro

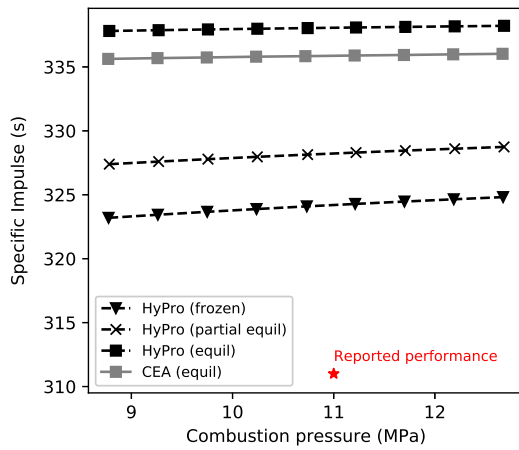
	CEA	HyPro		
	Equil	Equil	Partial	Frozen
Chamber Conditions				
Temperature [K]	3631	3646	3646	3646
Chamber Pressure [MPa]	10.72	11.01	11.01	11.00
Exit Conditions				
Exit Temperature [K]	1040	1040	734.3	688.8
Exit Pressure [Pa]	3784	3846	2914	2839
Performance				
Specific Impulse (vac) [s]	370.6	372.9	357.1	352.1
Thrust [kN]	1068	1090	1044	1045
Mass Flow [kg s^{-1}]	294	298	298	302
Relative Error				
Specific Impulse (vac) [%]	6.49	7.16	2.61	1.19
Thrust [%]	14.3	16.7	11.7	11.9
Exit Mass Fractions				
CO	0.275	0.269	0.448	0.455
CO ₂	0.516	0.512	0.241	0.230
H	0.0	0.0	0.001 02	0.001 22
H ₂	0.0214	0.0220	0.0107	0.0108
H ₂ O	0.187	0.190	0.27	0.264
O	0.0	0.0	0.002 27	0.0034
OH	0.0	0.0	0.0218	0.0279
O ₂	0.0	0.0	0.004 93	0.0071

Table 5.14 Extracts of Merlin 1D mass fractions through the engine and plume from [FAA \(2020\)](#)

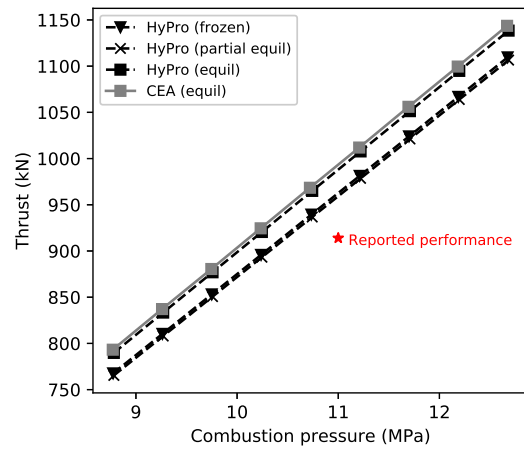
Species	Mass fraction				
	"Mixed" chamber	Chamber exit	Gas generator	Engine exit	Plume
CO	0.4114	0.2536	0.3035	0.2476	0.0
CO ₂	0.2551	0.4230	0.0625	0.4062	0.0335
H ₂ O	0.2172	0.2538	0.0918	0.2434	0.013
O ₂	0.0628	0.0367	0.0	0.0351	-
OH	0.0318	0.0064	0.0	0.0066	0.0
H ₂	0.0132	0.0086	0.00003	0.0081	0.0
C (gr)	0.0	0.0066	0.0003	0.005	0.0

Table 5.14 also shows that the plume reactions to some extent reduce the need to model rocket engines in more detail. When exposed to the entrained air in the plume, all CO and other trace species react fully (to the level of precision visible in the report), leaving only CO₂ and H₂O. It is unlikely this is the case at all altitudes, as discussed in section 2.3 and section 4.3, but this will need further investigation.

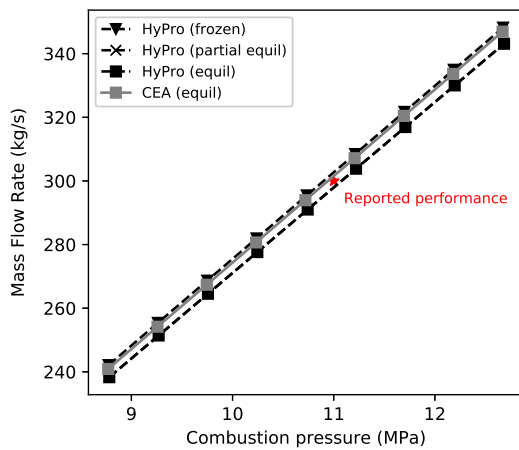
The approach taken in FAA (2020) also predicts the amount of soot 'C (gr)' produced in the engine. It is interesting to note that higher mass fractions are the result of combustion in the chamber compared to the gas generator, which runs fuel rich. This indicates that the main source of soot production areas of low O/F ratios in the combustor, rather than the gas generator, something that is discussed in Simmons (2000). The mass fraction of soot produced at the engine exit is 0.005, which is an order of magnitude greater than the 0.00042 predicted by the simple regression in fig. 4.5. This supports the previous discussion that full scale rocket engines are unable to achieve the low sooting rates that model motors can achieve.



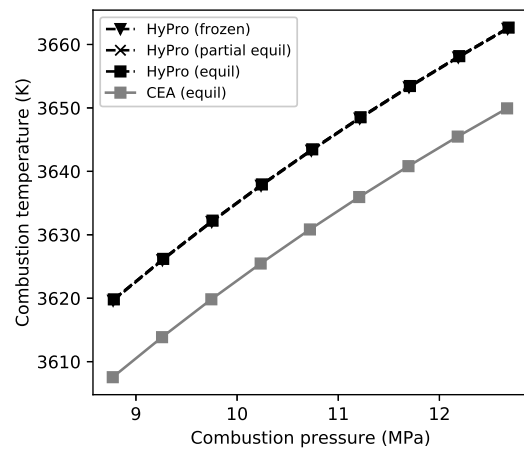
(a) Specific impulse vs combustion pressure



(b) Thrust vs combustion pressure

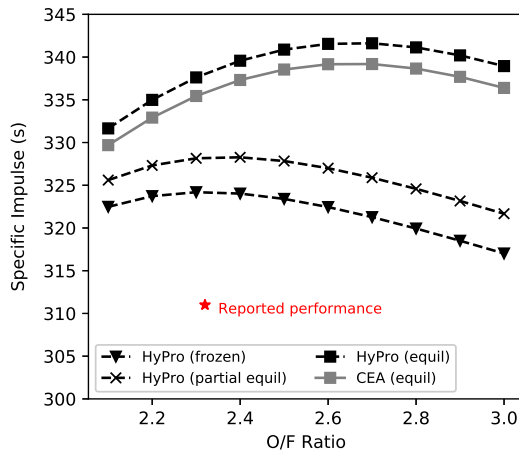


(c) Mass flow rate vs combustion pressure

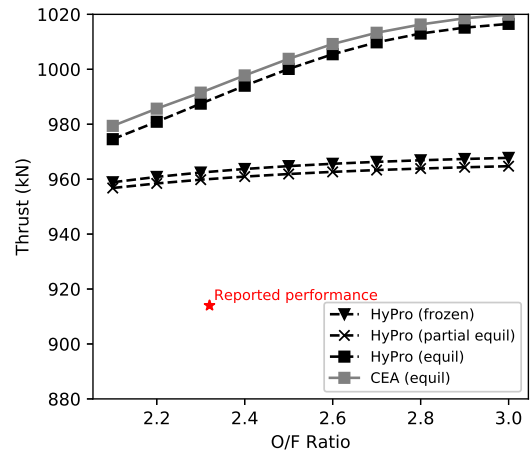


(d) Combustion temperature vs pressure

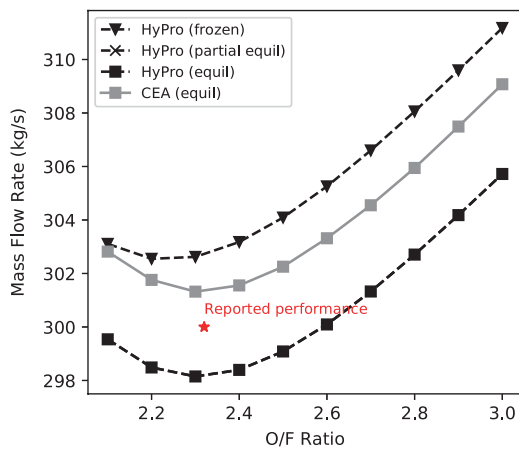
Fig. 5.10 Performance of a kerosene fuelled rocket engine based on the Merlin 1D engine across a range of combustion pressures. Results shown frozen flow, partial equilibrium (freezing at the nozzle throat) and equilibrium flow to the nozzle exit are shown.



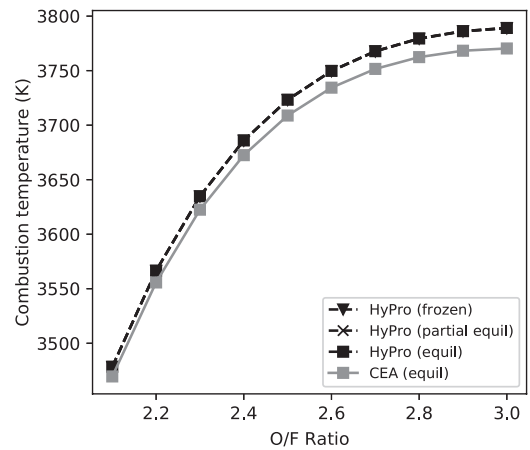
(a) Specific impulse vs O/F ratio



(b) Thrust vs O/F ratio

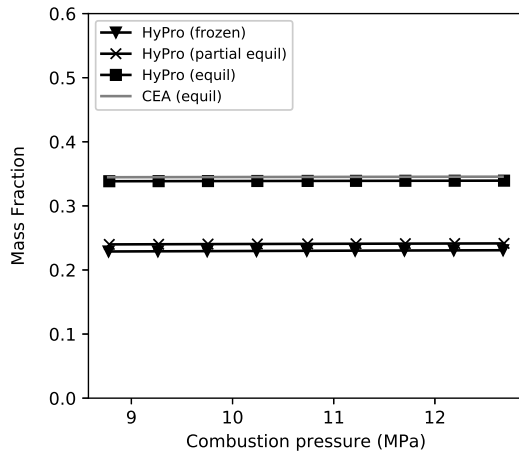


(c) Mass flow rate vs O/F ratio

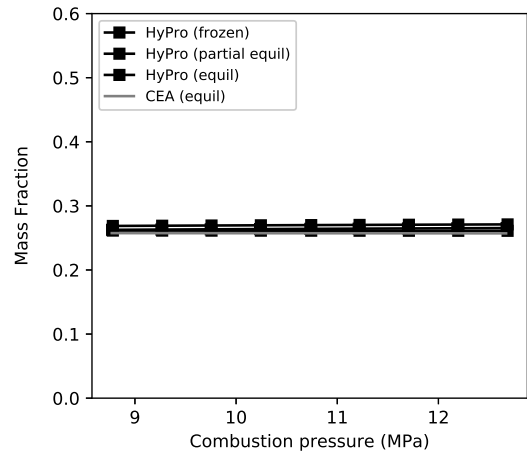


(d) Combustion temperature vs O/F ratio

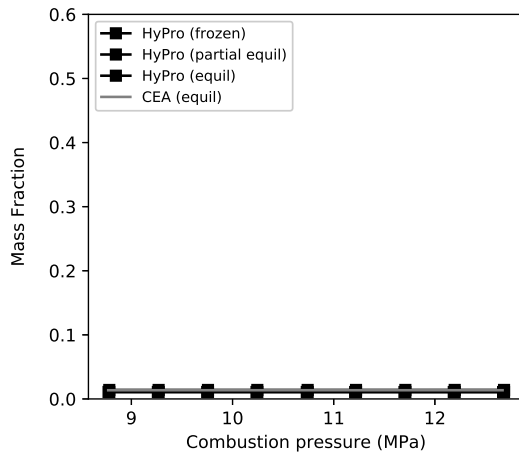
Fig. 5.11 Performance of a kerosene fuelled rocket engine based on the Merlin 1D engine across a range of mixture ratios. Results shown frozen flow, partial equilibrium (freezing at the nozzle throat) and equilibrium flow to the nozzle exit are shown.



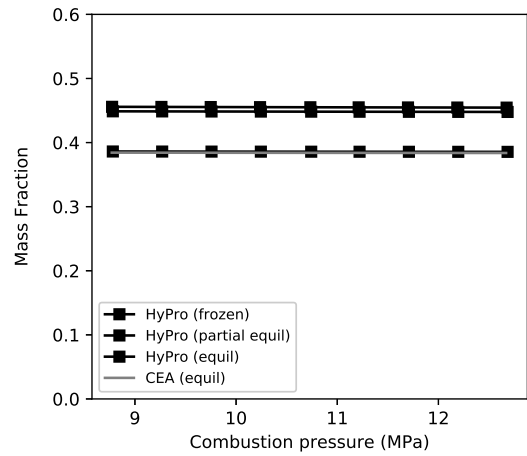
(a) CO₂



(b) H₂O

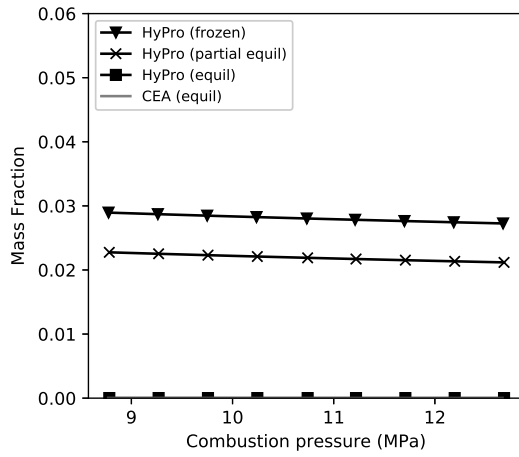


(c) H₂

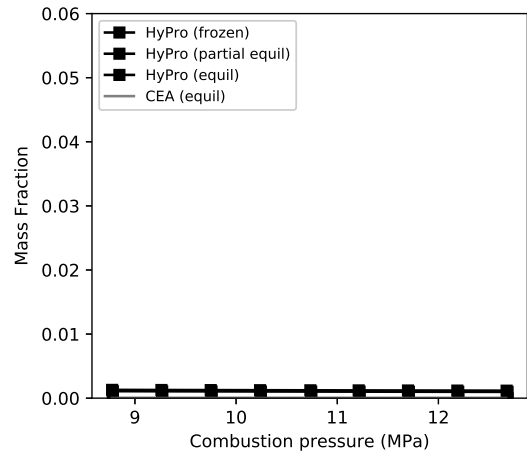


(d) CO

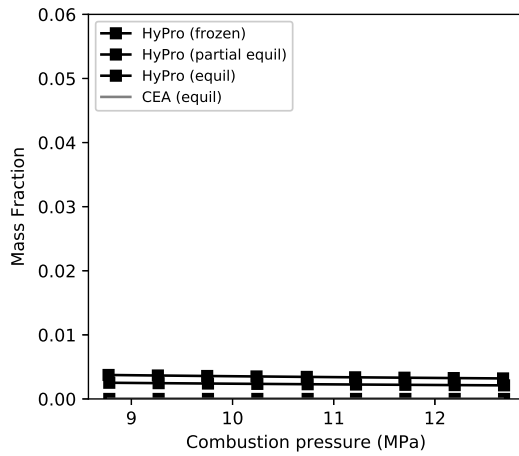
Fig. 5.12 Major species emissions of a kerosene fuelled rocket engine based on the Merlin 1D engine across a range of combustion pressures. Results shown frozen flow, partial equilibrium (freezing at the nozzle throat) and equilibrium flow to the nozzle exit are shown.



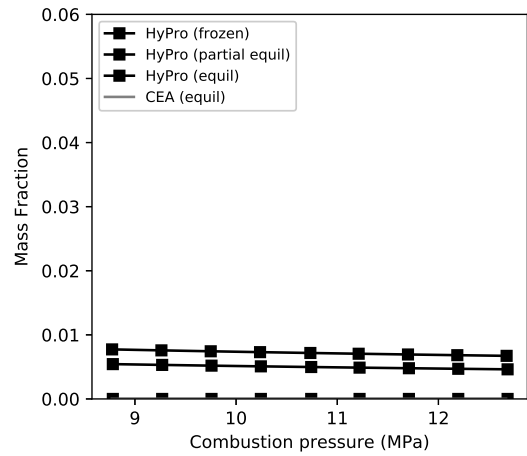
(a) OH



(b) H

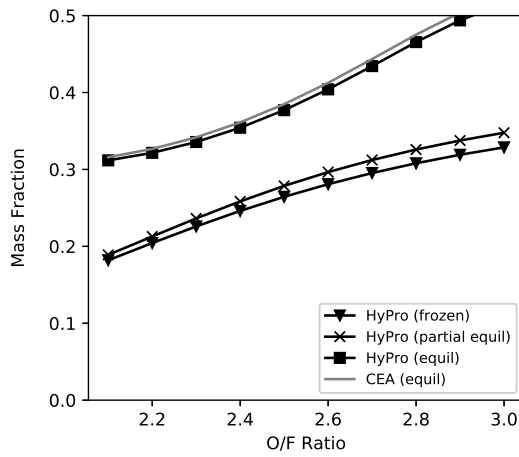


(c) O

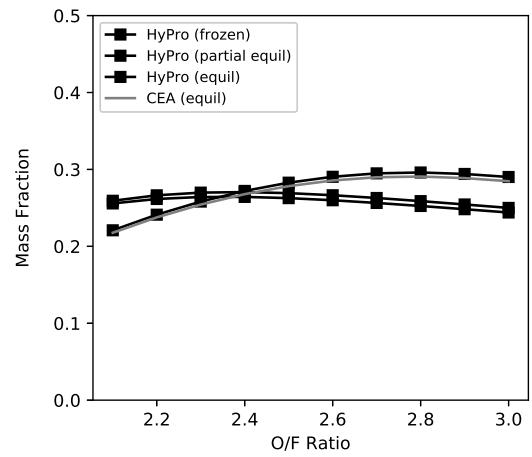


(d) O₂

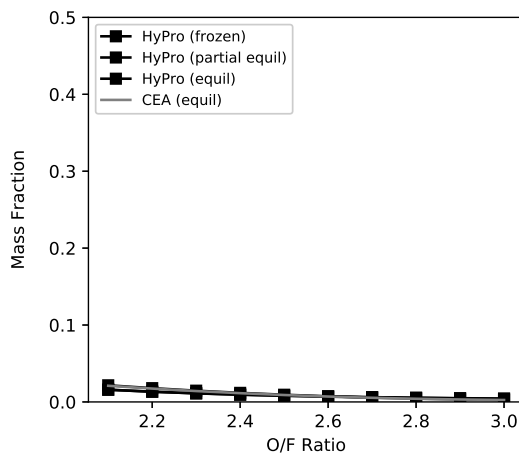
Fig. 5.13 Minor species emissions of a kerosene fuelled rocket engine based on the Merlin 1D engine across a range of combustion pressures. Results shown frozen flow, partial equilibrium (freezing at the nozzle throat) and equilibrium flow to the nozzle exit are shown.



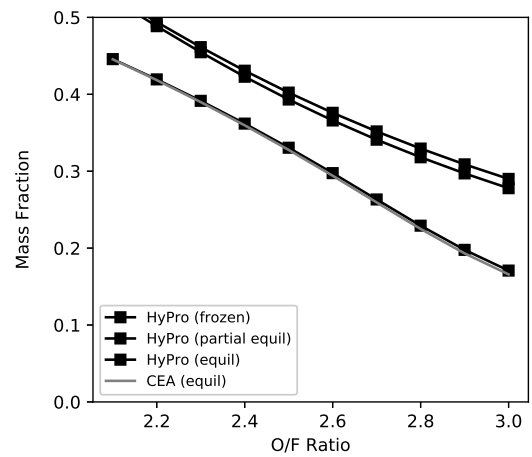
(a) CO₂



(b) H₂O

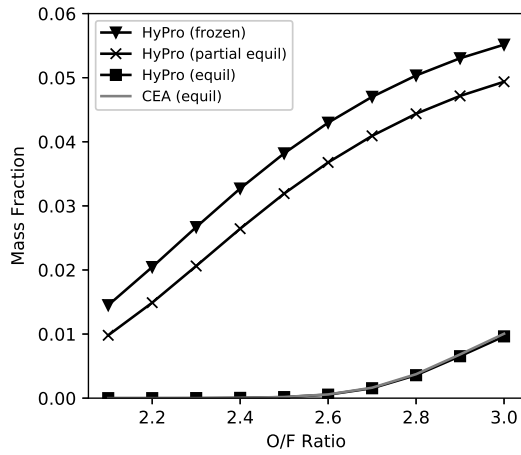


(c) H₂

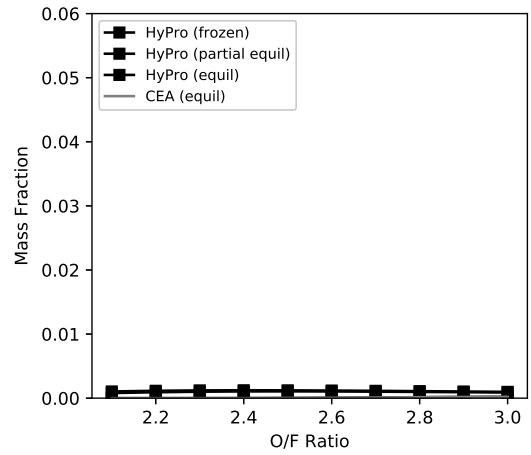


(d) CO

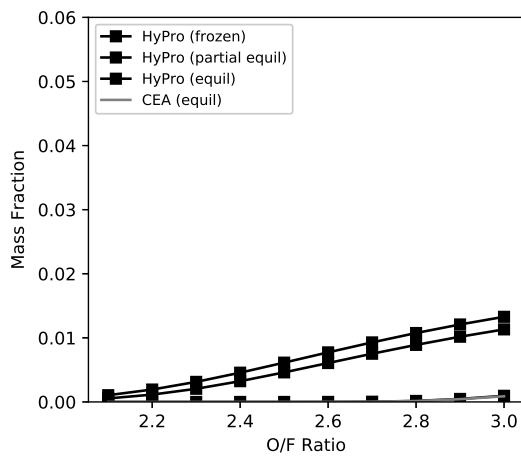
Fig. 5.14 Major species emissions of a kerosene fuelled rocket engine based on the Merlin 1D engine across a range of mixture ratios. Results shown frozen flow, partial equilibrium (freezing at the nozzle throat) and equilibrium flow to the nozzle exit are shown.



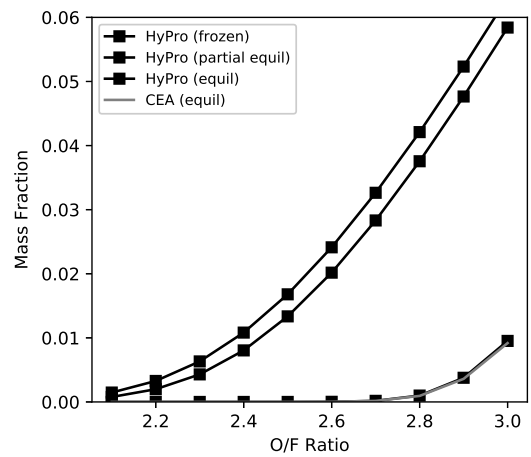
(a) OH



(b) H



(c) O



(d) O₂

Fig. 5.15 Minor species emissions of a kerosene fuelled rocket engine based on the Merlin 1D engine across a range of mixture ratios. Results shown frozen flow, partial equilibrium (freezing at the nozzle throat) and equilibrium flow to the nozzle exit are shown.

5.2.6 Raptor

The final comparison case is the SpaceX Raptor engine, intended for use on the Super Heavy first stage and Starship upper stage and spacecraft. This propulsion system uses CH_4 for its fuel and LOX as its oxidiser. It is also the first full-flow staged combustion rocket engine to fly (on the starhopper vehicle in July 2019) and represents the state-of-the-art in rocket technology.

The preliminary environment assessment (NASA, 2019) contains some key parameters of the Raptor engine's design, including the chamber pressure, oxidiser-fuel ratio and throat and exit areas, shown in table 5.15. These are used as the basis for the engine model in HyPro. The results for the engine parameters in table 5.15 are shown in table 5.16. The engine parameters here are the most certain of those analysed in this thesis, as they are explicitly included in the preliminary environment assessment. The results show relatively close agreement between the equilibrium modes of CEA and HyPro, with the differences likely explained by differences between the models discussed in section 5.2.4 and section 5.2.5.

Table 5.15 Raptor propulsion specification

Chamber pressure P_c , MPa	25.3
Mixture ratio O/F	3.6
Throat area A^* , m^2	0.03856
Exit area A_e , m^2	1.329

As with the other rocket engines simulated in this thesis, the results across a range of combustion pressures and mixture ratios are modelled. Figures 5.16 and 5.17 show the performance curves across a range of combustion pressures between 15 MPa and 30 MPa, and mixture ratios between 2.5 and 4.5. The combustion pressure has a larger impact on the thrust of the engine, and a minor impact on the specific impulse, whilst the inverse is true of the mixture ratio. The Raptor engine has been designed with an O/F ratio of 3.6, the optimum specific impulse for the equilibrium chemistry curves.

Additionally, the influence of these combustion pressures and mixture ratios are shown in figs. 5.18 to 5.21. As with the other rocket engines in this chapter, the combustion pressure has a mostly minor impact on the emissions produced, at least with the modelling approach used here. Figures 5.20a, 5.20b and 5.20d show an interesting pattern in both the CEA

Table 5.16 Raptor modelled by CEA and HyPro

	CEA	HyPro		
	Equil	Equil	Partial	Frozen
Chamber Conditions				
Temperature [K]	3736	3784	3784	3783
Chamber Pressure [MPa]	25.28	25.28	25.30	25.30
Exit Conditions				
Exit Temperature [K]	2032	2100	1387	1317
Exit Pressure [Pa]	81 160	81 830	60 920	60 010
Performance				
Specific Impulse (vac) [s]	367.6	371.7	352.8	348.4
Thrust [kN]	1927	1920	1822	1825
Mass Flow [kg s^{-1}]	534	534	526	526
Relative Error compared to reported performance				
Specific Impulse (vac) [%]	5.15	6.33	0.9	-0.34
Thrust [%]	7.02	6.62	1.18	1.36
Exit Mass Fractions				
CO	0.0969	0.0985	0.189	0.199
CO ₂	0.444	0.442	0.299	0.284
H	0.000 02	0.000 03	0.000 673	0.000 767
H ₂	0.003 71	0.003 61	0.005 37	0.005 71
H ₂ O	0.455	0.455	0.409	0.402
O	0.0	0.000 009	0.006 47	0.007 81
OH	0.000 540	0.000 847	0.0476	0.0542
O ₂	0.000 04	0.000 113	0.0422	0.0467

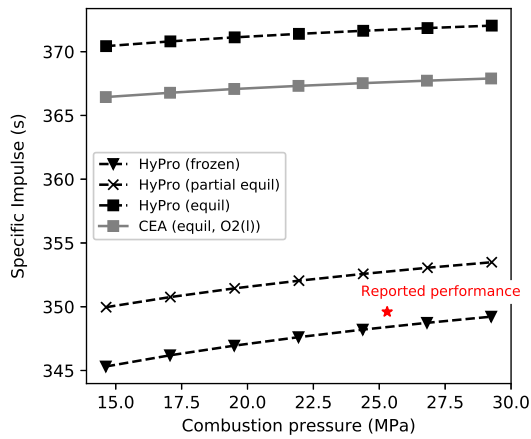
and HyPro results, whereby the mass fraction of CO₂ appears to decreased in equilibrium mode from O/F 2.5 - 3.0, and then increases, whilst the CO decreases across the range (as expected - there is more oxygen able to completely oxidise the carbon).

In the case of the Raptor engine, there are published exit mass fraction at the end of the combustor modelled using the Viscous Interaction Performance Evaluation Routine (VIPER) tool. Table 5.17 shows the nozzle exit mass fractions from NASA (2019) compared to the nozzle exit mass fractions from HyPro, in all three modes.

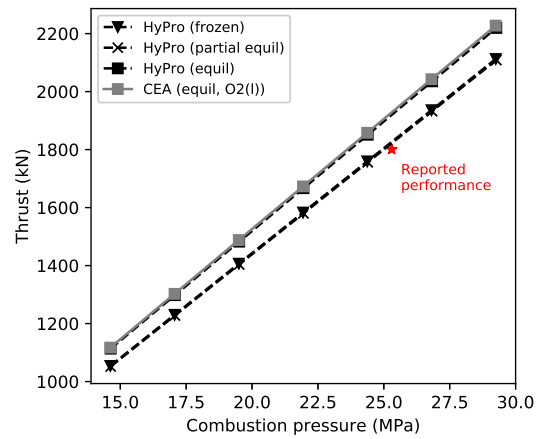
The mass fractions of major species (CO, CO₂ and H₂O) are shown in table 5.17. The assumption in this thesis has been that the exit mass fractions of an engine can be bounded by the equilibrium and frozen simulation cases, which is supported by this comparison. This does compare a model vs. a model, and so it is possible that a real rocket engine performs differently. The vast majority of the emissions are CO₂ and H₂O, with about 12% CO produced. Note that there is very little (less than 1e-5) CH₄ remaining in any of the HyPro simulations. Since this is true of the frozen case, all of the CH₄ must be reacted in the combustion chamber. VIPER also simulates the cooling flow, and has empirical corrections for phenomenon such as injection, either of which may explain this remaining fuel.

Table 5.17 Raptor combustion chamber exit mass fractions from NASA (2019) compared to HyPro

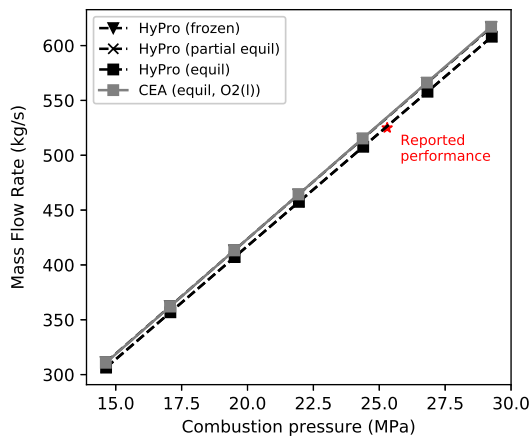
Species	Mass Fractions			
	VIPER	Frozen	Partial	Equil
CO ₂	0.400	0.284	0.299	0.442
H ₂ O	0.413	0.402	0.409	0.455
CO	0.121	0.199	0.189	0.0985
O ₂	0.0548	0.0467	0.0422	0.000 113
H ₂	0.007 46	0.005 71	0.005 37	0.003 61
OH	0.003 59	0.0542	0.0476	0.000 847
O	0.000 536	0.007 81	0.006 47	<0.000 01
CH ₄	0.000 072 8	<0.000 01	<0.000 01	<0.000 01
H	0.000 052 1	0.000 767	0.000 673	0.000 029 9



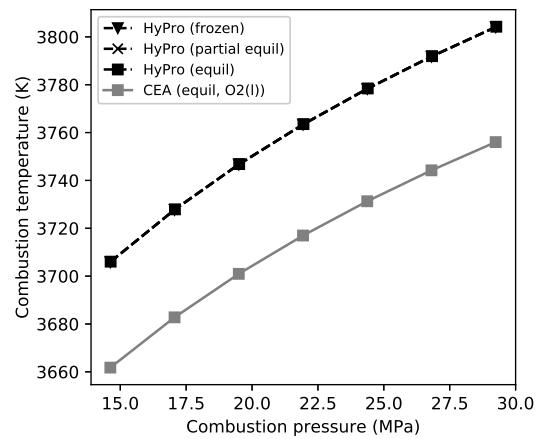
(a) Specific impulse vs combustion pressure



(b) Thrust vs combustion pressure

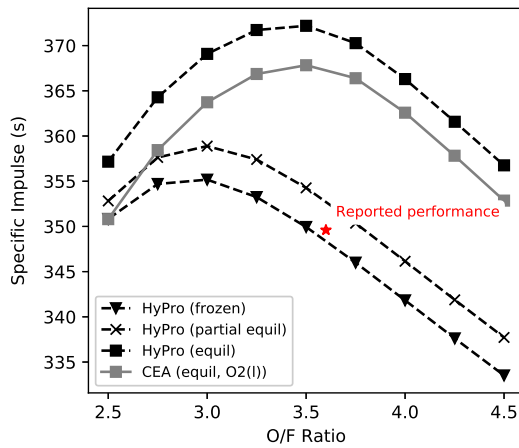


(c) Mass flow rate vs combustion pressure

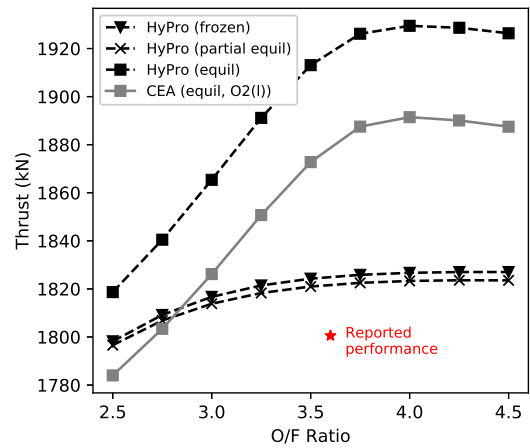


(d) Combustion temperature vs pressure

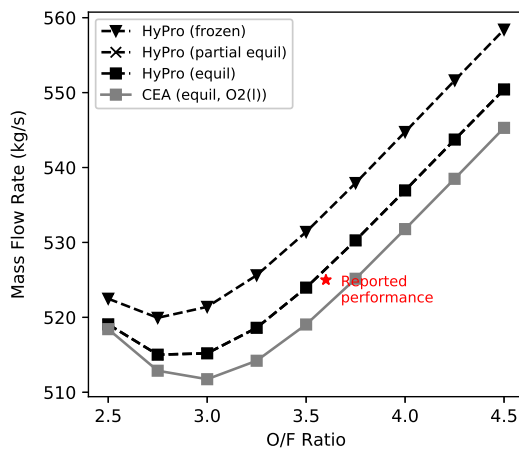
Fig. 5.16 Performance of a methane fuelled rocket engine based on the Raptor engine across a range of combustion pressures. Results shown frozen flow, partial equilibrium (freezing at the nozzle throat) and equilibrium flow to the nozzle exit are shown. Reported performance from NASA (2019)



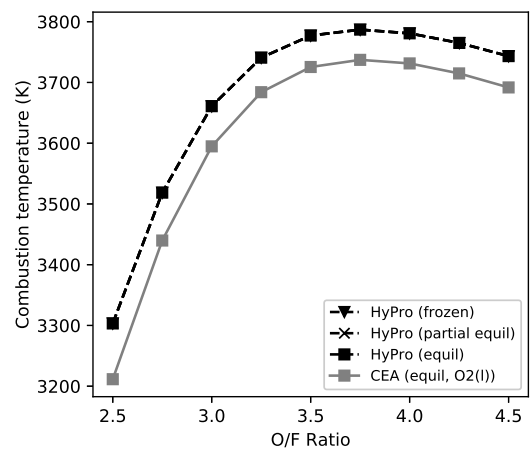
(a) Specific impulse vs O/F ratio



(b) Thrust vs O/F ratio



(c) Mass flow rate vs O/F ratio



(d) Combustion temperature vs O/F ratio

Fig. 5.17 Performance of a methane fuelled rocket engine based on the Raptor engine across a range of mixture ratios. Results shown frozen flow, partial equilibrium (freezing at the nozzle throat) and equilibrium flow to the nozzle exit are shown. Reported performance from [NASA \(2019\)](#)

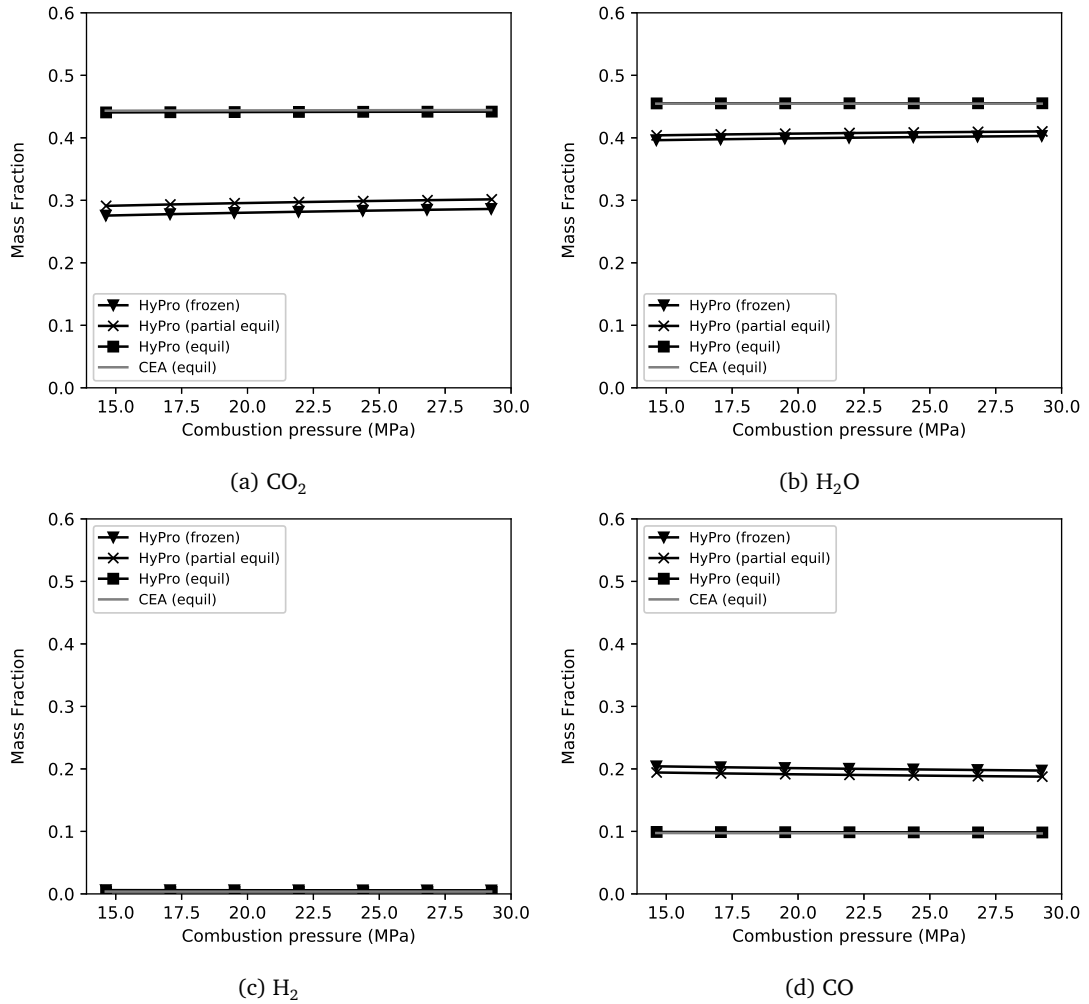


Fig. 5.18 Major species emissions of a methane fuelled rocket engine based on the Raptor engine across a range of combustion pressures. Results shown frozen flow, partial equilibrium (freezing at the nozzle throat) and equilibrium flow to the nozzle exit are shown.

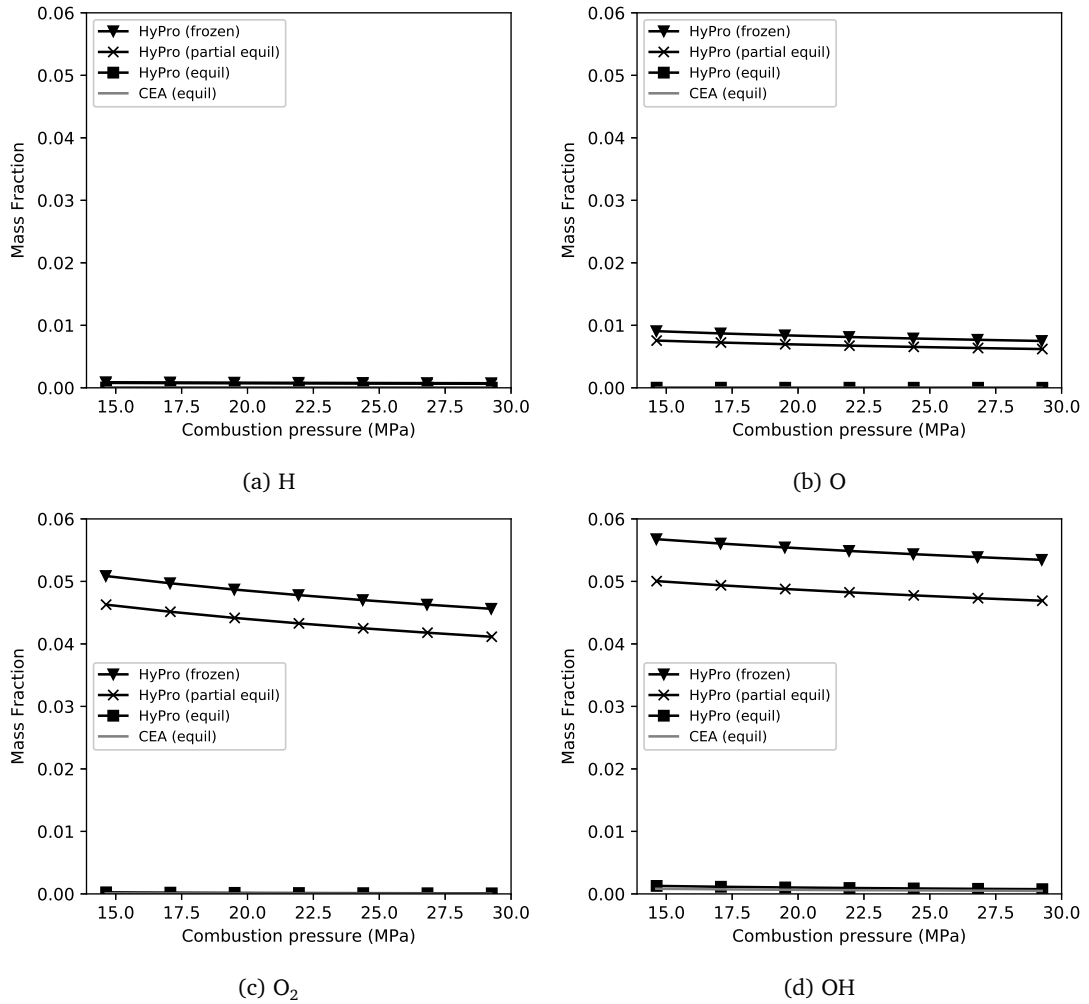
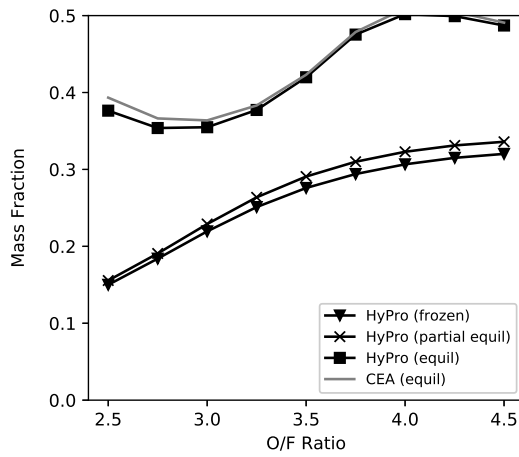
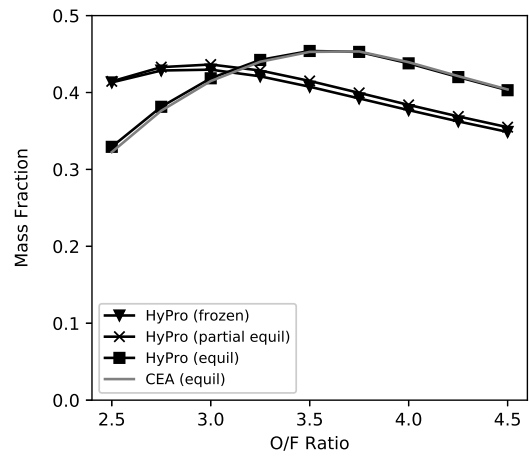


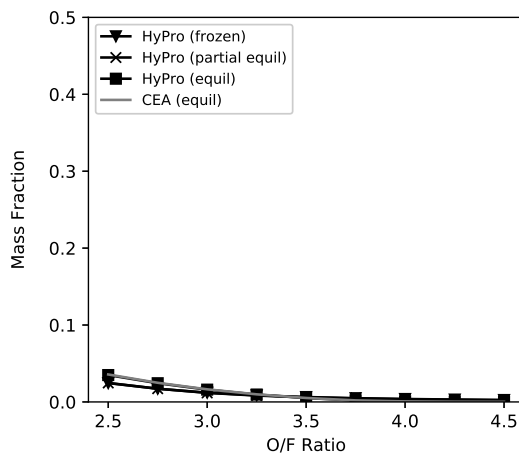
Fig. 5.19 Minor species emissions of a methane fuelled rocket engine based on the Raptor engine across a range of combustion pressures. Results shown frozen flow, partial equilibrium (freezing at the nozzle throat) and equilibrium flow to the nozzle exit are shown.



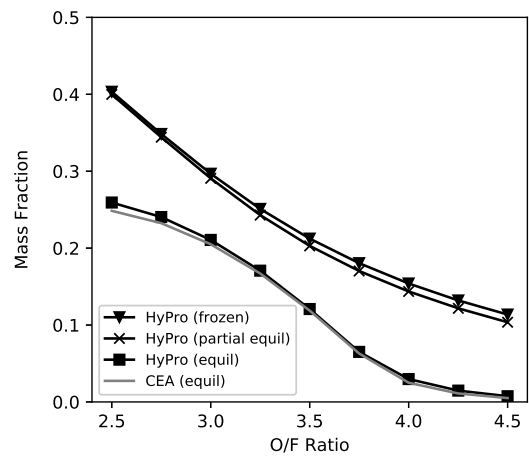
(a) CO₂



(b) H₂O



(c) H₂



(d) CO

Fig. 5.20 Major species emissions of a methane fuelled rocket engine based on the Raptor engine across a range of mixture ratios. Results shown frozen flow, partial equilibrium (freezing at the nozzle throat) and equilibrium flow to the nozzle exit are shown.

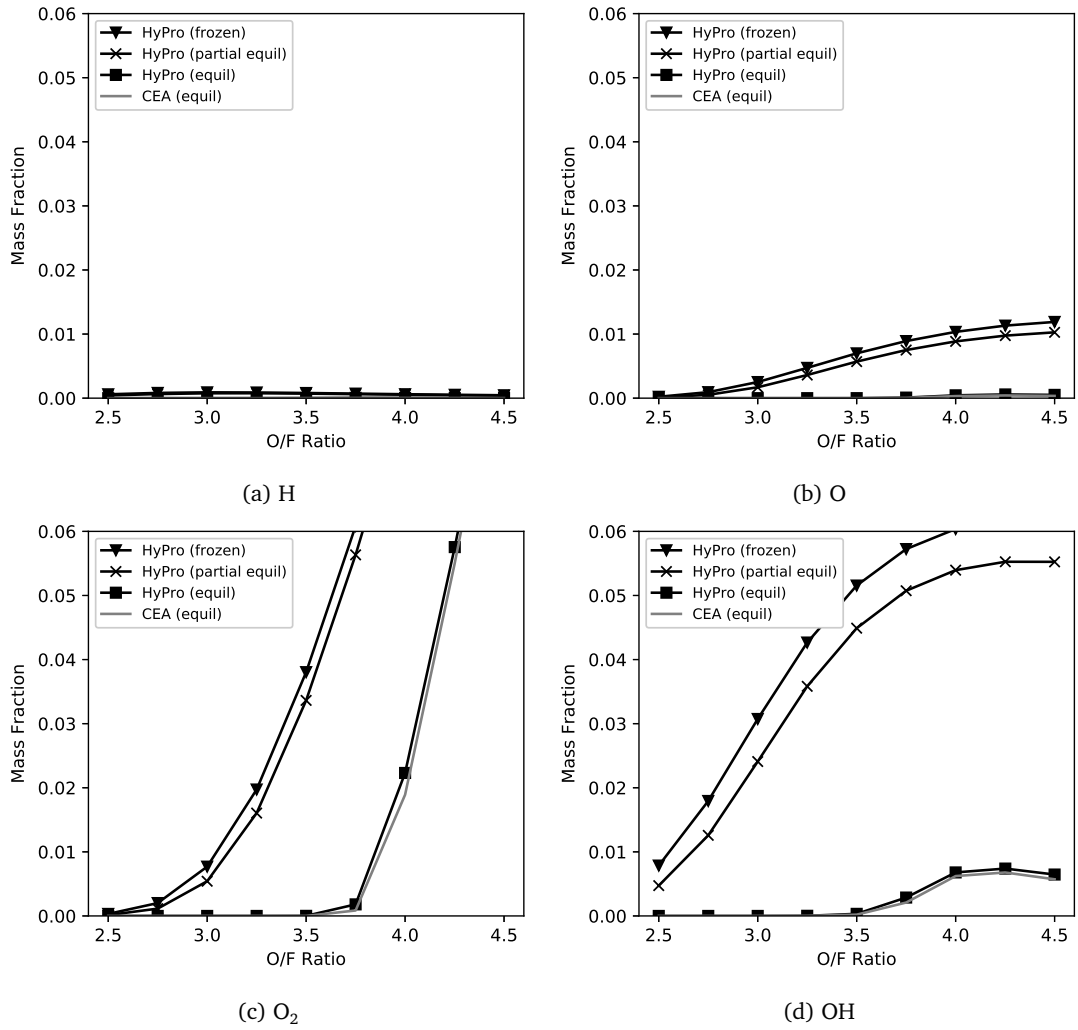


Fig. 5.21 Minor species emissions of a methane fuelled rocket engine based on the Raptor engine across a range of mixture ratios. Results shown frozen flow, partial equilibrium (freezing at the nozzle throat) and equilibrium flow to the nozzle exit are shown.

5.3 Rocket based combined-cycle

Although currently only the subject of development activities, airbreathing powered SSTO vehicles are an interesting concept for space access, and cannot be ignored when fully comparing the range of future space access vehicles that might be used over the next decades. Here, models of the propulsion system are developed for a RBCC-powered SSTO spaceplane based on the vehicle *Hyperion* conceptualised by [Olds et al. \(1999\)](#) using preliminary design tools.

This concept used an ejector scramjet RBCC, which combines an ejector (air-augmented rocket), a ramjet, a scramjet and a pure rocket into a single engine flowpath. The engine is assumed to use liquid hydrogen as a fuel, and the vehicle carries liquid oxygen for operating in ejector and rocket modes. A quasi-one-dimensional combined cycle design tool called SCCREAM was used to design *Hyperion*'s engine, which was in some ways very similar to HyPro ([Olds and Bradford, 2001](#)). [Mogavero \(2016\)](#); [Mogavero and Brown \(2018\)](#) used the *Hyperion* engine as one of the test cases to compare HyPro against, but were unable to match exactly the results of SCCREAM, stating that it wasn't possible to conclude that HyPro performed worse than SCCREAM. A series of discrepancies made it difficult to identify why the results from HyPro and SCCREAM diverge, particularly relating to the method of accounting for thrust, and the exact areas used in the engines. HyPro also performed well when compared against a series of additional test cases with more robust data. It should be noted that the methods used in SCCREAM ([Bradford and Olds, 1999](#); [Olds and Bradford, 2001](#)) may be of a higher fidelity than the models of HyPro, using the method of influences ([Shapiro, 1953](#)) for the combustor calculations (i.e. integrating down the length of the combustor rather than the stepped 1D approach of HyPro). However, it remains one of the most comprehensive examples of an RBCC in open literature, has the benefit of aerodynamics models appropriate for use in trajectory design, and is likely to be able show the main features of airbreathing powered vehicles.

Hyperion is not a real engine, and has been designed largely as an exercise to develop and apply conceptual design tools. Therefore the modelled performance does not necessarily represent the performance that could be achieved from a real ejector-scramjet engine. Analysis with higher fidelity methods such as CFD have never been performed on the full

engine, and so the predicted performance from any of the tools has a great deal of uncertainty attached. In the context of this thesis, which is to examine how key design decisions and future developments in the launch market may affect the environmental impact, it is still useful to compare the key differences between a vehicle like Hyperion and traditional launchers, in particular, the effect of an air-breathing engine and the lifting body design. Some insight may be gained on the class of SSTO vehicles that may be developed, such as the Reaction Engines Skylon vehicle.

Here, the model of Mogavero (2016) is extended and used to establish one bound of the possible emissions from an engine like Hyperion. This assumes complete combustion for the combustor, where nitrogen species are not included in the combustion reactions, and the performance is tuned by a set of efficiency factors (tuned to the original model of SCCREAM). The original model is modified by including a specific scramjet mode, this exchanges the adapting throat inlet used for the ramjet mode with a fixed scramjet inlet, as described in section 5.1.3.

Figure 5.22 and fig. 5.23 show the modelled performance in ejector and ramjet modes, compared to the simulations used by SCCREAM (Olds and Bradford, 2001). Figure 5.24 shows the estimate performance for the scramjet mode against SCCREAM, as well as the two reference engine flowpaths that Olds and Bradford (2001) compares SCCREAM against.

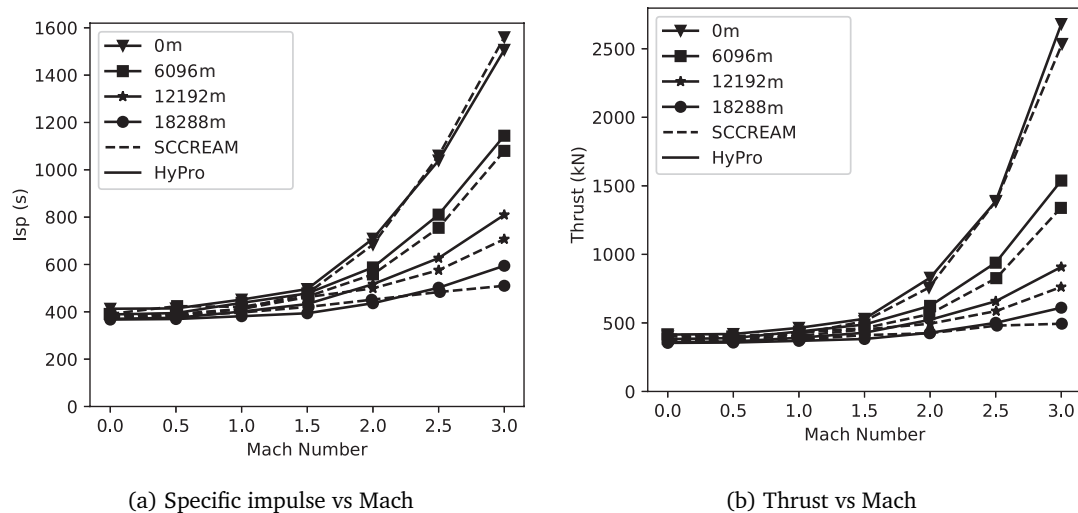


Fig. 5.22 Performance of the Hyperion ejector mode at a series of altitudes (indicated in the legend as altitude in m) modelled in HyPro and compared to Olds and Bradford (2001)

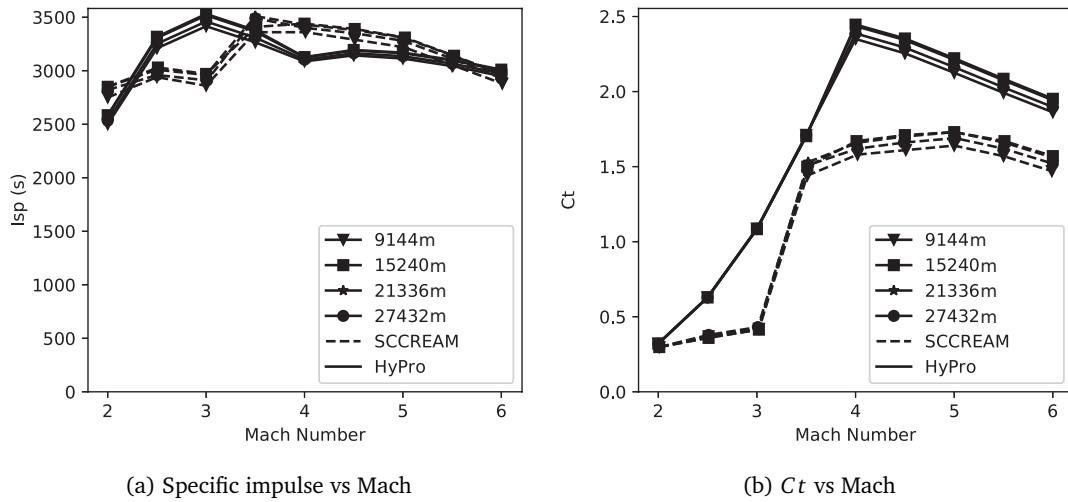


Fig. 5.23 Performance of the Hyperion ramjet mode at a series of altitudes (indicated in the legend as altitude in m) modelled in HyPro and compared to [Olds and Bradford \(2001\)](#)

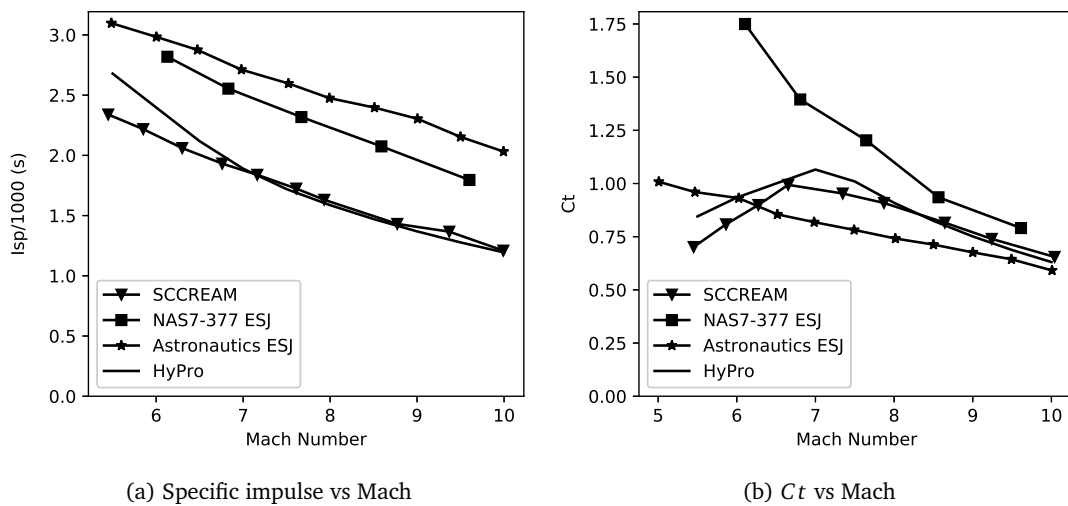


Fig. 5.24 Performance of the Hyperion scramjet mode modelled in HyPro and compared to [Olds and Bradford \(2001\)](#)

For use in the trajectory optimisation software the performance of engine was mapped using a curve fit function. Calling HyPro with TROPICO is not computationally efficient if the purpose of trajectory optimisation is on trajectory design or mission performance studies - surrogate methods like curvefits are several orders of magnitude quicker. However, HyPro was designed for use in configurational optimisation, and so performance can be tuned for quick calculations, usually by reducing significantly the numbers of species in its thermodynamic model. A 3-dimensional dataset of engine performance for ejector, ramjet and scramjet modes was generated, as a function of altitude and Mach number. HyPro requires the incoming atmospheric condition, but as altitude is one of the state parameters

used in TROPICO, this parameter was used to compile the database. The specific impulse, thrust and mass flow rate datasets were then fit using the curvefit utility in MATLAB, as shown in figs. 5.25 to 5.27 . The outputs of the model in TROPICO are thrust and mass flow rate, so the specific impulse model is only used to understand the performance. Of all three modes, ejector (fig. 5.25a), ramjet (fig. 5.26a) and scramjet (fig. 5.27a), the ramjet has the highest peak specific impulse at around Mach 3. These contour plots also show where the dynamic pressure exceeds 120 kPa as red dots - this is to provide some idea of the part of the engine regime where a dynamic pressure constraint applied in the trajectory optimise will limit the use of the engine.

The mass flow rate of the each major species in the engine was also fit to a polynomial. Unlike rocket engines where the emission indices are a function of the engine only (at least by the nozzle exit), the flight condition has an impact for airbreathing engines, and so the emission indices needs to be tabulated for each engine condition. Figure 5.25 shows the resultant curvefit plotted as a contour for the complete combustion case for the Hyperion ejector. Figure 5.25c shows the total injected mass flow of both the primary and secondary injectors, whilst fig. 5.25d shows the emissions of H₂O at the exit of the engine. This same process is also performed for the ramjet mode in fig. 5.26 and scramjet mode in fig. 5.27. Errors in the surrogates are evaluated when the surrogate is generated, and are usually minimal compared to other modelling errors. One approach to minimise the effect of any errors is to re-generate the trajectory of the optimal control law using a high tolerance adaptive integrator, and optionally include data from HyPro directly.

An additional challenge when considering combined-cycle propulsion models is how the transitions between modes are handled. During detailed design and evaluation, combined cycle-engines need to be simulated across the entire flight regime, including the transitions. The process to change engine mode depends on the transition being considered, but in many cases (e.g. ramjet to scramjet) a mechanical change in the flowpath is needed. This level of detail is beyond what is can be modelled by a tool like HyPro, but can be accounted for using mid-fidelity models such as that of [Torrez et al. \(2013b\)](#), which explored the ram-scram transition in dual-mode scramjets. This would need to be extended to the other transition modes as well.

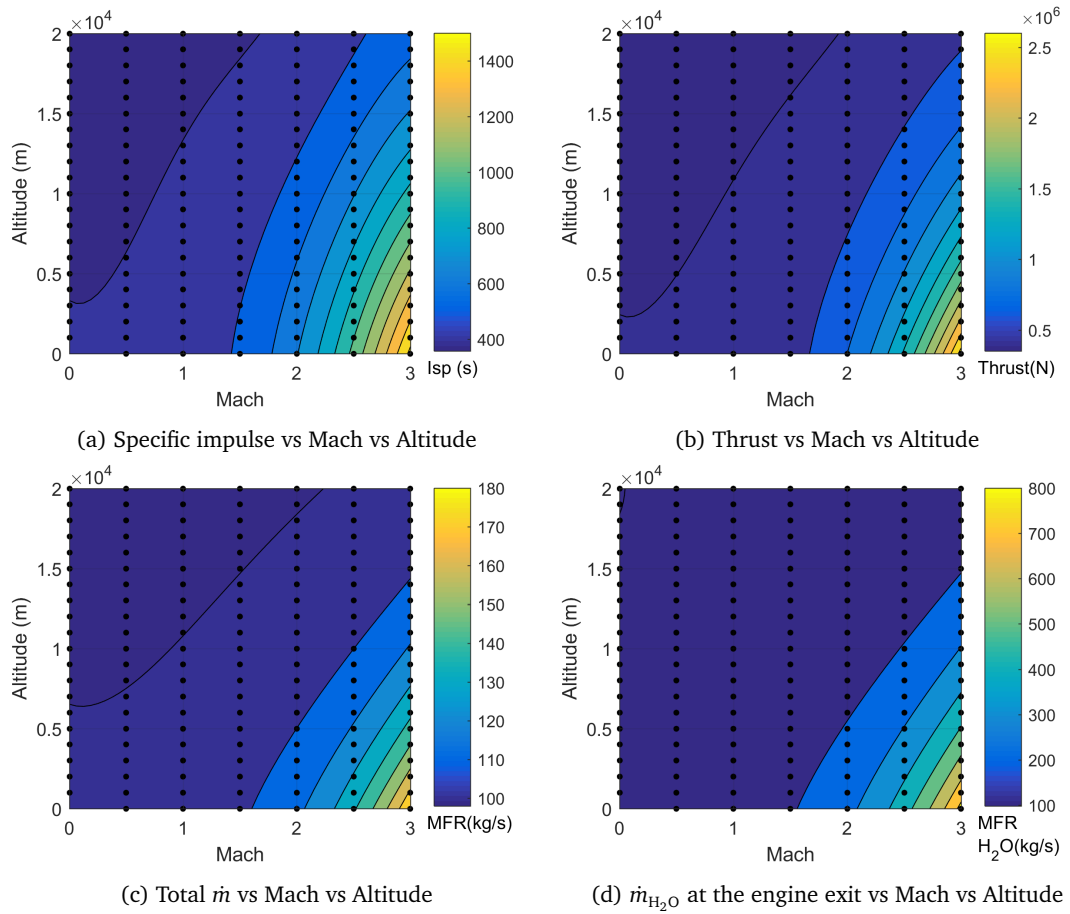


Fig. 5.25 Curve fit contour plots for the Hyperion ejector

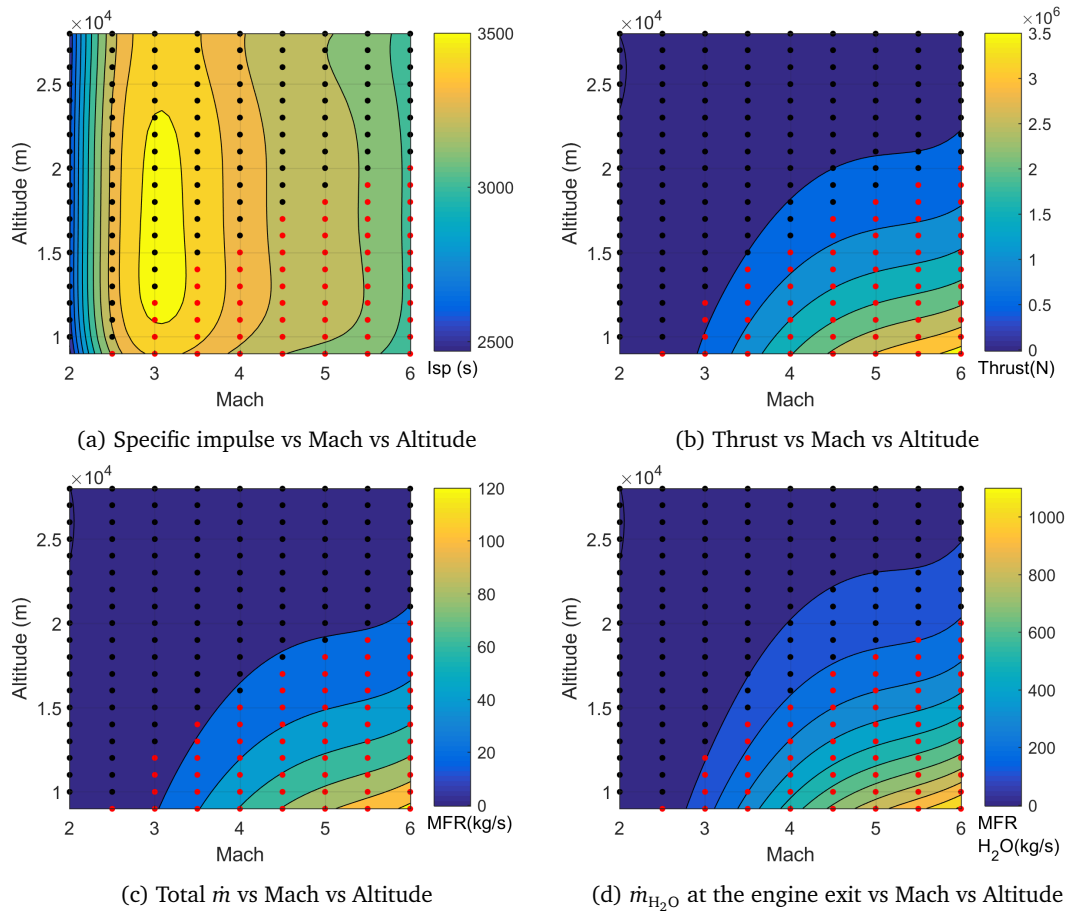


Fig. 5.26 Curve fit contour plots for the Hyperion ramjet mode. Point data are the points evaluated with HyPro. Red points indicate where dynamic pressure, $q > 120$ kPa.

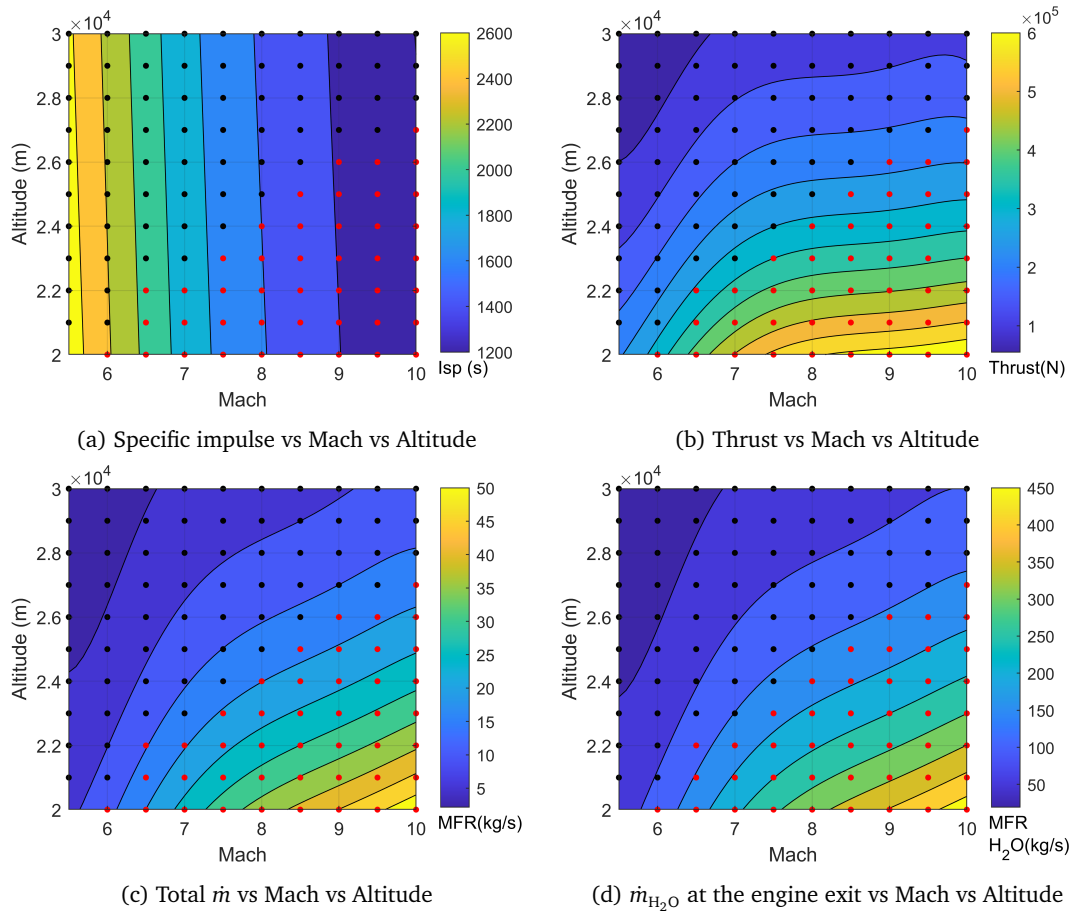


Fig. 5.27 Curve fit contour plots for the Hyperion scramjet mode. Point data are the points evaluated with HyPro. Red points indicate where dynamic pressure, $q > 120$ kPa.

In [Olds et al. \(1999\)](#), transitions were handled slightly differently - in the transition regions (e.g. Mach 2.5 to 3.0 for the transition from ejector to ramjet), the ejector engine mode was linearly throttled down and the ramjet throttled up. This may not be realistic as it treats the performance of each engine modes independently, but smooths the thrust profile. This may have been required for the trajectory optimisation approach - local optimisers are not as effective where there are discontinuities in models.

Here, the approach taken here is to model the four engine modes independently, and switch between modes at the end of a flight phase. This does mean there is a step change in performance, but the approach to trajectory optimisation splits the trajectory into discrete phases, which enables discontinuities like this be included. This shall be discussed further in section [6.6](#).

5.4 Summary

As shown in the previous sections, HyPro predicts the ideal level of performance for a range of rocket engines. It consistently overpredicts the I_{sp} of rocket engines it models using the equilibrium chemistry assumption compared to CEA2 by a few percent, but as shown in section [5.2.4](#) this is most likely because HyPro does not account for the latent heat of vaporisation required for liquid propellants to vaporise. Both HyPro and CEA2 overpredict the performance of RP-1 fuelled engines by a significant amount. This might indicate that inefficiencies in the combustion of RP-1 cannot be modelled by the assumptions of equilibrium combustion or frozen/equilibrium nozzle flow, but it is likely that the lack of certainty in the associated engine design contributes to this issue.

The similarity of the exit composition between HyPro and CEA for nozzles with shifting equilibrium, the only common mode for a finite area combustion shows that even if there is a difference in calculated performance, that the emissions produced by HyPro are reasonable without adding to the complexity of the simulation. The inclusion of modes to calculate performance using frozen or partially frozen flow assumptions (for a finite area combustor) provides an opportunity to better understand what the performance will be, and especially how much chemistry in the divergent part of the nozzle affects the composition of the flow at the exit plane. For rocket engines, the key parameter that drives the production

of major species that constitute the exhaust flow is the mixture ratio in the engine. This ratio sets the amount of unreacted or incomplete species (CO in hydrocarbon fuels and H or H₂ in hydrogen fuels) that are generated in the combustion chamber, and the frozen and equilibrium nozzle assumptions bound how much of these are further converted into CO₂ in the nozzle.

Improvements in the ability of HyPro to predict rocket engine performance could be made by including additional physics, such including an enthalpy loss term for latent heat of vaporisation or a droplet model or by adding correction factors. The simplest of these would be a correction factor to account for possible nozzle losses, as shown in section 5.2.2. A different approach could be taken as in [Way and Olds \(1999\)](#), where a large number of known rocket engines are modelled, and the average difference between real and simulated performance is applied as a performance correction. Additionally, comparisons of HyPro results with higher fidelity models in sections 5.2.5 and 5.2.6 show that further detail in propulsion models needs to be balanced with the inclusion of plume models, to quantify how minor species will evolve after exiting the nozzle. This may not be feasible during conceptual design, as the plume should be modelled across the various flight conditions.

6 | TRAJECTORY AND EMISSION DETERMINATION

This chapter introduces the launch vehicles considered within this thesis, including the assumptions and models used in the simulations. It presents the optimal trajectories for each vehicle, found using the approach introduced in chapter 3 and once coupled with the propulsion models discussed in chapter 5, the emissions profiles that have been generated. The selected test cases cover a range of existing and conceptual vehicles with payload capacities from 150 kg to 100 000 kg, which enables a comparison between the biggest design trades of propellant, propulsion systems and vehicle sizing. Table 6.1 shows a table of the launch vehicles analysed, with links to their appropriate sections.

Two are chosen as points of the comparison against existing vehicles (the medium kerosene and hydrogen fuelled rockets), whilst the others been selected based on the direction of travel of in-development and future configurations. This provides a snapshot of the environmental effects of future transatmospheric flight operations.

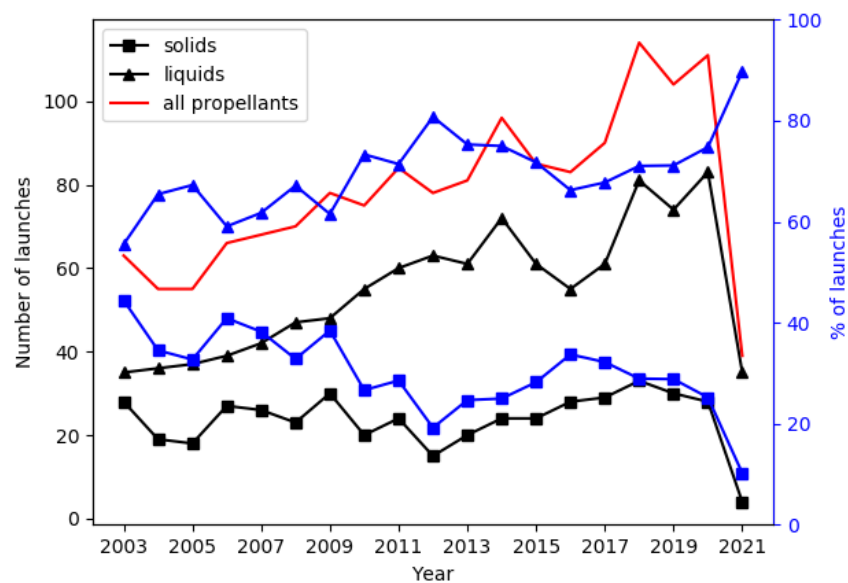
Table 6.1 The classes and propellants of vehicles

Class	Propellant	Example vehicles	Section
Medium Launch	LOX/Kerosene	Falcon 9, Atlas V	Section 6.1
Medium Launch	LOX/LH ₂	Delta IV	Section 6.2
Heavy Lift	LOX/Methane	Super Heavy	Section 6.3
Small Launcher	LOX/Kerosene	Electron	Section 6.4
Airlaunch TSTO spaceplane	LOX/Kerosene	Orbital Access 500R	Section 6.5
RBCC Spaceplane	LOX/LH ₂	Hyperion	Section 6.6

There is a general trend in the market of reducing utilization of solid rockets, dropping from 40 % of launches to less than 30 % since 2005, shown in fig. 6.1. Part of this is the

domination of SpaceX in the commercial launch service market, as well as the development of their own Starlink satellite constellations. Previous research (Brady et al., 1997; Ross and Sheaffer, 2014) clearly shows that solid rocket motors are significantly worse (several orders of magnitude) for the environment than most liquid engines, with the exception of hypergolic propellant vehicles. If environmental impacts are included as a criteria within the system design process, the first step would be to immediately discard their use. The differences between liquid propellants may be more subtle, and investigating these is the objective of this thesis.

Fig. 6.1 Share of solid and liquid launch attempts 2003 - present. Launch vehicles are classed as 'solid' if any part of their first two-stages, including boosters, are solid rocket motors, but doesn't include kick-stages or apogee motors. Launch history data from Kyle (2019).



6.1 Medium lift rocket - kerosene

Kerosene has been one of the main fuels used in launch vehicles since the dawn of the space age. Goddard's first liquid rocket used gasoline, a hydrocarbon similar in makeup to kerosene. Today, kerosene is the workhorse fuel for medium lift rockets. Although it has a lower specific impulse than liquid hydrogen, its lower cost, non-cryogenic storage and higher density make it a highly attractive propellant choice. Table 6.2 shows a selection of current medium lift kerosene fuelled launch vehicles.

Table 6.2 Kerosene fuelled vertical launch vehicles

Family	Configurations	Mass to LEO t ^a	Mass to GTO t
Atlas V ^b	401	9.8	4.75
	411	12.03	5.85
	421	13.60	6.89
	431	15.26	7.70
	501	8.21	3.78
	521	13.50	6.48
	531	15.53	7.45
	541	17.41	8.29
	551	18.85	8.90
Falcon 9	Block 5 (Expend)	22.8	
	Block 5 (Recov)	8.3	5.5
Soyuz	U	22.8	
	2-b/Fregat	8.5 (51.6°)	3.0 (Korou)

^a200 km 28.5° unless otherwise stated

^bThe first digit of the configuration no. defines the diameter of the fairing, the second digit the number of solid rocket boosters and the third digit the number of upper stage RL-10 engines

The Atlas V family of launchers are one of two families operated by the United Launch Alliance (ULA), the other being the Delta IV. Since 2002, the Atlas V has provided launch services to government and commercial customers, with 79 out of 80 attempts being successful. The configuration can be customised to the requirements of the customers' mission, by adding solid rocket boosters or varying the fairing diameter. The central core uses a single Russian RD-180, a dual combustion chamber, dual nozzle design with a vacuum specific impulse of 338 s and a vacuum thrust of 4.15 MN. Concerns around the availability of the Russian-provided engine given deteriorating US-Russian diplomatic relations led ULA to seek an alternative, US produced engine. In 2014, ULA announced that they had selected the Blue Origin BE-4, a liquefied natural gas fuelled engine as the main alternative. When the Atlas V begins to launch powered by the BE-4, the Atlas V will no longer be kerosene-fuelled at all, as its upper stage is hydrogen-fueled.

The SpaceX Falcon 9 (F9) family of launch vehicles are two-stage-to-orbit rockets designed for both commercial and government launch contracts. The first flight of the v1.0 F9 was in 2010, and it has been continuously improved and developed since its introduction, with the most recent version being capable of launching almost twice as much as the first,

as shown in table 6.3. It is also the only current launch vehicle with first stage re-usability, with vertical landing capability at the launch site or on an automated ocean-going barge.

Table 6.3 Falcon 9 Versions - flight data as of end of 2021 (Space Launch Report, 2021)

Version	v1.0	v1.1	FT	Block 5
1st Stage Engines	9 Merlin 1C	9 Merlin 1D	9 Merlin 1D+	9 Merlin 1D+
2nd Stage Engines	1 Merlin 1C Vac	1 Merlin 1D Vac	1 Merlin 1D Vac	1 Merlin 1D Vac
Payload to LEO	9000	13 150	22 800	22 800
No. Launched	5	15	36 ^a	77
Success Rate	4 (1 partial)	14	36	77

^aNote: This does not include the Amos-6 Falcon 9 failure, which occurred during propellant loading before a static test fire

The Falcon 9 was chosen as the base for a kerosene medium lift test case due to its dominance of the commercial launch market (> 40% in 2017), and its potential to reduce launch costs through reusability. It represents the state-of-the-art kerosene-fuelled vehicle today.

It consists of a two-staged kerosene-fuelled launch vehicle. The first stage is powered by nine Merlin 1D engines, and the second stage by a single vacuum-optimised derivative of the same engine. The gross take off weight, or GTOW is the mass of loaded vehicle plus the maximum payload to orbit, 22800 kg in the case of the Falcon 9 Block 5 in expendable mode. The assumed masses are summarised in table 6.4. The uncertainty in these masses means that the final mass of the payload produced by the optimisation may not match reported payload capability.

It is important to establish the capability of the trajectory tool to produce realistic flight trajectories for launch vehicles. This is done by comparing the reported payload capacity of the Falcon 9 with the predicted payload capacity from an optimised trajectory in TROPICO. The reference orbit chosen is shown in table 6.5, and the reference payload is based on publicly available estimates of the rocket in a fully expendable configuration. To compile a complete, global emissions inventory based on accurate historic or forecast launch rates, it would be important to represent the range of possible launch sites and trajectories flown by the different vehicles available. However, in this case, the objective is to gain an

Table 6.4 Mass breakdown of the medium lift kerosene fuelled rocket (Blau, 2018b)

Stage		Mass (kg)
Stage 1	Dry Mass	22 200
	Propellant	412 854
	Subtotal	435 054
Stage 2	Dry mass	4500
	Propellant	107 500
	Subtotal	112 000
Fairing		2000
Total		571 854

understanding of the influence of design on the emissions profiles, and so the important factor is for the target orbit to be consistent, where possible, across the vehicle test cases. The primary reason for this choice is that its a common target for conceptual vehicle studies being from one of the busiest spaceports to one of the lowest stable orbits, and should be achievable for any size of launch vehicle.

Table 6.5 Falcon 9 Target Orbit

LEO	
Altitude	200 km
Inclination	28.5°
Reference	22.800
Payload	
Launch Site	Cape Canaveral

Table 6.6 Initial conditions for medium lift kerosene, 28° 200 km orbit

Altitude h , km	0.001
Velocity v , m s ⁻¹	1
Flight path angle γ , °	89
Heading angle χ , °	90
Latitude λ , °	28.6083
Longitude θ , °	-80.6041
Mass m , kg	571 854

The setup of the optimal control problem is as discussed in section 3.2.2. The initial conditions are set as fixed constraints, and are shown in table 6.6. The launch is split into three phases, the bounds of which are shown in table 6.7. For the first five to twenty seconds of the flight, a fixed control law with the launcher at full throttle and zero angle of attack is used, which addresses instabilities in the dynamic equations close to the singularity in the flight path angle at 90° and at low velocities. The second phase is used for the remainder of the first stage burn, where the control law composed of throttle and the angle of thrust is optimised, and the third is the second stage burn phase of flight, which has significantly higher phase time bounds and contains three multiple shooting elements.

Table 6.7 Bounds for medium lift kerosene test case, 28° 200 km orbit

	Phase 1	Phase 2	Phase 3
Altitude h , km	[0.001, 100]	[0.01, 100]	[30, 200]
Velocity v , m s^{-1}	[1, 4e3]	[10, 4e3]	[2e3, 8e3]
Flight path angle γ , $^\circ$	[-90, 90]	[-90, 90]	[-90, 90]
Heading angle χ , $^\circ$	[0, 360]	[0, 360]	[0, 360]
Latitude λ , $^\circ$	[-90, 90]	[-90, 90]	[-90, 90]
Longitude θ , $^\circ$	[-180, 180]	[-180, 180]	[-180, 180]
Angle of attack α , $^\circ$	[0, 0]	[-10, 10]	[-10, 10]
Throttle τ	[1, 1]	[0.7, 1]	[0, 1]
Time t , s	[5, 20]	[60, 280]	[12, 1000]

The constraints on the states shown in table 6.7 are not tightly bound, in many cases not excluding any of the state space, for example flight path angle, heading, latitude and longitude for example are not constrained except at phase and element boundaries. As discussed in section 3.2.2, the final time, t_f , of each phase is an optimisation parameter. The time bounds are the constraint applied to the final time of each phase, for example, phase 1 can be between 5 and 20 seconds in length. The time of flight is therefore the sum of the optimised t_f per phase:

$$\text{tof} = \sum_{i=1}^n t_{f,i}, \quad (6.1)$$

where:

n is the number of phases

i is the phase

tof is the total time of flight for the optimised trajectory

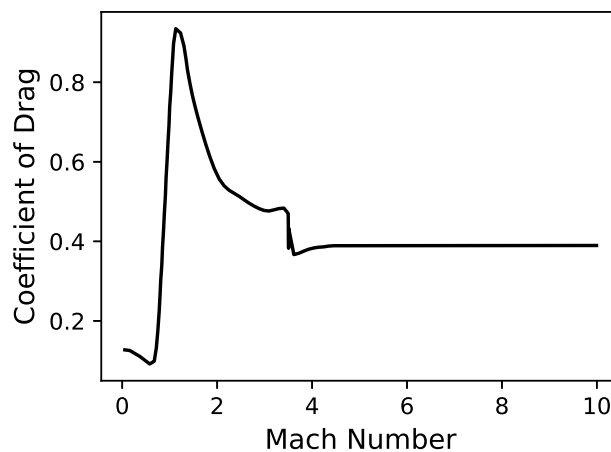
$t_{f,i}$ is the time of flight for phase i

Path constraints are applied to limit the acceleration, $a < 6g$, and the dynamic pressure, $q < 35 \times 10^3 \text{ Pa}$. The cost function is to maximise the final payload mass to orbit.

The coefficient of drag, $C_D(M, \alpha)$, and coefficient of lift, $C_L(M, \alpha)$, are both functions of angle of attack and Mach number. These are usually characterised using CFD and wind tunnel testing for detailed vehicle design studies and development. For preliminary design studies, libraries such as Missile DATCOM generate lookup tables for these parameters for an arbitrary geometry or design (Rosema et al., 2011). However, Missile DATCOM is not available outside the US, and the use of CFD or wind tunnel testing in preliminary design or analysis is not feasible.

Rocket aerodynamics in this thesis are based on the aerodynamic coefficients generated by MDATCOM for a two-stage rocket from the thesis of Ritter (2012). These provide the coefficient of drag with Mach number for an angle-of-attack of zero, which includes multiple components of drag, including skin and shape drag. These are interpolated to provide a two-dimensional curve, shown in fig. 6.2.

Fig. 6.2 C_D with M number for rockets (Ritter, 2012)



This same set of data is used for all the vertical launch test cases in this section. Using a consistent set of aerodynamic models across the different vertical test cases is an advantage

here, as we are mostly interested in the system level design decisions such as propulsion system and vehicle sizing, rather than the specific aerodynamics of each.

A simplified approach to modelling the performance of the Merlin 1D rocket engine was used within the trajectory model. The performance from HyPro matches closely with this simple model, so it is not necessary to include a surrogate or wrapper, reducing the computation time significantly. The emissions produced by the propulsion system for each species, i are taken directly as the mass fraction at the exit of the nozzle from the HyPro model, Y_i multiplied by the mass flow of the engine and throttle:

$$EI_i = Y_i \dot{m} \tau, \quad (6.2)$$

which assumes a direct relationship between the throttle and mass flow rate. Throttling in rocket engines is a complex process that may involve alterations in the mixture ratio, mass flow rates of the oxidiser and fuel and changes in injection pressure.

The position in terms of altitude and time, altitude and ground track, and geographically of the optimal trajectories for the medium kerosene case are shown in fig. 6.3. The colours represent the individual phases of flight (i.e. blue is the fixed-dynamics phase, orange is the remaining first stage phase, yellow is the second stage phase up until orbital insertion) and the '+' symbols represent the interface between multiple shooting elements, which includes phase boundaries. Note that the first phase, in blue is only visible in fig. 6.3a because it is a very short phase lasting less than 20 seconds during the slowest phase of flight, and so in the scale of the whole trajectory is not visible for the ground track views.

The altitude and velocity time histories of the launch vehicle during flight are shown in figs. 6.3a and 6.5c and the control law, in terms of throttle and angle of attack are in figs. 6.4a and 6.4b. The throttle curve shows a reduction from full throttle to 0.9 about 70 s into the flight, which corresponds with the maximum dynamic pressure, one of the path constraints applied. The circles in these figures represent the control nodes of the control law. The velocity (fig. 6.5c) and flight path angle (fig. 6.5b) curves both respectively show the expected result for a two-stage vertical vehicle, with an increase rate of velocity increase as the vehicle gets lighter through both stage 1 and stage 2 burns, and a slow pitch from

vertical following a gravity turn (Sutton and Biblarz, 2010), and eventually reaching 0° at the end of the launch, as expected for a circular orbit.

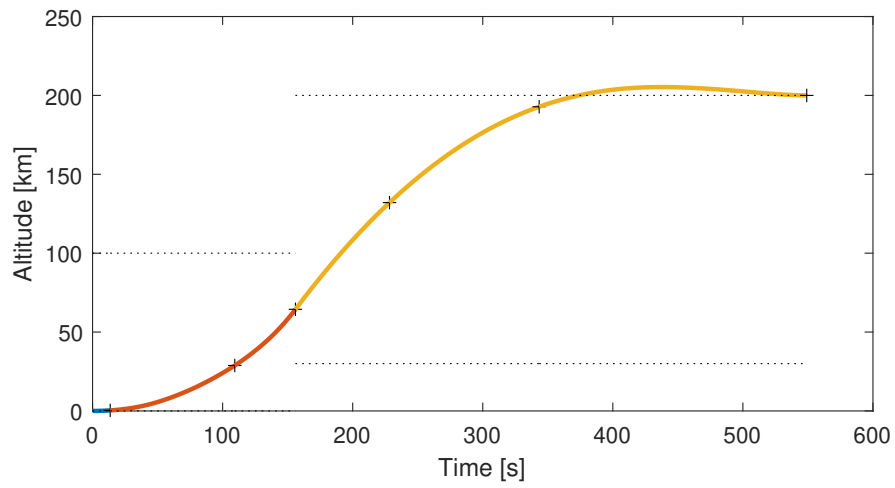
The optimised mass, calculated by taking the final mass of the vehicle (the final point in fig. 6.5a) from the optimised trajectory and subtracting the mass of the second stage, was 23 283 kg, which is higher than the nominal mass in expendable mode of 22 800 kg. This is an optimised mass because the objective function was the maximum payload equation shown in eq. (3.23). The reason for this difference is difficult to identify precisely due to uncertainty in the various source data used to construct the problem, but could be due to the mass, aerodynamics, or details that have been neglected here such as propellant ullage. Regardless, this represents an error of only 2% and is acceptable for the purposes here.

Equation (6.2) is used alongside the nozzle exit mass fractions for the equilibrium, frozen and partial equilibrium engine models presented in table 5.12 and table 5.13 to generate a mass emission profile, how much of each species is emitted at each timestep. This mass emission profile is then binned by altitude to produce fig. 6.6, the distribution of all emissions by altitude across the optimised trajectory. It is clear that the vast majority are emitted by the first stage, during the first portion of the flight. Similarly, fig. 6.7 shows the same distribution, but with individual species components. The overall mass of emissions is dominated by the major species produced by the combustion of kerosene - CO_2 , CO , and H_2O . There is also a build up of mass emitted at the top altitudes on this trajectory. This is due to the length of time the launch vehicle spends increasing its perigee, as can be seen in fig. 6.3a.

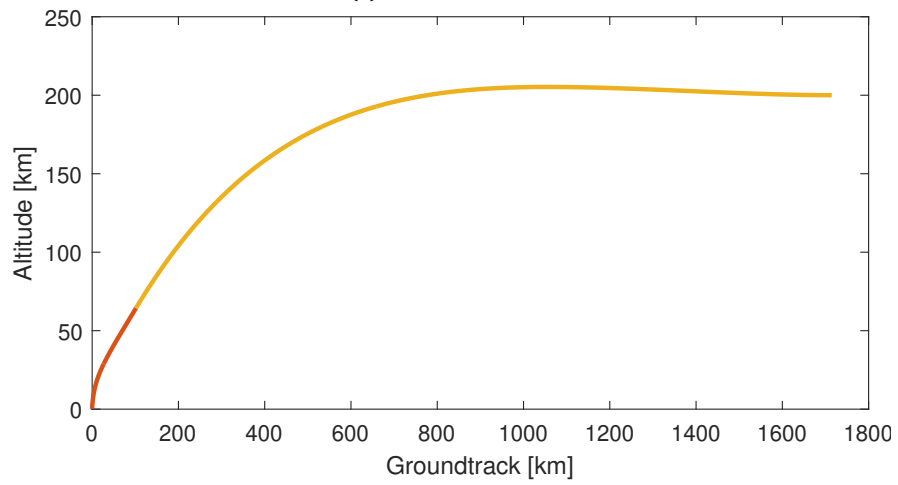
As discussed in section 5.2.5, kerosene rocket engines often run fuel rich, so there are unreacted species emitted may react with other species in the air entrained in the plume, resulting in an increase of species in the atmosphere greater than the propellant on board the rocket. This is similar to airbreathing engines where emissions from the engine are defined based on an emission index, measured in g kg^{-1} and calculated based on the mass of the emission and fuel mass:

$$\text{EI}_x = \frac{m_x}{m_p}. \quad (6.3)$$

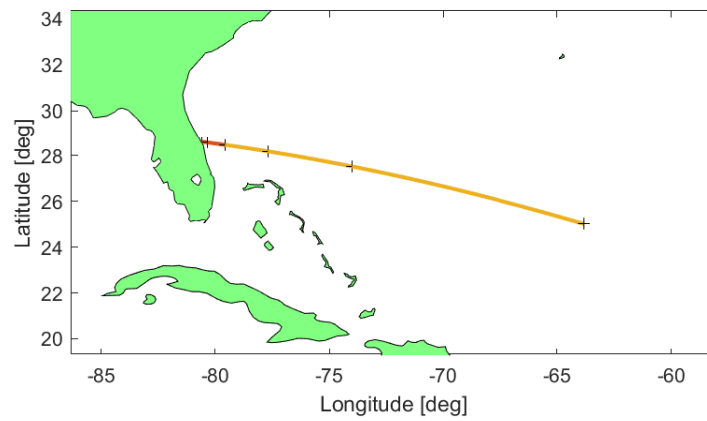
Kerosene rocket engines produce significant amounts of carbon monoxide (CO) depending on how fuel rich they are. CO is likely to react with entrained air in the plume, forming



(a) Altitude vs. time



(b) Altitude vs. ground track



(c) Ground track map view

Fig. 6.3 Position time history of the optimised solution for the medium-lift kerosene

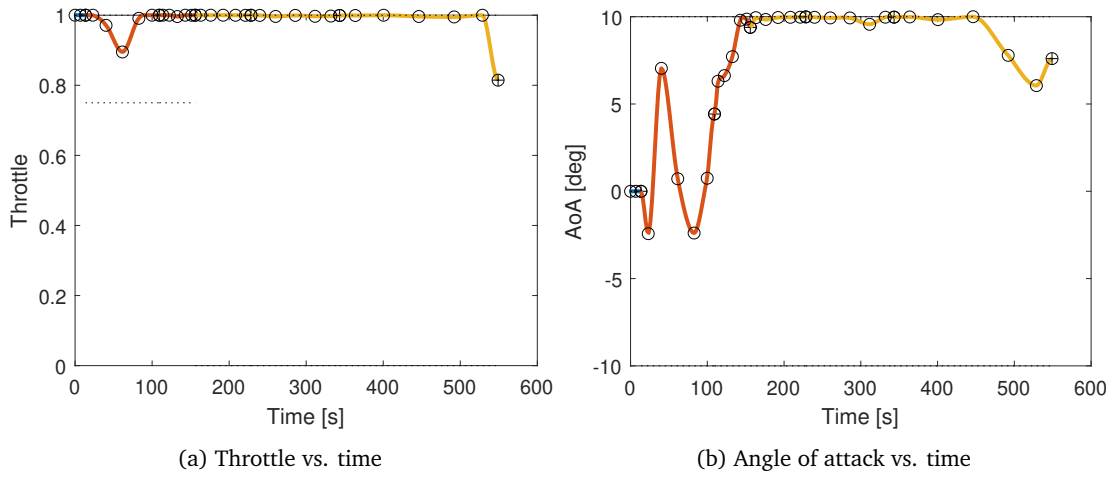


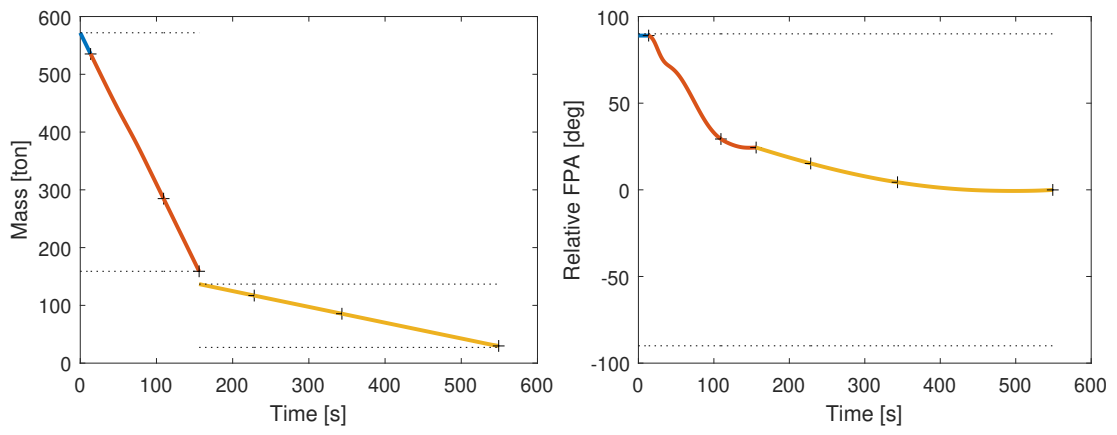
Fig. 6.4 Control time history of the optimised solution for the medium-lift kerosene

CO₂. CO that survives the plume is a weak greenhouse gas, but it reacts with OH radicals in the atmosphere to form carbon dioxide in a significantly shorter time than the residence time of CO₂. This means it is a reasonable assumption to consider this mass of CO₂ as a direct emission from the launch vehicle, and the emission indices in this case can be greater than one:

$$\sum_x EI_x > 1. \quad (6.4)$$

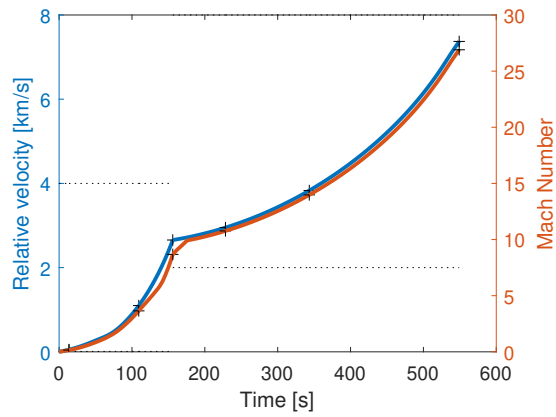
This has been a previous assumption of other attempts to quantify launch emissions (DeSain and Brady, 2014; Ross and Sheaffer, 2014), and was also demonstrated in the plume modelling for the environmental assessment of the Falcon 1 and Falcon 9 vehicles (Aerostar Environmental Services Inc, 2007).

One way to include this is to calculate the amount of CO₂ that would be formed by the reaction of CO with oxygen in the atmosphere, and to use this mass of CO₂ in radiative forcing calculations. This is an assumption, which could be removed by modelling the plume and the afterburning that occurs in the plume in detail. The reactions of CO, CO₂ and other species are likely to be more complex than this, but the maximum amount of CO₂ that could be formed is based on the reaction $2\text{CO} + \text{O}_2 \longrightarrow 2\text{CO}_2$. This results in a mass conversion ratio of 1.57 from CO to CO₂, which can be used as a guide to calculate a scaled amount of emission deposited in the atmosphere (i.e. converting CO to CO₂). Figure 6.6b shows the mass added to the atmosphere in blue, as well as the added mass of CO₂ made from reacting CO, highlighted in orange. The corrected emissions profiles for the three nozzle



(a) Vehicle mass vs. time

(b) Flight path angle vs. time

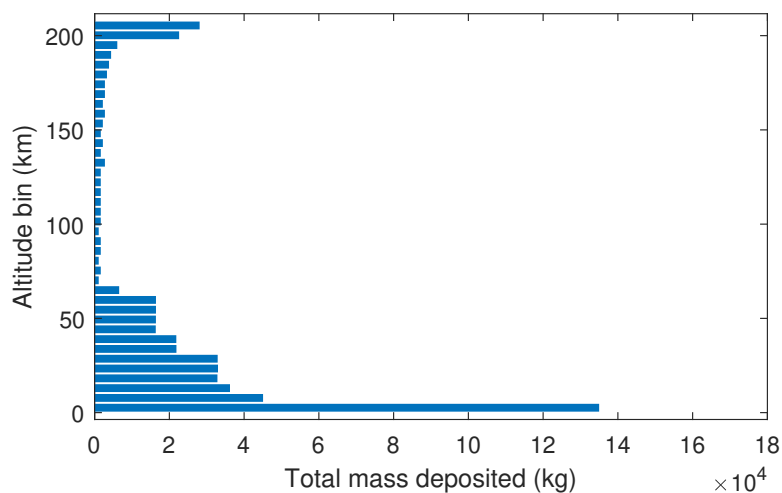


(c) Relative velocity and Mach number vs. time

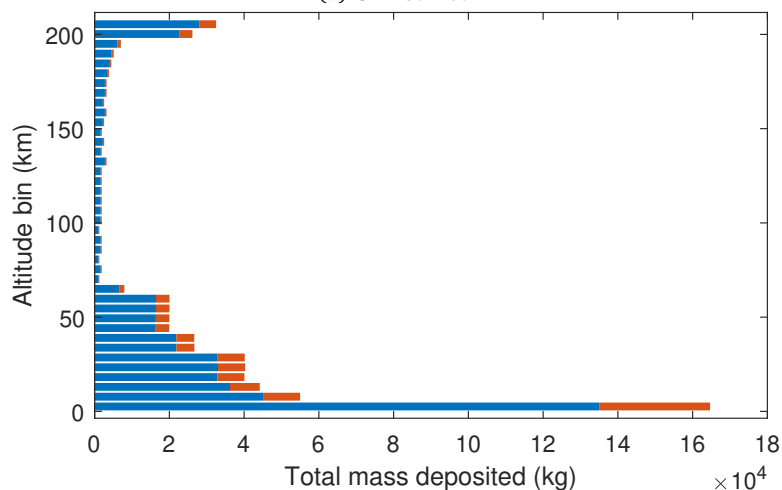
Fig. 6.5 Additional state parameter time history of the optimised solution for the medium-lift kerosene rocket

chemistry assumptions are shown in fig. 6.7b, fig. 6.7d and fig. 6.7f. Further discussion of the implications of this correction are discussed in section 7.2.1.

The results shown here are likely to represent the lower bound of soot produced by the Falcon 9, and a sensitivity analysis of various assumed soot production rates is performed in section 7.2.2.



(a) Unmodified



(b) Corrected

Fig. 6.6 Total mass of emissions by altitude bin for the medium kerosene test case

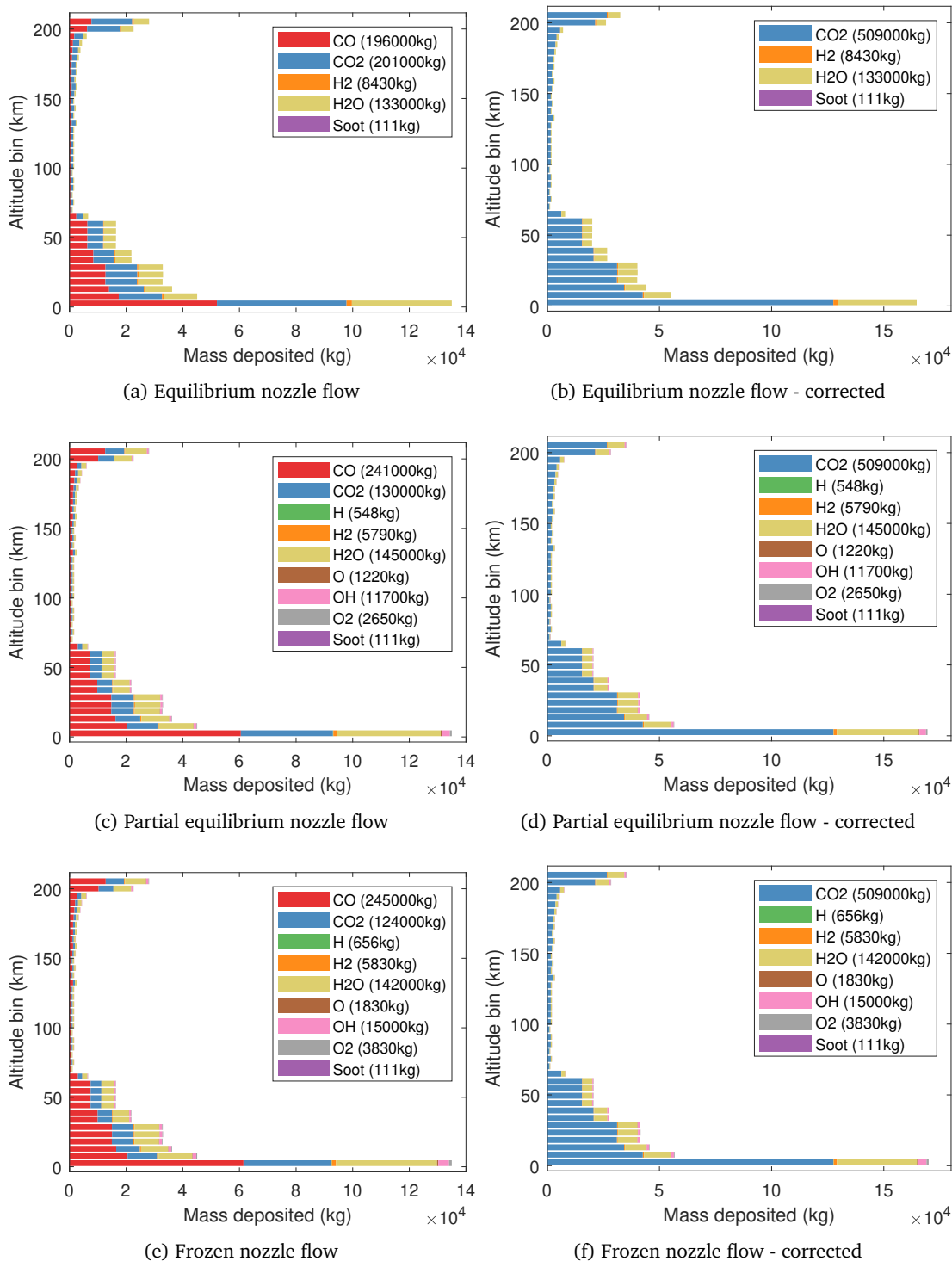


Fig. 6.7 Major species emission by altitude bin for medium kerosene test case

6.2 Medium lift rocket - hydrogen

Hydrogen is a highly desirable propellant because of its high specific impulse, but has drawbacks such as its handling difficulty and low density, which increases the tank volume. The United Launch Alliance Delta IV is the only expendable medium lift hydrogen launch vehicle in the US fleet. It is one of two rocket families currently built and manufactured by ULA, and is the latest of the Delta family of launch vehicles originally developed by Boeing. The Delta IV was available for commercial use, but with the exception of the inaugural launch of a commercial satellite for Eutelsat, all of its launches have been US government payloads (SpaceLaunchReport.com, 2018). By 2019, ULA phased out all Delta IV launchers except the Delta IV Heavy, offering the Atlas V instead for these missions (Gruss, 2015).

All of the Delta IV's core stages use liquid hydrogen and liquid oxygen as propellant (United Launch Alliance, 2013). The first stage consists of either one, or three in the case of the heavy 5 m diameter *Common Booster Cores* (CBC), each powered by a single $1\text{H}_2/1\text{O}_2$ RS-68A rocket engine. The second stage, called the *Delta Cryogenic Second Stage* (DCSS) has variants with two diameters, at 4 m and 5 m. It uses the Rocketdyne RL10-B2 upper stage engine. Orbital ATK GEM-60 solid rocket boosters may optionally be added to increase the first stage thrust. Table 6.8 shows all five current Delta IV configurations.

Table 6.8 Variants of the Delta-IV Launch Vehicle (United Launch Alliance, 2013)

Version	Medium	M+(4,2)	M+(5,2)	M+(5,4)	Heavy
First Stage	1 CBC	1 CBC	1 CBC	1 CBC	3 CBC
Boosters	0	2	2	4	0
Upper Stage Diameter	4 m	4 m	5 m	5 m	5 m
Payload Capability in kg					
GEO	1270	2320	2250	3120	6750
GTO (1804 m s^{-1})	4440	6390	5490	7300	14220
GTO (1500 m s^{-1})	3060	4490	4100	5400	10100
LEO (200 km x 200 km, 28.7°)	9420	13140	11470	14370	28790
LEO (200 km x 200 km, 90°)	7690	10250	9600	11600	23560

The hydrogen-propellant test case is based on the Delta IV M, as one of few current launch vehicles to use liquid hydrogen. Cryogenic liquid hydrogen and oxygen powered

vehicles are perceived as environmentally friendly since they only produce water as an exhaust product. However, water vapour does have an impact on the atmosphere, and hydrogen fuelled rockets are often used in conjunction with solid rocket boosters, which have even greater potential to damage the atmosphere.

Table 6.9 Mass breakdown of the Delta-IV M (4,0) vehicle (Blau, 2018c)

Stage		Mass (kg)
Stage 1	Dry Mass	26,400
	Propellant	202,000
	Subtotal	228,400
Stage 2	Dry mass	2,850
	Propellant	21,320
	Subtotal	24,170
Fairing		2800
Total		255,370

The vehicle was modelled as a two-stage rocket, with the mass breakdown shown in table 6.9. As with the medium kerosene case, a simplified approach to modelling the performance of the RS-68A rocket engine and RL-10B was used within the trajectory model, using the nominal reported performance.

A feasible solution with the nominal mass breakdown shown in table 6.9 and a cost function to maximise the payload could not be found. This is likely because the second stage engine has a relatively low thrust, but very high specific impulse. For comparison, the Falcon 9 and Delta IV M are similarly sized vehicles, but the upper stage engine on the Falcon 9 has a nominal thrust of ~ 980 kN, compared to ~ 110 kN for the RL-10. This limits its ability to add delta-V to the upper stage for a given upper-stage mass, especially on low altitude trajectories like the reference orbit. To address this, two actions were taken for this specific test case. First, the target orbit was modified to a 400 km orbit, with otherwise the same parameters as table 6.5. This is likely to have very limited impact on the emissions profile, as the first stage burn and the initial altitude increase of stage two will likely be very similar, and only the distribution of emissions above the atmosphere will be affected. Secondly, as the specific propellant masses for the second stage tanks are determined for each launch vehicle configuration and individual mission, the tanks may not be filled to

maximum capacity, the gross takeoff weight of the second stage, GTOW_2 was added as an optimisation parameter, within the bounds:

$$\text{GTOW}_2 = [0.7(m_{ws_2} + m_p), m_{ws_2} + m_p] \quad (6.5)$$

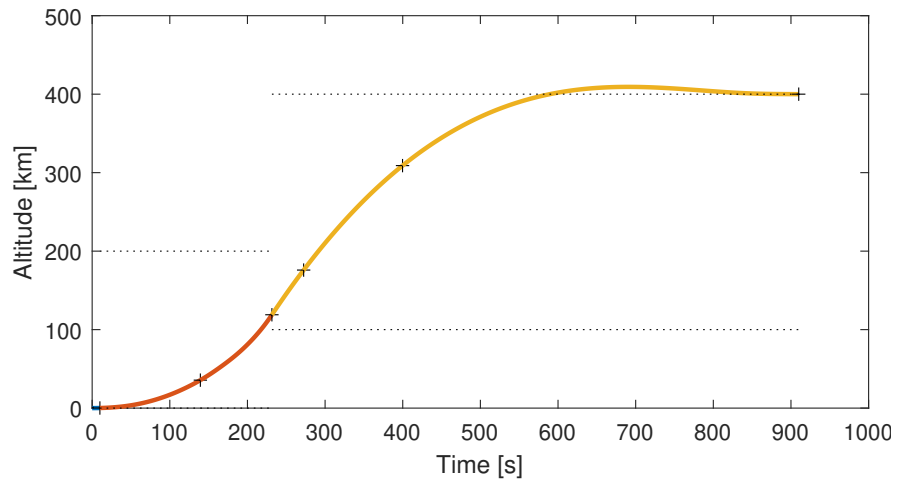
where m_{ws_2} is the mass of the wet second stage and m_p is the mass of the payload. This converged successfully and resulted in a GTOW_2 of 28 492 kg, corresponding to a propellant mass of 16 222 kg.

Overall, the trajectories and optimised control law, shown in figs. 6.8 to 6.10 are very similar to the medium kerosene case, with a few subtle differences. There is no throttle down for the point of maximum dynamic pressure in fig. 6.9a, despite having the same dynamic pressure constraint. Note as well that the overall time for the mission is almost two hundred seconds longer, this is because of the lower thrust-to-weight ratio, particularly in the upper stage. This does not have implications for the emission release, as the total emissions are driven by the mass of propellant rather than the time of flight. Finally, the staging altitude is significantly different, at about 60 km for the medium kerosene case to well over 100 km for the hydrogen vehicle.

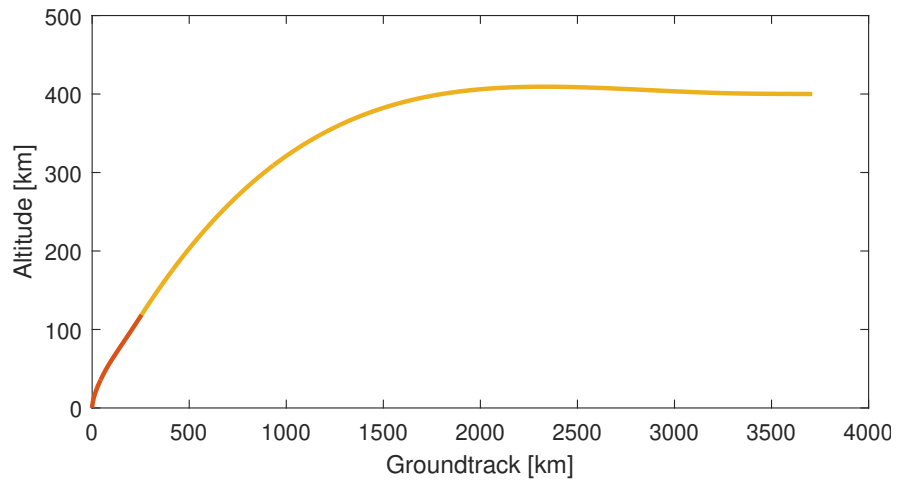
The emissions produced by the propulsion system are taken directly as the mass fractions at the exit of the nozzle in the HyPro model multiplied by the mass flow of the engine (after the throttle). As with the medium kerosene case, a direct relationship between the throttle, the mass flow and thrust is assumed.

The emission profiles shown in figs. 6.11 and 6.12 are very similar in shape to those of the medium kerosene case. However, comparing fig. 6.11 with fig. 6.6, the dense band of the delta IV emissions stretches up to more than 100 km, where staging occurs. The approach used to quantify radiative forcing in chapter 7 accounts for all H_2O emissions above 15 km, so this will have no impact on this calculation, but its not clear whether there are further implications.

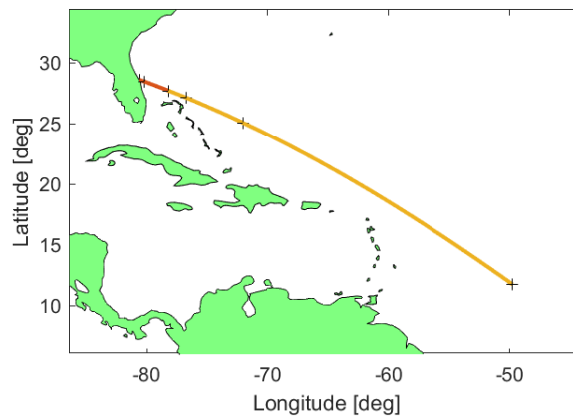
Unlike the kerosene and methane fuelled rocket engines which produce significant amounts of CO due to incomplete combustion in engine and nozzle, only small amounts of minor species from hydrogen-fuelled engines are produced, around 0.03 % H_2 in the



(a) Altitude vs. time



(b) Altitude vs. ground track



(c) Ground track map view

Fig. 6.8 Position time history of the optimised solution for the medium-lift hydrogen rocket

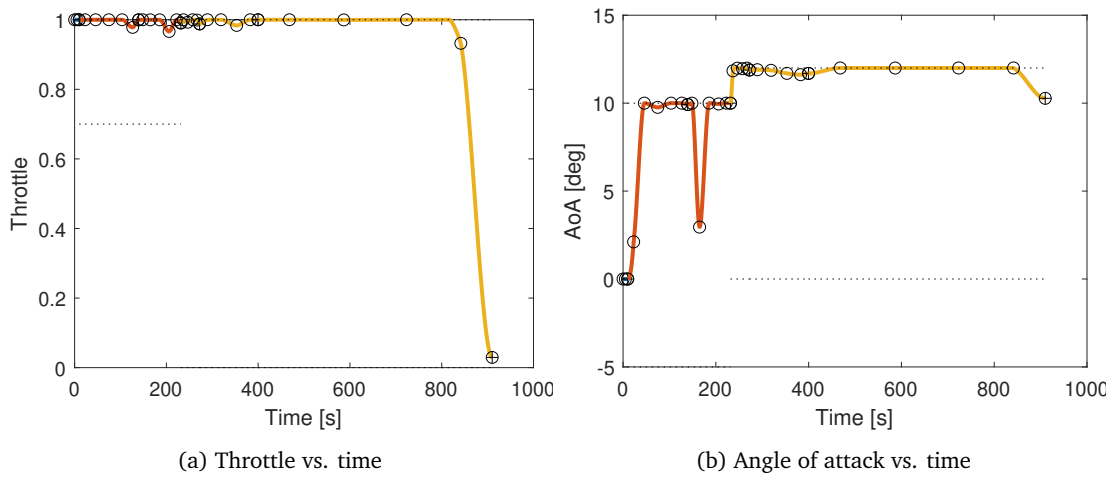
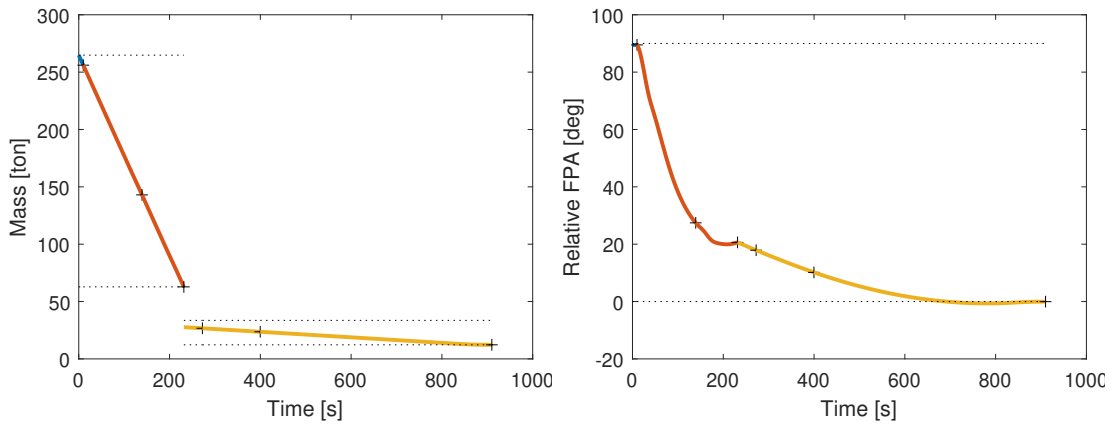


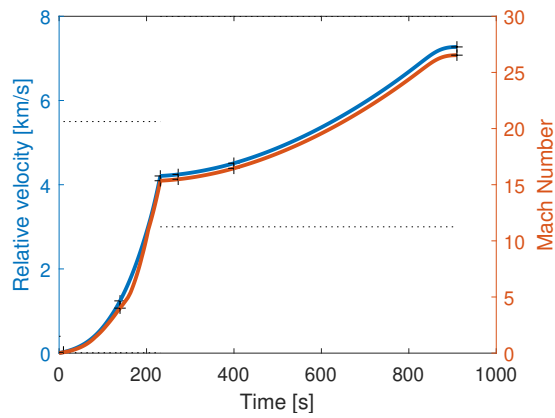
Fig. 6.9 Control time history of the optimised solution for the medium-lift hydrogen rocket

equilibrium case, and so whilst a similar correction could be conceived, it will have only a minor effect.



(a) Vehicle mass vs. time

(b) Flight path angle vs. time



(c) Relative velocity and Mach number vs. time

Fig. 6.10 Additional state parameter time history of the optimised solution for the medium-lift hydrogen rocket

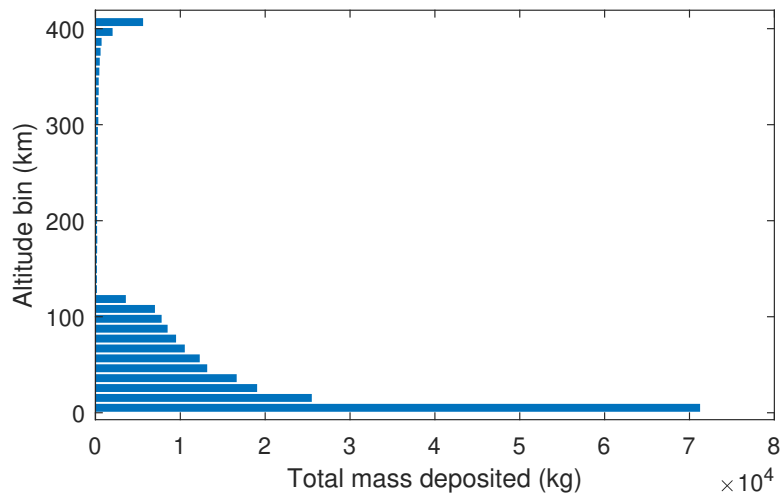
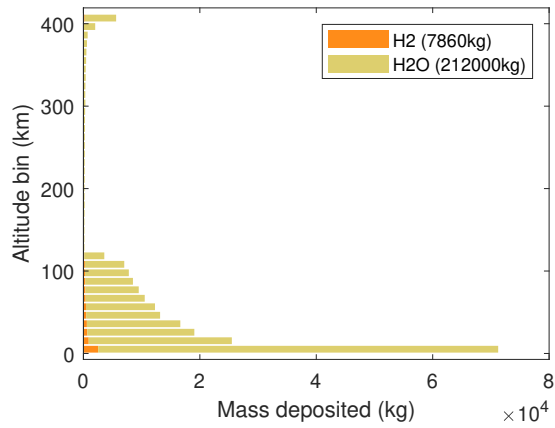
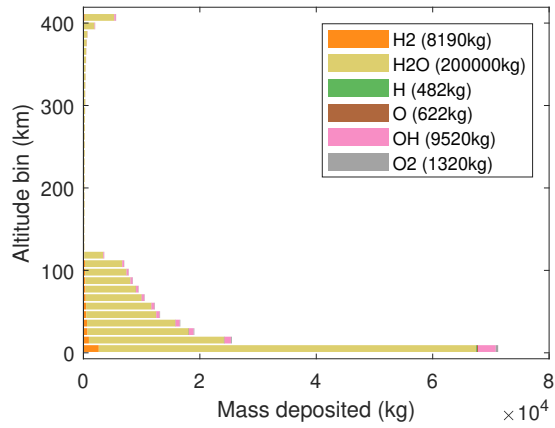


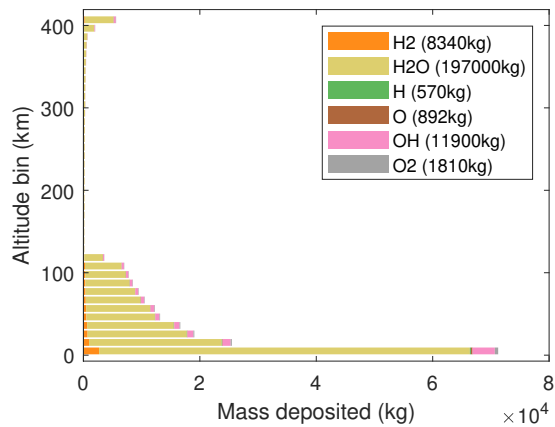
Fig. 6.11 Total mass of emissions by altitude bin for the medium hydrogen rocket test case



(a) Equilibrium nozzle flow



(b) Partial equilibrium nozzle flow



(c) Frozen nozzle flow

Fig. 6.12 Major species emission by altitude bin for medium hydrogen rocket test case

6.3 Superheavy rocket - methane

Super heavy lift launchers, here defined by $m_{\text{payload}} > 50$ t, have in the past been government developed and operated as part of large programmes (e.g. Saturn V, N1, Space Shuttle). In the 2010s SpaceX and Blue Origin indicated their intention to develop commercial super heavy lift vehicles, with the Super Heavy/Starship and New Glenn rockets respectively. As of the writing of this thesis, SpaceX have developed and tested the main engine for their superheavy launch system, Raptor, and have launched and successfully recovered Starship in suborbital flights. As both vehicles are in a highly iterative development state, public information on the specification, configuration and performance is limited. A representative superheavy launch system based on best estimates of the Super Heavy/Starship system design is constructed. The results are therefore only indicative of vehicles in this class rather than the specific configuration that may be operational in the future.

The super heavy test case is a two-stage, fully reusable vehicle. SpaceX have opted for methane as the fuel given the balance of performance (I_{sp} is between kerosene and hydrogen), propellant cost and ease of handling, and reduced system complexity through autogenous pressurisation of the propellant tanks. Reuse is provided through vertical landing of the first stage, for which 10% of the vehicle's propellant is reserved. This is included as part of the first stage m_0 . For the first time, it is expected that the second stage, Starship, is also reusable with a thermal protection system protecting the steel structure during high thermal loads of re-entry and as with the first stage, vertical landing. Table 6.10 shows the assumed mass breakdown for the vehicle modelled.

The propulsion system is based on the SpaceX Raptor engine, which is still in development. Reported performance estimates vary wildly between 8000 kN and the likely thrust of 2000 kN. The trajectory simulations assume a nominal vacuum thrust of 2000 kN, $I_{sp,v}$ of 380 s. The first stage has 31 Raptor engines, and the upper stage has 7, as described in NASA (2019).

The setup in TROPICO for Starship is very similar to the medium kerosene case, as seen in table 6.11. This results in a similar launch trajectory (figs. 6.13 to 6.15). The upper stage of the super heavy vehicle throttles to zero from about 500 s into the flight, before throttling up to about 0.1 at 600 s. This indicates it only needs one out of the seven upper stage engines

Table 6.10 Mass breakdown of the super heavy lift methane fuelled rocket

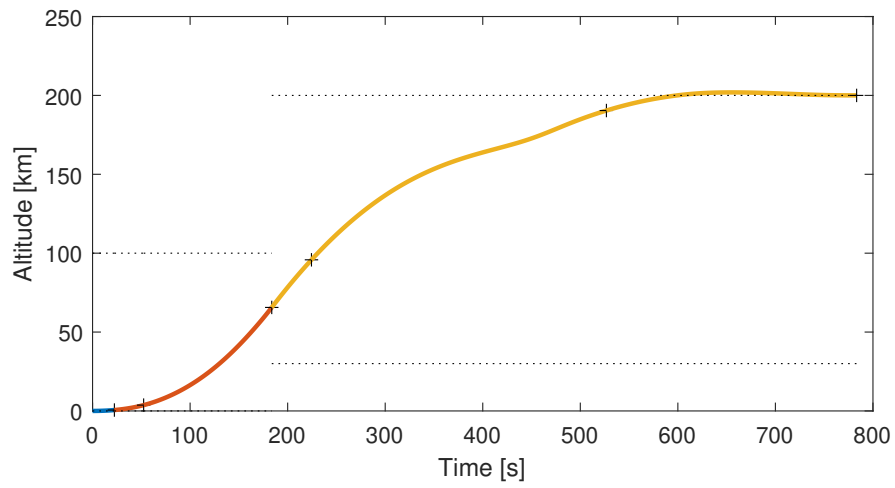
Stage		Mass (kg)
Stage 1	Dry Mass	230,000
	Propellant	3,300,000
	Subtotal	3,530,000
Stage 2	Dry mass	120,000
	Propellant	1,200,000
	Subtotal	1,320,000
Payload		100,000
Total		4,950,000

for orbital insertion in this case. This behaviour is a two-burn orbital insertion strategy, where the perigee is raised later in the flight in a separate burn, a common approach.

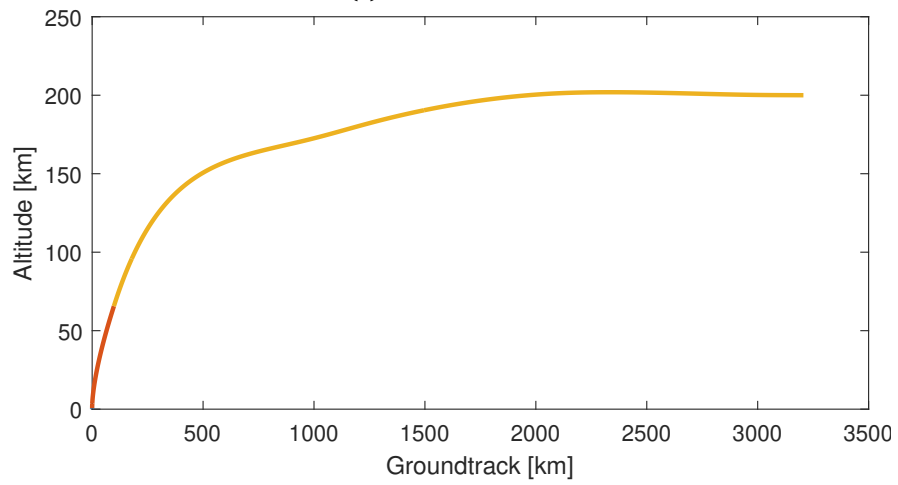
Table 6.11 Bounds for super heavy test case, 28° 200 km orbit

	Phase 1	Phase 2	Phase 3
Altitude h , km	[0.001, 100]	[0.01, 100]	[30, 200]
Velocity v , m s^{-1}	[1, 4e3]	[10, 4e3]	[2e3, 8e3]
Flight path angle γ , °	[-90, 90]	[-90, 90]	[-90, 90]
Heading angle χ , °	[0, 360]	[0, 360]	[0, 360]
Latitude λ , °	[-90, 90]	[-90, 90]	[-90, 90]
Longitude θ , °	[-180, 180]	[-180, 180]	[-180, 180]
Angle of attack α , °	[0, 0]	[-5, 5]	[-8, 8]
Throttle τ	[1, 1]	[0.7, 1]	[0, 1]
Time t , s	[5, 10]	[60, 240]	[30, 300]

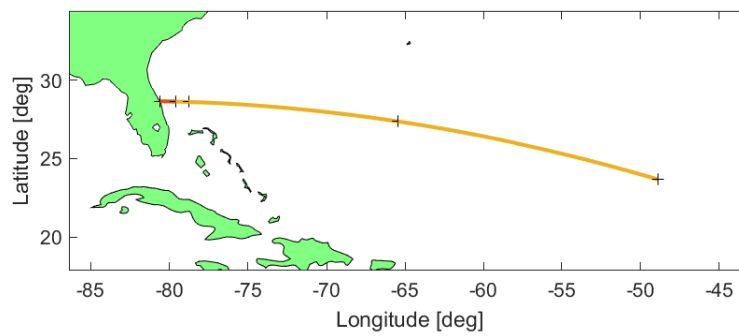
According to [NASA \(2019\)](#), separation of Super Heavy and Starship occurs at 70 km, and ignition of Starship's engines at 80 km. The reason for this has not been specified, and does not appear in the optimal solution, where separation occurs at 65 km. The mass to orbit is 295.6 t, considerably more than the combined mass of Starship and a 100 t payload. Part of this remaining mass will be used for Starship for re-entry, descent and landing burns. It is also possible that the fact that the previous assumption of 10% of the first stage's propellant for landing is incorrect.



(a) Altitude vs. time



(b) Altitude vs. ground track



(c) Ground track map view

Fig. 6.13 Position time history of the optimised solution for the methane-fuelled super heavy rocket

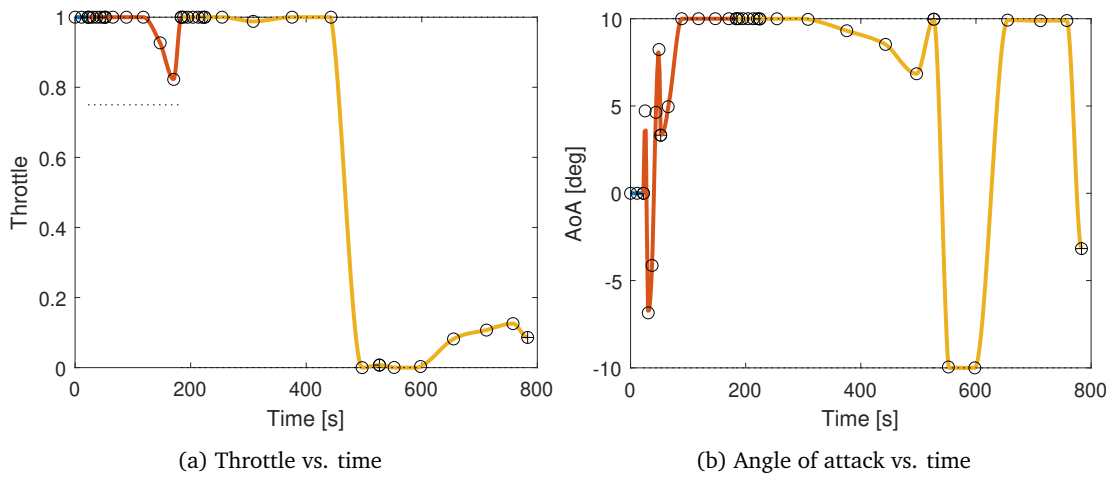
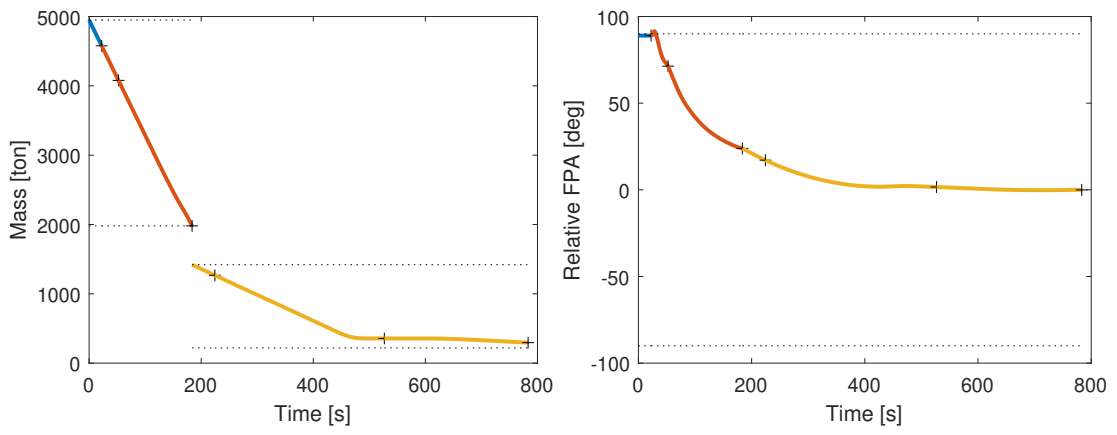


Fig. 6.14 Control time history of the optimised solution for the methane-fuelled super heavy rocket

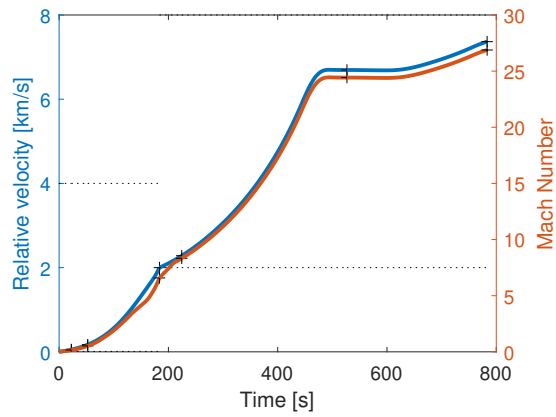
The emission indices (table 5.16) used for this test case are based on the analysis in section 5.2.6. As with the other test cases, the indices for the frozen, partially frozen and equilibrium nozzle flow conditions are used to bound the possible emission release scenarios. The emission release profiles are shown in fig. 6.16 and fig. 6.17. As with the medium kerosene rocket (section 6.1), there are significant amounts of carbon monoxide present in the exhaust, including in equilibrium flow where the majority of the minor emissions react to extinction. This carbon monoxide is a function of mixture ratio - the lower the fuel to oxidiser ratio is, the less CO will be present.

The emissions profiles are very similar in shape between the super heavy launcher and the medium kerosene case. However, there is clearly a relative increase across the entire upper stage burn. As discussed in the problem setup, 10% of the upper stage propellant is reserved for re-entry and landing burns. This propellant must be carried to orbit, rather than being expelled during the second stage burn. Additionally, the 100 s throttle down in the upper stage is clearly visible in the emissions profile from 180 km to 200 km.



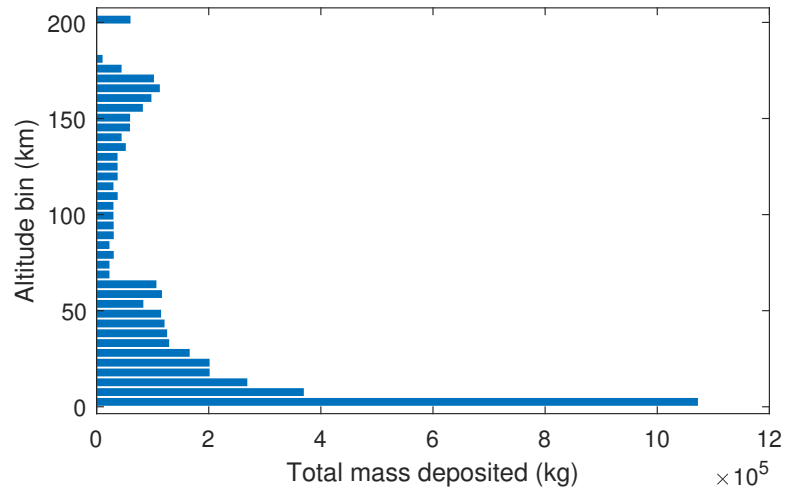
(a) Vehicle mass vs. time

(b) Flight path angle vs. time

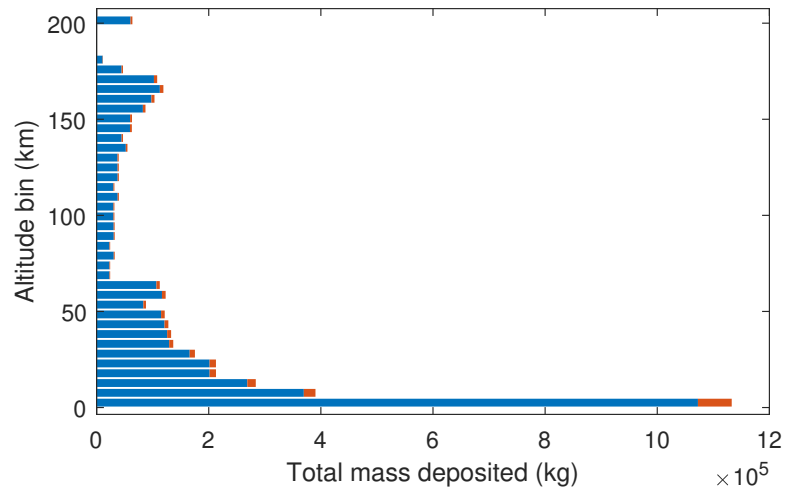


(c) Relative velocity and Mach number vs. time

Fig. 6.15 Additional state parameter time history of the optimised solution for the methane-fuelled super heavy rocket



(a) Unmodified



(b) Corrected

Fig. 6.16 Total mass of emissions by altitude bin for the super heavy methane rocket

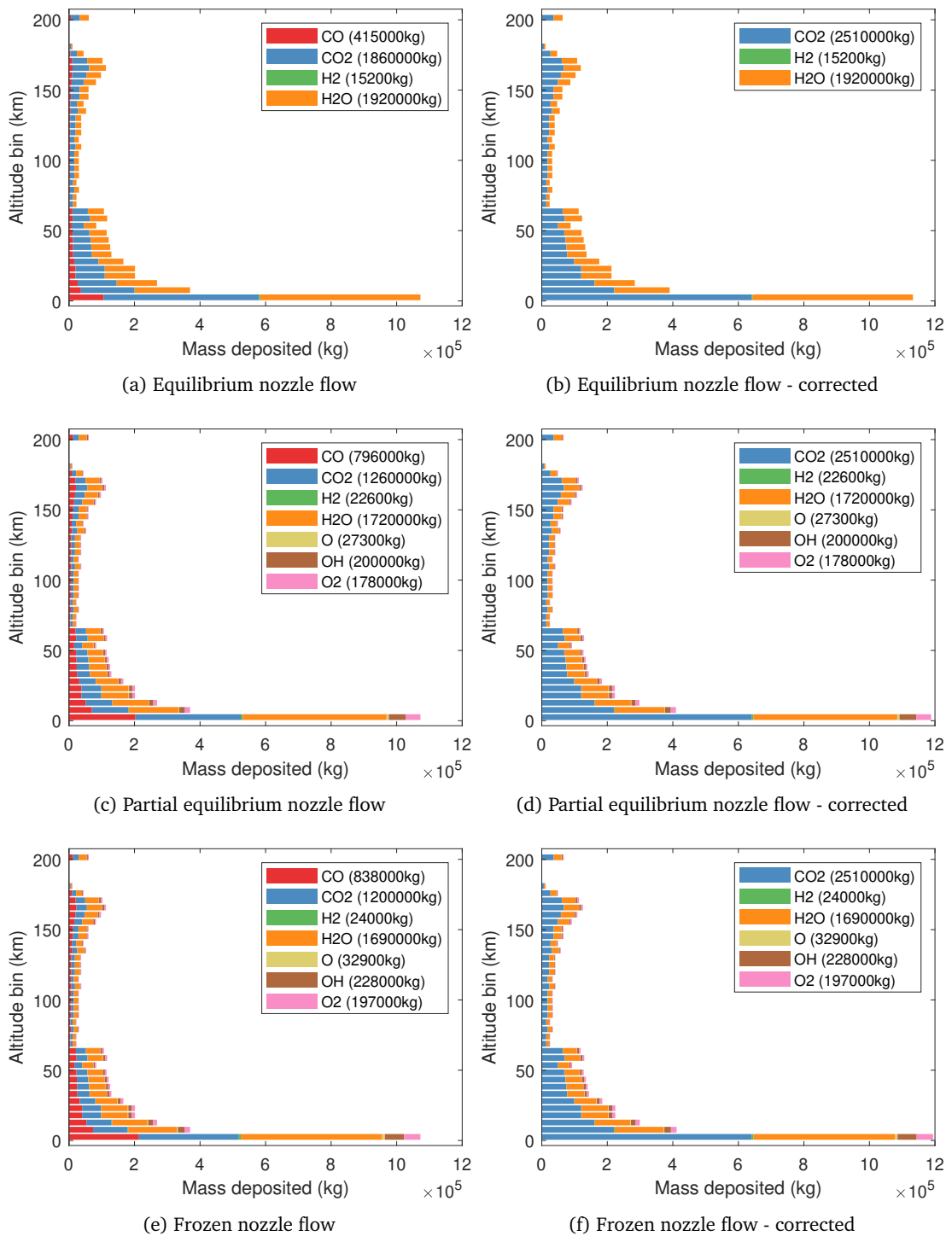


Fig. 6.17 Major species emission by altitude bin for the super heavy methane test case

6.4 Small launcher - kerosene

A small launcher based on the Rocket Lab Electron rocket has been chosen to represent the range of new small launchers that have been developed in recent years, discussed in section 2.2. Whilst there is relatively little publicly available information on the specific characteristics of the Electron rocket and its Rutherford rocket engine, many of the new vehicles developed are using kerosene fuel in their propulsion systems. This test should be seen as representative of the class and size of a range of vehicles currently operating or beginning operations in the early 2020's.

Table 6.12 Assumed mass breakdown of the small kerosene-fuelled rocket

Stage		Mass (kg)
Stage 1	Dry Mass	950
	Propellant	9250
	Subtotal	10200
Stage 2	Dry mass	250
	Propellant	2050
	Subtotal	2300
Fairing		50
Payload		225
Total		12775

A kerosene rocket engine with performance close to the reported performance of the Rutherford rocket engine (RocketLab, 2019) has been constructed, shown in table 6.13. As previously discussed in section 4.1, how well the shifting equilibrium assumption predicts the real nozzle flow depends on the rate of the chemical kinetics and the length of the nozzle. Modelling of equilibrium, frozen and non-equilibrium flows by Zhukov (2019) shows that the shifting equilibrium assumption to the nozzle throat provides very similar results to non-equilibrium approaches for methane rocket engines, overpredicting specific impulse performance by $\sim 1\%$.

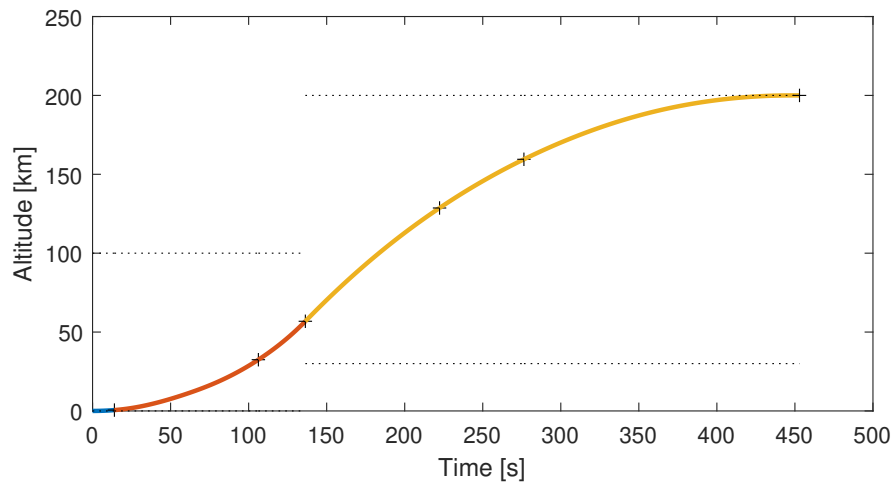
The trajectory optimisation was set up using the same configuration as the medium kerosene rocket, with appropriate changes to the masses (see table 6.12) and the propulsion models. The resultant trajectory (see figs. 6.18 and 6.20) and control law (see fig. 6.19)

Table 6.13 Rutherford Engine Specs

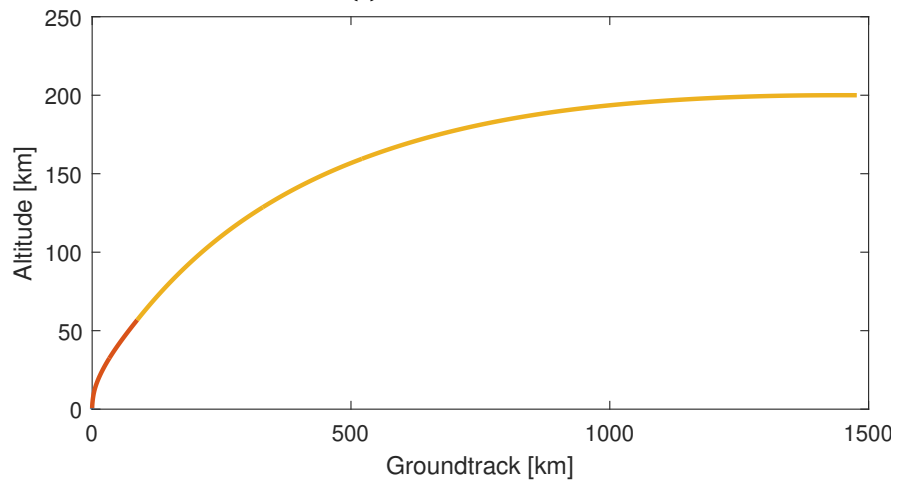
		Rutherford	Rutherford Vac
Thrust (Vac)	[kN]	24	24
Specific Impulse (Vac)	[s]	311	343
Estimated \dot{m}	[kg s ⁻¹]	7.87	7.13
Assumed			
Mixture Ratio	[-]	2.8:1	2.8:1
Expansion Ratio	[-]	12	40
Chamber Pressure	[MPa]	5.4	5.4
Calculated (assumes shifting equilibrium until nozzle throat)			
Mass Flow Rate	[kg s ⁻¹]	7.650	7.254
Exit Area	[m ²]	0.029 50	0.098 32
Throat Area	[m ²]	0.002 458	0.002 458
Thrust (Vac)	[kN]	23 250	24 690
Specific Impulse (Vac)	[s]	315.6	335.2

are similar to those seen in the previous test cases. The throttle down due to the dynamic pressure constraint is present in fig. 6.19a and the staging point occurs at the earliest point of any of these test cases at just over 50 km (see fig. 6.18a).

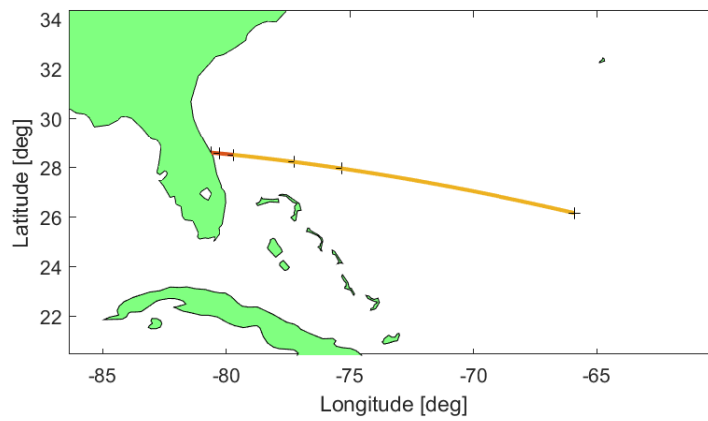
The emission profiles (figs. 6.21 and 6.22) are similar to the other vertical launch vehicles. As this is a kerosene fuelled rocket, the same correction described in section 6.1 is applied to convert CO into CO₂.



(a) Altitude vs. time



(b) Altitude vs. ground track



(c) Ground track map view

Fig. 6.18 Position time history of the optimised solution for the small kerosene-fuelled rocket

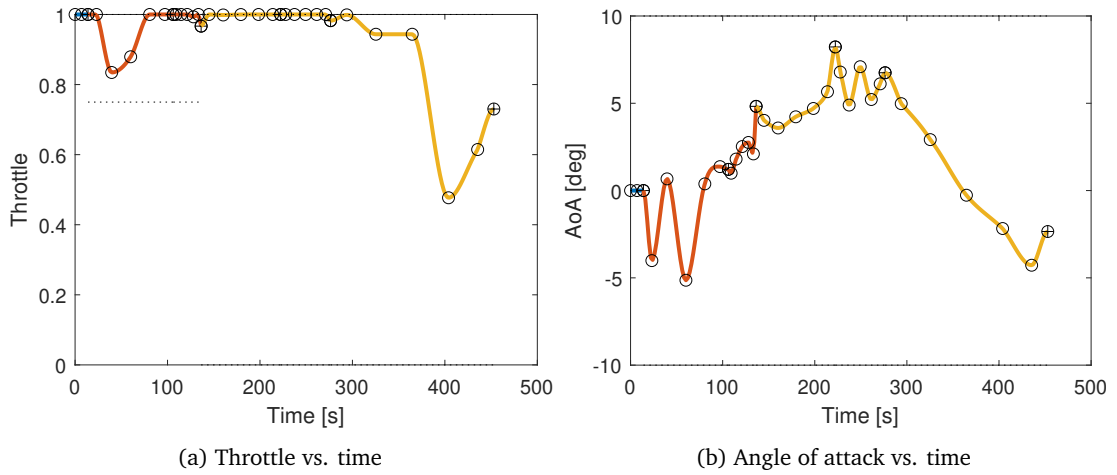


Fig. 6.19 Control time history of the optimised solution for the small kerosene-fuelled rocket

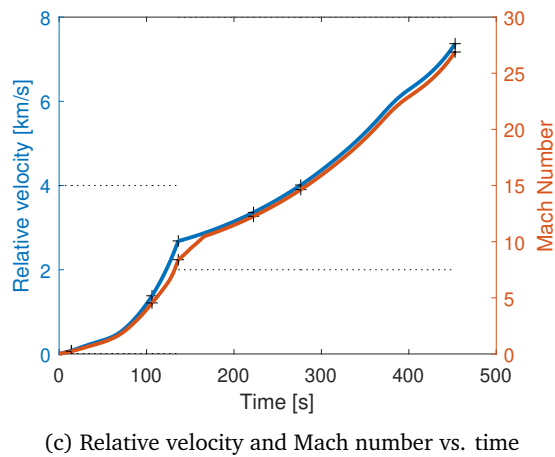
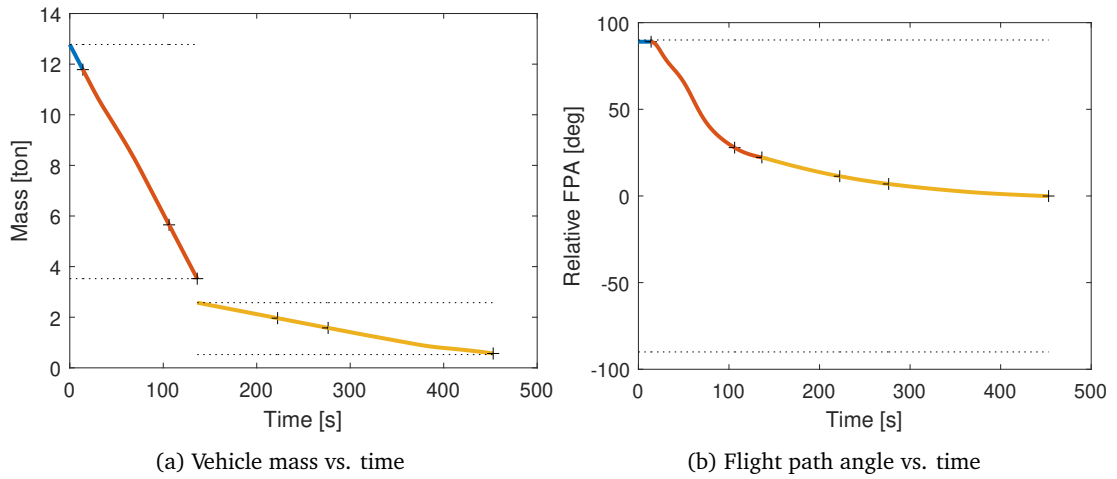
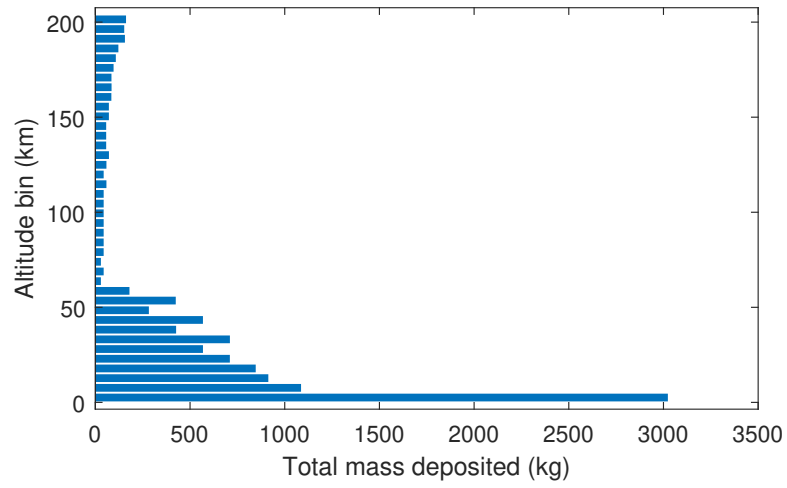
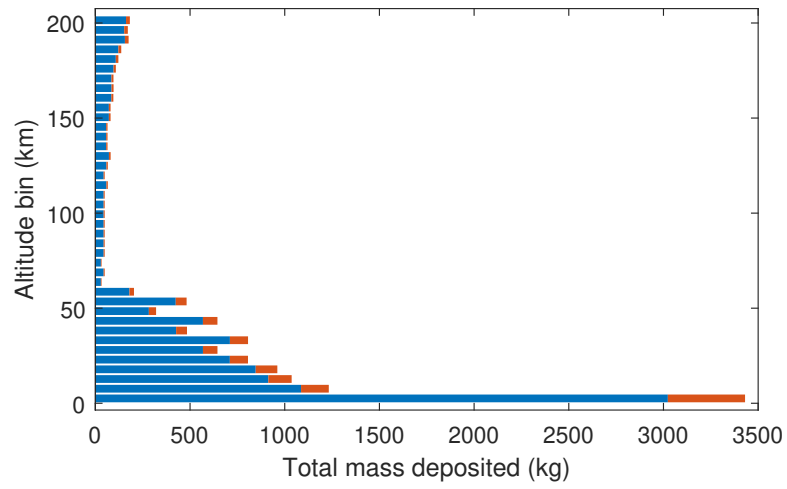


Fig. 6.20 Additional state parameter time history of the optimised solution for the small kerosene-fuelled rocket



(a) Unmodified



(b) Corrected

Fig. 6.21 Total mass of emissions by altitude bin for the small kerosene-fuelled rocket

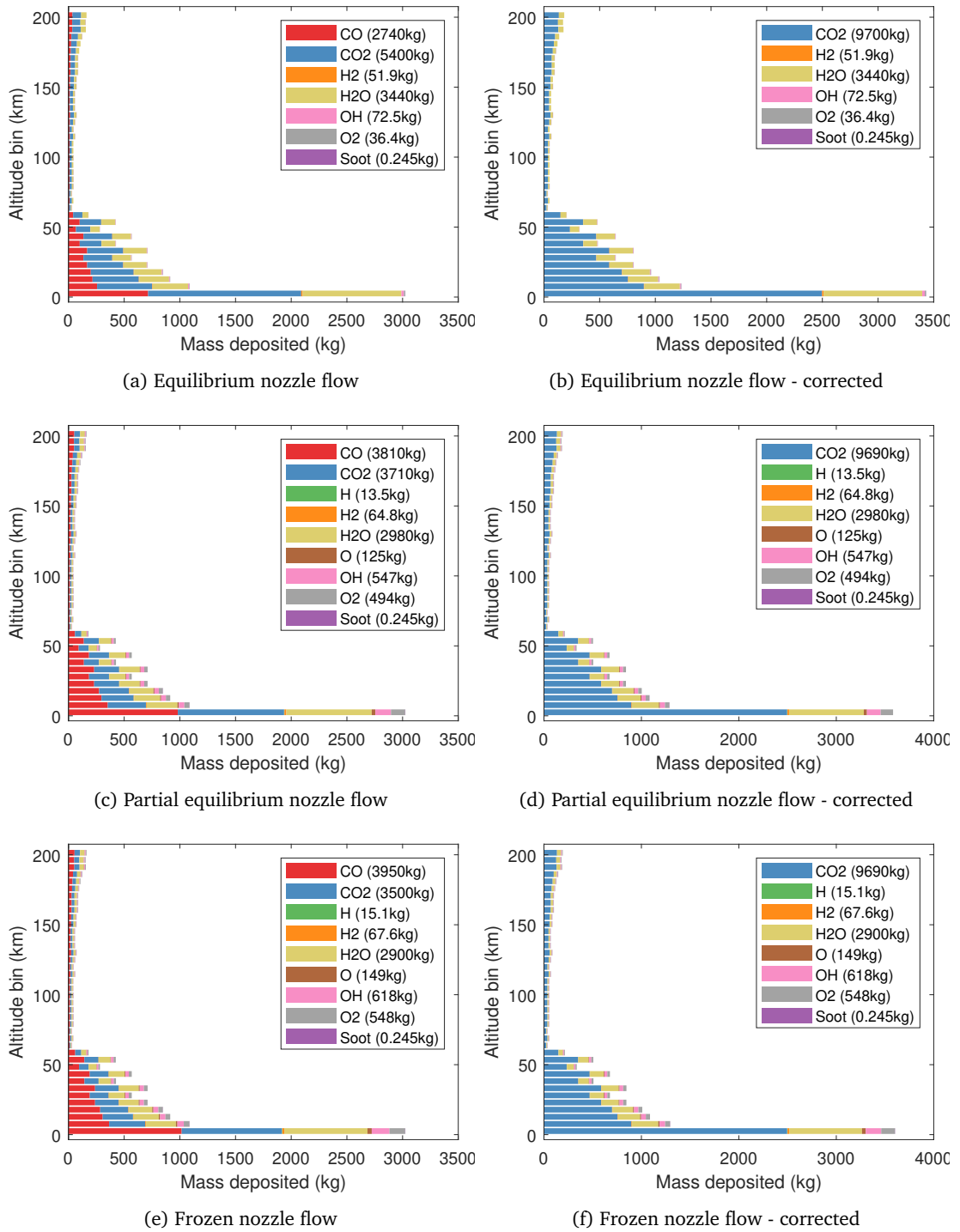


Fig. 6.22 Major species emission by altitude bin for the small kerosene-fueled rocket

6.5 Air-launched spaceplane - kerosene

The air-launched test case is based on the Orbital Access 500R, a conceptual two-stage-to-orbit semi-reusable launch system (Maddock et al., 2018). This employs a reusable first stage capable of unpowered (gliding) and powered flight, with an expendable upper stage. This vehicle assembly is dropped from a carrier aircraft. Propulsion on the first and upper stage are rocket engines. This was chosen as a test case, because its indicative of a class of air launched vehicles that are carried by an aircraft before release and rocket flight. An additional dimension is that it has been designed to be partially reusable, which is another element that will affect environmental impacts.

A multidisciplinary design optimisation was performed to understand the key design drivers and establish the basis for a design trade-off in Maddock et al. (2018). The vehicle was designed for a nominal mission of 500 kg to a 86.4° 650 km orbit, based on the requirements for replenishment launches of the OneWeb constellation. For this test case, the final orbit is the same 28° 200 km orbit in prior test cases, and the mass breakdown is shown in table 6.14.

Table 6.14 Assumed mass breakdown of the air-launched spaceplane

Stage		Mass (kg)
Stage 1	Dry Mass	11343
	Propellant	47030
	Subtotal	58373
Stage 2	Dry mass	1856
	Propellant	10143
	Subtotal	12499
Payload		500
Total		70872

The first stage engine is based on the Yuzhnoye RD-8 rocket engine. It has a vacuum specific impulse of 332 s and a vacuum thrust of 866.91 kN, and uses LOX/RG1 (a Russian rocket kerosene variant) at a mixture ratio of 2.6. The second stage engine is based on the RD809K, also utilising kerosene and with a 352 s and a vacuum thrust of 98.07 kN. These are modelled in HyPro to produce the emission indices as in the other test cases.

Table 6.15 Initial conditions for the air-launched spaceplane

Altitude h , km	12
Velocity v , m s ⁻¹	200
Flight path angle γ , °	15
Heading angle χ , °	90
Latitude λ , °	28.6
Longitude θ , °	-80.6
Mass m , kg	70872

The trajectory optimisation was set up with two phases; the first with two elements and seven control nodes, the second phase with two elements and eight control nodes. The initial conditions are shown in table 6.15 and the optimisation bounds shown in table 6.16.

Table 6.16 Bounds for air-launched spaceplane case, 28° 200 km orbit

	Phase 1	Phase 2
Altitude h , km	[0.001, 100]	[30, 200]
Velocity v , m s ⁻¹	[1, 4e3]	[2e3, 8e3]
Flight path angle γ , °	[-90, 90]	[-90, 90]
Heading angle χ , °	[0, 360]	[0, 360]
Latitude λ , °	[-90, 90]	[-90, 90]
Longitude θ , °	[-180, 180]	[-180, 180]
Angle of attack α , °	[-5, 20]	[-15, 40]
Throttle τ	[0.7, 1]	[0, 1]
Time t , s	[60, 300]	[10, 1000]

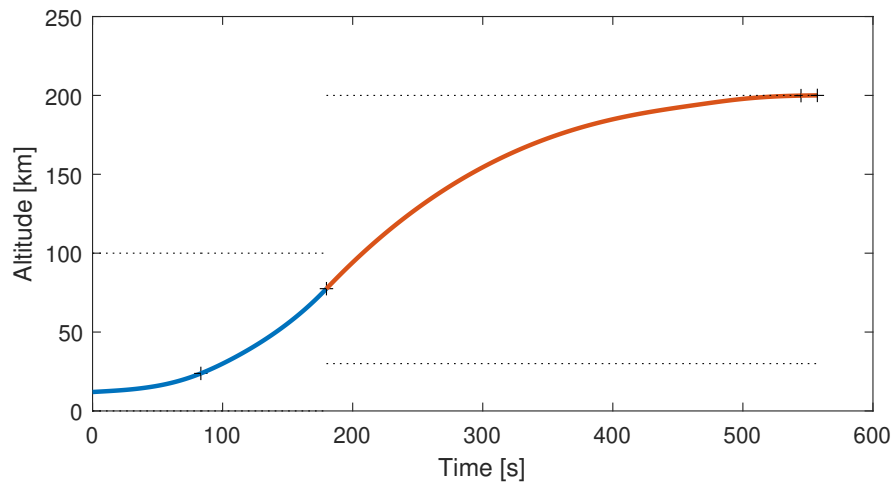
The final mass was 2.96 t, which results in a useful mass to the orbit of 1.1 t, including the 500 kg nominal payload. Compared to the second stage propellant mass in the original paper, 10.643 t, here it is 9.6 t, which accounts for the difference. The resulting trajectories, shown in figs. 6.23 and 6.25, are not dissimilar to other vehicles explored here. However, turning to the control law (fig. 6.24), the angle-of-attack is above 8° until 400 s into the flight, this is because the Orbital Access 500R features a winged design that generates lift.

Only the trajectory of the rocket itself is considered as the flight paths of the captive-carry phase are deliberately extremely variable. The environmental impact of this phase of the flight can be found using methods used for conventional aviation, and could be in the range of a typical short-haul flight to a long-haul flight, depending on the mission in question. In

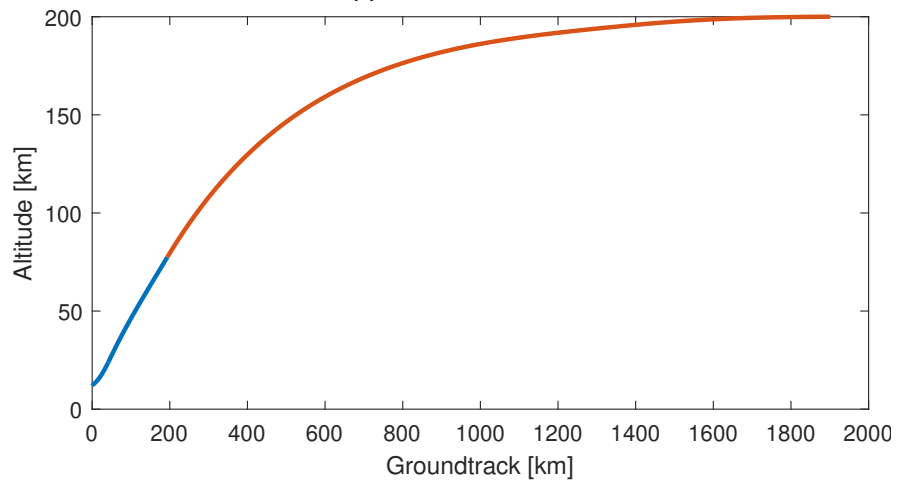
the federally required assessment of environment effects, the FAA calculated the amount of CO₂ equivalent emissions of the carry phase and the launch phase of the LauncherOne rocket, shown in table 6.17 (FAA, 2017). It is interesting to note that the amount of GHGs emitted for the carry phase significantly outweigh the amount produced during the launch phase.

Table 6.17 Proposed Action GHG Emissions per Activity in Metric Tons (FAA, 2017)

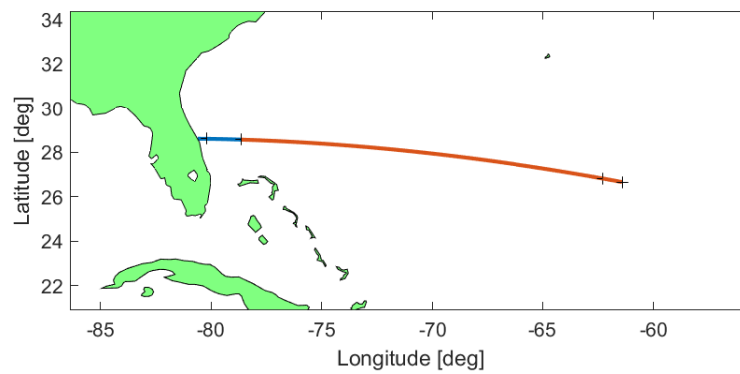
Scenario/Activity	Metric Tons Produced			
	CO ₂	CH ₄	N ₂ O	CO ₂ e
GHG Emissions of Carrier Vehicle Per Landing and Takeoff Cycle (<3000ft)	11.28	0.000242	0.00363	11.401
GHG Emissions of Carrier Vehicle Per Flight to Southern Drop Point (>3000ft)	89.41	N/A	0.00848	91.939
GHG Emissions of Carrier Vehicle Per Flight to Northern Drop Point (> 3,000 ft)	143.05	N/A	0.01358	147.105
GHG Emissions per Launch of Rocket	11.676	N/A	N/A	11.677
Total GHG Emissions for one Launch Event to the Southern Drop Zone	112.375	0.000242	0.00885	115.02
Total GHG Emissions for one Launch Event to the Northern Drop Zone	166.021	0.000242	0.0139	170.18



(a) Altitude vs. time



(b) Altitude vs. ground track



(c) Ground track map view

Fig. 6.23 Position time history of the optimised solution for the air-launched spaceplane

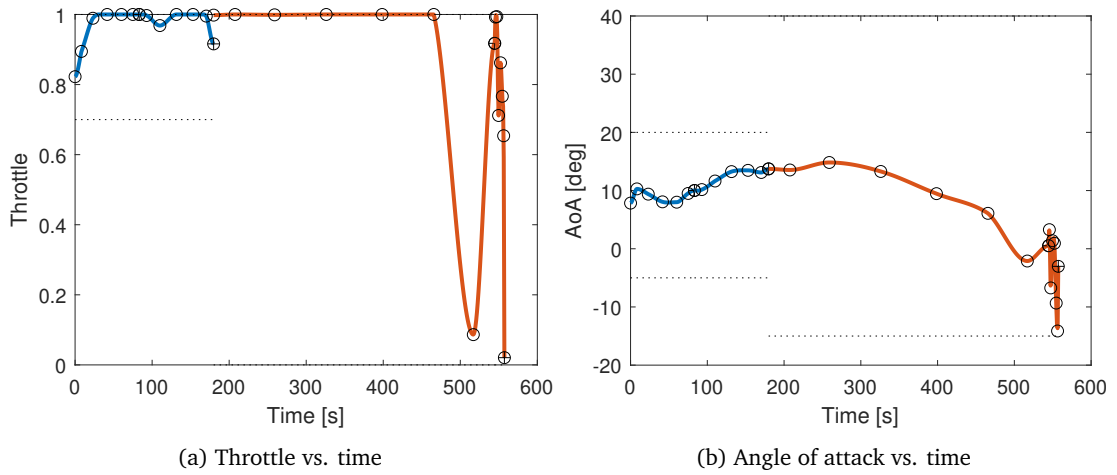


Fig. 6.24 Control time history of the optimised solution for the air-launched spaceplane

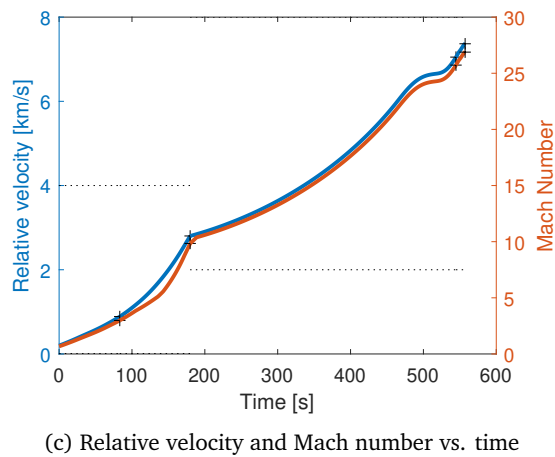
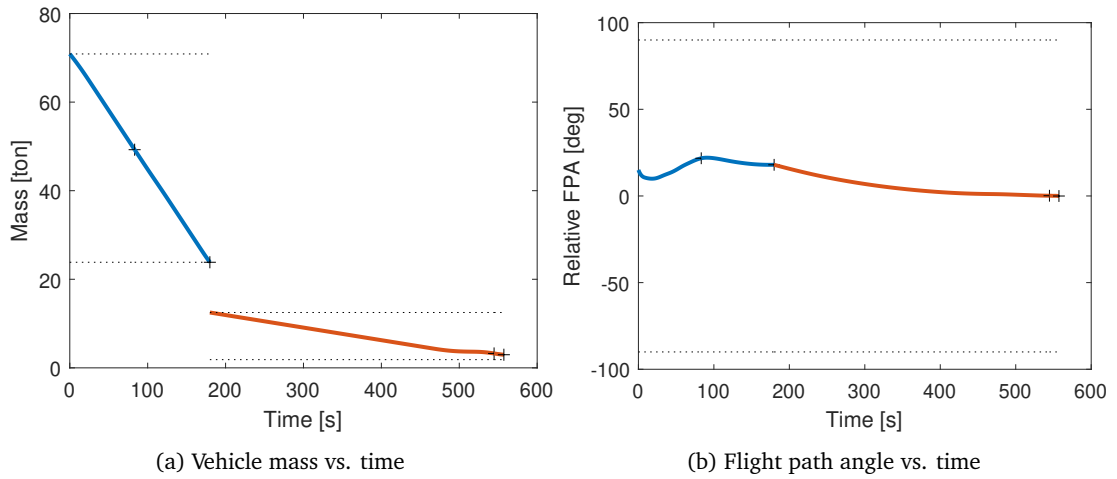
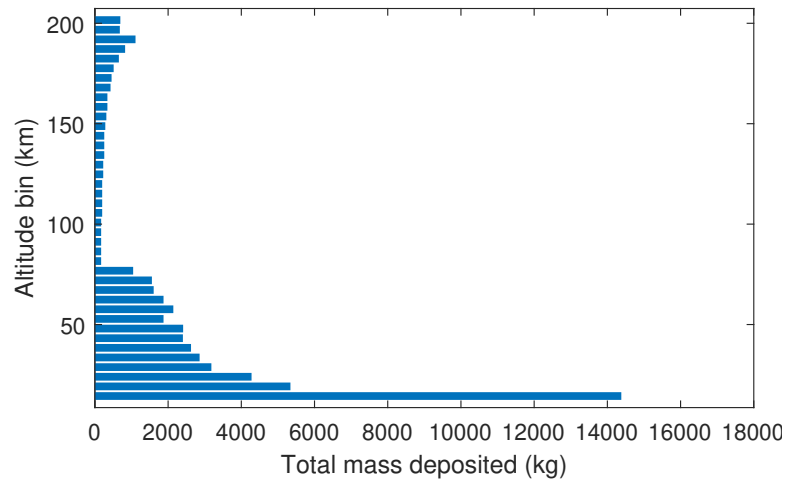
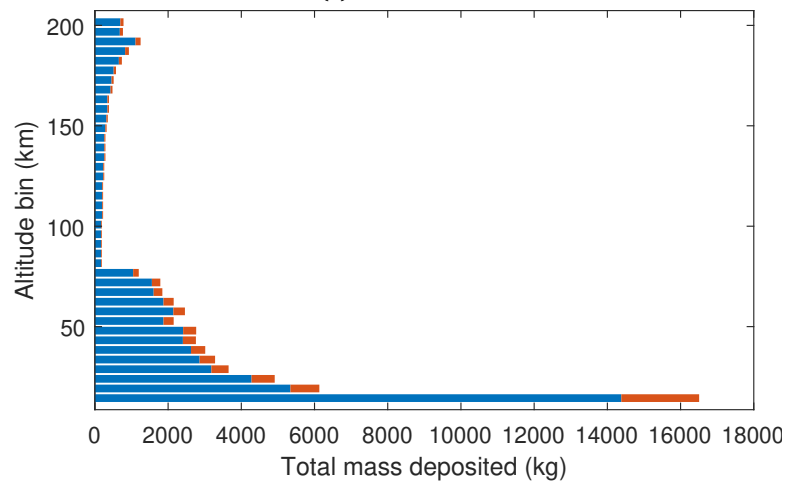


Fig. 6.25 Additional state parameter time history of the optimised solution for the air-launched spaceplane

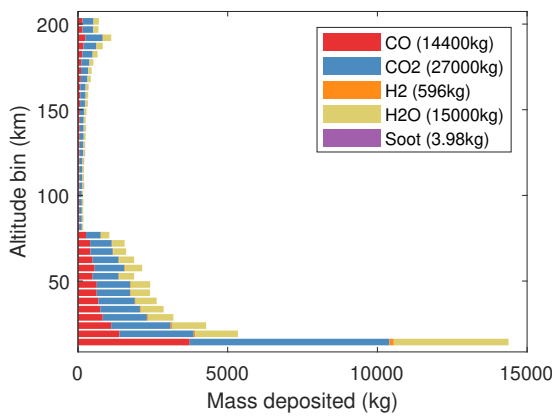


(a) Unmodified

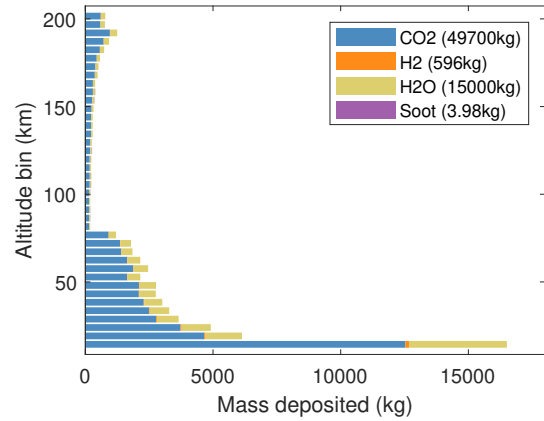


(b) Corrected

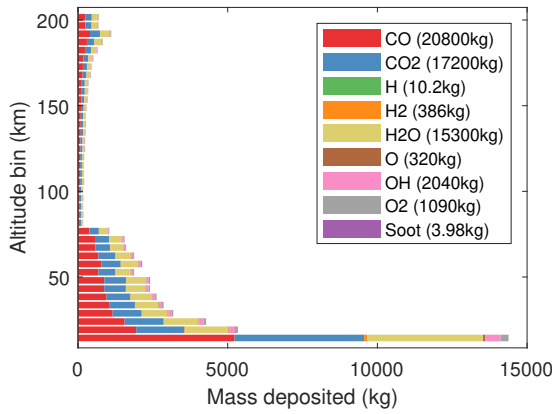
Fig. 6.26 Total mass of emissions by altitude bin for the super heavy methane rocket



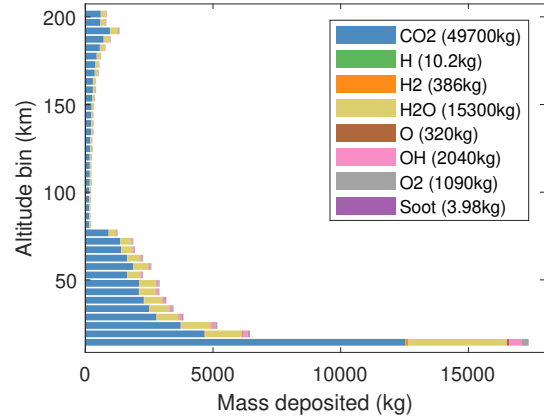
(a) Equilibrium nozzle flow



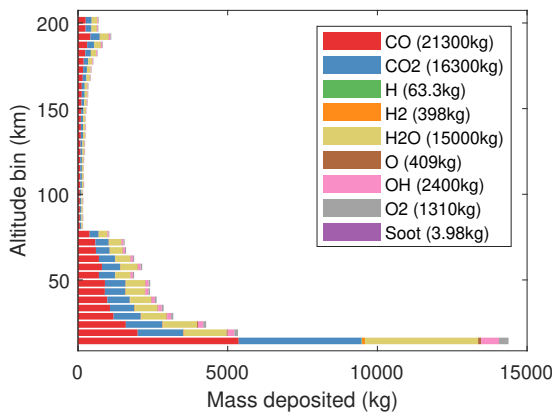
(b) Equilibrium nozzle flow - corrected



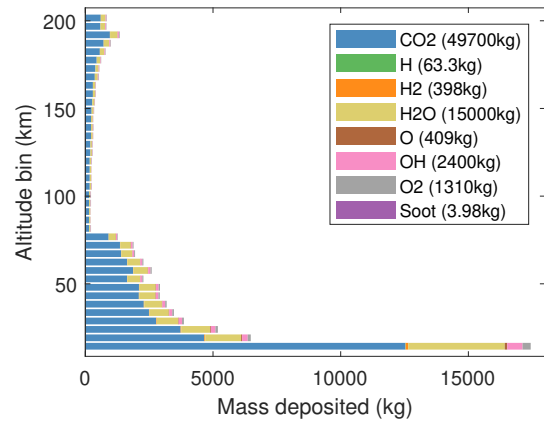
(c) Partial equilibrium nozzle flow



(d) Partial equilibrium nozzle flow - corrected



(e) Frozen nozzle flow



(f) Frozen nozzle flow - corrected

Fig. 6.27 Major species emission by altitude bin for the super heavy methane test case

6.6 RBCC spaceplane - hydrogen

This test case is intended to see how the inclusion of not only an aerodynamic design with lift, but also a propulsion system with atmospheric dependence could affect the profile emissions released into the atmosphere. This is done by modelling the trajectory of a theoretical air-breathing spaceplane, based on the *Hyperion* single-stage-to-orbit vehicle originally conceptualised by [Olds and Bradford \(2001\)](#); [Olds et al. \(1999\)](#). This test case is more complex than the previous vertical launch vehicles, four different propulsion systems, three of which have limited operating regimes. The ejector operates from $0 \leq \text{Mach} \leq 3$, the ramjet from $3 \leq \text{Mach} \leq 6$, the scramjet from $6 \leq \text{Mach} \leq 10$ and the rocket $\text{Mach} \geq 6$. The major constraint on the flight is the dynamic pressure. In the original paper, *Hyperion* flew on a constant dynamic pressure at 95 kPa. In [figs. 5.22 to 5.24](#) the curvefits used in this test case are shown. These figures also show which performance points which exceed a high dynamic pressure, $q > 120$ kPa. This limits the operational range of the engines significantly, and also means there is a large search area that is invalid for the optimiser.

Many previous studies of spaceplanes, including the work by [Olds and Bradford \(1997, 2001\)](#) assumed a general guidance law based on some user-defined criteria. In the case of *Hyperion*, the assumption was made that the optimal trajectory would be a constant-dynamic pressure trajectory, since this is optimal for the engine. However, this approach will not necessarily capture the optimal control when the various nonlinear effects such as the aerodynamics and propulsion system performance are coupled together.

The aerodynamic model is extracted from the *Hyperion*-derived model for a sled-launch SSTO vehicle ([Young et al., 2006](#)). The aerodynamic model is only given at Mach 4, 6 and 18, so the subsonic aerodynamic performance is based on the supersonic performance. This model was also designed for a different vehicle concept, which additionally used a sled to perform initial acceleration unlike the *Hyperion* conceptual vehicle.

To address the consequences of these differences and find feasible trajectories, several measures were taken. Firstly, the takeoff and early stages of the flight are not modelled in detail, it is assumed that the ejector mode of the engine is capable of producing enough thrust to takeoff from the runway. Additionally, the allowable angle attack bounds are

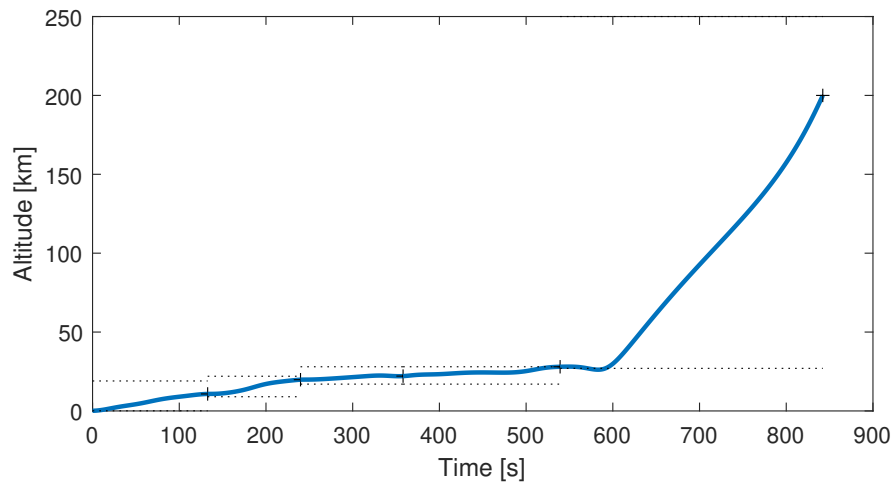
extended to between $-2 \leq \alpha \leq 16^\circ$ in the first phase of flight, and the number of engines on the vehicle is introduced as an optimisation parameter between 5 and 6.

Another difference with the original approach is how transitions between propulsion system modes are managed (i.e. scramjet to rocket). In [Olds et al. \(1999\)](#) the transitions were somehow smoothed between modes, but it is unclear how this was actually implemented, and so the approach here assumes that instantaneous transitions between engine modes are possible. This have been specified based on known operational limitations of the engine modes, and are therefore not optimised:

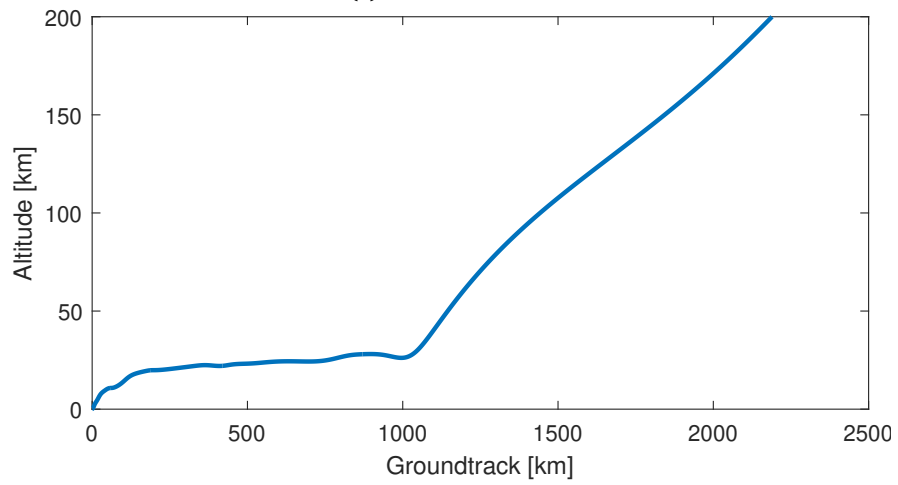
- Ejector mode to ramjet - Mach 2,
- Ramjet mode to scramjet - 22.4 km, 1790.2 m s^{-1} , Mach
- Scramjet mode to rocket - 28 km, 2790.3 m s^{-1} , Mach

To be directly comparable to the other test cases, the final orbital conditions are a 200km final orbit, whereas the original optimisation was a 50nmi x 100nmi holding orbit. For spaceplanes, a noncircular, orbit like this is a useful way of boosting mass into the final orbit because a kick-stage only has to add energy to the payload rather than the full vehicle.

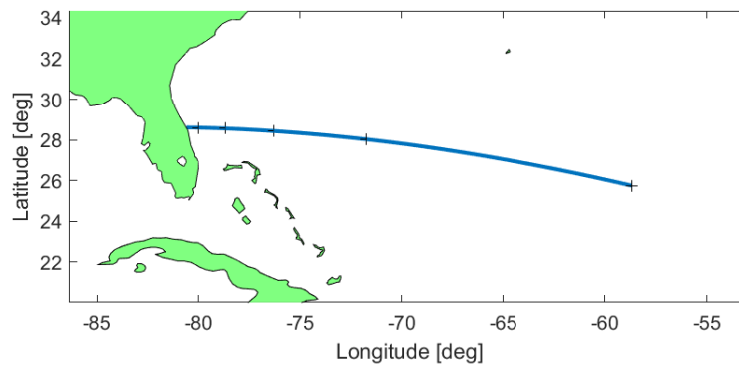
Even with these differences with the original work, a feasible trajectory is found which can be used to indicate the key features of an air-breathing SSTO to compare against the other vehicles considered. It is clear that the limitations of this modelling approach will affect the accuracy of any emissions profile quantification, but considering the uncertainties involve in other aspects of the approach, it is likely to suitable to understand the overarching behaviour. The trajectory shown in [fig. 6.28](#) and [fig. 6.30](#) is very different to those of a vertical launch vehicle. It clearly stays inside the atmosphere for a much longer period of time due to the high efficiency of the airbreathing propulsion systems. Whilst using airbreathing engines, part of the emitted mass is from the atmosphere, as only the fuel is stored in the vehicle. The resulting control law, shown in [fig. 6.29](#) is significantly more complicated than any of the other vehicles studied investigated, due to the additional size of the solution space. At the beginning of the trajectory, the angle-of-attack is very high, due to the low lift being generated at low velocities. As the velocity increases, lift increases and the angle-of-attack is able to be reduced.



(a) Altitude vs. time



(b) Altitude vs. ground track



(c) Ground track map view

Fig. 6.28 Position time history of the optimised solution for the RBCC SSTO spaceplane

Table 6.18 Initial conditions for RBCC SSTO spaceplane, 28° 200 km orbit

Altitude h , km	0.1
Velocity v , m s ⁻¹	300
Flight path angle γ , °	2
Heading angle χ , °	90
Latitude λ , °	28.6083
Longitude θ , °	-80.6041
Mass m , kg	363000

Table 6.19 Bounds for the RBCC SSTO spaceplane test case, 28° 200 km orbit

	Phase 1	Phase 2	Phase 3	Phase 4
Altitude h , km	[0.09, 19]	[9, 22]	[17, 28]	[27, 250]
Velocity v , m s ⁻¹	[250, 4e2]	[800, 2e3]	[1.5e3, 3.5e3]	[2.5e3, 10e3]
Flight path angle γ , °	[-90, 90]	[-90, 90]	[-30, 30]	[-30, 30]
Heading angle χ , °	[0, 360]	[0, 360]	[0, 360]	
Latitude λ , °	[-90, 90]	[-90, 90]	[-90, 90]	
Longitude θ , °	[-180, 180]	[-180, 180]	[-180, 180]	
Angle of attack α , °	[-2, 30]	[-2, 10]	[-2, 10]	[-2, 10]
Throttle τ	[0.8, 1]	[0.8, 1]	[0.8, 1]	[0.6, 1]
Time t , s	[30, 300]	[25, 200]	[50, 500]	[100, 800]

The emission profile for the RBCC spaceplane are shown in fig. 6.31a and stacked by engine mode in fig. 6.31b. The vast majority of the time of flight is spent in either scramjet or rocket mode, both of which operate entirely in the stratosphere or above, and represent the majority of the emissions produced. This is consistent with the performance and application of the different engine modes of the RBCC engine, the ejector is only active until the $M \approx 2.5$ and the ramjet is the most efficient stage of flight with highest specific impulse and the lowest fuel burn (visible in fig. 6.30a).

The emissions profiles for the RBCC spaceplane are clearly very different to the vertical launch vehicles (e.g. figs. 6.6, 6.11, 6.16 and 6.21), with peak emissions during the scramjet mode between 22 km and 28 km. This emissions profile is consistent with the performance of the engine. The ejector mode is relatively inefficient, but is only active until the vehicle reaches Mach 2, a relatively short proportion of the overall flight. The ramjet mode is the highest efficiency, with peak specific impulse reaching 3500 s, and so fuel burn and emissions

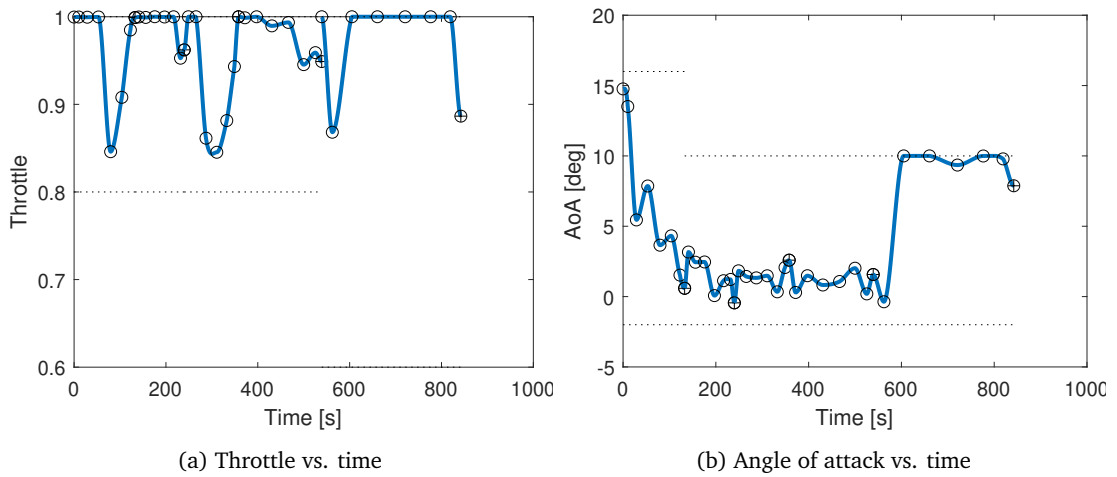


Fig. 6.29 Control time history of the optimised solution for the RBCC SSTO spaceplane

are effectively lowest for this portion of flight. The scramjet is significantly less efficient than the ramjet, and is active for almost 200 s. As only H_2O is being considered here, the environmental impacts are straightforward to evaluate (as discussed in chapter 7). Only stratospheric water emissions (over 15 km) are included in the radiative forcing calculations, so very little of the ejector mode's emissions contribute. If a propulsion model was used capable of predicting other emissions such as NO_x , this picture might change, particularly as ramjets reduce the incoming flow to subsonic velocity, resulting in higher combustion temperatures and longer residence times.

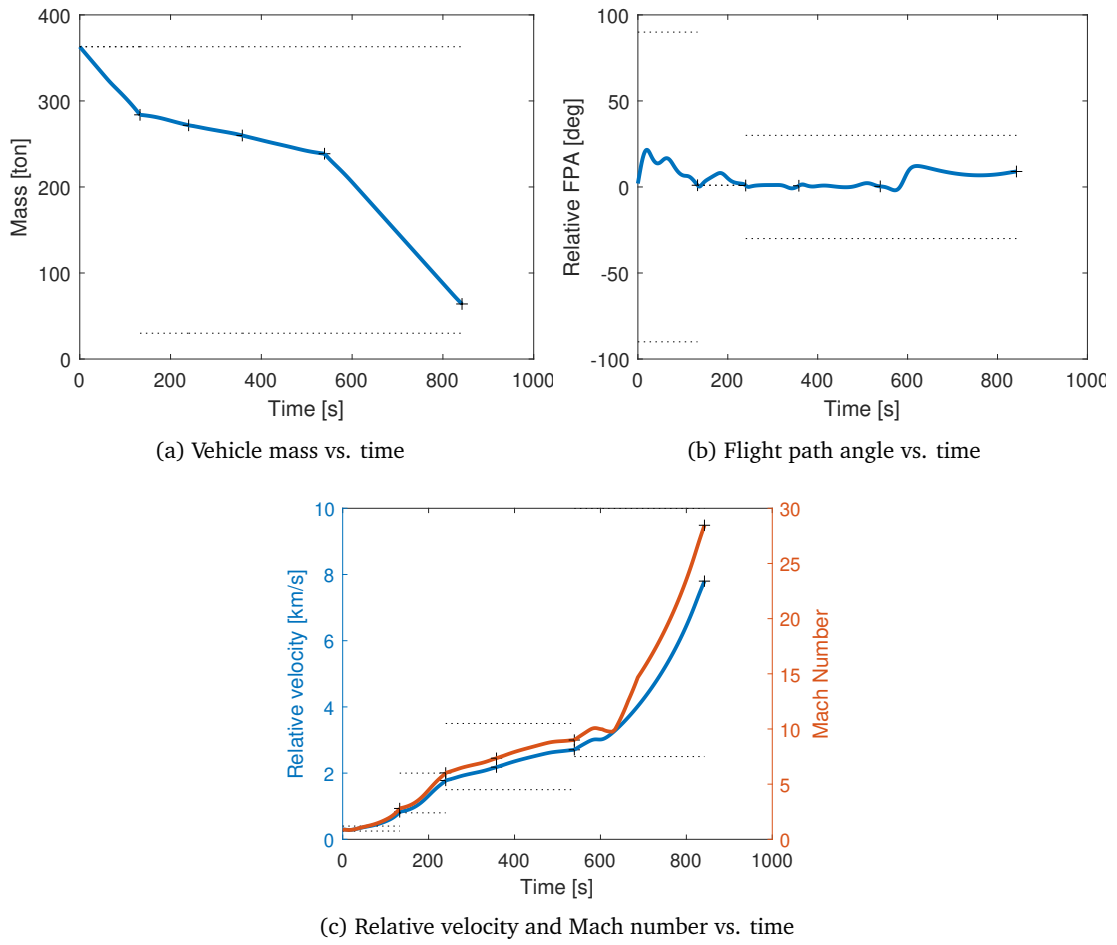


Fig. 6.30 Additional state parameter time history of the optimised solution for the RBCC SSTO spaceplane

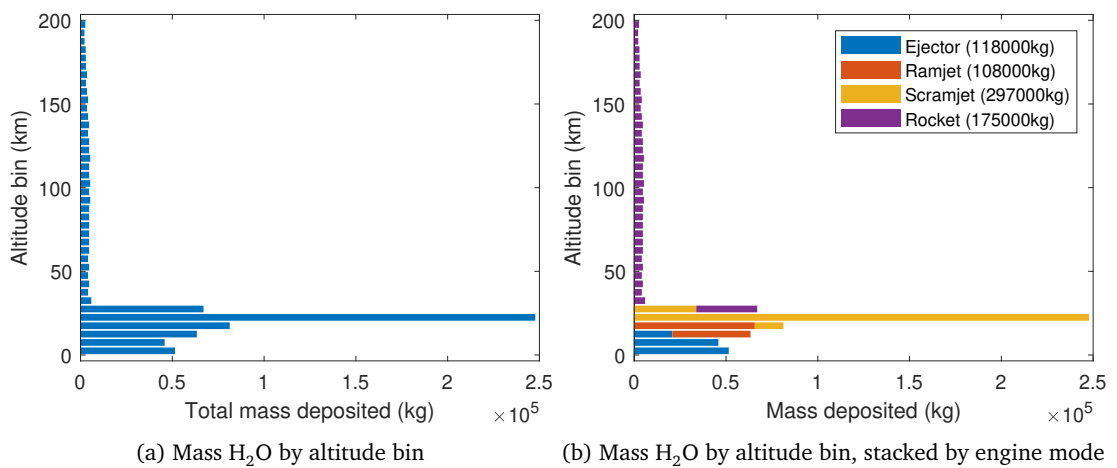


Fig. 6.31 Emissions profiles for the RBCC SSTO spaceplane

6.7 Summary

In this chapter, the setup and assumptions use to model a series of launch vehicles trajectories have been setup. The final optimised and feasible trajectories are combined with the emission indices for each vehicle to produce emission profiles. This combines the tools described in chapter 3 and chapter 5, which enables the emissions profile of any launch vehicle to be estimate if appropriate models for the propulsion systems and aerodynamics are available.

The vehicles chosen for the test cases represent some key design tradeoffs; hydrogen vs. kerosene fuel for medium lift rockets, the sizing of the vehicle ranging from small launchers to heavy lift, air-dropped winged vehicles and air-breathing powered single-stage-to-orbit. Where possible, these have been based on real vehicles where some data exists to compare performance against, but several are in-development or purely conceptual. This shows the flexibility that this modelling-based approach provides.

The trajectories and emissions profiles of the vertical vehicles are very similar in shape. This confirms the idea that the design of the vehicle to some extent sets the optimal trajectory. Differences in the optimal control laws do have an impact, particularly the staging time which governs the altitude at which the majority of emissions occur. The two other vehicles modelled here provide insight into the amount of influence the overall concept of operations, along with the subsequent design, have on the emissions profile. Both the air-launched winged spaceplane and the RBCC spaceplane exhaust a significantly higher proportion of their emissions in the stratosphere, the prior due to its engine start at altitude, and the latter because of its airbreathing engines. How much this contributes to additional environment impacts is explored in chapter 7.

7 | QUANTIFICATION AND EVALUATION OF ENVIRONMENTAL IMPACT

This chapter begins with a discussion of different approaches to quantify the environmental impact of launches in section 7.1, including global warming potential and radiative forcing indices. Section 7.1.3 subsequently describes a method of estimating the radiative forcing for launches (Ross and Sheaffer, 2014), which are then applied to the launch vehicle emission profiles from chapter 6 in section 7.2, which contains the main findings of this work. These include the use of corrective factors to include post-plume chemistry (section 7.2.1), the sensitivity of radiative forcing due to the black carbon produced by kerosene-fuelled engines (section 7.2.2) and the influence of vehicle design (section 7.3).

The last part of this chapter introduces and discusses several experiments to investigate how emissions can be considered during the design of a launch vehicle:

- Selecting propellants for an environmentally optimised small satellite launcher between kerosene, methane and propane (section 7.4.1)
- Minimising the radiative forcing as the cost function in the trajectory optimiser (section 7.4.2)

7.1 Quantifying environmental impact

The next step is to evaluate the impact of emissions deposited in the atmosphere. Comparing only emission masses is flawed because it does not account for the specific environmental

impacts of individual emissions, nor does it enable effective comparison between different propellant combinations or vehicle architectures. The environmental impact considered here is the effect of these emissions on the climate. Whilst other impacts such as ozone loss could have been considered, there is a relatively sparse consideration of radiative forcing in the literature, whilst significant efforts were made to understand the impacts of launch activities on ozone in the 1990s and 2000s, as discussed in section 2.3. However, there is no reason that the emissions profiles generated in chapter 6 could not be used to inform their effect on other environmental impacts.

As discussed previously, afterburning reactions in the plume largely remove radical and minor species, and can also complete the combustion of intermediary species such as CO and soot. In section 4.3 and section 6.1, the approach used in this thesis to account for this process has been discussed for these two species.

Two different approaches to quantifying the environmental impact of launcher emissions are discussed in this section. The first is to convert the emissions into standard metrics commonly used for life cycle assessment, whilst the second is to use simple models to estimate the direct radiative forcing caused by launch operations.

7.1.1 Global warming potential (GWP)

A common metric used to characterise the effects of emissions on global warming used in life cycle assessment is the global warming potential characterisation factor, which estimates the potential warming effect from emissions in terms of kgCO₂-eq. The standard values of methane and nitrous oxide are shown in table 7.1.

Table 7.1 Global warming potential (IPCC, 2013). Other substances are included in the IPCC GWP figures, but they are species not related to spaceflight.

Name	Chemical formula	GWP (100-year time horizon)
Carbon dioxide	CO ₂	1
Methane	CH ₄	28
Nitrous oxide	N ₂ O	265

The main drawbacks of GWP are that it only includes the direct global warming effects of a few key species and does not account for indirect radiative forcing contributions, as it is intended to be used for well-mixed gases with long lifetimes in the atmosphere. These

neglected but potentially significant sources of indirect radiative forcing include: ozone formation from NO_x , which scales not only with NO_x emissions but with time and location, contrail formation and stratospheric water. As such, [Jungbluth and Meili \(2019\)](#) concluded that GWP is not usable on its own for quantifying aviation's impact. A useful measure of the impact of aviation is difficult to define due to the timescales that the effects may be present over, CO_2 remains in the atmosphere for centuries, whilst other indirect effects are over a much shorter timescale. The same conclusion holds true for space launches, with some of the most significant atmospheric effects occurring on timescales well below the residence time of CO_2 . Averaging times used to calculate GWP are usually 20-, 100- or 500-years, which represents the timeframe over which the energy absorbed by the species in question is calculated. The choice of these time horizons has an impact on the value that is calculated, for example, GWP estimates for methane on a 20- averaging time are in the range of 84–87 $\text{kgCO}_2\text{-eq}$ compared to the 28 $\text{kgCO}_2\text{-eq}$ in table 7.1 ([Vallero, 2019](#)). Shorter averaging times prioritise short-lived gases, in this case methane which has significantly shorter lifetime than CO_2 . Some of the radiative forcing impacts for aviation and spaceflight are intense, time-dependent and very short term and are overlooked by using this type of metric.

These current life cycle assessment characterisation factors relate only to ground-based emissions and therefore may only have limited direct utility when applied to flight emissions. However they are valuable for characterising emissions during ground operations, for example the use of methane as a fuel (fuelling, defueling, recycling etc) or in the event of a failure which results in significant amounts of methane vaporising rather than combusting. Methane is a significantly more powerful greenhouse gas than CO_2 , and so excess gas is usually burnt in pilot flames when being handled. It is interesting to note that ground-based operations of methane-fuelled vehicles have the potential to contribute more to climate change than the launch operations themselves.

7.1.2 Radiative Forcing Index

Another possible metric for evaluating the impact of emissions during launch is to estimate the radiative forcing index (RFI). RFIs have been used to create an aviation-specific characteristic factor that can account for all the impacts on the atmosphere, based on more

detailed simulations or observations of radiative forcing. The RFI is a factor which can be multiplied by direct CO₂ emissions to account for all other climate change effects that can be attributed to the total aircraft emissions within a reference year. These are also propellant specific.

Even for aviation, a standard methodology is not defined and there are a range of RFIs that can be used, with some debate about which numbers to use in LCA. [Jungbluth and Meili \(2019\)](#) recommend using a factor 5.2 kgCO₂-eq /kgCO₂ for the lower stratosphere and upper troposphere, but the range in estimates is from 1 - 8.5.

It is possible that the effect of emissions from launch vehicles using a kerosene derived fuel could be estimated using RFIs like these, with the caveat that there are certainly differences between launch vehicles and aviation, particularly the emissions rates of black carbon and NO_x, and the trajectories of launch vehicles that fly beyond the lower stratosphere. Unfortunately, RFIs cannot be established for other propellant combinations because there is not an appropriate body of detailed evidence to draw upon, and so another approach is needed.

7.1.3 Estimating Radiative forcing

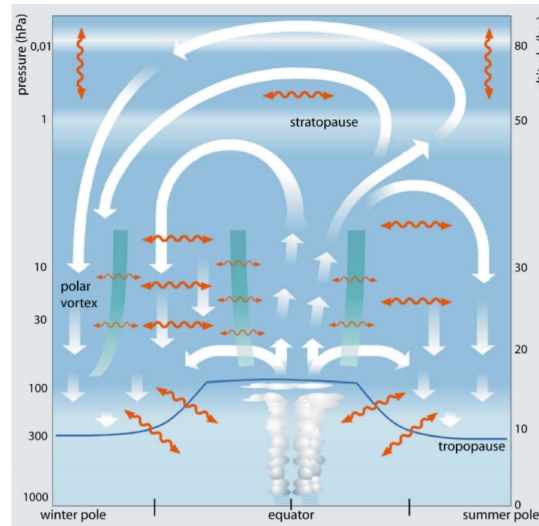
Another group of approaches is to choose the radiative forcing as the parameter that can be compared across different launch concepts, propulsion systems and trajectories. Ideally this would be done with detailed atmospheric chemistry models, but these are out of scope for preliminary design. Two attempts ([DeSain and Brady, 2014](#); [Ross and Sheaffer, 2014](#)) to produce parametric and simplified models of the radiative forcing have been made in the literature, both of which are described in the following sections for the three species consider, CO₂, H₂O and soot.

Conventional rockets burn most of their propellant above 15 km which is considered as the beginning of the stratosphere here. In terms of climate impacts, the effect of many chemicals emitted into the stratosphere are of a higher concern than in the troposphere due to the increase in lifetime - typical lifetimes in the troposphere are of the order of several weeks, whilst stratospheric emissions can be on the order of 4 - 6 years.

The altitude of the tropopause, the interface between the troposphere and the stratosphere, varies with latitude, as shown in fig. 7.1 from [Bönisch et al. \(2011\)](#). It can be as low

as 10 km at the poles, to more than 15 km near the equator. Figure 7.1 also shows several mechanisms which lead to long lifetimes in the stratosphere. The white lines represent the overall stratospheric residual circulation, the red lines two-way mixing processes and the green lines stratospheric transport.

Fig. 7.1 Schematic of Brewer-Dobson circulation (BDC) showing the circulation of [Bönisch et al. \(2011\)](#)



[Waugh and Hall \(2002\)](#) calculated the mean age of tracer species within the stratosphere based on a series of models and measured results. The lifetime ($\tau = 4$) used by [Ross and Sheaffer \(2014\)](#) for species in the stratosphere is based on the average of these. However, it is clear that the altitude and latitude of emitted species is important in determining the radiative forcing of a particular launch.

[Ross and Sheaffer \(2014\)](#) explain that their ‘nonstandard approach’ for estimating radiative forcing is appropriate for their purpose of providing order of magnitude estimates to compare various propellant combinations and launches against other sources of radiative forcing. Here, the objective is similar, but the comparison is extended to different vehicle architectures, and also to include vehicle performance.

In this approach, the instantaneous RF is defined as the change in flux at the top of the atmosphere, considering the effects of species in the stratosphere on the flux. Scattering and absorption are assumed to be separable into shortwave (SW) and longwave (LW) components, then the instantaneous RF is difference between integrals of the SW and LW fluxes:

$$\text{RF} = \left\{ \int I(\lambda)_{LW} \sigma_a(\lambda)_{LW} d\lambda - \int I(\lambda)_{SW} \sigma_s(\lambda)_{SW} d\lambda \right\} MA^{-1} \quad (7.1)$$

RF is the instantaneous radiative forcing

$I(\lambda)_{LW}$ and $I(\lambda)_{SW}$ are the mean solar SW and terrestrial LW flux spectra

σ_a is the mass-specific absorption coefficient

σ_s is the mass-specific scattering coefficient

M is the mass of the particular species in question

A is surface of area of the accumulation region

This equation is modified for each specific emission considering the characteristics it has.

Carbon dioxide

Carbon dioxide is a greenhouse gas with a long lifetime in the atmosphere, several hundred years, and the CO₂ released by the first orbital launches is still having an a radiative forcing effect today, and will for the next several hundred years (Archer and Brovkin, 2008). However, the amount released to date is very small compared to other anthropogenic sources, Ross and Sheaffer (2014) estimate around 10×10^6 t since the dawn of the space age. Carbon dioxide is well mixed within the atmosphere, so emissions from all altitudes need to be considered.

The radiative forcing can be estimated for CO₂ by considering the long wave absorption component of eq. (7.1):

$$\text{RF}_{\text{CO}_2} = \frac{I_{LW} \sigma_{\text{CO}_2} (\overline{M}_{\text{CO}_2} + NM_{\text{CO}_2})}{A_E} \quad (7.2)$$

where

RF_{CO_2} is the radiative forcing due to the released CO₂

I_{LW} is the integrated long wave flux, assumed to be 235 W m^{-2} (Ross and Sheaffer, 2014)

σ_{CO_2} is the mass-specific absorption coefficient, equal to $0.005 \text{ m}^2 \text{ kg}^{-1}$

$\overline{M}_{\text{CO}_2}$ is the accumulated CO_2 burden of the atmosphere due to all prior launches

N is the number of years from 2013

M_{CO_2} is the mass of CO_2 released by the launch

A_E is the area of the surface of Earth illuminated by the sun, assumed here to be equal to 50% of the surface area of the Earth, $\approx 2.5505 \times 10^{14} \text{ m}^2$

This equation may be modified to estimate the impulse effect of a single launch (compared to the effect of steady state accumulation) by neglecting prior launches ($\overline{M}_{\text{CO}_2} = 0$) and setting $N = 1$. Note that this equation is formulated with respect to 2013 due to the calculation of all prior CO_2 emissions (e.g. $\overline{M}_{\text{CO}_2}$) in the original paper.

Ross and Sheaffer (2014) used this approach to quantify the emissions for a single launch of a reference vehicle with different propulsion systems. The results shown in Ross's paper are not directly reproducible from inputs they have published in the paper ($1.38 \times 10^{-9} \text{ W m}^{-2}$ instead of $6 \times 10^{-9} \text{ W m}^{-2}$ for a kerosene rocket, and $4.61 \times 10^{-10} \text{ W m}^{-2}$ instead of $2 \times 10^{-9} \text{ W m}^{-2}$ for a SRM, a consistent difference of a factor of 4.34). It is not clear if this is a publishing error or if the specific results are incorrect. DeSain and Brady (2014) found that these results were broadly consistent with their own approach, where the emitted mass of CO_2 from a launch (or a set of launches) was compared to overall expected trends in carbon dioxide addition into the atmosphere:

$$\text{RF}_{\text{CO}_2} = \frac{M_{\text{CO}_2}}{M_{\text{total,CO}_2}} \frac{12 \text{ g}}{44 \text{ g}} \Delta\phi_{\text{CO}_2} \text{RE} \quad (7.3)$$

where

RF_{CO_2} is the radiative forcing due to the released CO_2

M_{CO_2} is the mass of the CO_2 released by the launch vehicles considered (e.g. a single launch, or all US launches, etc)

$M_{\text{total,CO}_2}$ is the global CO_2 emissions from all sources per year, assumed to be 7 Gtyr^{-1}

$\Delta\phi_{\text{CO}_2}$ is the growth rate in CO_2 volumetric concentration, assumed to 1.9 ppmv yr^{-1}

RE is the radiative efficiency, radiative forcing per CO₂ volumetric concentration, assumed to be 0.015 48 Wm⁻² ppmv⁻¹ based on the value used by IPCC to estimate GWP figures (Ramaswamy et al., 2001)

Water Vapour

Stratospheric water vapour can have two separate influences on radiative forcing, first by warming the troposphere through LW and SW absorption and also by cooling the stratosphere through LW emission. Ross and Sheaffer (2014) estimated the amount of radiative forcing with:

$$RF_{H_2O} = \frac{\sigma_{H_2O} I_{LW} M_{H_2O}}{A} \quad (7.4)$$

where,

RF_{H_2O} is the radiative forcing due to the release of stratospheric water vapour

I_{LW} is the integrated long wave flux, assumed to be 235 W m⁻²

σ_{H_2O} is the mass-specific absorption coefficient, equal to 4 m² kg⁻¹

M_{H_2O} is the mass of H₂O released by the launch

A is the area of the accumulation region (15 - 30km and 30°N - 80°N)

This approach made a series of assumptions and specifically noted that the uncertainty could introduce errors of a factor of three. It also neglects any potential atmospheric effects of mesospheric cloud formation.

The approach taken by DeSain and Brady (2014) is slightly different, by calculating the cumulative effects as a sum of the first order reactions:

$$[m_{H_2O}]_t = \sum_{t_1=1985}^{t_2=2013} [m_{H_2O}]_{t_1} e^{t/\tau} \quad (7.5)$$

The amount of radiative forcing is found by small perturbations, where the adjusted radiative forcing, $\Delta RF = f(x) - f(x_0)$:

$$\Delta RF = \frac{0.76}{\sqrt{1+0.01(x+x_0)}} + \frac{0.293(x+x_0)}{1+0.046(x+x_0)} - \frac{0.76}{\sqrt{1+0.01x_0}} - \frac{0.293x_0}{(1+0.046x_0)} \quad (7.6)$$

where x_0 is the initial water vapour concentration and x is the small perturbation. [DeSain and Brady \(2014\)](#) found that the two methods were in reasonable agreement when other factors were equivalent.

Black Carbon

Black carbon accumulates in the stratosphere with relative absorbs solar SW radiation, and does not interact with terrestrial LW, and so the eq. (7.1) can be simplified to:

$$RF_{BC} = \frac{I_{SW}\sigma_{BC}M_{BC}}{A} \quad (7.7)$$

where,

RF_{BC} is the radiative forcing due to the release of stratospheric black carbon

I_{SW} is the integrated short wave flux, assumed to be 342 W m^{-2}

σ_{BC} is the mass-specific absorption coefficient, equal to $1 \times 10^4 \text{ m}^2 \text{ kg}^{-1}$

M_{BC} is the mass of BC released by the launch

A is the area of the accumulation region (15 - 30km and 30°N - 80°N)

Similarly to the previous cases, the approach used in [DeSain and Brady \(2014\)](#) is to scale the estimated RF from all source anthropogenic black carbon by the amount predicted to be emitted from launch vehicles.

7.2 Comparison

The simplest comparison between the launch vehicles modelled in chapter 6 is to compare the total mass of each emission during the numerically calculated trajectories (table 7.2). In this case, the emission profiles are summed across all altitude bins. There is some utility in understanding the mass of these emissions, particularly when considering only one emission across the vehicles. For example, it is clear that the super heavy methane vehicle emits the most CO_2 and H_2O . However, the varying sizes of the launch vehicles disguises how much of each emission is produced relative to the capability of the vehicle. This can be better

expressed by calculating a mass of each emission normalised by payload capability to the reference orbit:

$$\hat{M}_x = \frac{\sum_{h=1}^{h_{max}} m_{h,x}}{m_{payload}}, \quad (7.8)$$

where,

\hat{M}_x is the normalised mass of emissions for species x across the entire flight

$m_{h,x}$ is the mass of emission species x emitted in altitude band h

h_{max} is the index of the highest altitude band

$m_{payload}$ is the mass of the useful payload for the trajectory associated with this emissions profile

Table 7.2 Total emitted mass by species (where applicable, equilibrium rocket models are assumed and corrective factors are included)

Class	Mass (tonne)			Normalised Mass ^a		
	CO ₂	H ₂ O	BC	CO ₂	H ₂ O	BC
Medium kerosene ^b	508	133	0.111	21.8	5.71	0.00477
Medium hydrogen	-	212.3	-	-	22.5	-
Super heavy methane	2510	1910	-	25.1	19.1	-
Small kerosene	9.70	3.44	2.45×10^{-1}	43.1	15.3	0.00109
RBCC spaceplane	-	698	-	-	87.1	-
Airlaunch kerosene	49.7	15.0	0.00398	99.4	30.1	0.0100

^aNormalised mass is the mass of emission divided by the delivered mass to orbit, as shown in eq. (7.8)

^bTotal mass is greater than the propellant mass as this includes corrections in which ambient air is involved

This is an improved metric, as it enables a more intuitive and fair comparison of each vehicle in each type of emission, but it is in most cases difficult to evaluate and understand the overall effect of a vehicle across all the emissions. The exception is comparing vehicles within the same propellant class, for example the hydrogen fuelled rocket produces a quarter of the H₂O of the hydrogen-fuelled RBCC spaceplane or the medium kerosene launcher with

the small kerosene launcher and the airlaunch kerosene, which clearly shows an advantage towards the larger vehicle. This aspect is explored further in section 7.3.

As introduced in section 7.1.3, estimating the radiative forcing is a more useful way to compare and evaluate the potential for environmental impact of different vehicles because it accounts for the environmental impact of all emissions with respect to their impact on the climate.

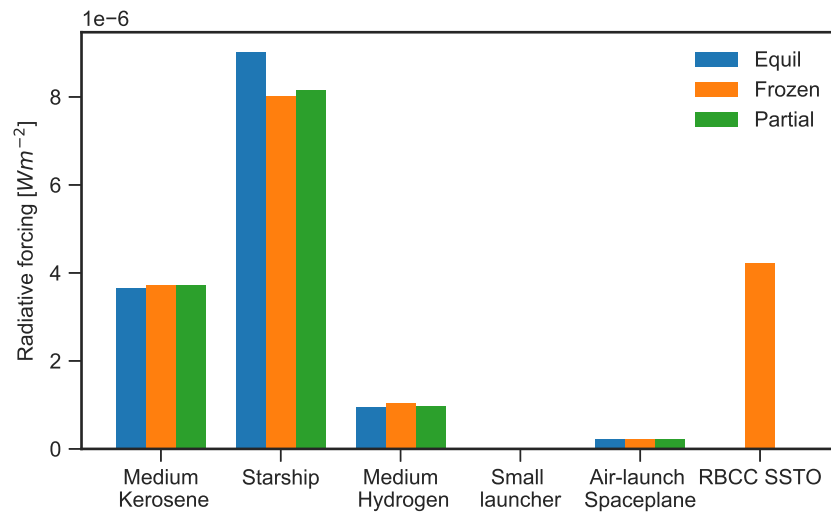


Fig. 7.2 Radiative forcing for all launch vehicles by nozzle chemistry

Table 7.3 Radiative forcing by species (where applicable, equilibrium rocket models are assumed and corrective factors are included)

Class	RF (W m^{-2})			
	CO_2	H_2O	BC	Total
Medium kerosene	2.34×10^{-9}	5.99×10^{-7}	3.04×10^{-6}	3.64×10^{-6}
Medium hydrogen	-	1.03×10^{-6}	-	1.03×10^{-6}
Super heavy methane	1.16×10^{-8}	9.01×10^{-6}	-	9.02×10^{-6}
Small Kerosene	4.47×10^{-11}	1.58×10^{-8}	6.66×10^{-9}	2.25×10^{-8}
RBCC spaceplane	-	4.21×10^{-6}	-	4.21×10^{-6}
Airlaunch kerosene	2.29×10^{-10}	9.49×10^{-8}	1.12×10^{-7}	2.07×10^{-7}

Figure 7.2 shows the radiative forcing calculated as previously described for all sources including consideration for the nozzle chemistry model. Table 7.3 contains the same

information in a table for the equilibrium nozzle model. In absolute terms, the super heavy vehicle, the RBCC SSTO spaceplane, and the medium kerosene vehicle contribute the most instantaneous radiative forcing for a single launch. Table 7.3 enables a comparison of the contributions of different emissions, which is not possible with fig. 7.2. However, as with comparing masses of emissions, the varying size of the vehicles disguises the impact of the underlying emissions contribution.

To make a fair comparison between the different launch vehicle test cases in, the total emissions are normalised with the payload mass to the reference orbit:

$$\hat{RF}_i = \frac{RF_i}{m_{\text{payload}}}, \quad (7.9)$$

\hat{RF}_i is the normalised radiative forcing contribution for species i across the entire flight

RF_i is the radiative forcing for species i across the entire flight

m_{payload} is the mass of the useful payload for the trajectory associated with this emissions profile

Alternatives to this might be to normalise by propellant mass or GTOW, but the advantage of using payload mass is that it provides measure of the amount of radiative forcing relative to the performance provided by the launcher. This is somewhat analogous to the measures used in other industries by combining environmental impact and production. The results of this normalisation are shown in fig. 7.3 and table 7.4.

With this measure, the worse performers are the air-launch spaceplane and the RBCC spaceplane. The impact of the air-launch spaceplane will be even more significant when considering the environmental impact of the air-carrier phase of flight. This is primarily a result of the reduced payload margin, the emissions produced are not counterbalanced by higher performance in terms of payload delivery. Otherwise, the super heavy methane fuelled rocket has the lowest relative radiative forcing, most likely a combination of the impressive mass margin and a hydrocarbon fuel that does not produce soot.

Further examination of table 7.4 also shows that stratospheric black carbon emissions are the most significant contributor to radiative forcing, followed by stratospheric water.

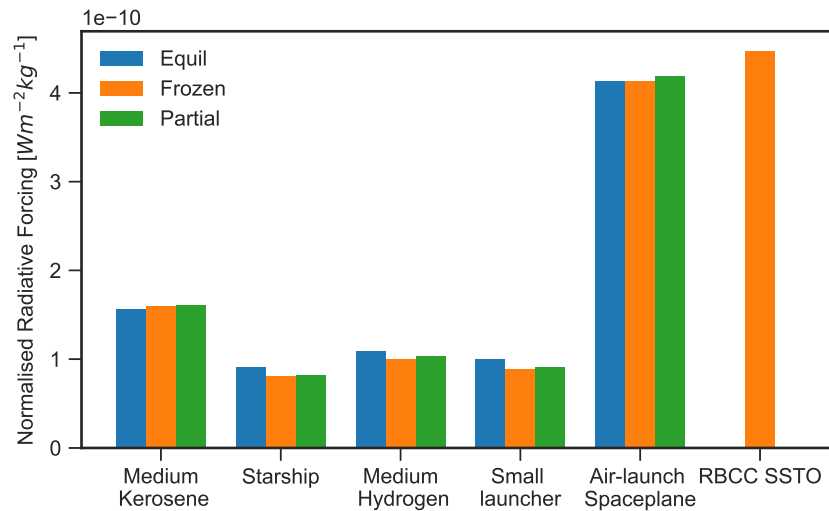


Fig. 7.3 Normalised radiative forcing for all launch vehicles by nozzle chemistry

Whilst CO₂ is two orders of magnitude lower in terms of instantaneous radiative forcing, care should be taken when excluding it, since it has an extremely long lifetime when compared to black carbon and water.

These results also enable a view to be drawn on the requirements of propulsion system models for the purposes of quantifying environmental impacts, at least in terms of radiative forcing. The differences between the equilibrium, frozen and partial equilibrium nozzle assumptions are minimal. The greatest difference is for the super heavy methane vehicle, which is due to the significant amounts of unreacted OH and O₂ at the nozzle exit for the frozen and partial equilibrium assumptions. Some of this is likely to react with CO in the plume, or otherwise be deposited in the atmosphere, but no correction factor has been applied here. Under the equilibrium assumption, the mass fractions of O, O₂ or OH are equal to 0. These results indicate that any of these models are capable of identifying the scale of emissions in terms of major species, such as CO₂ or H₂O, and that for early design, priority should be given to accurate prediction of performance instead. Modelling of minor species, such as OH, which have an important role in plume afterburning as well as in the atmosphere, requires higher fidelity models at the end of the nozzle, including chemistry and dynamics in the plume and the atmospheric response. The exception to this is black carbon, which due to its importance as a radiative forcing contributor and the complexity

Table 7.4 Normalised radiative forcing by (where applicable, equilibrium rocket models are assumed and corrective factors are included)

Class	Normalised RF ($\text{W m}^{-2} \text{kg}^{-1}$)			
	CO_2	H_2O	BC	Total
Medium kerosene	1.01×10^{-13}	2.57×10^{-11}	1.30×10^{-10}	1.56×10^{-10}
Medium hydrogen	-	1.09×10^{-10}	-	1.09×10^{-10}
Super heavy methane	1.16×10^{-13}	9.01×10^{-11}	-	9.02×10^{-11}
Small Kerosene	1.99×10^{-13}	7.01×10^{-11}	2.96×10^{-11}	9.98×10^{-11}
RBCC spaceplane	-	4.47×10^{-10}	-	4.47×10^{-10}
Airlaunch kerosene	4.58×10^{-13}	1.90×10^{-10}	2.23×10^{-10}	4.13×10^{-10}

of its production, requires higher fidelity modelling (assuming there is sufficient data to validate it).

Two issues that require further discussion are the impact of the corrected factors introduced in section 6.1, which are discussed in section 7.2.1 and the sensitivity of the radiative forcing to the soot production rate, explored in section 7.2.2.

7.2.1 Corrective factors

In section 6.1, a correction was introduced to account for the relative fuel-rich conditions of the kerosene fuelled rocket engines commonly used for launch vehicles. Carbon monoxide, formed when carbon does not have the time or presence of oxygen to form CO_2 was assumed to be able to react with oxygen in other species within the atmosphere to form CO_2 . The effects of this correction on radiative forcing in the case of the medium kerosene rocket are shown in fig. 7.4.

CO is present in the stratosphere and interacts with other greenhouse gases including methane and carbon dioxide. It can be produced through the oxidation of methane and the ultraviolet photodissociation of carbon dioxide. However, the loss through formation of CO_2 by oxidation with OH:



exceeds the production at all latitude and pressure levels, and the loss lifetime is generally between 20 and 30 days (Minschwaner et al., 2010). Small amounts of OH may remain in the plumes of launch vehicles, between 7 - 9 t in the partial and frozen propulsion models whereas all OH reacts according to an equilibrium nozzle assumption, but it is expected that the vast majority of this reactant is already present in the atmosphere.

It is therefore sensible to include the additional CO₂ in the radiative forcing impacts of the launcher. A consequence of applying this correction is that it removes any value that can be obtained from the differences in emissions based on the nozzle chemistry assumptions. It is essentially driven by the mixture ratio of the rocket engine and the amount of carbon present to be oxidised.

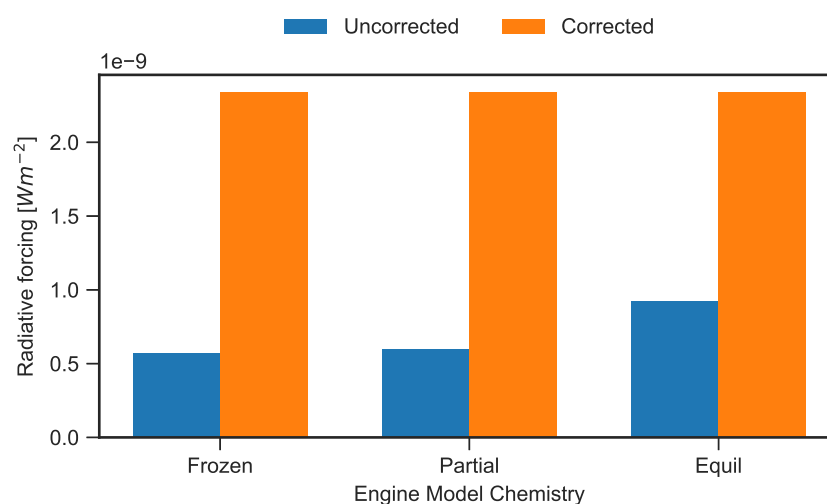


Fig. 7.4 Radiative forcing from CO₂ emissions with and without CO corrections for the medium kerosene rocket

In the kerosene-fuelled vehicles, this effect is overwhelmed by the contribution of black carbon on radiative forcing, which dominates by at least three orders of magnitude, and by water vapour emissions by two orders of magnitude, as shown in table 7.5. The key concern with CO₂ is the extremely long lifetime in the atmosphere, this small amount of radiative forcing stays in effect for the lifetime of CO₂ in the atmosphere - several hundred years.

In the the medium kerosene case, even with the equilibrium nozzle assumption, 36% of the emissions are of CO, which corresponds well to the exit mass fractions of tables 5.12 and 5.13. This is only slightly less than the 37% of the exhaust that is CO₂, so the overall mass of CO₂ after ambient oxygen reacts with carbon monoxide is significantly higher than

the direct emissions. This drives the large increase in radiative forcing shown in fig. 7.4 and table 7.5. This may also be understating the influence of carbon monoxide emissions on radiative forcing, as they can be involved in other processes that affect OH and CH₄ respectively (Minschwaner et al., 2010).

Table 7.5 Radiative forcing components for equilibrium nozzle for the medium kerosene launch vehicle

Radiative Forcing	Species		
	CO ₂	H ₂ O	BC
Corrected	2.34×10^{-9}	5.99×10^{-7}	3.04×10^{-6}
Uncorrected	9.27×10^{-10}	5.99×10^{-7}	3.04×10^{-6}

Given the central assumption here is that once in the atmosphere, carbon monoxide will eventually form carbon dioxide with oxygen in the ambient air, a custom GWP factor can be defined that is simply the relative molecular masses of CO and CO₂ in eq. (7.10), which is a factor of 1.57 kgCO₂-eq. This might be a reasonable assumption as the lifetime of CO is 20-30 days compared to the lifetime of CO₂ and the 100-year averaging period commonly used to calculate GWPs. This is likely a lower bound since it does not account for the radiative forcing of other processes with OH and CH₄ mentioned previously.

This value cannot be directly used from the mass of kerosene onboard a vehicle, as the mass fraction of CO generated by rocket engines is influenced by both mixture ratio and nozzle properties (specifically, nozzle area ratio). This can be seen in the difference in mass fraction between the Merlin 1D and Merlin 1D Vac engine variants (tables 5.12 and 5.13) and so the relative masses fractions of carbon monoxide and carbon dioxide need to be calculated for each launch vehicle and its engines before this GWP can be used.

7.2.2 Sensitivity to black carbon

Black carbon has the largest impact of any of the emissions investigated here, but as discussed in section 4.3, its production in real hydrocarbon rockets engines is poorly understood, as is its impact on radiative forcing. A simple approach was proposed in this thesis based on older test data from small engines, but it was clear from the few credible data points available that this significantly understates the production rate. An alternative approach is to make conservative assumptions such as those by Ross and Sheaffer (2014), which are conservative

both in the production rate and the lack of any consideration of consumption in the plume which has been observed. Given the dominance of black carbon on the overall radiative forcing, this may overstate the issue. Either way, more information is needed before the impact of *BC* can be credibly evaluated.

To provide some insight into the potential influence that uncertainty in the amount of soot produced in real kerosene engines, four scenarios were tested assuming different soot production rates:

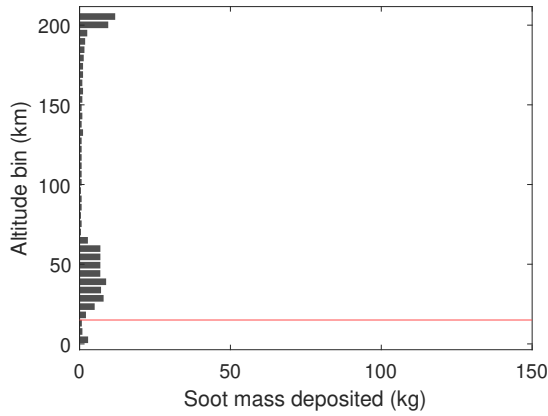
- The method described in section 4.3 that estimates the Y_{soot} as a function of mixture ratio based on previous experiments and includes an atmospheric loss approximation
- A $Y_{\text{soot}} = 0.005$ which is the estimate mass fraction at the engine exit as calculated on behalf of SpaceX for the FAA's environmental assessment with an atmospheric loss approximation (FAA, 2020)
- A $Y_{\text{soot}} = 0.005$ which is the estimate mass fraction at the engine exit as calculated on behalf of SpaceX for the FAA's environmental assessment without the atmospheric loss approximation (FAA, 2020)
- The central assumption from Ross and Sheaffer (2014) of 20 g kg^{-1} , equivalent to $Y_{\text{soot}} = 0.02$ without an atmospheric loss approximation

These modified black carbon production rates were assumed in the medium kerosene test case, using the same trajectories described in section 6.1.

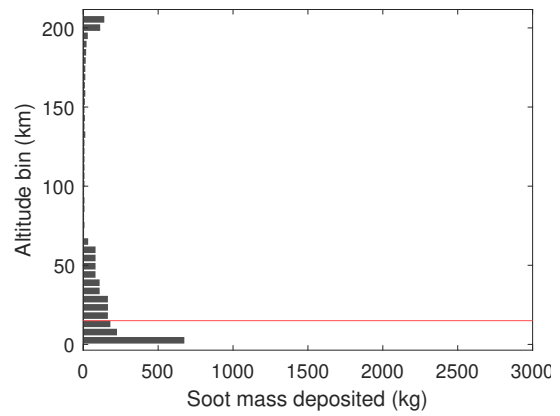
Table 7.6 Results from black carbon sensitivity experiments

	$M_{\text{BC,total}}$ [kg]	$M_{\text{BC,strat}}$ [kg]	RF_{BC} [W m ⁻²]
$Y_{\text{soot}}(MR)$ with altitude loss approximation	111.1	106.6	3.04×10^{-6}
$Y_{\text{soot}} = 0.05$ without altitude loss approximation	2693	1611	4.59×10^{-5}
Assuming $Y_{\text{soot}} = 0.05$ with altitude loss approximation	1322	1268	3.61×10^{-5}
$Y_{\text{soot}} = 0.02$ without altitude loss approximation	10 770	6445	1.84×10^{-4}

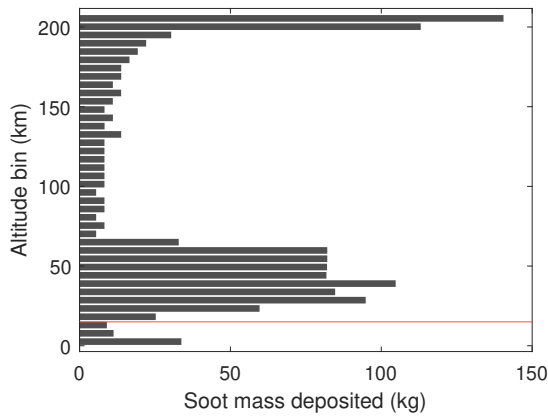
It is interesting to note the shape of the mass distribution profiles shown in the results of these experiments (fig. 7.5). These profiles are effectively a combination of the overall



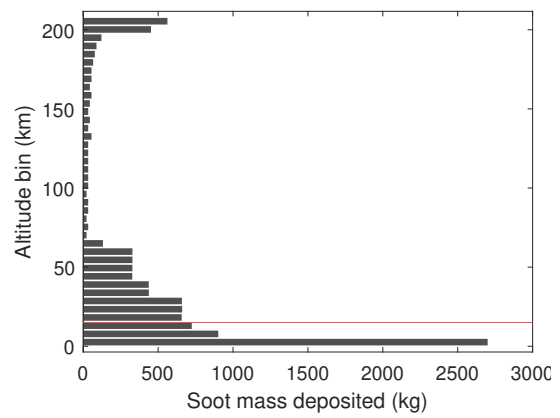
(a) Assuming $Y_{soot}(MR)$ as in section 4.3 with altitude loss approximation



(b) Assuming $Y_{soot} = 0.05$ without altitude loss approximation



(c) Assuming $Y_{soot} = 0.05$ with altitude loss approximation



(d) Assuming $Y_{soot} = 0.02$ without altitude loss approximation

Fig. 7.5 Soot mass distribution profiles with altitude with various assumptions about soot production. Red line indicates the stratospheric boundary used to calculate radiative forcing.

mass flow rate of the rocket with the trajectory and in the cases of fig. 7.5a and fig. 7.5c, the atmospheric loss approximation. This was assumed to be linear with altitude, and modifies the profile shown in fig. 7.5d and fig. 7.5b, which matches the overall mass distribution of launcher shown previously in fig. 6.6a. Peak production shifts from lower altitudes to the upper stratosphere and 200 km where the vehicle burns for a long time.

The methods and data available to estimate the black carbon emissions in literature are flawed, leading to high level of uncertainty in the production masses of at least two orders of magnitude (table 7.6). It seems likely that the 20 g kg^{-1} assumption is very conservative, and the opposite is true of the approach proposed here.

This has a directly proportional impact on the scale of uncertainty of radiative forcing, between $1.84 \times 10^{-4} - 3.04 \times 10^{-6} \text{ W m}^{-2}$. However, in even the best case scenario, which is perhaps the approach proposed in this thesis where an unachievable level of soot production is assumed combined with a first-order approximation of reactions in the plume, the contribution of black carbon dominates over all other emissions. The true level of concern with black carbon emission rates depends directly on which end of this scale the production rates are, and therefore it is critical that this is investigated in more depth.

7.3 Influence of vehicle design

The approach demonstrated in this research enables the impact on the environment of some key design considerations to be explored. The concept of operations, design and propulsion system of a vehicle can have a major impact on the trajectory and therefore the altitude at which emissions are generated. Ross and Sheaffer (2014) assumes that 2/3 of emissions occur into the stratosphere or above. This compares relatively well with the simulations performed here for vertical launch rockets, with between 58 % and 62 % of mass emitted above 15 km. However, this assumption breaks down when considering other launch architectures including the air-carried launch vehicle, where 80 % of the rocket's emissions occur above 15 km, predominantly due to being released from the carrier aircraft in the high troposphere, resulting in a larger proportion of emissions released in the stratosphere. Similarly 77 % of the RBCC's emissions occur above the stratosphere, which is expected

given 75% of the trajectory is above this altitude, with the most efficient stage, the ramjet, active for part of this phase.

Table 7.2 can be modified to display the mass of each emitted chemical below and above 15 km, as in table 7.7. This is valuable because the approach used to quantify radiative forcing is based on this assumption for H₂O and BC, and observing the normalised mass columns in particular is a reflection of the emissions and trajectory with performance already accounted for.

Although the impact of reusability on emissions has not been investigated in detail here, it is possible to draw some limited conclusions. Firstly, there is an impact in terms of propellant emissions for the provided benefit of the launch. The payload margin is reduced in order to retain enough propellant for return and landing burns (particularly with a VTOL approach like that of SpaceX). Secondly, reuse capability of some vehicles requires an increased dry mass compared to the payload mass, which is the additional mass required to enable the reuse capability. The two reusable vehicles in table 7.7, the RBCC spaceplane and the Airlaunch kerosene vehicle are both reusable, and both have significantly higher relative mass of the emissions for this reason. The propellant burned to reach orbit is not used for "useful" payload, but instead to carry the mass of the vehicle. This is clear also from the radiative forcing calculations, where these two vehicles have the highest normalised radiative forcing. The RBCC spaceplane has the additional disadvantage in that as well as expending propellant on bringing the entire vehicle to orbit, its airbreathing engines means more of its propellant is fuel, and so its total mass of emissions can exceed the fuel carried by the vehicle significantly. In this case, a total of 700 t of emissions vs. 300 t of fuel and oxidiser onboard.

The reduction of payload also has an impact on partially reusable vertical launch vehicles. The medium kerosene vehicle is based on the Falcon 9, which has a demonstrated track record of reuse of the first stage. The values for radiative forcing shown in fig. 7.3 use the optimised payload mass for the rocket in expendable mode, 23 283 kg, as found in section 6.1. When the first stage is recovered instead of expended, the useful payload capability of the Falcon 9 reduces by 34 % (Space Launch Report, 2021), which has an associated increase in the normalised radiative forcing per flight. However, when the entire life cycle of a vehicle is considered, these environmental costs are likely to be minimal in

comparison to the environmental savings of manufacturing fewer launch vehicles, due to the resource depletion during manufacturing.

When possible partial reusability of the vertical launch systems is considered, the picture may be more unclear. The small kerosene launcher is based on Electron, which RocketLab have been attempting to recover and reuse. Given the lower per-launch environment costs compared to the airlaunch kerosene, and the reuse of the most resource-intensive part of the vehicle, the first stage, this approach may have a lower lifetime environmental cost.

Accounting for the above discussion, the key design decisions that drive the emissions profile and associated environmental impact can be summarised into the following four areas:

Concept of operations From the analysis in section 7.2, the concept of operations of the launch vehicle plays a critical role in influencing the environmental impacts. The design decision for this element is typically made during early in conceptual design, after the top level business and technical requirements are identified, as they drive many of the lower level requirements and design decisions. Looking at the emissions profiles in figs. 6.7, 6.12, 6.17, 6.22, 6.27 and 6.31, and the previous discussion around mass distribution between the troposphere and stratosphere, the influence of concepts of operations is clear. As tropospheric level emissions for two of the species considered do not have associated impacts (e.g. BC and H₂O), a concept of operations that biases emissions towards lower altitudes, such as a vertical launcher, reduces the overall radiative forcing contributions.

Any use of a carrier aircraft, such as the air-launched spaceplane, has an additional burden due to the captive carry portion of the flight, which brings operational flexibility at the expense of additional fuel burn. In the case of the air-launched spaceplane in section 6.5, the CO₂ produced is around three times higher from the carrier aircraft than the spaceplane.

Propellant selection The propellant selected, including the mixture ratio, is a strong factor in the environmental impact. In section 2.3.3 and chapter 6, the environmental impact of solid rocket motors was discussed. Whilst they were not included here, their impact on stratospheric ozone needs to be carefully accounted for considering them

as a potentially propellant. The next most significant emission is soot, produced by kerosene rocket engines, as can be seen in table 7.4. Of the emissions considered, this has the most uncertainty, partly because of the lack of a comprehensive body of published knowledge, but also because the propulsion modelling approaches described in chapter 5 are not able to model it. These issues are explored in section 7.2.2. Soot can be reduced by maximising the mixture ratio, or removed from the equation by selecting either hydrogen or hydrocarbon fuels that do not produce soot (propane or methane). Hydrogen cannot be considered a clean fuel, as the majority of its exhaust products are H₂O which when emitted in the stratosphere, is the second largest contribution to the radiative forcing studied here (table 7.4). It is likely that other requirements will drive the selection of propellant, but this work has developed a methodology to be able to explore the environmental impact as part of a trade study. A practical example of this is described in section 7.4.1.

Reusability The result of designing reusable launch systems is inevitably a lower payload margin, either due to the need for additional fuel for entry and landing burns (such as the medium kerosene vehicle based on the Falcon 9, or the super heavy methane rocket) or due to the weight of additional aerodynamic and propulsion systems (as in the RBCC and air-launched spaceplane). These increase the normalised RF metric that has been introduced here. However, the benefits of reusability are not visible in the emissions of the launch activity itself. A full life cycle assessment is required to enable this design decision to be made. It is likely, given the results of previous life cycle assessments, that the design and manufacturing benefits of a reusable launch vehicle will counteract any drawbacks of the lower payload fraction.

Trajectory design The final potential area that is trajectory design, by selecting a control law that optimises for environmental impact, rather than some other design parameter. Typically, the design of a launch vehicle, including its concept of operations, staging strategy, relative stage masses and propellants dictate the optimal trajectory of the launcher. As such is there is less opportunity to design low environmental impact trajectories, and it may be better to optimise for payload mass. This idea is explored in more detail in section 7.4.2.

These recommended considerations should be used with care, as they are based on a single, instantaneous radiative forcing calculation, and ignore the environmental impacts of the full life cycle, as well as other impact categories such as air quality.

Table 7.7 Total emitted mass by species split by mass emitted below the stratosphere (where applicable, equilibrium rocket models are assumed and corrective factors included)

Class	Mass (tonne)			Normalised Mass		
	CO ₂	H ₂ O	BC	CO ₂	H ₂ O	BC
<15km						
Medium kerosene	204	56.5	0.004 55	8.76	2.43	0.000 195
Medium hydrogen	-	81.44	-	-	8.65	-
Super heavy methane	1000	764	-	10.0	7.64	-
Small kerosene	4.04	1.43	0.000 011 0	17.9	6.37	0.000 049 8
RBCC spaceplane	-	161	-	-	20.1	-
Airlaunch kerosene	9.50	2.91	0.000 063 0	19.0	5.82	0.000 126
>15km						
Medium kerosene	304	76.4	0.107	13.1	3.28	0.004 58
Medium hydrogen	-	130.9	-	-	13.9	-
Super heavy methane	2510	1910	-	25.1	19.1	-
Small kerosene	5.67	2.01	0.000 234	25.2	8.94	0.001 04
RBCC spaceplane	-	537	-	-	67.1	-
Airlaunch kerosene	40.2	12.1	0.003 91	80.4	24.2	0.007 82

7.4 Reducing RF through vehicle and trajectory design

In section 7.3 several key design decisions that influence the environmental impact of a launch vehicle have been identified. One of the benefits of assessing the emissions and environmental impact with the types of tools described in this thesis is the ability to include the effects as design considerations and to quantify their benefit. The following subsections include two examples of how the tools developed in chapters 3, 5 and 6 could be used in different ways during the design process to account for environmental impact.

7.4.1 Design study: propellant choice in small launchers

In this subsection, the methodology developed in this thesis is used to demonstrate how the choice of propellant can be included within a trade-off study. The baseline case is the small kerosene launcher previously discussed in section 6.4.

The alternative propellants are liquid propane and liquid methane, chosen because they are all hydrocarbons with relatively similar propellant properties. The design of the vehicle is assumed to be similar in terms of structure, mass and performance. The rocket engine used for the small vertical launch rocket section 6.4 is modified to use liquid propane and liquid methane.

The engine design is only minimally modified, with a simple exchange of mixture ratio, fuel and injection temperature. The engine cross-sectional areas and injection pressures are kept the same. This is unrealistic in the sense that the design space for new rocket engines is larger than propellant choice and mixture ratio alone, but it allows for a comparison of the overall difference that a change in propellants might enable for a similar engine design. The effect of these changes on performance is shown on in table 7.8 and table 7.9.

Any change in propellant would cascade into other modifications to the rocket, including the tank volumes and pressurant systems due to the different properties of kerosene, methane and propane. These design considerations are neglected in this experiment, but would need to be accounted for in a detailed design trade study.

The propulsion system modifications improves the performance of the rockets to orbit, resulting in an increase from a kerosene useful payload of 278.2 kg, to 363.0 kg for methane

Table 7.8 Sea level engine comparison for kerosene, methane and propane

		Kerosene	Methane	Propane
Assumed				
Mixture Ratio	[-]	2.8:1	3.2:1	2.3:1
Expansion Ratio	[-]	12	12	12
Calculated (assumes shifting equilibrium until nozzle throat)				
Thrust (Vac)	[kN]	23 250	23 310	23 150
Specific Impulse (Vac)	[s]	315.6	331.7	327.3

Table 7.9 Vacuum engine comparison for kerosene, methane and propane

		Kerosene	Methane	Propane
Assumed				
Mixture Ratio	[-]	2.8:1	3.2:1	2.3:1
Expansion Ratio	[-]	40	40	40
Calculated (assumes shifting equilibrium until nozzle throat)				
Thrust (Vac)	[kN]	24 690	24 780	24 510
Specific Impulse (Vac)	[s]	335.2	352.7	346.5

and 334.1 kg for propane, which will have a proportionate benefit on relative radiative forcing during the launch event.

As shown in table 7.10 the methane variant increases the estimated radiative forcing compared to the baseline kerosene case. This is a result of the high production of stratospheric H₂O due the lower carbon-hydrogen ratio in methane. The increased performance reduces the relative forcing by more than a 15% reduction.

In this experiment, the propane variant results in an overall reduction in RF and relative RF. However, experimental results have shown that LOX/propane can generate soot at lower mixture ratios (although less than kerosene), which hasn't been considered here (Hernandez and Mercer, 1987). Whilst some benefit of making specific trade-off decisions is apparent in this case for the launch event itself, any decision would need to be supported by life cycle assessment. There may be other environmental impacts related to production and manufacturing of the rocket engines or the propellant itself that would counteract the benefit, and these have not been considered here.

Table 7.10 Comparison of the radiative forcing for kerosene, methane and propane small launcher variant

		Kerosene	Methane	Propane
Payload	[kg]	278.2	363.0	334.1
Radiative Forcing	[W m ⁻²]	2.033 × 10 ⁻⁸	2.280 × 10 ⁻⁸	1.746 × 10 ⁻⁸
Difference	[%]	-	10.95	-16.06
Relative RF	[W m ⁻² kg ⁻¹]	7.310 × 10 ⁻¹¹	6.280 × 10 ⁻¹¹	5.240 × 10 ⁻¹¹
Difference	[%]	-	-16.19	-39.38

7.4.2 Cost function: minimise RF

Optimisation has been used to plan environmentally efficient trajectories for aircraft previously. For example, [Mcenteggart and Whidborne \(2012\)](#) minimised multiple objectives for noise and emissions during aircraft take of and landing cycles, and [Grewe et al. \(2010\)](#) used simplified emission calculation methods within multi-disciplinary optimisation to design a more sustainable supersonic business jet. Small gains aircraft efficiency can have big impacts in reducing environmental when amortised over large numbers of daily flights.

It is not expected that the same approach would be as successful for conventional vertical launch vehicles, as the trajectories of vertical rockets are largely defined by the design and configuration of the vehicle. To test this hypothesis, an experiment was devised where the trajectory of a vertical launch rocket is optimised to reduce the radiative forcing. The cost function is to minimise the RF:

$$\min \text{RF}_{\text{total}} \quad (7.11)$$

where:

$$\text{RF}_{\text{total}} = \text{RF}_{\text{CO}_2} + \text{RF}_{\text{H}_2\text{O}} + \text{RF}_{\text{BC}}. \quad (7.12)$$

The medium kerosene rocket is used for this experiment, using the equilibrium emission indices. The problem settings used for the trajectory discussed in section 6.1 are kept the same, but the optimisation is cold-started (i.e. without using a prior optimisation solution as an initial guess).

As can be seen in table 7.11, TROPICO is able to reduce the value of RF_{total} . However, when considering the payload loss associated with this optimised solution, the normalised RF increases. This is possibly due to the simplified approach used to calculate the radiative forcing, which only includes CO_2 below the tropopause. Additionally, the biggest contributing factor to the radiative forcing is the BC emitted, which has an altitude dependency as previously discussed (section 4.3). A solution that produces less black carbon may also spend more time in the atmosphere, increasing delta-V losses due to drag. It is clear that the amount that radiative forcing can be decreased by optimising the trajectory (through a different cost function) is limited, primarily because most of the parameters which govern the final trajectory are set with the vehicle design (propellant, staging ratios, vehicle type and concept).

A second attempt to optimise the radiative forcing was made by minimising the normalised RF :

$$\min\left(\frac{RF_{\text{total}}}{\text{payload}}\right). \quad (7.13)$$

Overall, neither emissions-optimised trajectories result in higher payload masses (-4.53% and -1.15% respectively), but do result in small benefits to RF and normalised RF .

Table 7.11 Results from using cost functions that minimise radiative forcing

Cost function	Payload Mass kg	RF_{total} W m^{-2}	Normalised RF $\text{W m}^{-2} \text{kg}^{-1}$
$\max m_{\text{payload}}$	23 283	3.6379×10^{-6}	1.5624×10^{-10}
$\min RF_{\text{total}}$	22 228	3.5308×10^{-6}	1.5884×10^{-10}
$\min(RF_{\text{total}}/m_{\text{payload}})$	23 015	3.5428×10^{-6}	1.5393×10^{-10}

The main drawback of using an approach like this is that the differences are sufficiently small in magnitude that highly accurate models of both the emissions produced and the atmospheric response would be required to be confident that the trajectory can be improved. There may be more opportunity for this considering horizontal launch systems or airbreathing vehicles where there is more opportunity for varying trajectories.

7.5 Summary

In this chapter, various approaches to quantifying and evaluating environmental impact of emissions from space access vehicles are introduced and discussed. The first two approaches, global warming potential and radiative forcing index have limited application to launch vehicles, but estimating radiative forcing is more useful, enabling comparisons across emissions species and vehicles.

Radiative forcing was estimated for the emission profiles generated in chapter 6. The launch vehicles modelled ranged in size from small satellite payloads to more than 100 t, and so the overall radiative forcing is difficult to compare. To address this, a measure of relative radiative forcing, calculated by normalising the radiative forcing by payload mass was introduced, which enables a fair comparison of launchers accounting for their performance. In section 6.1 a corrective factor was introduced that accounted for the natural reaction of CO emissions into CO₂, which has a much longer atmospheric lifetime. The effect of this correction and its application was then discussed. Additionally, the uncertainty in predicting the production of black carbon has a large impact in the comparison with other vehicles of kerosene-fuelled rockets.

A key conclusion from this chapter is that the two elements that have a big impact when accounting for performance are the mass required to enable reusability which reduces usable payload, and the launch vehicle concept of operation. The air-dropped reusable kerosene vehicle for example is one of the worst performing vehicles due to the emissions being released almost entirely in the stratosphere. Life cycle assessment is needed to understand how effective the reduced environmental impact from reusing the vehicle is in comparison to this.

Section 7.3 discusses the key design considerations that can have an effect on the environmental impact, in terms of radiative forcing, including concept of operations, propellant selection, reusability and trajectory design. In the last part of the chapter, two of these approaches for reducing the environmental impact of launch vehicles using the methodology developed in this research were explored. The first demonstrated how a design trade-off of the launcher propellant combinations can include environmental effects, as well as the

performance. The second experiment investigated whether the optimisation approach used to find optimal trajectories could be extended to minimise the radiative forcing.

8 | CONCLUSIONS AND FUTURE

WORK

The overall aim of this thesis this was to develop an approach to characterise the chemical emissions of novel and existing launch vehicles during design, and to estimate their potential environment impact. This was addressed by combining three tools and models intended for use together during preliminary design where in-depth and high-fidelity models are not appropriate:

- a low-fidelity propulsion model capable of predicting the performance and major species produced by rocket and airbreathing engines used for space access vehicles;
- a trajectory optimisation tool that can determine feasible and optimal trajectories for conceptual vehicles and estimate the associated emission profiles;
- an approach to consider how these emissions impact the atmosphere.

An existing propulsion modelling tool was extended to include more approaches to consider chemistry, enabling the rocket engines to be modelled and providing more options for considering combustion of airbreathing engines. Several rocket engines were then modelled in the tool, and the results were compared against the mixture ratio of fuel and oxidiser, which controls the amount of emissions produced within the engine. The first research question was to evaluate the extent to which low fidelity propulsion models could be used to predict emissions during early design. Chapter 5 compared the model developed here against an industry-standard tool, CEA, and against published results from higher-fidelity models, with consistent results in predicting major species. Section 7.2 demonstrated that these is suitable for estimating the key environmental impacts in terms of radiative

forcing, except for black carbon, which requires much higher fidelity models that may be difficult to apply in conceptual design. Any increase in fidelity of the propulsion model requires a more rigorous approach to modelling the plume.

The propulsion model was then used to estimate emission profiles for a group of existing and future launch vehicle and configurations, including expendable medium kerosene- and hydrogen- fuelled rockets, a methane-fuelled super heavy launcher, a small kerosene-fuelled rocket, an air-launched winged rocket vehicle and an airbreathing SSTO vehicle. For each simulation, an optimal trajectory was coupled with the emissions models to produce emissions profiles. Similar previously published results align with these when the differences in the models are accounted for, but in particular the emissions profiles for the super heavy launcher and winged vehicles are novel.

Whilst greenhouse gases are emitted by many anthropogenic activities, emissions produced by launches are almost unique in that significant mass is emitted above the troposphere. Several metrics for measuring the impact of emissions are considered, including mass, global warming potential and radiative forcing index. These are rejected in favour of radiative forcing estimations (Ross and Sheaffer, 2014), which are able to account for all of the concerning emission species, even if there is uncertainty around the precise results. Additionally, there is a compelling argument that CO emissions should be considered as contributing to the overall CO₂ emitted by launch operations, due to the rate of conversion compared to the lifetime of CO₂ in the atmosphere (a simplistic plume assumption). Even combined, their radiative forcing contributions are small compared to stratospheric water vapour and black carbon, but they are still present. Some launch vehicle operators are already discussing offsetting their carbon dioxide output (Orbex, 2021), but its unclear if this is an effective activity.

The combination of these three tools enables a new lens through which to view launch vehicle environmental impact. Key design decisions such vehicle concepts of operations and propellant choices can be explored, considering the radiative forcing and performance of the vehicle in an integrated fashion, addressing the third research question: to identify strategies to reduce the environmental impact of launch vehicles. Comparing the radiative forcing from the vehicles implemented in chapter 6 shows that two vehicles featuring full reusability in particular having the highest relative radiative forcing, due to the performance

cost of carrying a reusable lifting body to orbit. This is likely to be offset by the overall life cycle impacts of reusable versus expendable vehicles. This addressed directly the second research question, which was to understand the environmental impact of expected changes in launch vehicles. Another future vehicle, the super heavy methane fuelled vehicle has both the lowest normalised radiative forcing, and the advantage of being fully reusable.

The third research question was further explored by considering propellant selection section 7.4.1, with an example comparing the trade-offs between three hydrocarbon propellants; methane, propane and kerosene. In this particular scenario with these models, both improvements in performance and reductions in radiative forcing result in clear indicators that changing propellants can improve environmental performance, although these would need to be confirmed with more detailed analysis.

A second experiment was also performed to see integrating the radiative forcing estimations as the objective function in the trajectory optimisation function. This was applied to a two-stage vertical rocket in section 7.4.2 to see whether an environmentally-improved trajectory could be found. Whilst this was a success, it is unclear whether it would be a useful process to perform given the uncertainty in the production rates of emissions, the simplistic approach to plume interactions and radiative forcing estimations. Optimal control laws for vertical launch vehicles are also limited in flexibility as they are effectively determined by the vehicle design, such as staging ratios and performance. There may be some additional utility applying this approach to winged airbreathing vehicles.

It is clear that at current launch rates that the space sector is a very small contribution to humanity's influence on the atmosphere, and space exploration and applications can have a huge benefit on the environment and society (e.g. monitoring the climate, deforestation or illegal fishing). However, with many nations aiming for net-zero in the long term, the space sector should be proactive in addressing concerns. This requires being able to accurately characterise the environmental impact of the full design, manufacture and operation of launches, and to demonstrate that reasonable steps are being taken to reduce the overall impact. This is especially true given the potential growth in the space sector, and with the development of new vehicles and new types of vehicles, which has already been shown to have a significant further impact if realised (Wilson, 2019).

8.1 Recommendations for future work

During the course of this research, several areas of further work were identified:

- This thesis identified that the lack of confidence in the amount of black carbon produced in hydrocarbon fuel rocket engines prevents an accurate characterisation of the environmental impacts of launchers, given the large number of vehicles that use this type of fuel. Accurate and verifiable data or models on the production rates in real rocket engines exists do not exist in the public domain, and should be measured or developed so that the emission rates of black carbon can be estimated for current and future vehicles.
- A useful next step would be to extend the propulsion models used within this thesis to more accurately model the flowpath of air-breathing engines such as dual-mode ramjets and scramjets by considering the rate of mixing and finite-rate rate chemistry of specific engine configurations. This would enable the prediction of other pollutants produced by these types of engines such as NO_x which could then be included within the emissions assessment.
- The influence of rocket pollutants in the atmosphere on radiative forcing has been estimated using relatively simple models available in literature. A valuable development would be to include within the assessment framework or optimisation the effects of residence time of emissions within the atmosphere and their non-instantaneous radiative forcing, enabling the totality of the launch activity to be considered during conceptual design and potentially life cycle assessment.
- A key question throughout this work has been to understand the extent to which early stage design tools can be used to predict the environmental consequences of launches from new vehicles. The use of higher fidelity models or data at each stage, from detailed rocket cycle models considering non-equilibrium combustion and nozzle chemistry, to plume expansion models and atmospheric chemistry to compare against the simpler approaches would increase the confidence of these estimates. Even if

carried out for a few specific scenarios, this would support the extent to which these models can be used effectively.

- The inclusion of emissions within a trajectory optimisation framework for launch vehicles is a new capability. Traditionally, evaluating the environment impact of launchers has required assumptions about the emissions profiles of the vehicles. Whilst these are generally suitable for expendable multi-stage launch vehicles with rocket propulsion, new types of vehicles with either lifting bodies or airbreathing propulsion systems require different assumptions. This capability could be used to create these baseline emission profiles. Another interesting avenue is to understand whether an emissions-optimised vehicle design could be discovered, as the design and trajectory solution space of these types of vehicles is wider.

REFERENCES

- Aerojet Rocketdyne. RL10 Data Sheet, 2018. URL https://www.rocket.com/sites/default/files/documents/Capabilities/PDFs/RL10_data_sheet.pdf.
- Aerostar Environmental Services Inc. Environmental Assessment for the Operation and Launch of the Falcon 1 and Falcon 9 Space Vehicles at Cape Canaveral Air Force Station Florid. 2007.
- Airbus. Global Market Forecast: Global Networks, Global Citizens. Technical report, Airbus, 2018. URL <https://www.airbus.com/aircraft/market/global-market-forecast.html>.
- A. A. Alexeenko, N. E. Gimelshein, D. a. Levin, R. J. Collins, R. Rao, G. V. Candler, S. F. Gimelshein, J. S. Hong, and T. Schilling. Modeling of Flow and Radiation in the Atlas Plume. *Journal of Thermophysics and Heat Transfer*, 16(1):50–57, 2002. ISSN 0887-8722. doi: 10.2514/2.6651. URL <https://arc.aiaa.org/doi/pdf/10.2514/2.6651>.
- B. E. Anderson, G. Chen, and D. R. Blake. Hydrocarbon emissions from a modern commercial airliner. *Atmospheric Environment*, 40(19):3601–3612, 6 2006. ISSN 1352-2310. doi: 10.1016/J.ATMOENV.2005.09.072.
- J. D. Anderson. *Fundamentals of Aerodynamics*. McGraw-Hill, third edit edition, 2001.
- D. Archer and V. Brovkin. The millennial atmospheric lifetime of anthropogenic CO₂. *Climatic Change*, 90(3):283–297, 2008. ISSN 01650009. doi: 10.1007/s10584-008-9413-1.
- S. R. H. Barrett, R. E. Britter, and I. A. Waitz. Global Mortality Attributable to Aircraft Cruise Emissions. *Environmental Science & Technology*, 44(19):7736–7742, 10 2010. ISSN 0013-936X. doi: 10.1021/es101325r. URL <http://pubs.acs.org/doi/abs/10.1021/es101325r>.
- C. Bauer, A. Koch, F. Minutolo, and P. Grenard. Engineering model for rocket exhaust plumes verified by CFD results. In *29th ISTS*, 2013.
- J. T. Betts. Survey of Numerical Methods for Trajectory Optimization. *Journal of Guidance, Control, and Dynamics*, 21(2):193–207, 3 1998. ISSN 0731-5090. doi: 10.2514/2.4231. URL <http://arc.aiaa.org/doi/abs/10.2514/2.4231>.
- J. T. Betts. *Practical Methods for Optimal Control and Estimation Using Nonlinear Programming*. Society for Industrial and Applied Mathematics, 1 2010. doi: 10.1137/1.9780898718577.
- C. H. Birzer and C. J. Doolan. Quasi-one-dimensional model of hydrogen-fueled scramjet combustors. *Journal of propulsion and power*, 25(6):1220–1225, 2009. ISSN 0748-4658. doi: 10.2514/1.43716. URL <http://arc.aiaa.org/doi/pdf/10.2514/1.43716>.

- S. Blakey, L. Rye, and C. W. Wilson. Aviation gas turbine alternative fuels: A review. *Proceedings of the Combustion Institute*, 2011. ISSN 15407489. doi: 10.1016/j.proci.2010.09.011.
- P. Blau. SpaceFlight101.net Delta IV Heavy, 2018a. URL <http://www.spaceflight101.net/delta-iv-heavy-rs-68a.html>.
- P. Blau. Spaceflight101: Falcon 9 FT (Falcon 9 v1.2), 2018b. URL <http://spaceflight101.com/spacerockets/falcon-9-ft/>.
- P. Blau. Spaceflight101: Delta IV Medium+ (4,2), 2018c. URL <http://spaceflight101.com/spacerockets/delta-iv-medium-42/>.
- H. Bönisch, A. Engel, T. Birner, P. Hoor, D. W. Tarasick, and E. A. Ray. On the structural changes in the Brewer-Dobson circulation after 2000. *Atmospheric Chemistry and Physics*, 11(8):3937–3948, 2011. ISSN 16807316. doi: 10.5194/acp-11-3937-2011.
- J. Bradford and J. R. Olds. SCCREAM v5: A Web-Based Airbreathing Propulsion Analysis Tool. In *35th AIAA/ASME/SAE/ASEE Joint Propulsion Conference*, 1999.
- B. B. Brady, L. R. Martin, and V. I. Lang. Effects of Launch Vehicle Emissions in the Stratosphere. *Journal of Spacecraft and Rockets*, 34(6):774–779, 11 1997. ISSN 0022-4650. doi: 10.2514/2.3285. URL <http://arc.aiaa.org/doi/10.2514/2.3285>.
- G. P. Brasseur, M. Gupta, B. E. Anderson, S. Balasubramanian, S. R. H. Barrett, D. Duda, G. Fleming, P. M. Forster, J. Fuglestedt, A. Gettelman, R. N. Halthore, S. D. Jacob, M. Z. Jacobson, A. Khodayari, K.-N. Liou, M. T. Lund, R. C. Miake-Lye, P. Minnis, S. Olsen, J. E. Penner, R. Prinn, U. Schumann, H. B. Selkirk, A. Sokolov, N. Unger, P. Wolfe, H.-W. Wong, D. W. Wuebbles, B. Yi, P. Yang, and C. Zhou. Impact of Aviation on Climate: FAA's Aviation Climate Change Research Initiative (ACCRI) Phase II. *Bulletin of the American Meteorological Society*, 97(4):561–583, 4 2016. ISSN 0003-0007. doi: 10.1175/BAMS-D-13-00089.1. URL <http://journals.ametsoc.org/doi/10.1175/BAMS-D-13-00089.1>.
- G. L. Brauer, D. E. Cornick, A. R. Habeger, F. M. Petersen, and R. Stevenson. Program to Optimize Simulated Trajectories (POST). Volume 1: Formulation Manual. Technical report, 1975. URL <https://ntrs.nasa.gov/search.jsp?R=19750024073>.
- G. L. Brauer, D. E. Cornick, and R. Stevenson. Capabilities and Applications of the Program to Optimize and Simulate Trajectories: Program Summary. Technical Report February 1977, 1977.
- A. Burcat and B. J. McBride. *1997 Ideal Gas Thermodynamic Data for Combustion and Air-Pollution Use*. Technion-IIT, Faculty of Aerospace Engineering, 1997.
- H. Burkhardt, M. Sippel, A. Herbertz, and J. Klevanski. Kerosene vs. Methane: A Propellant Tradeoff for Reusable Liquid Booster Stages. *Journal of Spacecraft and Rockets*, 41(5): 762–769, 2004. ISSN 0022-4650. doi: 10.2514/1.2672. URL <http://arc.aiaa.org/doi/10.2514/1.2672>.
- D. Byun and S. W. Baek. Numerical investigation of combustion with non-gray thermal radiation and soot formation effect in a liquid rocket engine. *International Journal of Heat and Mass Transfer*, 50(3-4):412–422, 2007. ISSN 00179310. doi: 10.1016/j.ijheatmasstransfer.2006.09.020.

- G. Cai, J. Fang, X. Xu, and M. Liu. Performance prediction and optimization for liquid rocket engine nozzle. *Aerospace Science and Technology*, 11(2-3):155–162, 2007. ISSN 12709638. doi: 10.1016/j.ast.2006.07.002.
- M. A. Cameron, M. Z. Jacobson, S. R. H. Barrett, H. Bian, C. C. Chen, S. D. Eastham, A. Gettelman, A. Khodayari, Q. Liang, H. B. Selkirk, N. Unger, D. J. Wuebbles, and X. Yue. An intercomparative study of the effects of aircraft emissions on surface air quality. *Journal of Geophysical Research*, 122(15):8325–8344, 2017. ISSN 21562202. doi: 10.1002/2016JD025594.
- W. R. Cofer, G. G. Lala, and J. P. Wightman. Analysis of mid-tropospheric space shuttle exhausted aluminum oxide particles. *Atmospheric Environment (1967)*, 21(5):1187–1196, 1 1987. ISSN 00046981. doi: 10.1016/0004-6981(87)90246-0. URL <http://linkinghub.elsevier.com/retrieve/pii/0004698187902460>.
- W. R. Cofer, G. C. Purgold, E. L. Winstead, and R. A. Edahl. Space shuttle exhausted aluminum oxide: A measured particle size distribution. *Journal of Geophysical Research*, 96(D9):17371, 1991. ISSN 0148-0227. doi: 10.1029/91JD01713. URL <http://doi.wiley.com/10.1029/91JD01713>.
- B. A. Conway. A Survey of Methods Available for the Numerical Optimization of Continuous Dynamic Systems. *Journal of Optimization Theory and Applications*, 152(2):271–306, 2012. ISSN 00223239. doi: 10.1007/s10957-011-9918-z.
- D. J. Cziczo. Composition of individual particles in the wakes of an Athena II rocket and the space shuttle. *Geophysical Research Letters*, 29(21):2037, 2002. ISSN 0094-8276. doi: 10.1029/2002GL015991. URL <http://doi.wiley.com/10.1029/2002GL015991>.
- M. Y. Danilin. Quantifying uptake of HNO₃ and H₂O by alumina particles in Athena-2 rocket plume. *Journal of Geophysical Research*, 108(D4):4141, 2003. ISSN 0148-0227. doi: 10.1029/2002JD002601. URL <http://doi.wiley.com/10.1029/2002JD002601>.
- M. Y. Danilin, R. L. Shia, M. K. Ko, D. K. Weisenstein, N. D. Sze, J. J. Lamb, T. W. Smith, P. D. Lohn, and M. J. Prather. Global stratospheric effects of the alumina emissions by solid-fueled rocket motors. *Journal of Geophysical Research Atmospheres*, 106(D12):12727–12738, 2001. ISSN 01480227. doi: 10.1029/2001JD900022.
- J. Davis, S. Striepe, R. Maddock, S. Paschall, R. Bishop, A. Johnson, B. Cohanin, G. Hines, M. Johnson, T. Fill, and others. Advances in POST2 end-to-end descent and landing simulation for the ALHAT project. In *AIAA/AAS Astrodynamics Specialist Conference and Exhibit*, page 6938, 2008.
- J. L. Davis, J. D. Shidner, and D. W. Way. Mars Science Laboratory Post-Landing Location Estimation Using POST2 Trajectory Simulation. 2013.
- M. R. Denison, J. J. Lamb, W. D. Bjordahl, E. Y. Wong, and P. D. Lohn. Solid rocket exhaust in the stratosphere - Plume diffusion and chemical reactions. *Journal of Spacecraft and Rockets*, 31(3):435–442, 5 1994. ISSN 0022-4650. doi: 10.2514/3.26457. URL <http://arc.aiaa.org/doi/10.2514/3.26457>.
- Department for Business Energy & Industrial Strategy. Greenhouse gas report: conversion factors 2020. Technical report, BEIS, 2020. URL <https://www.gov.uk/government/publications/greenhouse-gas-reporting-conversion-factors-2020>.

- Department for Transport. Guidance to the regulator on environmental objectives relating to the exercise of its functions under the Space Industry Act 2018. Technical report, 2021. URL https://assets.publishing.service.gov.uk/government/uploads/system/uploads/attachment_data/file/995153/guidance-to-the-regulator-on-environmental-objectives-relating-to-the-exercise-of-its-functions-under-the-act-2018.pdf.
- J. D. DeSain and B. B. Brady. Potential Atmospheric Impact Generated by Space Launches Worldwide — Update for Emission Estimates from 1985 to 2013. Technical report, Aerospace Corporation, 2014.
- C. Doolan and R. Boyce. A Quasi-One-Dimensional Mixing and Combustion Code for Trajectory Optimisation and Design Studies. *15th AIAA International Space Planes and Hypersonic Systems and Technologies Conference*, 2008. doi: 10.2514/6.2008-2603. URL <http://arc.aiaa.org/doi/abs/10.2514/6.2008-2603>.
- D. DuBois and G. C. Paynter. "Fuel Flow Method2" for Estimating Aircraft Emissions. *SAE Transactions*, 115:1–14, 2006. ISSN 0096736X, 25771531. URL <http://www.jstor.org/stable/44657657>.
- S. Dunn and D. Coats. Nozzle performance predictions using the TDK 97 code. In *33rd Joint Propulsion Conference and Exhibit*, pages 1–13, Reston, Virginia, 7 1997. American Institute of Aeronautics and Astronautics. doi: 10.2514/6.1997-2807. URL <http://arc.aiaa.org/doi/10.2514/6.1997-2807>.
- T. Edwards. Liquid Fuels and Propellants for Aerospace Propulsion: 1903-2003. *Journal of Propulsion and Power*, 19(6):1089–1107, 2003. ISSN 0748-4658. doi: 10.2514/2.6946. URL <http://arc.aiaa.org/doi/10.2514/2.6946>.
- T. Edwards and L. Q. Maurice. Surrogate Mixtures to Represent Complex Aviation and Rocket Fuels. *Journal of Propulsion and Power*, 17(2):461–466, 2001. ISSN 0748-4658. doi: 10.2514/2.5765. URL <http://arc.aiaa.org/doi/10.2514/2.5765>.
- S. Elliott and R. M. Stringfield. Chemistry in next-generation rocket plume models. *Combustion Science and Technology*, 175(7):1179–1210, 7 2003. ISSN 0010-2202. doi: 10.1080/00102200302377. URL <http://www.tandfonline.com/doi/abs/10.1080/00102200302377>.
- ESA. ANNUAL SPACE ENVIRONMENT REPORT. Technical report, 2021.
- W. J. D. Escher and J. E. Roddy. Marquardt's Mach 4.5 Supercharged Ejector Ramjet (SERJ) High-Performance Aircraft Engine Project; Unfulfilled Aspirations Ca.1970. In *36th AIAA/ASME/SAE/ASEE Joint Propulsion Conference & Exhibit*, 2000.
- European Aviation Safety Agency, European Environment Agency, and EUROCONTROL. European Aviation Environmental Report 2016. Technical report, European Aviation Safety Agency, 2016. URL <https://ec.europa.eu/transport/sites/transport/files/european-aviation-environmental-report-2016-72dpi.pdf>.
- European Commission. Reducing emissions from aviation, 2021. URL https://ec.europa.eu/clima/policies/transport/aviation_en#tab-0-0.

- FAA. Finding of No Significant Impact and Record of Decision for Issuing Launch and Reentry License to Space Exploration Technologies Corp. for Falcon 9 Commercial Launch Operations at Cape Canaveral Air Force Station, Florida. Technical report, FAA, 2013. URL https://www.faa.gov/about/office_org/headquarters_offices/ast/media/20131023_Falcon9V1_1_FAAFONSI.pdf.
- FAA. Final Environmental Assessment and Finding of No Significant Impact for Issuing a License to Virgin Orbit (LauncherOne), LLC for LauncherOne Launches at the Mojave Air and Space Port, Kern County, California. Technical Report July, 2017.
- FAA. Draft Environmental Assessment for SpaceX Falcon Launches at Kennedy Space Center and Cape Canaveral Air Force Station. Technical Report February, FAA, 2020.
- R. C. Farmer and P. G. Anderson. Soot Formation in Rocket Propulsion Systems. *Final Report*, 1995.
- R. C. Farmer, P. G. Anderson, G. C. Cheng, B. L. Myruski, and R. W. Pike. Propellant Chemistry for CFD Applications. Technical report, NASA, 1997.
- J. L. Fisher, R. E. Lindberg, and M. K. Lockwood. Titan explorer entry, descent and landing trajectory design. 2006.
- R. O. Foelsche, J. M. Keen, W. C. Solomont, P. L. Buckley, and E. Corporan. Nonequilibrium combustion model for fuel-rich gas generators. *Journal of Propulsion and Power*, 10(4): 461–472, 1994. ISSN 07484658. doi: 10.2514/3.23796.
- J. Foust. OneWeb founder Wyler calls for responsible smallsat operations, 8 2019a. URL <https://spacenews.com/oneweb-founder-wyler-calls-for-responsible-smallsat-operations/>.
- J. Foust. OneWeb disputes Virgin Orbit lawsuit, says LauncherOne is too expensive, 8 2019b. URL <https://spacenews.com/oneweb-disputes-virgin-orbit-lawsuit-says-launcherone-is-too-expensive/>.
- Frost and Sullivan. UK Spaceport Business Case Evaluation. Technical report, Frost and Sullivan, 2018. URL www.frost.com.
- R. S. Fry. A Century of Ramjet Propulsion Technology Evolution. *Journal of Propulsion and Power*, 20(1):27–58, 2004. ISSN 15333876. doi: 10.2514/1.9178.
- A. Gallice, T. Maury, and E. Olmo. Environmental impact of the exploitation of the Ariane 6 launcher system. *Clean Space Industrial Days*, 2018.
- A. M. Gates. In situ measurements of carbon dioxide, 0.37–4.0 μm particles, and water vapor in the stratospheric plumes of small rockets. *Journal of Geophysical Research*, 107 (D22):4649, 2002. ISSN 0148-0227. doi: 10.1029/2002JD002121. URL <http://doi.wiley.com/10.1029/2002JD002121>.
- P. F. Gath. *CAMTOS-A software suite combining direct and indirect trajectory optimization methods*. PhD thesis, 2003. URL <http://elib.uni-stuttgart.de/opus/volltexte/2003/1273/>.
- A. Goldstein. Space transportation architecture study overview. *Acta Astronautica*, 18:5–12, 1 1988. ISSN 00945765. doi: 10.1016/0094-5765(88)90080-X. URL <https://www.sciencedirect.com/science/article/abs/pii/009457658890080X>.

- D. G. Goodwin, H. K. Moffat, and R. L. Speth. Cantera: An Object-oriented Software Toolkit for Chemical Kinetics, Thermodynamics, and Transport Processes, 2017. URL <http://www.cantera.org>.
- S. Gordon and B. J. McBride. Computer Program for Calculation of Complex Chemical Equilibrium Compositions and Applications I. Analysis. Technical report, NASA, 1994.
- V. Grewe, A. Stenke, M. Plohr, and V. D. Korovkin. Climate functions for the use in multi-disciplinary optimisation in the pre-design of supersonic business jet. Technical report, 2010. URL <http://www.hisacproject.com/>.
- M. D. Griffin and A. John D. On the application of boundary conditions to time dependent computations for quasi one-dimensional fluid flows. *Computers & Fluids*, 5(3):127–137, 9 1977. ISSN 0045-7930. doi: 10.1016/0045-7930(77)90019-6. URL <https://www.sciencedirect.com/science/article/abs/pii/0045793077900196>.
- D. F. Griffiths and D. J. Higham. *Numerical Methods for Ordinary Differential Equations*. Springer, 2010.
- M. Gruss. ULA Targets 2018 for Delta 4 Phase-out, Seeks Relaxation of RD-180 Ban, 2015. URL <http://spacenews.com/ula-targets-2018-for-delta-4-phase-out-seeks-relaxation-of-rd-180-ban/>.
- R. Hernandez and S. Mercer. Carbon deposition characteristics of LO2/HC propellants. In *23rd Joint Propulsion Conference*, number June, Reston, Virginia, 6 1987. American Institute of Aeronautics and Astronautics. doi: 10.2514/6.1987-1855. URL <https://arc.aiaa.org/doi/10.2514/6.1987-1855>.
- S. C. Herndon, J. T. Jayne, P. Lobo, T. B. Onasch, G. Fleming, D. E. Hagen, P. D. Whitefield, and R. C. Miake-Lye. Commercial Aircraft Engine Emissions Characterization of in-Use Aircraft at Hartsfield-Jackson Atlanta International Airport. *Environmental Science & Technology*, 2008. doi: 10.1021/ES072029+.
- A. C. Hindmarsh, P. N. Brown, K. E. Grant, S. L. Lee, R. Serban, D. E. Shumaker, and C. S. Woodward. SUNDIALS: Suite of Nonlinear and Differential/Algebraic Equation Solvers. *ACM Trans. Math. Softw.*, 31(3):363–396, 9 2005. ISSN 0098-3500. doi: 10.1145/1089014.1089020. URL <http://doi.acm.org/10.1145/1089014.1089020>.
- H. Hirakoso, T. Aoki, and T. Ito. A Concept of Lace for Space Plane to Earth Orbit. *International Journal of Hydrogen Energy*, 15(7):495–505, 1990.
- H. Hoshizaki, L. B. Anderson, R. J. Conti, N. Farlow, J. W. Meyer, T. Overcamp, K. O. Redler, and V. Watson. Aircraft wake microscale phenomena. *CIAP Monograph*, 1975.
- M. L. Huber, E. W. Lemmon, L. S. Ott, and T. J. Bruno. Preliminary surrogate mixture models for the thermophysical properties of rocket propellants rp-1 and rp-2. *Energy and Fuels*, 23(6):3083–3088, 2009. ISSN 08870624. doi: 10.1021/ef900216z.
- R. W. Humble, G. N. Henry, and W. J. Larson. *Space Propulsion Analysis and Design*. 1995. ISBN 0070313202.
- IATA. 2036 Forecast Reveals Air Passengers Will Nearly Double to 7.8 Billion, 2017. URL <https://www.iata.org/pressroom/pr/Pages/2017-10-24-01.aspx>.

- ICAO. Icao Environmental Report 2016 (Aviation and Climate Change). Technical report, ICAO, 2016.
- ICAO. Volume IV, Carbon Offsetting and Reduction Scheme for International Aviation (CORSA). *Annex 16 to the Convention on International Civil Aviation*, 2018. URL <https://www.unitingaviation.com/publications/Annex-16-Vol-04/#page=1>.
- A. Ingenito. NOx reduction strategies in scramjet combustors. *Aerospace Science and Technology*, 2016. ISSN 12709638. doi: 10.1016/j.ast.2016.10.020.
- International Civil Aviation Organisation. Air transport, passengers carrier, 2017. URL <https://data.worldbank.org/indicator/IS.AIR.PSGR?end=2017%5C&start=1970%5C&view=chart>.
- International Organization for Standardization. ISO 14040:2006 Environmental management – Life cycle assessment – Principles and framework, 2006a.
- International Organization for Standardization. ISO 14044:2006 Environmental management – Life cycle assessment – Requirements and guidelines, 2006b.
- IPCC. Climate change 2013: the physical science basis. Fifth Assessment Report of the Intergovernmental Panel on Climate Change (IPCC). Technical report, 2013.
- IPCC. Summary for Policymakers. Technical report, 2021.
- C. H. Jackman, D. B. Considine, and E. L. Fleming. Space shuttle's impact on the stratosphere: An update. *Journal of Geophysical Research: Atmospheres*, 101(D7), 1996.
- C. H. Jackman, D. B. Considine, and E. L. Fleming. A global modeling study of solid rocket aluminum oxide emission effects on stratospheric ozone. *Geophysical Research Letters*, 25(6):907–910, 1998. ISSN 00948276. doi: 10.1029/98GL00403.
- H. Johnston. Reduction of stratospheric ozone by nitrogen oxide catalysts from supersonic transport exhaust. *Science*, 173(3996):517–522, 1971. ISSN 00368075. doi: 10.1126/science.173.3996.517.
- A. E. Jones, S. Bekki, and J. A. Pyle. On the atmospheric impact of launching the Ariane 5 rocket. *Journal of Geophysical Research*, 100(D8):16651, 1995. ISSN 0148-0227. doi: 10.1029/95JD01539. URL <http://doi.wiley.com/10.1029/95JD01539>.
- E. Jones, T. Oliphant, P. Peterson, and others. {SciPy}: Open source scientific tools for {Python}. URL <http://www.scipy.org/>.
- N. Jungbluth and C. Meili. Recommendations for calculation of the global warming potential of aviation including the radiative forcing index. *International Journal of Life Cycle Assessment*, 24(3):404–411, 2019. ISSN 16147502. doi: 10.1007/s11367-018-1556-3.
- I. L. Karol, Y. E. Ozolin, and E. V. Rozanov. Effect of space rocket launches on ozone. In *Annales Geophysicae*, volume 10, pages 810–814, 1992. ISBN 0992-7689.
- R. Kee, M. Coltrin, and P. Glarborg. *Chemically Reacting Flow: Theory and Practice*. John Wiley & Sons, 2003.

- D. Koks. On the Use of Vectors, Reference Frames, and Coordinate Systems in Aerospace Analysis. Technical report, 2017. URL <https://www.dst.defence.gov.au/sites/default/files/publications/documents/DST-Group-TR-3309.pdf>.
- R. F. Kulakhmetov and T. L. Pourpoint. Preliminary modeling approach of carbon deposits in fuel rich RP-2/GOX combustion at rocket conditions. *AIAA Scitech 2019 Forum*, 2019. doi: 10.2514/6.2019-1494.
- E. Kyle. Space launch report launch archive, 2019. URL <https://spacelaunchreport.com/>.
- E. J. L. Larson, R. W. Portmann, K. H. Rosenlof, D. W. Fahey, J. S. Daniel, and M. N. Ross. Global atmospheric response to emissions from a proposed reusable space launch system. *Earth's Future*, 5(1):37–48, 1 2017. ISSN 23284277. doi: 10.1002/2016EF000399. URL <http://doi.wiley.com/10.1002/2016EF000399>.
- A. B. Lebedev, A. N. Secundov, A. M. Starik, N. S. Titova, and A. M. Schepin. Modeling study of gas-turbine combustor emission. *Proceedings of the Combustion Institute*, 32 II (2):2941–2947, 2009. ISSN 15407489. doi: 10.1016/j.proci.2008.05.015. URL <http://dx.doi.org/10.1016/j.proci.2008.05.015>.
- D. S. Lee, D. W. Fahey, P. M. Forster, P. J. Newton, R. C. Wit, L. L. Lim, B. Owen, and R. Sausen. Aviation and global climate change in the 21st century. *Atmospheric Environment*, 2009a. ISSN 13522310. doi: 10.1016/j.atmosenv.2009.04.024.
- D. S. Lee, G. Pitari, V. Grewe, K. Gierens, J. E. Penner, A. Petzold, M. J. Prather, U. Schumann, A. Bais, T. Berntsen, D. Iachetti, L. L. Lim, and R. Sausen. Transport impacts on atmosphere and climate: Aviation. *Atmospheric Environment*, 44(37):1–57, 2009b. ISSN 1352-2310. doi: 10.1016/j.atmosenv.2009.06.005. URL <http://dx.doi.org/10.1016/j.atmosenv.2009.06.005>.
- P. D. Lohn and E. Y. Wong. The Effects of Rocket Exhaust on Stratospheric Ozone: Chemistry and Diffusion. Technical report, TRW Space & Electronics Group, 1996.
- P. D. Lohn, E. P. Wong, T. W. Smith, J. R. Edwards, and D. Pilson. Rocket Exhaust Impact on Stratospheric Ozone. Technical Report September, TRW Space & Electronics Group, 1999.
- London Economics. Size & Health of the UK Space Industry 2018 About London Economics. Technical report, London Economics, 2019. URL https://assets.publishing.service.gov.uk/government/uploads/system/uploads/attachment_data/file/774450/LE-SHUKSI_2018-SUMMARY_REPORT-FINAL-Issue4-S2C250119.pdf.
- R. A. Lugo, J. D. Shidner, R. W. Powell, S. M. Marsh, J. A. Hoffman, D. K. Litton, and T. L. Schmitt. Launch Vehicle Ascent Trajectory Simulation Using the Program to Optimize Simulated Trajectories II (POST2). 2017.
- C. A. Maddock, L. Ricciardi, M. West, J. West, K. Kontis, S. Rengarajan, D. Evans, A. Milne, and S. McIntyre. Conceptual design analysis for a two-stage-to-orbit semi-reusable launch system for small satellites. *Acta Astronautica*, 152, 2018. ISSN 00945765. doi: 10.1016/j.actaastro.2018.08.021.
- J. C. Mankins. Highly reusable space transportation: Advanced concepts and the opening of the space frontier. *Acta Astronautica*, 51(10):727–742, 2002. ISSN 00945765. doi: 10.1016/S0094-5765(02)00020-6. URL www.elsevier.com/locate/actaastro.

- M. Masiol and R. M. Harrison. Aircraft engine exhaust emissions and other airport-related contributions to ambient air pollution: A review, 2014. ISSN 18732844.
- B. J. McBride and S. Gordon. Computer Program for Calculation of Complex Chemical Equilibrium Compositions and Applications: II-User Manual and Program Description, 1996.
- B. J. McBride, S. Gordon, M. A. Reno, A. Cleveland, and M. A. Reno. Coefficients for calculating thermodynamic and transport properties of individual species. Technical report, NASA, 1993.
- Q. Mcenteggart and J. Whidborne. A Multiobjective Trajectory Optimisation Method for Planning Environmentally Efficient Trajectories. In *UKACC International Conference on Control*, number September, 2012. ISBN 9781467315609. URL http://ieeexplore.ieee.org/xpls/abs_all.jsp?arnumber=6334618&tag=1.
- S. McKenzie. Campaign set up to oppose spaceport in Sutherland, 11 2018. URL <https://www.bbc.co.uk/news/uk-scotland-highlands-islands-46057479>.
- K. Minschwaner, G. L. Manney, N. J. Livesey, H. C. Pumphrey, H. M. Pickett, L. Froidevaux, A. Lambert, M. J. Schwartz, P. F. Bernath, K. A. Walker, and C. D. Boone. The photochemistry of carbon monoxide in the stratosphere and mesosphere evaluated from observations by the Microwave Limb Sounder on the Aura satellite. *Journal of Geophysical Research Atmospheres*, 115(13):1–9, 2010. ISSN 01480227. doi: 10.1029/2009JD012654.
- A. Mogavero. *Toward automated design of Combined Cycle Propulsion*. PhD thesis, University of Strathclyde, 2016.
- A. Mogavero and R. E. Brown. Modular, fast model for design and optimization of hypersonic vehicle propulsion systems. *Journal of Spacecraft and Rockets*, 55(5): 1261–1281, 2018. ISSN 00224650. doi: 10.2514/1.A33676.
- L. Mondale. Op-ed | Space tourism’s environmental price tag, 2021. URL <https://spacenews.com/op-ed-space-tourisms-environmental-price-tag/>.
- T. J. Muelhaupt, M. E. Sorge, J. Morin, and R. S. Wilson. Space traffic management in the new space era. *Journal of Space Safety Engineering*, 2019. ISSN 24688967. doi: 10.1016/j.jsse.2019.05.007.
- N. Murray, S. Bekki, R. Toumi, and T. Soares. On the uncertainties in assessing the atmospheric effects of launchers. In *Progress in Propulsion Physics*, volume 4, pages 671–688, Les Ulis, France, 3 2013. EDP Sciences. ISBN 978-2-7598-0876-2. doi: 10.1051/eucass/201304671. URL <http://www.eucass-proceedings.eu/10.1051/eucass/201304671>.
- NASA. Program to Optimize Simulated Trajectories II (POST2). URL <https://post2.larc.nasa.gov/latest-version/>.
- NASA. Draft Environmental Assessment for the SpaceX Starship and Super Heavy Launch Vehicle at Kennedy Space Center (KSC). Technical report, NASA, 2019. URL https://netpublic.grc.nasa.gov/main/20190801_Final_DRAFT_EA_SpaceX_Starship.pdf.

- T. Neill, D. Judd, E. Veith, and D. Rousar. Practical uses of liquid methane in rocket engine applications. *Acta Astronautica*, 65(5-6):696–705, 2009. ISSN 00945765. doi: 10.1016/j.actaastro.2009.01.052.
- S. S. Neumann. *Environmental Life Cycle Assessment of Commercial Space Transportation Activities in the United Space*. PhD thesis, The University of Texas at Arlington, 2018.
- G. R. Nickerson and C. W. Johnson. A soot prediction model for the TDK computer program. *AIAA/ASME/SAE/ASEE 28th Joint Propulsion Conference and Exhibit, 1992*, 1992. doi: 10.2514/6.1992-3391.
- G. R. Nickerson, L. D. Dang, and D. E. Coats. Two-Dimensional Kinetic Engineering and Programming Manual. Technical report, Software and Engineering Associates, Inc., 1985.
- C. Niederstrasser. Small Launch Vehicles: A 2018 State of the Industry Survey. *32nd Annual AIAA/USU Conference on Small Satellites*, page 12, 2018. URL <https://digitalcommons.usu.edu/cgi/viewcontent.cgi?article=4118&context=smallsat>.
- C. Niederstrasser. Small Launchers in a Pandemic World-2021 Edition of the Annual Industry Survey. In *Proceedings of the Small Satellite Conference*, 2021.
- NOAA and US Air Force. US standard atmosphere (1976). Technical report, NOAA-S/T, 1976.
- T. F. O'Brien, R. P. Starkey, and M. J. Lewis. Quasi-One-Dimensional High-Speed Engine Model with Finite-Rate Chemistry. *Journal of Propulsion and Power*, 17(6):1366–1374, 2001. doi: 10.2514/2.5889. URL <http://arc.aiaa.org/doi/abs/10.2514/2.5889>.
- J. R. Olds and J. Bradford. SCCREAM (Simulated Combined-Cycle Rocket Engine Analysis Module): A Conceptual RBCC Engine Design Tool. In *33rd AIAA/ASME/SAE/ASEE Joint Propulsion Conference*, 1997.
- J. R. Olds and J. E. Bradford. SCCREAM: A Conceptual Rocket-Based Combined-Cycle Engine Performance Analysis Tool. *Journal of Propulsion and Power*, 17(2):333–339, 3 2001. ISSN 0748-4658. doi: 10.2514/2.5746. URL <http://arc.aiaa.org/doi/10.2514/2.5746>.
- J. R. Olds, J. Bradford, A. Charania, L. Ledsinger, D. McCormick, and K. Sorensen. Hyperion: An SSTO Vision Vehicle Concept Utilizing Rocket-Based Combined Cycle Propulsion. In *9th International Space Planes and Hypersonic Systems and Technologies Conference*, 1999.
- Orbex. SSTL Partners with Orbex for UK Launches, 2019. URL <https://orbex.space/news/sstl-partners-with-orbex-for-uk-launches>.
- Orbex. Orbex set to launch world's most environmentally friendly space rocket, 2021. URL <https://orbex.space/news/orbex-set-to-launch-worlds-most-environmentally-friendly-space-rocket>.
- I. T. Osgerby. Literature Review of Turbine Combustor Modeling and Emissions. *AIAA Journal*, 12(6):743–754, 1974. ISSN 0001-1452. doi: 10.2514/3.49345.
- B. Ostro, R. Broadwin, S. Green, W.-Y. Feng, and M. Lipsett. Fine Particulate Air Pollution and Mortality in Nine California Counties: Results from CALFINE. *Environmental Health Perspectives*, 114(1):29–33, 1 2006. ISSN 0091-6765. doi: 10.1289/ehp.8335. URL <https://ehp.niehs.nih.gov/doi/10.1289/ehp.8335>.

- J. M. Picone, A. E. Hedin, D. P. Drob, and A. C. Aikin. NRLMSISE-00 empirical model of the atmosphere: Statistical comparisons and scientific issues. *J. Geophys. Res.*, 107(A12):1468, 2002. doi: 10.1029/2002JA009430. URL <http://nssdc.gsfc.nasa.gov/space/model/>.
- Planet. Planet - FAQs, 2019a. URL <https://www.planet.com/faqs/>.
- Planet. Planet - About, 2019b. URL <https://www.planet.com/company/>.
- Y. A. Plastinin, G. F. Karabadzak, B. A. Khmelinin, G. G. Baula, and A. V. Rodionov. Advanced model for soot radiation in the plume. *40th AIAA Aerospace Sciences Meeting and Exhibit*, 2002. doi: 10.2514/6.2002-798.
- Y. A. Plastinin, G. F. Karabadzak, B. A. Khmelinin, G. G. Baula, and A. V. Rodionov. Determination of soot particle density and dimension in the LOX/Kerosene engine Booster exhaust from Remote Measurements of Radiation Density. In *2nd International Conference on Green Propellants for Space Propulsion*, 2004.
- Y. A. Plastinin, G. F. Karabadzak, B. A. Khmelinin, G. G. Baula, and A. V. Rodionov. Investigation of soot density in the LOX/kerosene engine booster exhaust of atlas II and atlas III from remote measurements of radiation intensity. *43rd AIAA Aerospace Sciences Meeting and Exhibit - Meeting Papers*, 2005. doi: 10.2514/6.2005-769.
- P. J. Popp, B. A. Ridley, J. A. Neuman, L. M. Avallone, D. W. Toohey, P. F. Zittel, O. Schmid, R. L. Herman, R. S. Gao, M. J. Northway, J. C. Holecek, D. W. Fahey, T. L. Thompson, K. K. Kelly, J. G. Walega, F. E. Grahek, J. C. Wilson, M. N. Ross, and M. Y. Danilin. The emission and chemistry of reactive nitrogen species in the plume of an Athena II solid-fuel rocket motor. *Geophysical Research Letters*, 29(18):34–1, 9 2002. ISSN 00948276. doi: 10.1029/2002GL015197. URL <http://doi.wiley.com/10.1029/2002GL015197>.
- A. E. Potter. Environmental effects of the Space Shuttle. Technical report, NASA, 1978. URL <https://ntrs.nasa.gov/search.jsp?R=19780044943>.
- M. J. Prather, M. M. García, A. R. Douglass, C. H. Jackman, M. K. W. Ko, and N. D. Sze. The space shuttle's impact on the stratosphere. *Journal of Geophysical Research*, 95(D11): 18583, 1990. ISSN 0148-0227. doi: 10.1029/JD095iD11p18583. URL <http://doi.wiley.com/10.1029/JD095iD11p18583>.
- J. L. Prince and S. A. Striepe. Mars Reconnaissance Orbiter Operational Aerobraking Phase Assessment. 2007.
- C. Rackauckas and Q. Nie. DifferentialEquations.jl – A Performant and Feature-Rich Ecosystem for Solving Differential Equations in Julia. *Journal of Open Research Software*, 5(1):15, 2017. ISSN 2049-9647. doi: 10.5334/jors.151. URL <http://openresearchsoftware.metajnl.com/articles/10.5334/jors.151/>.
- V. Ramaswamy, O. Boucher, J. Haugh, D. Hauglustaine, J. Haywood, G. Myhre, T. Nakajima, G. Shi, S. Solomon, R. Betts, R. Charlson, C. Chuang, J. S. Daniel, A. Del Genio, R. van Dorland, J. Feichter, J. Fuglestedt, P. M. de F Forster, S. J. Ghan, A. Jones, J. T. Kiehl, D. Koch, C. Land, J. Lean, U. Lohmann, K. Minschwaner, J. E. Penner, D. L. Roberts, H. Rodhe, G. J. Roelofs, L. D. Rotstayn, T. L. Schneider, U. Schumann, S. E. Schwartz, M. D. Schwarzkopf, K. P. Shine, S. Smuth, D. S. Stevenson, F. Stordal, I. Tegen, and Y. Zhang. Radiative forcing of climate change. In *Climate Change 2001: The Scientific Basis*, volume 94, pages 363–373. 2001. doi: 10.1023/A:1026752230256.

- A. V. Rao. A Survey of Numerical Methods for Optimal Control. *Advances in the Astronautical Sciences*, 135(January 2010), 2010.
- P. A. Ritter. Optimization and Design for Heavy Lift Launch Vehicles. page 178, 2012.
- RocketLab. Rocket Lab Celebrates 100th Rutherford Engine Build, 2019. URL <https://www.rocketlabusa.com/news/updates/rocket-lab-celebrates-100th-rutherford-engine-build/>.
- C. Rosema, J. Doyle, L. Auman, M. Underwood, and W. B. Blake. Missile DATCOM User's Manual - 2011 Revision. Technical report, U.S. Army Aviation & Missile Research, 2011.
- M. N. Ross and P. M. Sheaffer. Radiative forcing caused by rocket engine emissions. *Earth's Future*, 2(4):2013EF000160, 2014. ISSN 2328-4277. doi: 10.1002/2013EF000160. URL <http://dx.doi.org/10.1002/2013EF000160>.
- M. N. Ross, J. O. Ballenthin, R. B. Gosselin, R. F. Meads, P. F. Zittel, J. R. Benbrook, and W. R. Sheldon. In-situ measurement of Cl₂ and O₃ in a stratospheric solid rocket motor exhaust plume. *Geophysical Research Letters*, 24(14):1755–1758, 7 1997a. ISSN 00948276. doi: 10.1029/97GL01592. URL <http://doi.wiley.com/10.1029/97GL01592>.
- M. N. Ross, J. R. Benbrook, W. R. Sheldon, P. F. Zittel, and D. L. McKenzie. Observation of stratospheric ozone depletion in rocket exhaust plumes. *Nature*, 390(6655):62–64, 11 1997b. ISSN 00280836. doi: 10.1038/36318. URL <http://www.nature.com/doi/10.1038/36318>.
- M. N. Ross, R. R. Friedl, D. E. Anderson, G. Ash, M. R. Berman, B. Gandrud, W. T. Rawlins, E. C. Richard, and A. F. Tuck. Study blazing new trails into effects of aviation and rocket exhaust in the atmosphere. *Eos, Transactions American Geophysical Union*, 80(38):437, 1999. ISSN 0096-3941. doi: 10.1029/99EO00316. URL <http://doi.wiley.com/10.1029/99EO00316>.
- M. N. Ross, D. W. Toohey, W. T. Rawlins, E. C. Richard, K. K. Kelly, A. F. Tuck, M. H. Proffitt, D. E. Hagen, A. R. Hopkins, P. D. Whitefield, J. R. Benbrook, and W. R. Sheldon. Observation of stratospheric ozone depletion associated with Delta II rocket emissions. *Geophysical Research Letters*, 27(15):2209–2212, 8 2000. ISSN 00948276. doi: 10.1029/1999GL011159. URL <http://doi.wiley.com/10.1029/1999GL011159>.
- M. N. Ross, M. Y. Danilin, D. K. Weisenstein, and M. K. W. Ko. Ozone depletion caused by NO and H₂O emissions from hydrazine-fueled rockets. *Journal of Geophysical Research: Atmospheres*, 109(D21):n/a–n/a, 11 2004. ISSN 01480227. doi: 10.1029/2003JD004370. URL <http://doi.wiley.com/10.1029/2003JD004370>.
- M. N. Ross, D. Toohey, M. Peinemann, and P. Ross. Limits on the Space Launch Market Related to Stratospheric Ozone Depletion. *Astropolitics*, 7(1):50–82, 3 2009. ISSN 1477-7622. doi: 10.1080/14777620902768867. URL <https://www.tandfonline.com/doi/full/10.1080/14777620902768867>.
- M. N. Ross, M. Mills, and D. Toohey. Potential climate impact of black carbon emitted by rockets. *Geophysical Research Letters*, 37(24):1–6, 2010. ISSN 00948276. doi: 10.1029/2010GL044548.

- R. Rückerl, A. Schneider, S. Breitner, J. Cyrus, and A. Peters. Health effects of particulate air pollution: A review of epidemiological evidence. *Inhalation Toxicology*, 23(10):555–592, 8 2011. ISSN 0895-8378. doi: 10.3109/08958378.2011.593587. URL <http://www.tandfonline.com/doi/full/10.3109/08958378.2011.593587>.
- O. Schmid. Size-resolved particle emission indices in the stratospheric plume of an Athena II rocket. *Journal of Geophysical Research*, 108(D8):4250, 2003. ISSN 0148-0227. doi: 10.1029/2002JD002486. URL <http://doi.wiley.com/10.1029/2002JD002486>.
- C. Segal. *The Scramjet Engine*. Cambridge University Press, 2009. ISBN 9780511627019. doi: 10.1017/CBO9780511627019. URL <http://ebooks.cambridge.org/ref/id/CBO9780511627019>.
- A. H. Shapiro. *The Dynamics and Thermodynamics of Compressible Fluid Flow Vol. 1*. New York, I, 1953.
- F. Simmons. *Rocket Exhaust Plume Phenomenology*. American Institute of Aeronautics and Astronautics, Inc., Washington, DC, 1 2000. ISBN 978-1-884989-08-7. doi: 10.2514/4.989087. URL <http://arc.aiaa.org/doi/book/10.2514/4.989087>.
- M. Sippel, O. Trivailo, L. Bussler, S. Lipp, C. Valluchi, S. Kaltenhäuser, and R. Molina. Evolution of the spaceliner towards a reusable tsto-launcher. In *Proceedings of the International Astronautical Congress, IAC*, 2016. URL <https://elib.dlr.de/107554/1/IAC-16D2.4.3.pdf>.
- Skyrora. Ecosene Rocket Fuel, 2021. URL <https://www.skyrora.com/ecosene>.
- M. K. Smart and M. R. Tetlow. Orbital delivery of small payloads using hypersonic airbreathing propulsion. In *Journal of Spacecraft and Rockets*, volume 46, pages 117–125, 2009. doi: 10.2514/1.38784.
- G. P. Smith, D. M. Golden, M. Frenklach, N. W. Moriarty, B. Eiteneer, M. Goldenberg, C. T. Bowman, R. K. Hanson, S. Song, W. C. Gardiner Jr., V. V. Lissianski, and Z. Qin. GRI-Mech 3.0. URL <http://combustion.berkeley.edu/gri-mech/version30/text30.html>.
- W. R. Smith and R. W. Missen. Chemical reaction equilibrium analysis: theory and algorithms. *New Yorkt Wiley—Interscience*, 139, 1982.
- E. Song and J. Song. Modeling of kerosene combustion under fuel-rich conditions. *Advances in Mechanical Engineering*, 9(7):1–11, 2017. ISSN 16878140. doi: 10.1177/1687814017711388.
- Space Foundation. The Space Report 2021 Q2. Technical report, 2021.
- Space Launch Report. Pegasus Datasheet, 2016. URL <https://www.spacelaunchreport.com/pegasus.html>.
- Space Launch Report. Falcon 9 launch report, 2021. URL <https://www.spacelaunchreport.com/falcon9ft.html>.
- Spaceflight Industries. Spaceflight Industries - Homepage, 2020. URL <https://spaceflight.com/>.
- SpaceLaunchReport.com. Space Launch Report: Delta IV Data Sheet, 2018. URL <http://www.spacelaunchreport.com/delta4.html>.

- SpaceWorks. 2019 Nano/Microsatellite Market Forecast, 9th Edition. Technical report, Space Works, 2019.
- SpaceX. Falcon User's Guide. Technical report, 2019. URL https://www.spacex.com/sites/spacex/files/falcon_users_guide_10_2019.pdf.
- Spire. About Spire, 2019. URL <https://www.spire.com/en/spire/about-spire>.
- SSTL. SSTL - About Us, 2019. URL <https://www.sstl.co.uk/about-us>.
- G. P. Sutton and O. Biblarz. *Rocket Propulsion Elements*. John Wiley & Sons, 8th edition, 2010. ISBN 978-0470080245.
- T. Tanbay, M. B. Uca, and A. Durmayaz. Assessment of NO_x emissions of the Scimitar engine at Mach 5 based on a thermodynamic cycle analysis. *International Journal of Hydrogen Energy*, 2019. ISSN 03603199. doi: 10.1016/j.ijhydene.2019.02.133.
- A. Tewari. *Atmospheric and Space Flight Dynamics: Modeling and Simulation with MATLAB® and Simulink®*. 2007. ISBN 9780817644376.
- S. M. Torrez, D. J. Dalle, and J. F. Driscoll. New Method for Computing Performance of Choked Reacting Flows and Ram-to-Scram Transition. *Journal of Propulsion and Power*, 29(2):433–445, 2013a. ISSN 0748-4658. doi: 10.2514/1.B34496. URL <http://arc.aiaa.org/doi/10.2514/1.B34496>.
- S. M. Torrez, D. J. Dalle, and J. F. Driscoll. New method for computing performance of choked reacting flows and ram-to-scram transition. *Journal of Propulsion and Power*, 29(2):433–445, 2013b. ISSN 07484658. doi: 10.2514/1.B34496.
- F. Toso and C. A. Maddock. Deployed payload analysis for a single stage to orbit spaceplane. *Proceedings of the International Astronautical Congress, IAC*, 2016. ISSN 00741795.
- UK Parliament. Space Industry Act, 2018. URL <https://www.legislation.gov.uk/ukpga/2018/5/contents/enacted>.
- United Launch Alliance. Delta IV User's Guide. Technical report, 2013. URL <https://www.ulalaunch.com/docs/default-source/rockets/delta-iv-user's-guide.pdf>.
- D. A. Vallero. *Air Pollution Calculations*. Elsevier, 1 2019. ISBN 978-0-12-814934-8. doi: 10.1016/B978-0-12-814934-8.00001-6.
- A. K. Varma, A. U. Chatwani, and F. V. Bracco. Studies of premixed laminar hydrogen air flames using elementary and global kinetics models. *Combustion and Flame*, 64(2): 233–236, 1986. ISSN 00102180. doi: 10.1016/0010-2180(86)90060-X.
- R. Varvill and A. Bond. A Comparison of Propulsion Concepts for SSTO Reusable Launchers. *Journal of the British Interplanetary Society*, 56:108–117, 2003.
- T. Villela, C. A. Costa, A. M. Brandão, F. T. Bueno, and R. Leonardi. Towards the thousandth CubeSat: A statistical overview. *International Journal of Aerospace Engineering*, 2019, 2019. ISSN 16875974. doi: 10.1155/2019/5063145.
- K. Viswanath, K. S. Brentner, D. A. Levin, and S. F. Gimelshein. Investigation of Soot Combustion in Underexpanded Jet Plume Flows. *Journal of Thermophysics and Heat Transfer*, 19(3):282–293, 2005. ISSN 0887-8722. doi: 10.2514/1.12956. URL <https://arc.aiaa.org/doi/pdf/10.2514/1.12956>.

- T.-S. Wang. Thermophysics Characterization of Kerosene Combustion. *Journal of Thermophysics and Heat Transfer*, 15(2):140–147, 2001. URL <http://citeseerx.ist.psu.edu/viewdoc/download?doi=10.1.1.476.1314&rep=rep1&type=pdf>.
- D. Wasiuk, M. Lowenberg, and D. Shallcross. An aircraft performance model implementation for the estimation of global and regional commercial aviation fuel burn and emissions. *Transportation Research Part D: Transport and Environment*, 35:142–159, 3 2015. ISSN 13619209. doi: 10.1016/j.trd.2014.11.022.
- D. K. Wasiuk, M. A. H. Khan, D. E. Shallcross, and M. H. Lowenberg. A commercial aircraft fuel burn and emissions inventory for 2005-2011. *Atmosphere*, 7(6):1–14, 2016. ISSN 20734433. doi: 10.3390/atmos7060078.
- D. W. Waugh and T. M. Hall. Age of stratospheric air: Theory, observations, and models. *Reviews of Geophysics*, 40(4), 2002. ISSN 87551209. doi: 10.1029/2000RG000101.
- D. W. Way and J. R. Olds. Scores: Web-based rocket propulsion analysis for space transportation system design. In *35th Joint Propulsion Conference and Exhibit*, 1999. doi: 10.2514/6.1999-2353. URL <http://titan.cad.gatech.edu/~dwway/SCORES>.
- R. Whitehouse and J. Reines. Chaos erupts in Cornwall Council chamber After Spaceport funding vote, 11 2019. URL <https://www.cornwalllive.com/news/cornwall-news/chaos-erupts-cornwall-council-chamber-3579848>.
- A. R. Wilson. *Advanced Methods of Life Cycle Assessment for Space Systems*. PhD thesis, University of Strathclyde, 2019.
- World Health Organisation. Fact Sheet: Climate Change and Health, 2019. URL <https://www.who.int/news-room/fact-sheets/detail/climate-change-and-health>.
- D. Wuebbles, M. Gupta, and M. K. W. Ko. Evaluating the Impacts of Aviation on Climate Change. *Eos, Transactions American Geophysical Union*, 88(14):157, 2007. ISSN 0096-3941. doi: 10.1029/2007EO140001.
- D. A. Young, T. Kokan, I. Clark, C. Tanner, A. Wilhite, A. Flexible, and R. Surface. Lazarus: A SSTO Hypersonic Vehicle Concept Utilizing RBCC and HEDM Propulsion Technologies. *14th AIAA/AHI Space Planes and Hypersonic Systems and Technologies Conference*, pages 1–14, 2006. doi: doi:10.2514/6.2006-8099. URL <http://soliton.ae.gatech.edu/labs/ssdl/papers/conferencePapers/AIAA-2006-8099.pdf>.
- J. Yu and C. Lee. Prediction of non-equilibrium kinetics of fuel-rich kerosene/LOX combustion in gas generator. *Journal of Mechanical Science and Technology*, 21(8): 1271–1283, 2007. ISSN 1738494X. doi: 10.1007/BF03179044.
- V. P. Zhukov. The impact of methane oxidation kinetics on a rocket nozzle flow. *Acta Astronautica*, 2019. ISSN 00945765. doi: 10.1016/j.actaastro.2019.01.001.

A | PROPULSION TABLES

A.1 Merlin1D Vacuum

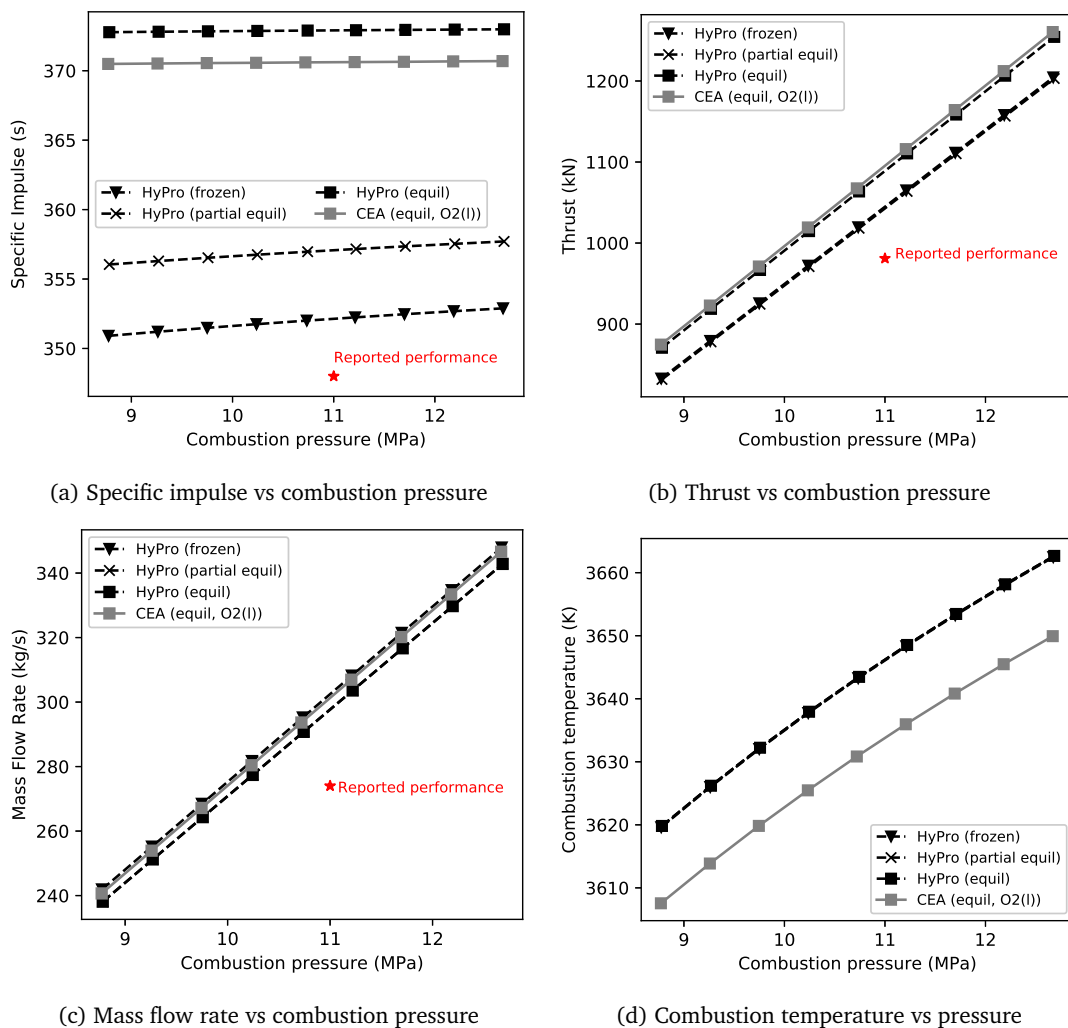
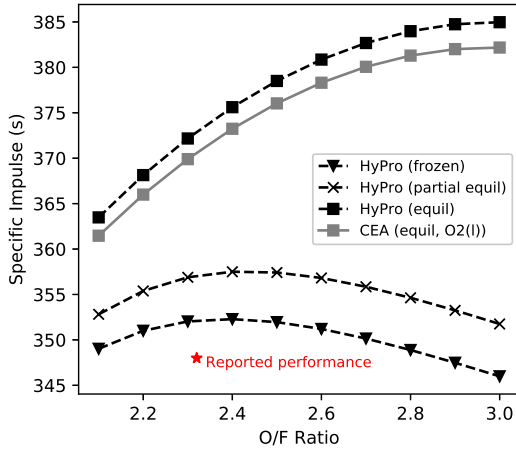
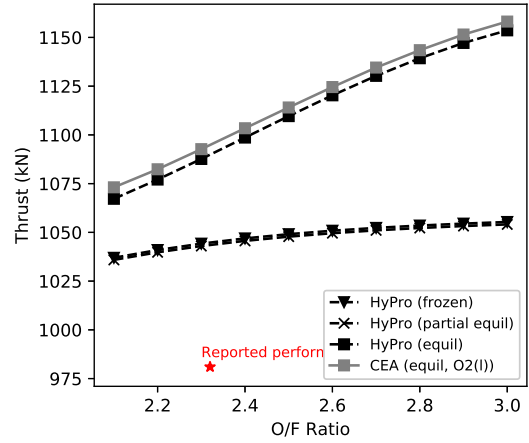


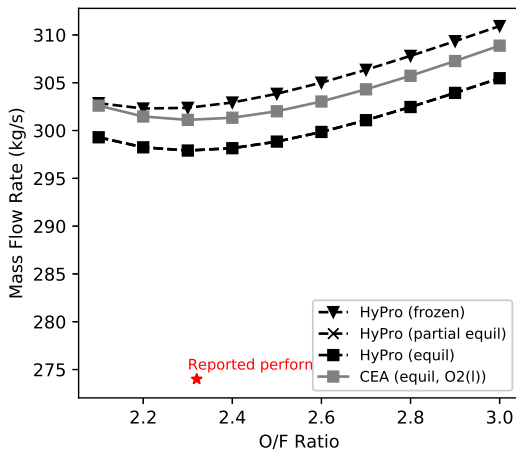
Fig. A.1 Performance of a kerosene fuelled rocket engine based on the Merlin 1D Vacuum engine across a range of combustion pressures. Results shown frozen flow, partial equilibrium (freezing at the nozzle throat) and equilibrium flow to the nozzle exit are shown.



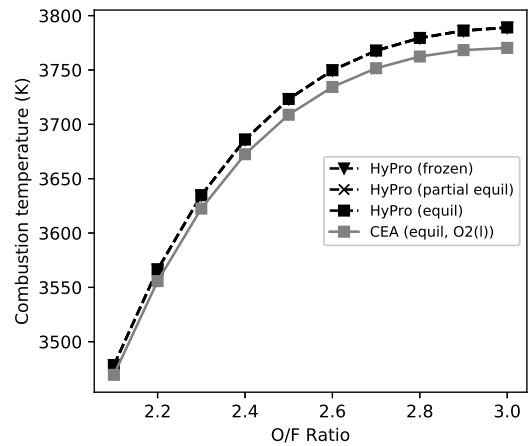
(a) Specific impulse vs O/F ratio



(b) Thrust vs O/F ratio

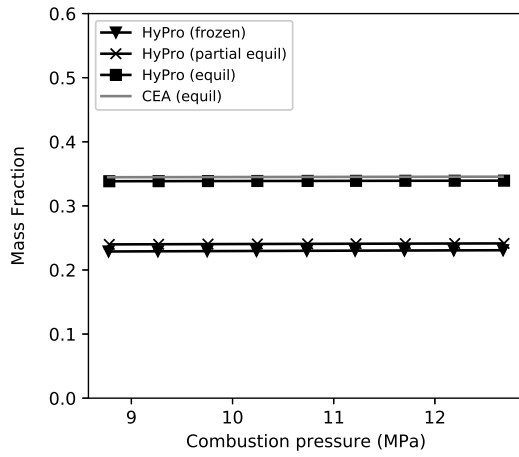


(c) Mass flow rate vs O/F ratio

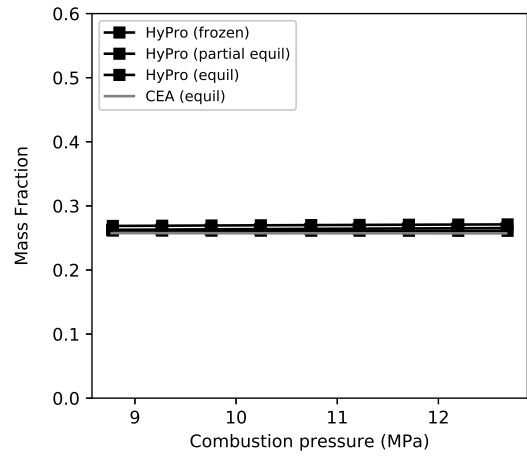


(d) Combustion temperature vs O/F ratio

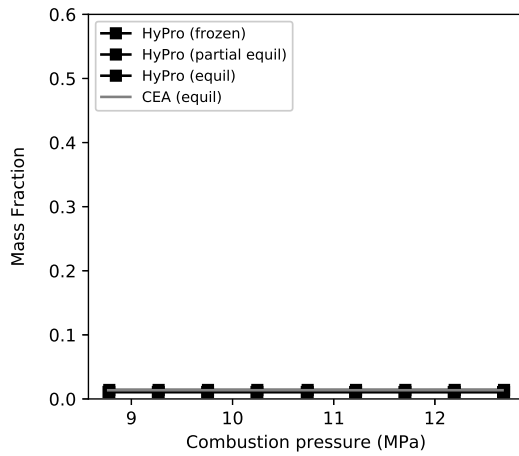
Fig. A.2 Performance of a kerosene fuelled rocket engine based on the Merlin 1D Vacuum engine across a range of mixture ratios. Results shown frozen flow, partial equilibrium (freezing at the nozzle throat) and equilibrium flow to the nozzle exit are shown.



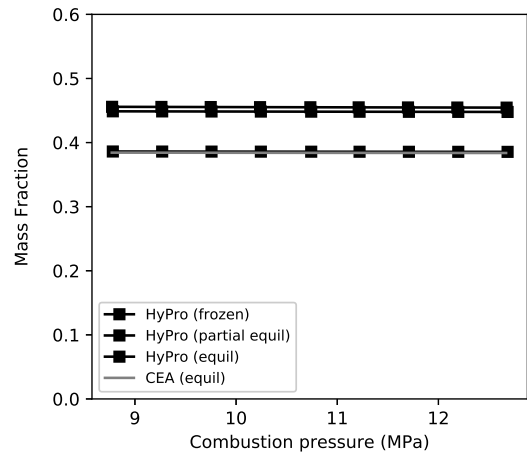
(a) CO₂



(b) H₂O

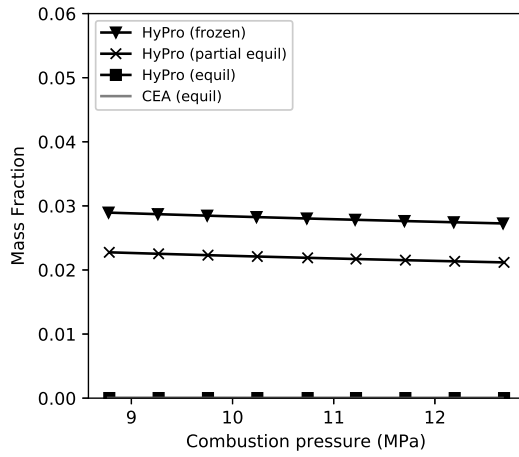


(c) H₂

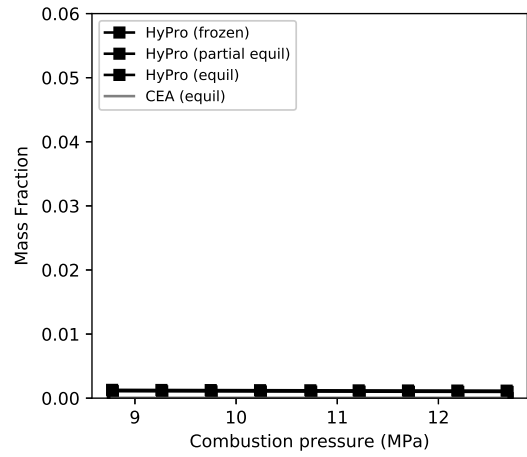


(d) CO

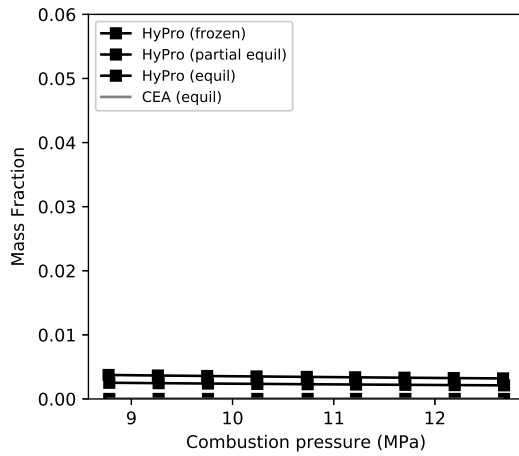
Fig. A.3 Major species emissions of a kerosene fuelled rocket engine based on the Merlin 1D Vacuum engine across a range of combustion pressure. Results shown frozen flow, partial equilibrium (freezing at the nozzle throat) and equilibrium flow to the nozzle exit are shown.



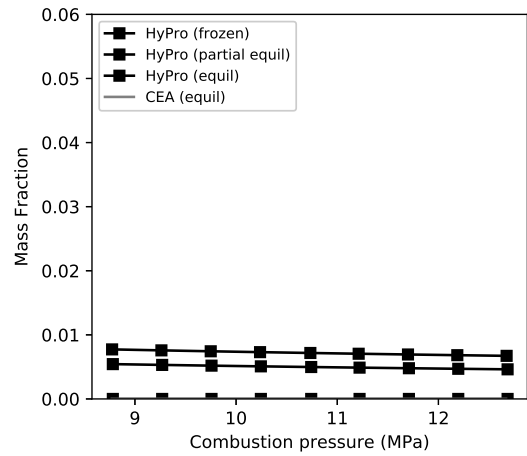
(a) OH



(b) H

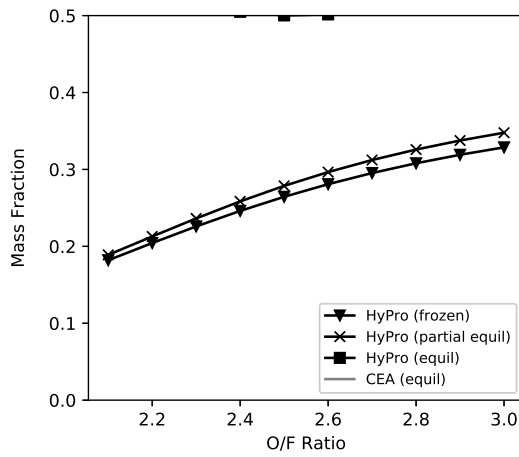


(c) O

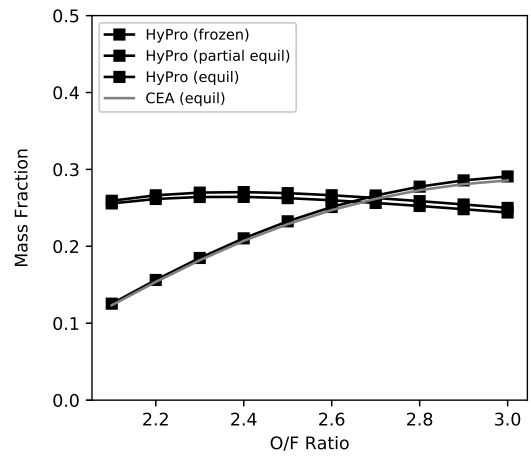


(d) O₂

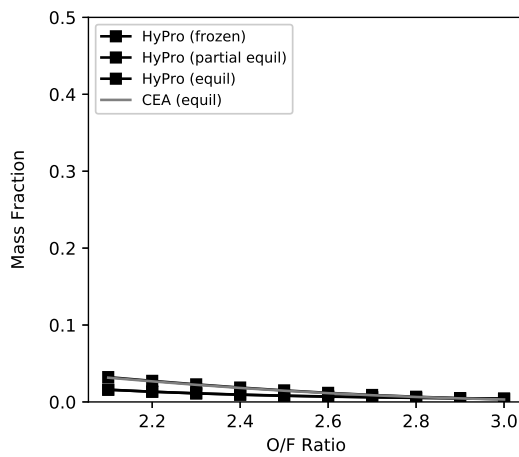
Fig. A.4 Minor species emissions of a kerosene fuelled rocket engine based on the Merlin 1D Vacuum engine across a range of combustion pressure. Results shown frozen flow, partial equilibrium (freezing at the nozzle throat) and equilibrium flow to the nozzle exit are shown.



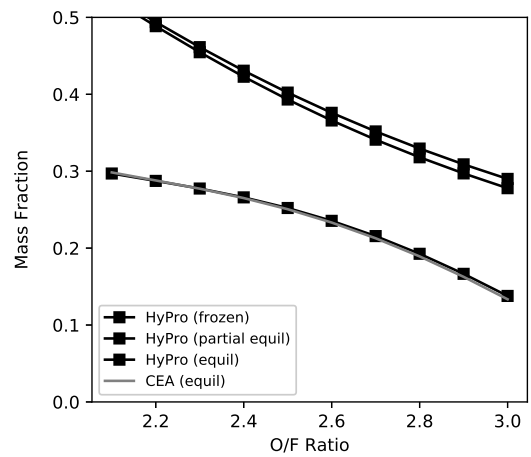
(a) CO₂



(b) H₂O

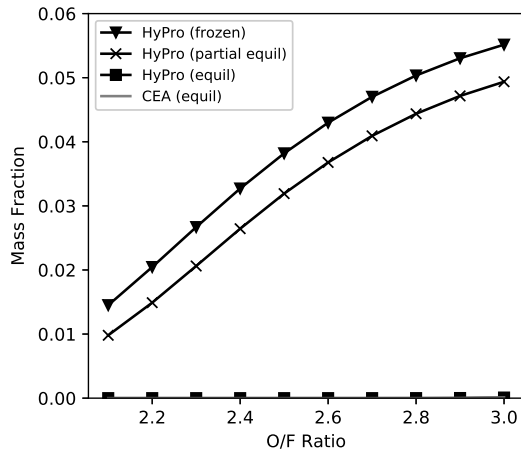


(c) H₂

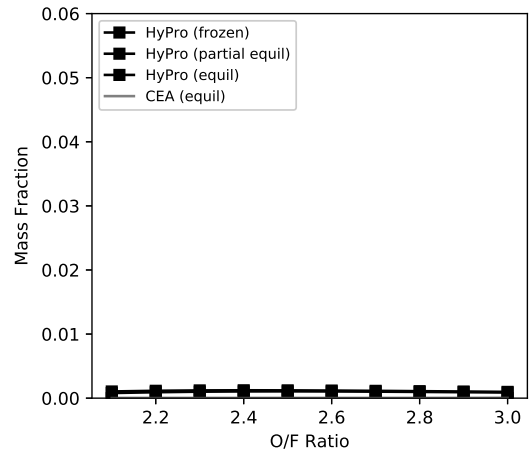


(d) CO

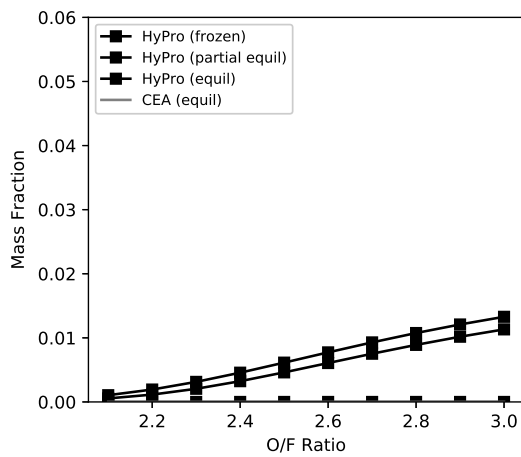
Fig. A.5 Major species emissions of a kerosene fuelled rocket engine based on the Merlin 1D Vacuum engine across a range of mixture ratios. Results shown frozen flow, partial equilibrium (freezing at the nozzle throat) and equilibrium flow to the nozzle exit are shown.



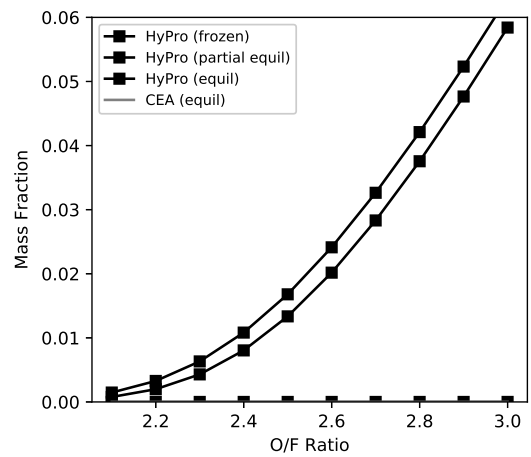
(a) OH



(b) H



(c) O



(d) O₂

Fig. A.6 Minor species emissions of a kerosene fuelled rocket engine based on the Merlin 1D Vacuum engine across a range of mixture ratios. Results shown frozen flow, partial equilibrium (freezing at the nozzle throat) and equilibrium flow to the nozzle exit are shown.